PhD Thesis

Resonance Raman spectroscopy of single wall carbon nanotubes

Alexander Grüneis

Department of Physics
Tohoku University
September, 2004

Acknowledgement

I thank Prof. R. Saito deeply for guiding me through three years PhD course. I am very much indebted to Dr. J. Jiang for stimulating discussions. I am grateful for discussions with Dr. W. Izumida, N. Kobayasi and T. Mesaki. I would like to thank our collaborators Ge. G. Samsonidze and Prof. M. Dresselhaus and Prof. G. Dresselhaus at MIT for many discussions during their visits to Japan and during my visit to MIT in Dec. 2002. I appreciate that they used the graphite force constant fitting program and the matrix elements for optical transition to calculate new experimental configurations. I wish to express my gratitude to Prof. M. A. Pimenta, Prof. A. Jorio and L. G. Cançado at UFMG in Brazil for their experimental findings that were stimulated by the calculations in this thesis, particularly the optical matrix element for nanographite ribbons. I also thank Dr. A. G. Souza Filho from UFC in Brazil for his work on Stokes anti–Stokes ratio Raman spectroscopy for determining the resonance condition in nanotubes. I am indebted to Monbukagakusho for financing my stay in Japan. Part of the work is supported by the 21st century COE program and CREST, JST. Lastly, I thank my family for their continuous support.

Contents

Chapter 1

Introduction

1.1 Purpose of this thesis

A carbon nanotube is a quasi one–dimensional (1D) solid with a diameter of about 1nm and a macroscopic length of up to 1mm. Carbon nanotubes were discovered by Iijima in multi wall form in 1991 [1] and two years later in single wall form [2]. Single wall carbon nanotubes (SWNTs) can be imagined as a rolled–up graphene sheet into a cylinder. The physical properties of SWNTs are determined by the diameter and the angle of rolling up relative to the graphite lattice (also known as chirality). One third of SWNTs are metallic and two thirds are semiconducting with an energy gap, that is inversely proportional to the tube diameter [3, 4]. If the number of carbon atoms around the circumference of the SWNT changes by one, the SWNT can change from semiconductor to metal or vice versa. Such a behaviour does not occur in bulk solid materials and is characteristic for nanomaterials in which quantum mechanics plays an important role. Carbon nanotubes are candidates for many applications in electronic devices such as field emitters [5, 6], field effect transistors [7, 8] or molecular wires [9].

Optical spectroscopy has been proven to be a powerful way to characterize SWNTs. Many experimental results of Raman measurements for bundles [10, 11] and individual tubes [12, 13] are available in the literature. Recently photo–luminescence (PL) spectra of isolated SWNTs have been measured by several groups [14, 15, 16]. Their optical properties are observed at the maxima in the electronic joint density of states (JDOS), known as van Hove singularities (VHSs) [17]. The VHSs are a characteristic of 1D systems and are very important to the optical properties. Optical absorption and the Raman cross section are strongly enhanced (resonance effect) if the laser energy matches the energy separation between the VHSs in the valence and conduction energy bands. Such a strict resonance condition selects only a few SWNTs in the mixed sample that contribute to the spectrum. Although the spectral position has been studied, no detailed investigation on the dependence of the intensity of this optical process on the chiral angle and diameter has been discussed. To explain optical or Raman spectra, a calculation of the scattering processes is needed. The understanding of the efficiency of the optical absorption and emission processes in SWNTs is important for the use of spectroscopy to study and characterize these systems. The purpose of the present thesis is to calculate optical absorption and Raman intensities of graphene and SWNTs. Especially we have calculated electron photon and electron phonon matrix elements. We have developed a set of computer programs for calculating the

matrix elements. Such a calculation involves calculating the electronic and phonon dispersions and the matrix elements for electron photon and electron phonon scattering. The interaction between an electron and a photon is formulated for the solutions to the tight binding equations for electrons in a SWNT. In a similar manner we treat the problem of electron phonon interaction, where we employ a force constant approach for the phonons. Using electron photon and electron phonon matrix elements, many experimental results can be explained as a function of SWNT geometry, such as resonance Raman intensity, photoluminescence spectra, fast optics, relaxation of electron, photoconductivity and IR absorption spectra. In this thesis, we present the calculated optical absorption and resonance Raman spectra.

1.1.1 Organization

The present thesis is organized as follows: In the remaining part of Chapter 1, the backgound for understanding this thesis is given. In Chapter 2, the structure of SWNTs is reviewed and basic definitions of the lattice are given. In Chapter 3, we review the electronic structure of graphene and SWNTs. In Chapter 4, the status of the current research in the field of Raman spectroscopy of single wall carbon nanotubes is reviewed.

From Chapter 4, we will show our original results. In Chapter 5, the formulation of the electron−photon interaction matrix elements for graphite and SWNTs is given, which is one of the main results of this thesis. When we calculate the optical absorption of graphite as a function of the electron wavevector $\mathbf{k}$, we find that a node exists in the optical absorption for special $\mathbf{k}$. The origin of these nodes is investigated and a simple formula for the optical absorption in graphite is derived. These results are extended to SWNTs by adjusting the definition of dipole vector considering the curvature of the SWNT. In SWNTs, the main results of the calculation of electron photon matrix elements are the selection rules for optical transitions in different scattering geometries and the chirality dependence of optical absorption matrix elements. Based on the matrix element, we suggest a possibility for separating different types of semiconducting SWNTs in Sec. 5.7. The selection rules determine the resonance energies for light polarization parallel or perpendicular to the SWNT axis. The new resonance condition for perpendicular polarization works well for explaining experimental Raman spectra that have not been explained previously since they appear in the gap region of the resonance energy for parallel polarization.

In Chapter 6, we calculate the electron phonon interaction matrix elements for graphite and SWNTs, which is also one of the main results. The electron phonon interaction matrix element is strongly anisotropic in $\mathbf{k}$ space, which is responsible for the chirality dependence of Raman intensities.

In Chapter 7, we use the electron phonon matrix elements to assign the experimentally observed double resonance Raman spectra (G'–band) to the phonon branches identified by comparing the electron phonon matrix element to the intensity of Raman peaks. A fitting program is developed to determine the phonon dispersion relations of graphene by double resonance Raman spectroscopy. Analytical expressions for eigenvalues and eigenfunctions of the dynamical matrix are derived. In Chapter 8, a summary and conclusions of the present thesis are given.

1.2 Background

Hereafter in the introduction, we briefly introduce some basic knowledge that is needed for the following chapters.

1.2.1 Hybridization of carbon

The electronic configuration of a free carbon atom is $1s^2 2s^2 2p^2$. When a solid is formed from carbon atoms, the electrons in the 2s and 2p orbitals form so–called hybrid orbitals that point along the chemical bonds. Depending on the crystal that we have, a different number of the hybrid orbitals is required to point from two to four nearest neighbour atoms. Thus carbon forms sp^n hybrid orbitals with $n = 1$ (acetylene), $n = 2$ (graphite and SWNTs) and $n = 3$ (diamond). In this thesis we study sp^2 systems, which crystalize in a planar hexagonal lattice. That is, two 2s electrons and one 2p electron ($2p_x$ or $2p_y$ in the graphene plane) form three sp^2 hybrid orbitals and one $2p_z$ electron which is oriented perpendicular to the graphene plane. The in-plane sp^2 orbitals make strong σ bonds which are for covalent bonding between carbon atoms. The $2p_z$ electron makes a valence π bond, that is relevant to optical experiments with visible light (1eV–3eV). Hereafter we will consider mainly physical properties of π electrons of sp^2–carbon materials.

1.2.2 Synthesis and sample quality of SWNTs

Next, we mention the synthesis of SWNTs. SWNTs can be produced by (1) arc discharge [18], (2) laser ablation [19], (3) chemical vapour deposition (CVD) [20] or (4) the relatively new high pressure carbon mono–oxide (HipCo) process [21]. All methods have in common that production of SWNTs requires small amount of metal catalyst particles such as Co, Ni, Fe, Pd, Y etc. whereas synthesis of multi–wall carbon nanotubes does not require catalysts.

In the arc method, a DC voltage (about 20 V) is applied between two graphite rods placed in a reactor chamber at a helium atmosphere (500 Torr). The negative electrode rod contains the catalyst material from which the SWNTs grow in the chamber.

In the laser ablation process, a graphite target and a water cooled copper collector are put in a heated glass tube (about 1000°) under Ar gas flow at 30 Torr. A pulsed laser beam is irradiated on the graphite target, in which metal catalysts have been implanted. The irradiation causes the graphite and catalyst particles to evaporate. Due to the Ar gas flow, the evaporated particles are swept to the copper collector where they condensate and the SWNTs are formed.

In the CVD process, SWNTs grow from thermally decomposed hydrocarbons such as CH_4 (methane), C_2H_5OH (ethanol), CH_3OH (methanol) and so on. Catalyst particles such as iron are deposited on a Si wafer. This wafer is put into the CVD reactor for nanotube growth.

We now describe in more detail the production process by bias–enhanced CVD [22], since it is a typical and easy–to–use CVD method. A wafer with catalyst particles is put inside the CVD reactor. The experimentalist can let gas and microwave radiation enter the CVD reactor. Furthermore, a potential between the wafer and a metal electrode can be applied. The metal electrode serves as a source of catalyst particles. Microwave radiation is used to decompose the gas into charged fractions of the original molecule. The gas contains carbon atoms and we used methane (CH_4). The charged fractions of the gas are then accelerated in the electric field and deposited on the wafer. Sample preparation is done in three steps: (1) Hydrogen cleaning of

the wafer. Hydrogen gas is inserted to the CVD reactor for 5 minutes and under a pressure of 30 torr. A microwave output power of 400W is used. The bias voltage is zero and the metal electrode is not inside the reactor. (2) Catalyst adhesion. A catalyst bulk material (such as a wire a few cm long) is inserted to the CVD reactor and a bias voltage of –100V is applied between the wire and the wafer. The gas now contains about 0.5% methane (CH_4). A microwave output power of 400W and a pressure of 30 torr is used for 60 seconds. (3) Nanotube growth. A microwave output power of 400W and a pressure of 15 torr is applied for 60 seconds. In Fig. 1.1 we show a scanning electron microscope (SEM) image of a sample produced by the procedure just described. It should be noted that the above procedure is not optimized in any direction. The nanotube growth was found to be very stable and in fact, we can already grow carbon nanotubes by using only step 2 for a sufficiently long time. The sample shown in Fig. 1.1 is raw material. Further treatment, also known as purification such as removal of the catalyst particles is necessary. This can be done by centrifugation [23].

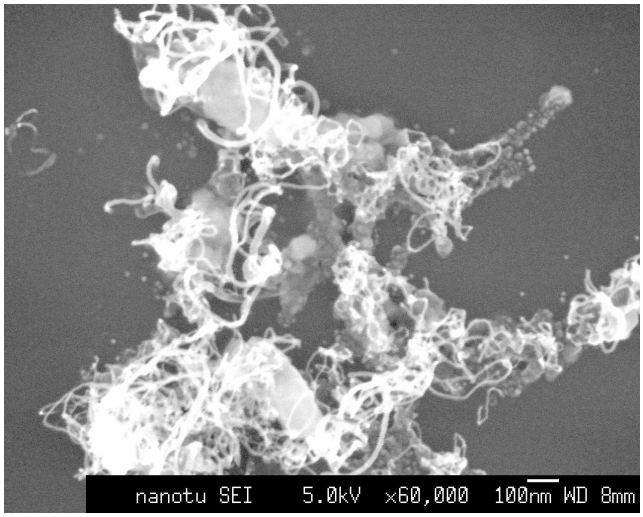

Figure 1.1: SEM image of a bias–enhanced CVD grown nanotube sample. The white particles are catalysts. Nanotube ropes are entangled with one another [22].

In the HipCo process, carbon monoxide mixed with a small amount of iron pentacarbonyl $Fe(CO)_5$ is heated to produce SWNT. The products of thermal decomposition of $Fe(CO)_5$ react to produce iron clusters and CO in gas phase. These metal clusters serve as catalysts on which SWNTs nucleate and grow.

For all methods, we generally get a mixed SWNT sample with different diameter and chirality. Individual SWNTs stick together in the sample by van der Waals forces to form bundles consisting of several tens of individual SWNTs that are in general a mix of metallic and semiconducting SWNTs. Caps close the SWNTs on one end and growth of a SWNT occurs at the surface of the catalyst particle. This model of growth is known as "root growth mode".

Up to now, synthesis of a single geometry (so–called unichiral) sample of SWNTs is not possible and thus the experimentalists try to make samples with a sharp diameter distribution. The mean diameter of SWNTs depends on the metal catalyst and the temperature that is used in the reaction chamber. Generally, in a SWNT sample all tubes have a cap at one end

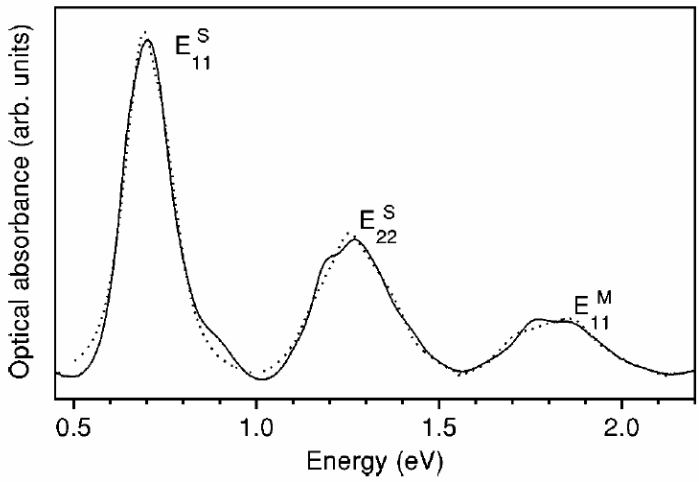

Figure 1.2: Optical absorption spectra of SWNT bundles. The three energetically lowest transitions are labelled [24].

of the SWNT. For a given SWNT, we expect many possible shapes of the closing cap. The number of possible caps and their formation energy varies as a function of chirality. Thus, the chiral distribution of the number of SWNTs is affected by the stability of the cap for a certain chirality and the temperature of the synthesis process. Thus, by changing the temperature for the synthesis, the chiral– or diameter distribution can be controlled.

Another more selective way of controlling the diameter distribution is irradiation of the SWNT sample during growth process by a laser [25]. When the resulting SWNT sample is analyzed after the growth, it was found that a specific diameter, which has a VHS equal to the laser energy used during growth, is missing in the Raman spectra. The reason is due to a strong heating of a SWNT by photo–excited electrons that avoid the crystal growth. Only specific SWNTs, that are resonant are heated and thus, the experimentalist also can selectively avoid growth of certain diameters.

SWNT diameter control is important for making a semiconducting device and other applications. Therefore, in general, SWNT samples must be first evaluated for determining its diameter by Raman spectroscopy. For a single SWNT device, we need to identify chirality which is now possible by single molecule Raman spectroscopy. One way to make isolated SWNT samples, is to dissolve SWNT bundles in a solvent with surfactants such as sodium dodecile sulfate (SDS), ultrasonicate and centrifugate (24 hrs, 20000 G) and then disperse them onto a Si substrate by so–called spinning surface.

Another way is to directly grow SWNTs on a Si substrate from nanometer–sized catalyst particles with a low density. The resulting sample contains a low density of a single or a few SWNTs per square μm and individual tubes can be probed by AFM or Raman spectroscopy. Such a SWNT is called isolated SWNT. As discussed, the synthesis of SWNT samples is still under development and optical spectroscopy has been the most important tool sample charac-

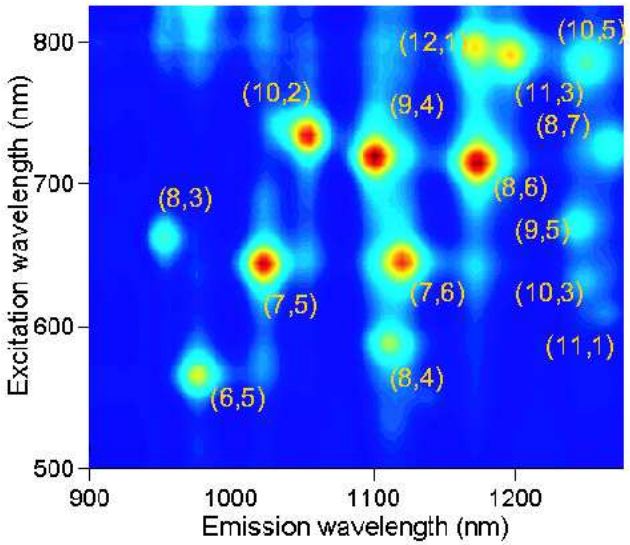

Figure 1.3: Photoluminescene spectra of SWNTs synthesized by a CVD process. The bright areas correspond to absorption of light at E_{22}^S and emission of light at E_{11}^S [26].

terization.

1.2.3 Optical absorption experiments

Optical measurements for isolated SWNTs have been widely observed by resonance Raman spectroscopy (in fact, most samples for isolated SWNT Raman spectra have been made from SWNTs grown by CVD on the substrate directly), photoluminescence and optical absorption. Early experiments were measurements of the optical absorption of bundled SWNTs in transmission or reflection geometry as a function of laser energy.

In Fig. 1.2 we show the measured optical absorption of a SWNT bundle as a function of excitation energy. The low energy spectrum of the absorption curves consists of three distinct peaks [24]. These peaks are attributed to the VHS in the joint density of electronic states (see Chapter 5 for detail). Tight binding calculations suggests, that from the three experimentally observed peaks, two lower peaks come from semiconducting SWNTs (with energies E_{11}^S and E_{22}^S) and the third peak originates from metallic SWNTs with energy E_{11}^M (see Chapter 3). Thus, metallic and semiconducting SWNTs in the mixed sample can be separately seen in the optical absorption spectra.

In the mixed sample, however, it is not possible to measure PL since an excited electron in a semiconducting SWNT relaxes to a nearby metallic SWNT and recombines with the hole without emitting a photon in the metallic SWNTs. Nevertheless, in the SDS wrapped SWNTs, we observe PL spectra for isolated semiconducting SWNTs. In Fig. 1.3 we show an example of a PL spectra. On the vertical and horizontal axes we plot the energies for the excitation at E_{22}^S and the emission at E_{11}^S, respectively. The bright dots in Fig. 1.3 correspond to absorption of light

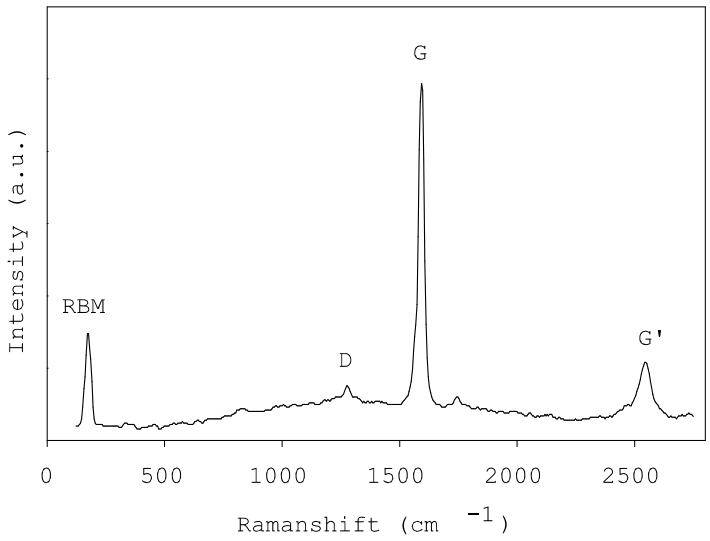

Figure 1.4: Experimental raman spectrum of a SWNT bundle sample with a laser wavelength of 1024 nm. The strongest peaks are indicated by their labels [11].

at E_{22}^S and emission of light at E_{11}^S. In an isolated semiconducting SWNT, the excited electron relaxes to the bottom of the conduction band by emitting phonons and then recombines with a hole at the top of the valence band. This is because the electron−phonon relaxation time (0.1 ps) is much less than electron−photon relaxation time (1 ns) and hot electron emission (PL emission before relaxation to the conduction band bottom) is therefore weak. The different intensities in Fig. 1.3 come from chiral and diameter dependence of the optical absorption or electron phonon interaction strengths or a chiral and diameter dependent distribution of SWNTs. Thus we cannot determine the diameter distribution of the abundance of SWNTs without knowing the matrix elements. The distribution of SWNT diameters and chiralities is thought to be a stronger influence on the PL intensity than the matrix elements.

1.2.4 Raman experiments

Raman spectroscopy is to observe an inelastic scattering of light and probes the vibrational properties by measurement of the energy shift from the incident light. The first (1st) and second (2nd) order Raman scattering are defined by one and two scattering events, respectively. The shift of energy can be either positive or negative, respectively by absorbing or emitting a phonon, which we call anti–Stokes or Stokes Raman processes. One and two phonon Raman spectra are defined, respectively, by one and two phonon emission during a scattering event. Here in this thesis, we will use the other definition, too; that is, the first order and second order Stokes Raman processes. The 1st order Raman spectroscopy always means one phonon Raman spectra.

The 2nd order Raman spectroscopy consists of either (1) two phonon scattering processes

or (2) one phonon and one elastic scattering processes. In all Raman processes, electron photon interactions appear two times in the absorption of a photon and the recombination of the electron–hole pair by emission of a photon. Furthermore, we have one electron phonon interaction in 1st order Raman process and two electron phonon interaction processes in the two phonon Raman process.

The first order (one phonon emission) spectra of a SWNT consist of only two strong bands, the radial breathing mode (RBM) at about 200 cm^{-1} and the graphite derived tangential mode or G band at about 1580 cm^{-1} as shown in Fig. 1.4.

Although group theory predicts 15 or 16 one phonon modes, experimentally only the G band and the RBM are observed [27, 28]. The first order Raman spectrum comes from phonon modes with wavevector $q \approx 0$. Details of Raman experiments will be given in Chapter 4 after introducing the lattice in Chapter 2 and electronic properties of graphite and SWNT in Chapter 3. 2nd order, one phonon Raman spectra can originate from phonons with a non zone–center wavevector ($\mathbf{q} \neq 0$). A typical 2nd order, one phonon Raman signal is the D band at about 1350 cm^{-1} for 2.41 eV laser energy. A characteristic of the D band spectra is that (1) the intensity of the D band depends on the defect concentration in SWNTs and (2) the D band frequency increases with increasing laser energy. A strong 2nd order, two phonon Raman mode is the G' band at 2700 cm^{-1} which is independent from the presence of defects. The intensity of the G band is comparable to the G band intensity. We will calculate the intensity of the G' band in Chapter 7. Combined with resonance conditions, the phonon dispersion relations can be known in the interior of the BZ by this mode (see details in Chapter 7).

Chapter 2

Geometry of single–wall carbon nanotubes

In this chapter we define the geometry of a single wall carbon nanotube and the Brillouin zone for calculating the electron and the phonon energy dispersion relations.

2.1 The unit cell

Graphene is a sheet of graphite with a hexagonal 2D lattice (Fig. 2.1) and the unit cell is a rhombus that contains two atoms as shown in the top–left of Fig. 2.1. Graphene has two inequivalent atoms (A and B) in the unit cell. Here "inequivalent atoms" means that A and B in the unit cell cannot be connected by unit vectors $\mathbf{a}_1$ and $\mathbf{a}_2$. A single–wall carbon nanotube (SWNT) is a graphene sheet that is rolled up into a cylinder with a diameter of a few nanometers (nm) and a macroscopic length of several micrometers (μm) or even up to 1 mm. The unit vectors of graphene have length $a = \sqrt{3}a_0 = |\mathbf{a}_1| = |\mathbf{a}_2| = 0.246$Å, where $a_0 = 1.42$Å is the C–C bond distance and are given by $\mathbf{a}_1 = \left(\frac{1}{2}, \frac{1}{2\sqrt{3}}\right) a$ and $\mathbf{a}_2 = \left(\frac{1}{2}, -\frac{1}{2\sqrt{3}}\right) a$. We specify a SWNT by a pair of integers or chiral indices (n, m) which are coefficients of the unit vectors $\mathbf{a}_1$ and $\mathbf{a}_2$ (Fig. 2.1). The resulting chiral vector $\mathbf{C}_h$ is written as

$$\mathbf{C}_h = n\mathbf{a}_1 + m\mathbf{a}_2 = (n, m). \tag{2.1}$$

The diameter d_t is given by $d_t = L/\pi$ where L is the length of $\mathbf{C}_h$ and the length around the circumference $L = \sqrt{\mathbf{C}_h \cdot \mathbf{C}_h}$. The chiral angle θ of a SWNT is the angle between $\mathbf{a}_1$ and $\mathbf{C}_\mathrm{h}$ and can be written as

$$\theta = \arccos \frac{\mathbf{C}_h \cdot \mathbf{a}_1}{|\mathbf{C}_h||\mathbf{a}_1|} = \arccos \frac{2n + m}{2\sqrt{n^2 + m^2 + nm}}. \tag{2.2}$$

To get the Eq. (2.2), we used the definition of $\mathbf{C}_h$ in Eq. (2.1). The two special cases $\theta = 0$ and $\theta = \pi/6$ are refered to as zigzag and armchair, respectively. Since zigzag and armchair SWNTs have a mirror symmetry along the tube axis, they are so–called achiral SWNTs. All other possible SWNTs are called chiral nanotubes. A chiral nanotube does not have an inversion center. The chiral indices for zigzag SWNTs are given by $(n, 0)$ and armchair SWNTs have

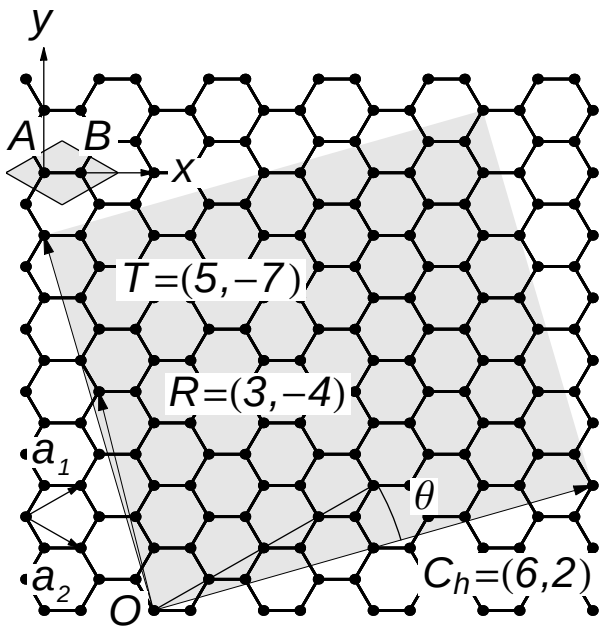

Figure 2.1: Geometry of a (6,2) SWNT. The origin is labelled **0**. The small shaded rhombus with two atoms (A and B) is the unit cell of graphene. It is defined by the graphene unit vectors $\mathbf{a}_1$ and $\mathbf{a}_2$. The large shaded rectangle, defined by the chiral vector $\mathbf{C}_h$ and the translation vector $\mathbf{T}$ is the SWNT unit cell. It contains $N = 52$ atoms of type A (B). The symmetry vector $\mathbf{R}$ generates coordinates of all A (B) atoms in the unit cell when shifting an initial A (B) atom N times by the vector $\mathbf{R}$ and translating back to the first unit cell. The chiral angle θ is the angle between $\mathbf{a}_1$ and $\mathbf{C}_h$. All vectors are expressed in multiples of $\mathbf{a}_1$ and $\mathbf{a}_2$.

chiral indices (n, n). Zigzag and armchair SWNTs have small unit cells compared to those of chiral SWNTs with the same diameter. In fact, the $(n, 0)$ SWNT and the (n, n) SWNT have $4n$ atoms in the unit cell.

In Fig. 2.1 we show the unit cell of an (6, 2) SWNT, which is specified by $\mathbf{C}_h$ around the circumference and by the translational vector $\mathbf{T}$ which is parallel to the axial direction. The direction and length of $\mathbf{T}$ are also determined by (n,m), since we take a vector perpendicular to $\mathbf{C}_h$ from an origin **O**. We go along direction perpendicular to $\mathbf{C}_h$ until we cross a lattice point. The length of $\mathbf{T}$ is determined by the first lattice point we cross. $\mathbf{T}$ is given by

$$\mathbf{T} = t_1\mathbf{a}_1 + t_2\mathbf{a}_2. \tag{2.3}$$

The integer coefficients t_1 and t_2 are calculated by $\mathbf{C}_h \cdot \mathbf{T} = 0$ and dividing the solution pair (t_1, t_2) of this equation by its greatest common divisor (gcd) to ensure that we take the shortest lattice vector. The solution is given by

$$t_1 = \frac{2m+n}{d_R}, \quad t_2 = -\frac{2n+m}{d_R} \quad \text{with} \quad d_R = \gcd(2n+m, 2m+n). \tag{2.4}$$

The expression for d_R in Eq. (2.4) can be simplified by repeatedly using Euclid's law that states $\gcd(i, j) = \gcd(i - j, j)$. We can define d as $d = \gcd(n, m)$ and by applying Euclid's law to d_R

in Eq. (2.4) we obtain

$$\begin{array}{lll} d_R = d & \text{if} & \mathrm{mod}(n-m, 3d) \neq 0 \\ d_R = 3d & \text{if} & \mathrm{mod}(n-m, 3d) = 0. \end{array} \tag{2.5}$$

Here the function mod gives the remainder of an integer division. The area of the SWNT unit cell is the shaded rectangle in Fig. 2.1 and it is equal to $|\mathbf{T} \times \mathbf{C}_h| = |(t_1 m - t_2 n)(\mathbf{a}_1 \times \mathbf{a}_2)|$. The number of graphene unit cells per SWNT unit cell, N is given by dividing the SWNT unit cell area by that of the graphene unit cell, which is $|\mathbf{a}_1 \times \mathbf{a}_2|$. We thus get $N = t_1 m - t_2 n$. Substituting t_1 and t_2 from Eq. (2.4) yields

$$N = \frac{2(n^2 + m^2 + nm)}{d_R}. \tag{2.6}$$

Note that N is an even number. We can now write the circumference L and the length of the unit cell $T = \sqrt{\mathbf{T} \cdot \mathbf{T}}$ by N and d_R as

$$L = a\sqrt{\frac{d_R N}{2}} \quad \text{and} \quad T = a\sqrt{\frac{3N}{2d_R}} = \frac{\sqrt{3}L}{d_R}. \tag{2.7}$$

If we want to generate coordinates of SWNTs, it is useful to define a symmetry vector $\mathbf{R}$. The symmetry vector $\mathbf{R}$ satisfies the following conditions: (a) it is a lattice vector, (b) its component along $\mathbf{C}_h$ is equal to L/N and (c) it is inside the unit cell. These three conditions are satisfied by the following equations:

$$\text{(a) } \mathbf{R} = p\mathbf{a}_1 + q\mathbf{a}_2, \quad \text{(b) } \frac{\mathbf{R} \cdot \mathbf{C}_h}{L} = \frac{L}{N}, \quad \text{and (c)} \quad \frac{1}{N} \leq \frac{\mathbf{R} \cdot \mathbf{T}}{\mathbf{T} \cdot \mathbf{T}} \leq 1. \tag{2.8}$$

Substituting Eq. (2.1) and Eq. 2.8(a) into Eq. 2.8(b), and Eq. (2.3) and Eq. 2.8(a) into Eq. 2.8(c) we have

$$qt_1 - pt_2 = 1 \quad \text{and} \quad 1 \leq pm + qn \leq N. \tag{2.9}$$

for determining the two integers p and q. Translation of a graphene unit cell by $i\mathbf{R}$ for $i = 0 \ldots N-1$ goes over all graphene unit cells in the SWNT unit cell. When we imagine a rolled up SWNT, the application of $\mathbf{R}$ means that we move along the SWNT axis in a spiral–like fashion. The projection of $\mathbf{R}$ to $\mathbf{T}$ is τ, which corresponds to a pitch of the spiral translation and is given by

$$\tau = \frac{\mathbf{T} \cdot \mathbf{R}}{T} = \frac{|\mathbf{C}_h \times \mathbf{R}|}{L} = \frac{(mp - nq)|\mathbf{a}_1 \times \mathbf{a}_2|}{L} = \frac{(mp - nq)T}{N}. \tag{2.10}$$

Thus, if we apply $\mathbf{R}$ for N times, we come back to the equivalent atom position that we started from. N times $\mathbf{R}$ can also be described by shifting $\mathbf{T}$ for M times.

$$N\mathbf{R} = M\mathbf{T} + \mathbf{C}_h \quad \text{and} \quad M = mp - nq. \tag{2.11}$$

The angle of $\mathbf{R}$ around the SWNT axis is $2\pi/N$ which can be obtained by Eq. 2.8(b). Since N is an even number, we can always find two corresponding A (or B) atoms separated by an angle π if we apply $\mathbf{R}$ for $N/2$ times. Although the two atoms are generally shifted by $\tau N/2$ with respect to each other along the SWNT axis, they are on opposite sides, when projected to $\mathbf{C}_h$.

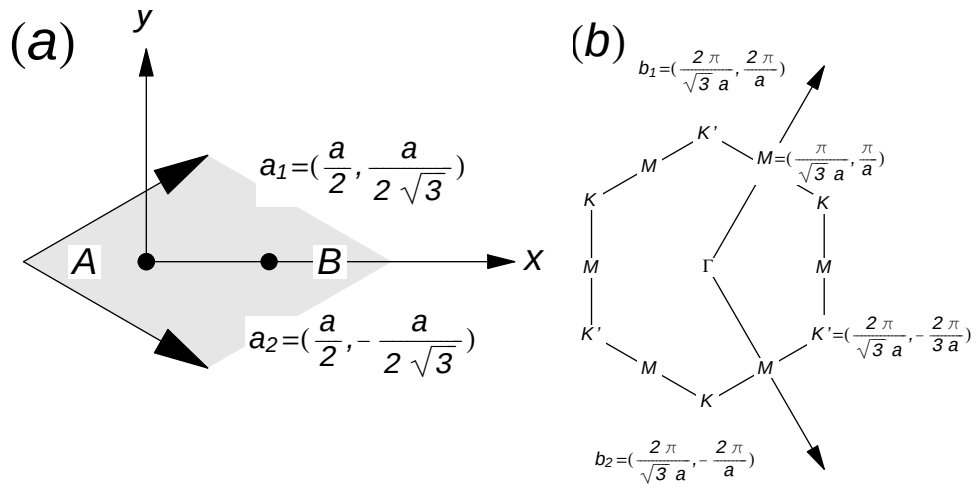

Figure 2.2: (a) The unit cell and (b) the first Brillouin zone (BZ) of graphene. The BZ is given by the reciprocal lattice vectors $\mathbf{b}_1$ and $\mathbf{b}_2$ with $|\mathbf{b}_1| = |\mathbf{b}_2| = \frac{4\pi}{\sqrt{3}a}$. The center of the BZ is the Γ point and the corners of the BZ are K and K' points. Between two nearest K and K' points, there are M points. Equivalent K (M) points are connected to each other by reciprocal lattice vectors.

2.2 Brillouin zone

The unit cell of graphene is shown again in Fig. 2.2(a). The first BZ of graphene is a hexagon as shown in Fig. 2.2(b). The symmetry points in the graphene BZ are BZ center $\mathbf{\Gamma} = (0, 0)$, a hexagonal corner $\mathbf{K} = 1/a(2\pi/\sqrt{3}, 2\pi/3)$ and the center of the hexagonal edge $\mathbf{M} = 1/a(2\pi/\sqrt{3}, 0)$, which are shown in Fig. 2.2. An important fact to notice is that there are two inequivalent [1] K points, with coordinates $\mathbf{K}$ and $\mathbf{K}'$ in the 2D BZ. As we will show in the next section, $\mathbf{K}$ and $\mathbf{K}'$ correspond the Fermi surface points of graphene. The reciprocal lattice vectors $\mathbf{b}_1$ and $\mathbf{b}_2$ for the first Brillouin zone (BZ) of graphene are given by the condition $\mathbf{a}_i \cdot \mathbf{b}_j = 2\pi\delta_{ij}$, where δ_{ij} is the Kronecker delta. The reciprocal lattice vectors are given by $\mathbf{b}_1 = 1/a(2\pi/\sqrt{3}, 2\pi)$ and $\mathbf{b}_2 = 1/a(2\pi/\sqrt{3}, -2\pi)$. The reciprocal lattice vectors of SWNT along the circumference and the nanotube axis, $\mathbf{K}_1$ and $\mathbf{K}_2$, respectively, are defined by

$$\mathbf{K}_1 \cdot \mathbf{T} = 0, \quad \mathbf{K}_1 \cdot \mathbf{C}_h = 2\pi, \quad \mathbf{K}_2 \cdot \mathbf{T} = 2\pi, \quad \text{and} \quad \mathbf{K}_2 \cdot \mathbf{C}_h = 0. \tag{2.12}$$

We substitute vectors $\mathbf{K}_1$ and $\mathbf{K}_2$ that are perpendicular to $\mathbf{C}_h$ and $\mathbf{T}$, respectively. Using definitions of Eq. (2.1) and Eq. (2.3),

$$\mathbf{K}_1 = \frac{1}{N}(-t_2\mathbf{b}_1 + t_1\mathbf{b}_2) \quad \text{and} \quad \mathbf{K}_2 = \frac{1}{N}(m\mathbf{b}_1 - n\mathbf{b}_2). \tag{2.13}$$

Since $\mathbf{K}_1$ is perpendicular to $\mathbf{T}$, and $\mathbf{T}$ is perpendicular to $\mathbf{C}_h$, $\mathbf{K}_1$ is parallel to $\mathbf{C}_h$, when we use parallel axes for real and reciprocal space x, y and k_x, k_y. A similar argument can be used

[1] We use "inequivalent K points" to express that K and K' points are not connected by reciprocal lattice vectors.

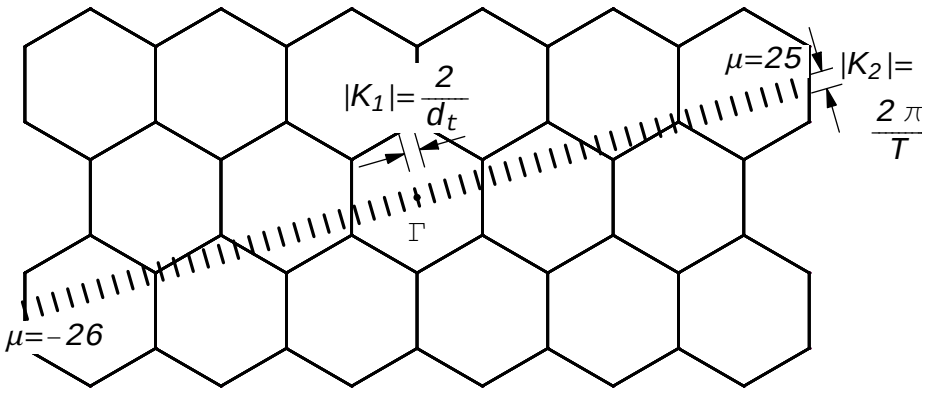

Figure 2.3: The first Brillouin zone (BZ) of (6,2) SWNT is given by the set of $N = 52$ parallel lines called cutting lines. The origin at the Γ point is marked by a dot. The distances between two adjacent cutting lines and the length of a cutting line are shown. The borders of the SWNT BZ are the cutting lines with indices $\mu = -26$ and $\mu = 25$.

for $\mathbf{K}_2$, which is parallel to $\mathbf{T}$. The lengths of $\mathbf{K}_1$ and $\mathbf{K}_2$ are given by

$$|\mathbf{K}_1| = \frac{2\pi}{L} = \frac{2}{d_t} \quad \text{and} \quad |\mathbf{K}_2| = \frac{2\pi}{T}. \tag{2.14}$$

The BZ of a SWNT is given by a set of N parallel cutting lines with length $|\mathbf{K}_2|$ and the separation between adjacent SWNTs is given by $|\mathbf{K}_1|$. The possible $\mathbf{k}$ values of a SWNT is then given by

$$\mathbf{k} = \mu\mathbf{K}_1 + k\frac{\mathbf{K}_2}{|\mathbf{K}_2|} \quad \text{with} \quad \mu = -\frac{N}{2}, \ldots, \frac{N}{2} - 1 \quad \text{and} \quad -\frac{\pi}{T} \leq k < \frac{\pi}{T}. \tag{2.15}$$

In Fig. 2.3 an example of the allowed 1D BZ for a (6,2) SWNT is shown in which $N = 52$, $d_t = 0.565$ nm and $T = 1.536$ nm. Each cutting line corresponds to a 1D BZ and N cutting lines give different electron and phonon subbands. Due to the symmetry of the Hamiltonian, we have for all energy bands $E(\mathbf{k}) = E(-\mathbf{k})$ and thus all subbands with $\mu = 1 \ldots N/2 - 1$ are doubly degenerate with subbands $\mu = -1 \ldots - N/2 + 1$. The subbands with indices $\mu = 0$ and $\mu = -N/2$ are not degenerate. The degenerate subbands are hereafter labelled by E_μ and the non–degenerate subbands are labelled A_1 ($\mu = 0$) and A_2 ($\mu = -N/2$). The A_1 band occurs at a high energy for all (n, m) SWNTs because it crosses Γ point of the graphene BZ. The A_2 band location can occur at an electron energy that is accesible by optical spectroscopy, as we will show in the next Chapter. In armchair SWNTs the A_2 band crosses both the K and K' point and is hereafter referred to as "metallic band".

Chapter 3

Electronic structure of carbon nanotubes

The tight binding method is used for calculating the electronic dispersion of a graphene sheet and SWNTs. Analytical expressions of the tight binding method for the π electrons are given.

3.1 Electronic structure of graphene

A simple tight binding method (or linear combination of atomic orbitals, LCAO) is used to calculate the electronic energy dispersion relation, that is the energy E as a function of wavevector $\mathbf{k}$. In the tight binding approximation of a crystal, the eigenfunctions of electrons are made up from corresponding atomic orbitals. Per one unit cell of graphene, we have 5 atomic orbitals (1s, 2s and three 2p) from each A and B atom, which give 10 atomic orbitals all together. Hereafter we consider only 4 valence electrons (2s and 2p) and neglect 1s electrons. In fact, the 1s orbital of a carbon atom is 258 eV below the vacuum level and thus the 1s energy bands are considered to be the same as atomic levels. The orbitals are labelled by their wavefunction (2s, $2p_x$, $2p_y$, $2p_z$) and atom index (A or B) as: $2s^A$, $2p_x^A$, $2p_y^A$, $2p_z^A$ and $2s^B$, $2p_x^B$, $2p_y^B$, $2p_z^B$. These 8 orbitals from the atoms make 8 electronic bands in the solid. The electron wavefunction for band with index $\jmath$ is given by given by

$$\Psi^\jmath(\mathbf{k},\mathbf{r}) = \sum_{s=2s^A \ldots 2p_z^B} c_s^\jmath(\mathbf{k})\Phi_s(\mathbf{k},\mathbf{r}), \quad (\jmath = 1 \ldots 8). \tag{3.1}$$

Here $\jmath = 1 \ldots 8$ is the electronic energy band index and s in the sum is taken over all 8 atomic orbitals as described earlier. The $c_s^\jmath(\mathbf{k})$ are wavefunction coefficients for the Bloch functions $\Phi_s(\mathbf{k},\mathbf{r})$. The Bloch wavefunctions are given by a sum over the atomic wavefunctions ϕ_s for each orbital at the u–th crystal site multiplied by a phase factor. There are U sites in the crystal, the atomic wavefunctions of orbital s are ϕ_s. The atomic orbital ϕ_s in the u unit cell is centered at $\mathbf{R}_s^u$.

$$\Phi_s(\mathbf{k},\mathbf{r}) = \frac{1}{\sqrt{U}} \sum_{u=0}^{U-1} e^{i\mathbf{k}\cdot\mathbf{R}_s^u} \phi_s(\mathbf{r}-\mathbf{R}_s^u), \quad (s = 2s^A \ldots 2p_z^B)\,. \tag{3.2}$$

We then minimize the ground state energy

$$E^{\jmath} = \frac{\langle \Psi^{\jmath} | H | \Psi^{\jmath} \rangle}{\langle \Psi^{\jmath} | \Psi^{\jmath} \rangle}, \quad (\jmath = 1 \ldots 8), \tag{3.3}$$

as a function of the wavefunction coefficients. The variational condition for finding the minimum is

$$\frac{\partial E^{\jmath}}{\partial c_s^{\jmath *}} = 0. \tag{3.4}$$

The resulting equations for $c_s^{\jmath}(\mathbf{k})$ after minimization are

$$\sum_{s'} H_{ss'} c_{s'}^{\jmath}(\mathbf{k}) + E^{\jmath} \sum_{s'} S_{ss'} c_{s'}^{\jmath}(\mathbf{k}) \quad (s, s' = 2\mathrm{s}^{\mathrm{A}} \ldots 2\mathrm{p}_z^{\mathrm{B}}). \tag{3.5}$$

Eq. (3.5) is the equation with index s. There are 8 equations (for $s = 2\mathrm{s}^{\mathrm{A}} \ldots 2\mathrm{p}_z^{\mathrm{B}}$) for one energy eigenvalue $E^{\jmath}(\mathbf{k})$ because the coefficients for eight atomic orbitals have to be determined. In matrix form, Eq. (3.5) becomes

$$H(\mathbf{k}) c^{\jmath}(\mathbf{k}) = E^{\jmath}(\mathbf{k}) S(\mathbf{k}) c^{\jmath}(\mathbf{k}) \quad \text{with a 8 component vector} \quad c^{\jmath}(\mathbf{k}) = \begin{pmatrix} c^{\jmath}_{(2\mathrm{s}^{\mathrm{A}})}(\mathbf{k}) \\ \vdots \\ c^{\jmath}_{(2\mathrm{p}_z^{\mathrm{B}})}(\mathbf{k}) \end{pmatrix}. \tag{3.6}$$

Here $H(\mathbf{k})$ and $S(\mathbf{k})$ are Hamiltonian and overlap matrices, respectively. The eigenvalues of $H(\mathbf{k})$ are calculated by solving the so–called secular equation for each $\mathbf{k}$

$$\det \{H(\mathbf{k}) - S(\mathbf{k}) E^{\jmath}(\mathbf{k})\} = 0. \tag{3.7}$$

When we solve Eq. (3.7) for $E^{\jmath}(\mathbf{k})$ we obtain eight values for $\jmath = 1 \ldots 8$ which are the energies of the bands with index $\jmath$ at wavevector $\mathbf{k}$. The 8×8 Hamiltonian and overlap matrices can be divided into four 4×4 submatrices

$$H(\mathbf{k}) = \begin{pmatrix} H_{\mathrm{AA}}(\mathbf{k}) & H_{\mathrm{AB}}(\mathbf{k}) \\ H_{\mathrm{BA}}(\mathbf{k}) & H_{\mathrm{BB}}(\mathbf{k}) \end{pmatrix} \text{ and } S(\mathbf{k}) = \begin{pmatrix} S_{\mathrm{AA}}(\mathbf{k}) & S_{\mathrm{AB}}(\mathbf{k}) \\ S_{\mathrm{BA}}(\mathbf{k}) & S_{\mathrm{BB}}(\mathbf{k}) \end{pmatrix}. \tag{3.8}$$

In Eq. (3.8) $H_{\mathrm{AA}}(\mathbf{k})$ is the matrix for A atom Bloch orbitals and $H_{\mathrm{AB}}(\mathbf{k})$ is the matrix for A and B Bloch orbitals and so on. The corresponding matrices for BA interaction are given by taking the transpose and complex conjugate of matrix elements for AB interaction. They are given by

$$H_{\mathrm{BA}}(\mathbf{k}) = {}^t H^*_{\mathrm{AB}}(\mathbf{k}), \quad S_{\mathrm{BA}}(\mathbf{k}) = {}^t S^*_{\mathrm{AB}}(\mathbf{k}). \tag{3.9}$$

We now show how to calculate the matrix elements $H_{ss'}$ that appear in Eq. (3.8) by taking all combinations with s and s' going from $2\mathrm{s}^{\mathrm{A}} \ldots 2\mathrm{p}_z^{\mathrm{B}}$.

$$H_{\mathrm{AB}}(\mathbf{k}) = \begin{pmatrix} \langle 2\mathrm{s}^{\mathrm{A}} | H | 2\mathrm{s}^{\mathrm{B}} \rangle & \langle 2\mathrm{s}^{\mathrm{A}} | H | 2\mathrm{p}_x^{\mathrm{B}} \rangle & \langle 2\mathrm{s}^{\mathrm{A}} | H | 2\mathrm{p}_y^{\mathrm{B}} \rangle & 0 \\ \langle 2\mathrm{p}_x^{\mathrm{A}} | H | 2\mathrm{s}^{\mathrm{B}} \rangle & \langle 2\mathrm{p}_x^{\mathrm{A}} | H | 2\mathrm{p}_x^{\mathrm{B}} \rangle & \langle 2\mathrm{p}_x^{\mathrm{A}} | H | 2\mathrm{p}_y^{\mathrm{B}} \rangle & 0 \\ \langle 2\mathrm{p}_y^{\mathrm{A}} | H | 2\mathrm{s}^{\mathrm{B}} \rangle & \langle 2\mathrm{p}_y^{\mathrm{A}} | H | 2\mathrm{p}_x^{\mathrm{B}} \rangle & \langle 2\mathrm{p}_y^{\mathrm{A}} | H | 2\mathrm{p}_y^{\mathrm{B}} \rangle & 0 \\ 0 & 0 & 0 & \langle 2\mathrm{p}_z^{\mathrm{A}} | H | 2\mathrm{p}_z^{\mathrm{B}} \rangle \end{pmatrix}. \tag{3.10}$$

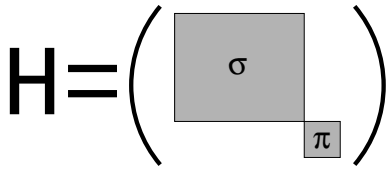

Figure 3.1: Form of the Hamiltonian for graphene. Non–zero elements are shaded grey. The 6×6 and 2×2 Hamiltonian submatrices for σ and π electrons are decoupled because of orthogonality of the wavefunctions.

In Eq. (3.10), the $|2s^{\rm A}\rangle \ldots |2{\rm p}_z^{\rm B}\rangle$ are the Bloch functions from Eq. (3.2) for the orbital $s = |2s^{\rm A}\rangle \ldots |2{\rm p}_z^{\rm B}\rangle$. Note that the matrix elements between $2{\rm p}_z$ orbitals and $2s$, $2{\rm p}_x$ and $2{\rm p}_y$ are zero because of the odd function of z. For the corresponding BA interaction we will take the complex conjugate and transpose to Eq. (3.10). The tight binding Hamiltonian $H_{AA}(\mathbf{k})$ for nearest neighbour interactions between for A atoms is

$$H_{\rm AA}(\mathbf{k}) = \begin{pmatrix} \langle 2{\rm s}^{\rm A}|H|2{\rm s}^{\rm A}\rangle & 0 & 0 & 0 \\ 0 & \langle 2{\rm p}_x^{\rm A}|H|2{\rm p}_x^{\rm A}\rangle & 0 & 0 \\ 0 & 0 & \langle 2{\rm p}_y^{\rm A}|H|2{\rm p}_y^{\rm A}\rangle & 0 \\ 0 & 0 & 0 & \langle 2{\rm p}_z^{\rm A}|H|2{\rm p}_z^{\rm A}\rangle \end{pmatrix}. \tag{3.11}$$

The shape of $H(\mathbf{k})$ is shown in Fig. 3.1 and it can be seen that the σ and π submatrices can be solved independently. In Eq. (3.11), we consider only on–site interaction with the same A atom and neglect the interaction between the A atom and the nearest A atom. We now give formulae for the matrix elements in Eq. (3.10). Since we only consider nearest neighbour interactions, Eq. (3.11) has no $\mathbf{k}$ dependence. We define the vectors $\mathbf{r}_A^\ell$ starting from one A atom to the three nearest neighbour B atoms with $\ell = 1, 2, 3$. Similarly we define $\mathbf{r}_B^\ell$ by $\mathbf{r}_B^\ell = -\mathbf{r}_A^\ell$. The $\mathbf{r}_A^\ell$ and $\mathbf{r}_B^\ell$ are given by

$$\begin{aligned} &\mathbf{r}_A^1 = (\frac{1}{\sqrt{3}}, 0)a, \quad \mathbf{r}_A^2 = (-\frac{1}{2\sqrt{3}}, \frac{1}{2})a, \quad \mathbf{r}_A^3 = (-\frac{1}{2\sqrt{3}}, -\frac{1}{2})a, \\ &\mathbf{r}_B^1 = (-\frac{1}{\sqrt{3}}, 0)a, \quad \mathbf{r}_B^2 = (\frac{1}{2\sqrt{3}}, -\frac{1}{2})a, \quad \mathbf{r}_B^3 = (\frac{1}{2\sqrt{3}}, \frac{1}{2})a, \end{aligned} \tag{3.12}$$

where a is the lattice constant of graphene and given in Sec. 2.1. In Fig. 3.2 we show the vectors defined in Eq. (3.12) connecting an A (B) atom with its three nearest neighbour atoms. We calculate the matrices in Eq. (3.10) and Eq. (3.11). The phase factors for $H_{\rm AB}(\mathbf{k})$, which come from the $\mathbf{k}$ dependence of the Bloch functions in Eq. (3.2) are

$$p_1 = \exp(i\mathbf{k}\cdot\mathbf{r}_A^1), \quad p_2 = \exp(i\mathbf{k}\cdot\mathbf{r}_A^2), \quad p_3 = \exp(i\mathbf{k}\cdot\mathbf{r}_A^3). \tag{3.13}$$

The unit of $\mathbf{k}$ in Eq. (3.13) and hereafter is $[1/a]$. We now explain in detail how to calculate $\langle 2{\rm p}_x^{\rm A}|H|2{\rm p}_y^{\rm B}\rangle$ as an example. The atomic wavefunctions $2{\rm p}_x^{\rm A}$ and $2{\rm p}_y^{\rm B}$ in $\langle 2{\rm p}_x^{\rm A}|H|2{\rm p}_y^{\rm B}\rangle$ are shown in Fig. 3.3(a). There are three nearest A atoms for the B atom in the center of Fig. 3.3(a). We put the origin to the B atom and calculate the transfer and overlap integrals. The A atom at $\mathbf{r}_B^1$ has an odd integrand in y and thus is equal to zero while the A atoms at $\mathbf{r}_B^2$ and $\mathbf{r}_B^3$ give non–zero integrals. To evaluate a large number of matrix elements it is useful to parameterize the integrals in π and σ overlap and transfer integrals. This is done by projecting the 2p wavefunctions to

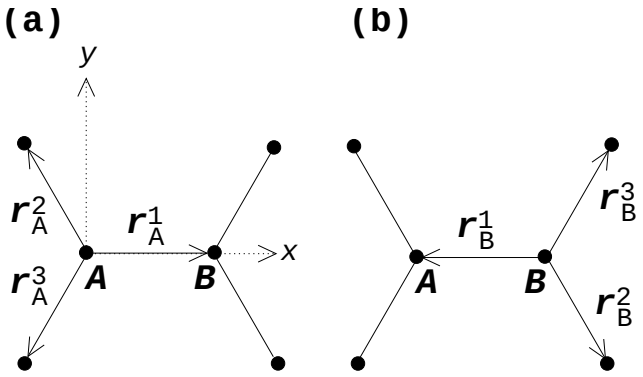

Figure 3.2: Vectors connecting nearest neighbour atoms in graphene for (a) the A atom and (b) the B atom. The vectors are given in Eq. (3.12)

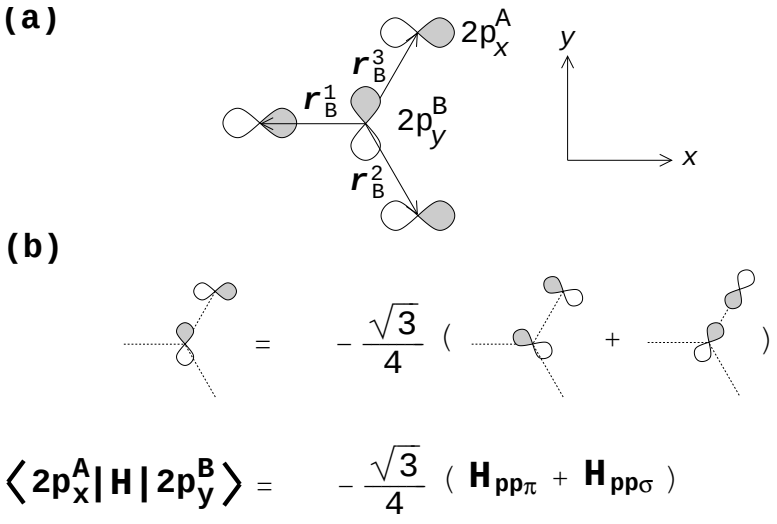

Figure 3.3: (a) The wavefunctions of $2p_y$ orbital at the B atom and of $2p_x$ orbital at A atom are shown. (b) As an example the calculation of the coupling between the center B atom with the A atom at $\mathbf{r}_B^3$ is shown. The integration can be decomposed into a π overlap with orbital perpendicular to the bond and a σ overlap with orbital parallel to the bond.

Table 3.1: Tight binding parameters of graphene obtained from a fit to first principles calculations [4]. ϵ_{2s} is defined relative to the setting $\epsilon_{2p} = 0$.

bond	H	value (eV)	S	value
ssσ	H_{2s2s}	-6.769	S_{2s2s}	0.212
spσ	H_{2s2p}	-5.580	S_{2s2p}	0.102
ppσ	$H_{pp\sigma}$	-5.037	$S_{pp\sigma}$	0.146
ppπ	$H_{pp\pi} = t$	-3.033	$S_{pp\pi} = s$	0.129
	ϵ_{2s}	-8.868		

the components perpendicular (π) or parallel (σ) to the bond as shown in Fig. 3.3(b). We thus get $\langle 2\mathrm{p}_x^{\mathrm{A}}|H|2\mathrm{p}_y^{\mathrm{B}}\rangle = -\sqrt{3}/4(H_{pp\pi} + H_{pp\sigma})$. The coefficient is $-\sqrt{3}/4$ given by the cosine of the angle between the orbital and the bond. Using the positive orbital we get $\cos(30^\circ) = \sqrt{3}/2$ for the B atom at the center and $\cos(120^\circ) = -1/2$ for the A atom at $\mathbf{r}_B^3$. Multiplying the two cosines give $-\sqrt{3}/4$ and this holds for both π and σ in this case. The other matrix elements in Eq. (3.10) are given by

$$
\begin{aligned}
\langle 2\mathrm{s}^{\mathrm{A}}|H|2\mathrm{s}^{\mathrm{B}}\rangle &= H_{2s2s}(p_1 + p_2 + p_3) \\
\langle 2\mathrm{p}_x^{\mathrm{A}}|H|2\mathrm{s}^{\mathrm{B}}\rangle &= H_{2s2p}\left(p_1 - \frac{p_2}{2} - \frac{p_3}{2}\right) \\
\langle 2\mathrm{p}_y^{\mathrm{A}}|H|2\mathrm{s}^{\mathrm{B}}\rangle &= \frac{\sqrt{3}}{2}H_{2s2p}\left(-p_2 + p_3\right) \\
\\
\langle 2\mathrm{s}^{\mathrm{A}}|H|2\mathrm{p}_x^{\mathrm{B}}\rangle &= \frac{\sqrt{3}}{2}H_{2s2p}(-p_1 + \frac{p_2 + p_3}{2}) \\
\langle 2\mathrm{p}_x^{\mathrm{A}}|H|2\mathrm{p}_x^{\mathrm{B}}\rangle &= H_\sigma\left(\frac{-p_1 - p_2 - p_3}{4}\right) + \frac{3}{4}H_\pi(p_2 + p_3) \\
\langle 2\mathrm{p}_y^{\mathrm{A}}|H|2\mathrm{p}_x^{\mathrm{B}}\rangle &= \frac{\sqrt{3}}{4}\left(H_\sigma + H_\pi\right)\left(p_2 - p_3\right) \\
\\
\langle 2\mathrm{s}^{\mathrm{A}}|H|2\mathrm{p}_y^{\mathrm{B}}\rangle &= \frac{\sqrt{3}}{2}H_{2s2p}(-p_2 + p_3) \\
\langle 2\mathrm{p}_x^{\mathrm{A}}|H|2\mathrm{p}_y^{\mathrm{B}}\rangle &= \frac{\sqrt{3}}{4}\left(H_\sigma + H_\pi\right)\left(p_2 - p_3\right) \\
\langle 2\mathrm{p}_y^{\mathrm{A}}|H|2\mathrm{p}_y^{\mathrm{B}}\rangle &= -\frac{3}{4}H_\sigma(p_2 + p_3) + H_\pi\left(p_1 + \frac{p_2 + p_3}{4}\right) \\
\\
\langle 2\mathrm{p}_z^{\mathrm{A}}|H|2\mathrm{p}_z^{\mathrm{B}}\rangle &= H_\pi\left(p_1 + p_2 + p_3\right).
\end{aligned}
\tag{3.14}
$$

For the on–site elements in H_{AA} and H_{BB}, we define

$$
\langle 2s^{\mathrm{A}}|H|2s^{\mathrm{A}}\rangle = \langle 2s^{\mathrm{B}}|H|2s^{\mathrm{B}}\rangle = \epsilon_s, \quad \langle 2p^{\mathrm{A}}|H|2p^{\mathrm{A}}\rangle = \langle 2p^{\mathrm{B}}|H|2p^{\mathrm{B}}\rangle = 0. \tag{3.15}
$$

Here tight binding parameters for Hamiltonian matrix elements are denoted by H and the orbital overlap in the subscript. The numerical values are listed in Table 3.1 and these values correspond to the energy of the bonding state. Their values can be determined by a fit to an ab–initio calculation or to experimental data. The values tabulated in Table 3.1 are from a fit to an ab–initio calculation [4]. The formulas for the wavefunction overlap are not given here but they are obtained by replacing the transfer integral constants in Eq. (3.14) by the constants

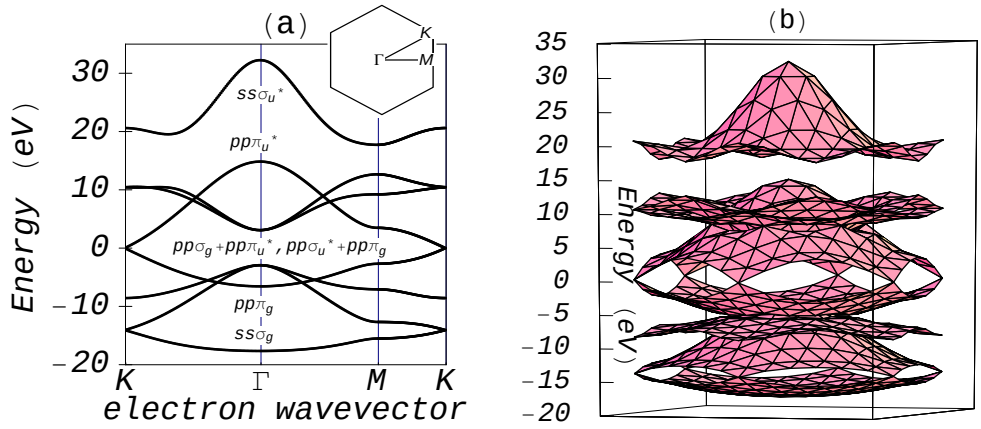

Figure 3.4: Electron energy dispersion relations in graphene. In (a) we solve the Schrödinger equation along the K–Γ–M–K lines and in (b) a plot over the whole 2D BZ is shown. The tight binding parameters in Table 3.1 have been used to calculate the matrix elements in Eq. (3.14).

for wavefunction overlap. The 1s overlap is not listed in Table 3.1 because it will be considered equal to zero.

3.2 Calculated results

In Fig. 3.4(a) we solve Eq. (3.6) for $E(\mathbf{k})$ along the high symmetry direction $K-\Gamma-M-K$ and in Fig. 3.4(b) the plot of $E(\mathbf{k})$ over the whole 2D BZ is shown. The subscripts "g" and "u" indicate even and odd mirror symmetries of the wavefunction of the two atoms that make one bond with respect to the plane perpendicular to the bond center. The superscript "*" indicates anti–bonding states, which have "u" symmetry. Program (3) in the appendix has been used to calculate electron energy dispersion shown in Fig.3.4.

The corresponding wavefunctions at the Γ point are shown in Fig. 3.5. It is clear that the anti–bonding combination of orbitals shown in Fig. 3.5(a) has a node in the charge density of electrons in between the two atoms. On the other hand, the bonding orbitals shown in Fig. 3.5(b) have a maximum value of charge density at the bond center. This is because the wavefunction sign is the same with respect to the mirror plane for σ bonds and for π bonds ("g" symmetry) for the bonding orbitals. At the K points valence and conduction π bands touch each other. This energy corresponds to the Fermi energy E_f. Since we set the on–site 2p energy equal to zero in this calculation, E_f appears at zero energy. With respect to the vacuum level, we have $E_f = -5.18$ eV. Since π electrons are important in graphene and SWNTs, we will derive analytic expressions for eigenvalues and eigenvectors of the π Hamiltonian in the following section.

3.3 π electrons in graphite and SWNTs

The total 8×8 Hamiltonian in Eq. (3.6) can be decomposed into a 6×6 Hamiltonian for σ and a 2×2 Hamiltonian for π electron bands since the wavefunctions of 2s, $2p_x$ and $2p_y$ are even

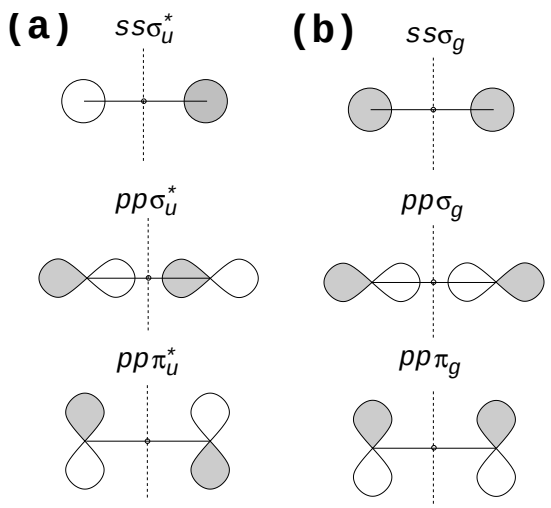

Figure 3.5: (a) Anti–bonding σ_u^* and π_u^* orbitals and (b) bonding σ_g and π_g orbitals at Γ point are shown. ss and pp refer to overlap of two 2s orbitals and two 2p orbitals, respectively. The index "*" refers to anti–bonding orbitals. The indices "g" and "u" refer to even and odd mirror symmetry, respectively. The shaded and white parts correspond to opposite sign of the wavefunction. The mirror symmetry plane through the bond centers is indicated by a dashed line.

functions of z (parallel to the graphene plane) while the $2p_z$ orbital is an odd function of z. As seen in Eq. (3.10) the sub–matrix is already decomposed into 3×3 and 1×1 matrices. The graphene Hamiltonian has such a form, that the π Hamiltonian can be decoupled from the σ Hamiltonian. Here, we consider the 2×2 π Hamiltonian with the shape of Eq. (3.8) and matrix elements

$$H_{AB} = \langle 2p_z^A | H | 2p_z^B \rangle = t \left\{ \exp(i\mathbf{k} \cdot \mathbf{r}_A^1) + \exp(i\mathbf{k} \cdot \mathbf{r}_A^2) + \exp(i\mathbf{k} \cdot \mathbf{r}_A^3) \right\} = t f(\mathbf{k}), \tag{3.16}$$

and

$$H_{BA} = \langle 2p_z^B | H | 2p_z^A \rangle = t \left\{ \exp(i\mathbf{k} \cdot \mathbf{r}_B^1) + \exp(i\mathbf{k} \cdot \mathbf{r}_B^2) + \exp(i\mathbf{k} \cdot \mathbf{r}_B^3) \right\} = t f^*(\mathbf{k}). \tag{3.17}$$

In Eq. (3.16) and in Eq. (3.17) we use $\mathbf{r}_A^\ell$ and $\mathbf{r}_B^\ell$ that are given in Fig. 3.2 and t from Table 3.1. The sum of the three phase factors $f(\mathbf{k})$ is defined by starting from an A atom and going to the three nearest neighbour B atoms. It can be simplified to

$$f(\mathbf{k}) = \exp(i\frac{k_x a}{\sqrt{3}}) + 2\exp(-\frac{ik_x a}{2\sqrt{3}}) \cos(\frac{k_y a}{2}). \tag{3.18}$$

Since in graphene the two atoms are the same type, we can put $H_{AA} = H_{BB} = \epsilon_p$ (note this is not the case for 3D graphite). The solution to the secular equation at a general $\mathbf{k}$ is then given by

$$\begin{aligned} & \det \begin{pmatrix} \epsilon_p - E(\mathbf{k}) & f(\mathbf{k})\{t - sE(\mathbf{k})\} \\ f^*(\mathbf{k})\{t - sE(\mathbf{k})\} & \epsilon_p - E(\mathbf{k}) \end{pmatrix} \\ = \; & \{\epsilon_p - E(\mathbf{k})\}^2 - \omega^2(\mathbf{k}) \{t - sE(\mathbf{k})\}^2 \\ = \; & \{\epsilon_p - E(\mathbf{k}) - \omega(\mathbf{k})(t - sE(\mathbf{k}))\} \{\epsilon_p - E(\mathbf{k}) + \omega(\mathbf{k})(t - sE(\mathbf{k}))\} \\ = \; & 0. \end{aligned} \tag{3.19}$$

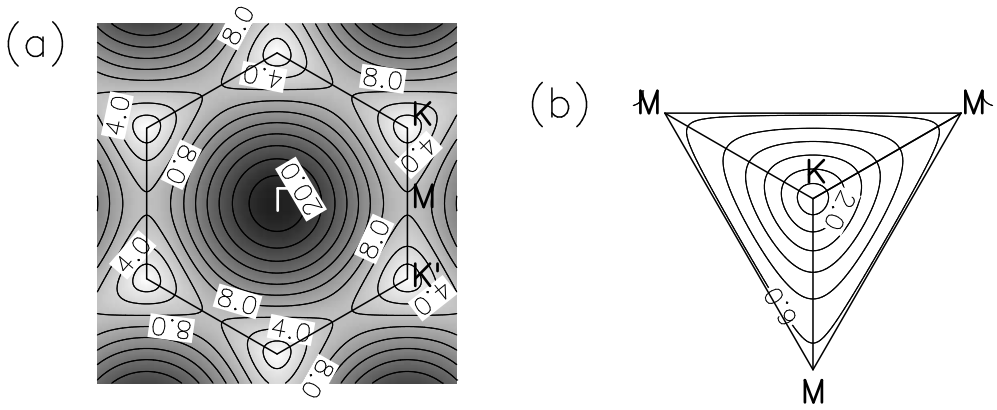

Figure 3.6: Energy difference between π and π^* electrons in graphene. In (a) we plot the contour lines over the whole BZ in steps of 2 eV. The bright (dark) shaded areas correspond low (high) electron energy. (b) The area around K point is magnified with contour lines in steps of 1 eV. Some of the countour lines are labeled by their energy value in eV. The tight binding parameter in Table 3.1 have been used.

Here we used $\omega^2(\mathbf{k}) = f^*(\mathbf{k})f(\mathbf{k})$. The two solutions of Eq. (3.19) are the valence band energy $E^v(\mathbf{k})$ and conduction band energy $E^c(\mathbf{k})$, respectively, and are given by

$$E^v(\mathbf{k}) = \frac{\epsilon_p + t\omega(\mathbf{k})}{1 + s\omega(\mathbf{k})}, \quad \text{and } E^c(\mathbf{k}) = \frac{\epsilon_p - t\omega(\mathbf{k})}{1 - s\omega(\mathbf{k})}. \tag{3.20}$$

Note that t is negative and s is positive. The parameter s is responsible for the asymmetry between valence and conduction bands. A larger value of s corresponds to a higher asymmetry. $s = 0$ corresponds to completely symmetric valence and conduction bands with respect to the Fermi energy. An almost perfect electron–hole symmetry was reported recently from transport measurements [29]. However, these measurements are valid only in the region close to the Fermi energy. Optical spectroscopy can probe a wider region of the BZ. In Fig. 3.6, we plot the optical transition energy $E^c(\mathbf{k}) - E^v(\mathbf{k})$ and it is clear that for visible light, we probe electrons on circles around K points.

In graphene, there are two carbon atoms in the unit cell and we now show why this property gives rise to special electronic structure at K point. To understand the special behaviour at K points, we solve the secular equation given in Eq. (3.7). The K points have coordinates $\mathbf{K}$ and at $\mathbf{k} = \mathbf{K}$, we get $f(\mathbf{K}) = 0$ and thus Eq. (3.19) becomes simply

$$\det \begin{pmatrix} H_{AA} - E(\mathbf{K}) & 0 \\ 0 & H_{BB} - E(\mathbf{K}) \end{pmatrix} = 0, \tag{3.21}$$

and its solutions are given by $E(\mathbf{K}) = H_{AA}$ and $E(\mathbf{K}) = H_{BB}$. A gap would occur at $\mathbf{K}$, if we had two atomic species with different on–site integrals H_{AA} and H_{BB}. Eq. (3.21) holds for π electrons at $\mathbf{K}$ of any solid with hexagonal crystal structure because the values of integral and wavefunction overlap, t and s, respectively, disappear when $f(\mathbf{K}) = 0$ and the energy is only determined by the values of H_{AA} and H_{BB}, respectively. Thus, if the two atoms in the unit cell are not the same, an energy gap at $\mathbf{K}$ can be observed. For example, a very similar material

to graphene is a sheet of hexagonal BN because it has the same crystal structure as graphene and atomic species are different to carbon by one coloumn in the periodic table. In BN, the A and B atoms of graphene are replaced respectively by a boron and a nitrogen atom. In such a case, the eigenvalues at **K** are not degenerate because B and N have different on–site energies. A sheet of BN and BN derived nanotubes are known to be wide–gap semiconductors [30] and can be used to insulate a metallic carbon nanotube by putting the metallic SWNT inside the BN tube. In 3D graphite, although the atomic species are the same, the on–site energies are for unit cell atoms are different from one another because of stacking of graphene sheets. Thus a small gap can occur in 3D graphite.

For a small electron wavevector $\mathbf{k}$, which is measured from K points, we expand Eq. (3.18) around $\mathbf{K}$ and $\mathbf{K}'$ as $f(\mathbf{K}+\mathbf{k})$ and $f(\mathbf{K}'+\mathbf{k})$. The K points have coordinates $\mathbf{K} = (0, -4\pi/(3a))$ and $\mathbf{K}' = (0, 4\pi/(3a))$. With $\mathbf{k} = (k_x, k_y)$ we obtain

$$f(\mathbf{K}+\mathbf{k}) = \frac{\sqrt{3}a}{2}(ik_x + k_y) \quad \text{and} \quad f(\mathbf{K}'+\mathbf{k}) = \frac{\sqrt{3}a}{2}(ik_x - k_y). \tag{3.22}$$

Substituting Eqs. (3.22) into Eq. (3.20) we get an approximation for the electron energy dispersion relations close to K points. It turns out that in the linear order approximation we get the same energy dispersion relation around K and K' points,

$$E(\mathbf{k}) = \pm\frac{\sqrt{3}at}{2}\sqrt{k_x^2 + k_y^2}. \tag{3.23}$$

Here the "+" sign is valid for valence band and the "–" sign is valid for conduction band. For high electron energies the equi–energy contours shown in Fig. 3.6 are generally different from each other at K and K' points. For small electron energies (less than 2 eV), however the contours in Fig. 3.6 are almost circles around K and K' points. The equi–energy circles deform to triangles, when going to higher electron energies. This is known as the trigonal warping effect in graphene [31]. The equi–energy contour connecting three nearest M points is a triangle as shown in Fig. 3.6(b).

Optical transitions occur between bonding and anti–bonding bands and from Fig. 3.4 it is clear that low energy optical spectroscopy in the region of visible light mainly probes electrons around K points between the π and π^* bands. In Fig. 3.6 we show the equi–energy contours of the π electrons.

3.3.1 Eigenvectors for π electrons

We now calculate the wavefunction coefficients for electrons for A and B atoms, $c_A^\imath$ and $c_B^\imath$, respectively. They are given by the eigenvectors of the Hamiltonian. Here $\imath = v, c$ can be valence or conduction band.

$$\begin{pmatrix} \epsilon_p - E^\imath(\mathbf{k}) & f(\mathbf{k})\{H_\pi - sE^\imath(\mathbf{k})\} \\ f^*(\mathbf{k})\{H_\pi - sE^\imath(\mathbf{k})\} & \epsilon_p - E^\imath(\mathbf{k}) \end{pmatrix} \begin{pmatrix} c_A^\imath(\mathbf{k}) \\ c_B^\imath(\mathbf{k}) \end{pmatrix} = \mathbf{0}. \tag{3.24}$$

The wavefunction coefficients are the eigenvectors that are obtained by solving Eq. (3.24). The normalization and orthogonality condition (orthonormality) is $\langle\Psi^\imath(\mathbf{r},\mathbf{k})|\Psi^\jmath(\mathbf{r},\mathbf{k})\rangle = \delta_{\imath\jmath}$ where $\Psi^\imath(\mathbf{r},\mathbf{k}) = c_A^\imath(\mathbf{k})\Phi_A(\mathbf{r},\mathbf{k}) + c_B^\imath(\mathbf{k})\Phi_B(\mathbf{r},\mathbf{k})$. Here, $c_A^\imath(\mathbf{k})$ and $c_B^\imath(\mathbf{k})$ are the wavefunction coefficients, which are the eigenvectors of Eq. (3.24). By putting the possible indices for $\imath$ and $\jmath$, we

can obtain four equations, that are needed to calculate the four wavefunction coefficients of the Bloch functions. The orthonormality conditions can be expanded in terms of Bloch functions as

$$\begin{aligned} & \langle \Psi^{\imath}(\mathbf{r},\mathbf{k})|\Psi^{\jmath}(\mathbf{r},\mathbf{k})\rangle \\ = \; & c_A^{*\imath}c_A^{\jmath}\langle\Phi_A(\mathbf{r})|\Phi_A(\mathbf{r})\rangle + c_A^{*\imath}c_B^{\jmath}\langle\Phi_A(\mathbf{r})|\Phi_B(\mathbf{r})\rangle + c_B^{*\imath}c_A^{\jmath}\langle\Phi_B(\mathbf{r})|\Phi_A(\mathbf{r})\rangle + c_B^{*\imath}c_B^{\jmath}\langle\Phi_B(\mathbf{r})|\Phi_B(\mathbf{r})\rangle. \end{aligned} \tag{3.25}$$

Using the Bloch functions in Eq. (3.2) which is also normalized, we get $\langle\Phi_A(\mathbf{r})|\Phi_A(\mathbf{r})\rangle = 1$ and $\langle\Phi_B(\mathbf{r})|\Phi_B(\mathbf{r})\rangle = 1$. Thus the orthonormality becomes

$$\begin{aligned} & \langle \Psi^{\imath}(\mathbf{r},\mathbf{k})|\Psi^{\jmath}(\mathbf{r},\mathbf{k})\rangle \\ = \; & c_A^{*\imath}(\mathbf{k})c_A^{\jmath}(\mathbf{k}) + c_B^{*\imath}(\mathbf{k})c_B^{\jmath}(\mathbf{k}) + sf(\mathbf{k})c_A^{*\imath}(\mathbf{k})c_B^{\jmath}(\mathbf{k}) + sf^*(\mathbf{k})c_B^{*\imath}(\mathbf{k})c_A^{\jmath}(\mathbf{k}) = \delta_{\imath\jmath}, \\ & (\imath = v,c \text{ and } \jmath = v,c). \end{aligned}$$

The relation between $c_A^{\jmath}$ and $c_B^{\jmath}$ is obtained from Eq. (3.24) and is given by

$$c_A^{\imath}(\mathbf{k}) = c_B^{\imath}(\mathbf{k})\frac{f(\mathbf{k})}{E^{\imath}(\mathbf{k})}\left\{H_\pi - sE^{\imath}(\mathbf{k})\right\}. \tag{3.26}$$

To calculate the value for $c_A^{\imath}(\mathbf{k})$ for $\imath = v,c$, we consider $\langle\Psi^{\imath}(\mathbf{r},\mathbf{k})|\Psi^{\imath}(\mathbf{r},\mathbf{k})\rangle = 1$. We expand $\Psi^{\imath}(\mathbf{r},\mathbf{k})$ into Bloch functions and use Eq. (3.26) to replace $c_B^{\imath}(\mathbf{k})$ by $c_A^{\imath}(\mathbf{k})$. Noting that

$$\frac{E_c(\mathbf{k})}{H_\pi - S_\pi E_c(\mathbf{k})} = -\omega(\mathbf{k}) \quad \text{and} \quad \frac{E_v(\mathbf{k})}{H_\pi - S_\pi E_v(\mathbf{k})} = \omega(\mathbf{k}), \tag{3.27}$$

we can obtain the coefficients for B atoms as

$$c_B^v(\mathbf{k}) = c_A^v\frac{f^*(\mathbf{k})}{\omega(\mathbf{k})} \quad \text{and} \quad c_B^c(\mathbf{k}) = -c_A^c\frac{f^*(\mathbf{k})}{\omega(\mathbf{k})}. \tag{3.28}$$

We need a phasefactor since from Eq. (3.26) we can only solve for the absolute values of c_A^v and c_A^c if we put $\imath = \jmath = v,c$ and solve the two equations we can get from Eq. (3.26). We can then obtain $c_A^{\imath}(\mathbf{k})$ for $\imath = v,c$ without the sign and the phase factor as

$$c_A^v(\mathbf{k}) = \exp(i\phi_v)\sqrt{\frac{1}{2\left\{1+s\omega(\mathbf{k})\right\}}} \quad \text{and} \quad c_A^c(\mathbf{k}) = \exp(i\phi_c)\sqrt{\frac{1}{2\left\{1-s\omega(\mathbf{k})\right\}}}. \tag{3.29}$$

The coefficients $c_B^v(\mathbf{k})$ and $c_B^c(\mathbf{k})$ are already given by substituting $c_A^{\imath}$ from Eq. (3.29) into Eq. (3.26). Note that the phasefactors Φ_v or Φ_c for Eq. (3.29) can be chosen arbitrarily because only the phase difference betweeen A and B atoms is important.

In order to obtain a symmetric solution, we choose $\Phi_v = \Phi_c = \sqrt{f(\mathbf{k})/\omega(\mathbf{k})}$. Thus we can get that the $c_A^{\imath}$ and $c_B^{\imath}$ (with $\imath = v,c$) are related to each other by complex conjugation. The wavefunction coefficients for π electrons are given by

$$\begin{aligned} c_A^v(\mathbf{k}) &= \sqrt{\frac{1}{2\{1+s\omega(\mathbf{k})\}}}\sqrt{\frac{f(\mathbf{k})}{\omega(\mathbf{k})}}, \quad c_A^c(\mathbf{k}) = \sqrt{\frac{1}{2\{1-s\omega(\mathbf{k})\}}}\sqrt{\frac{f(\mathbf{k})}{\omega(\mathbf{k})}}, \\ c_B^v(\mathbf{k}) &= \sqrt{\frac{1}{2\{1+s\omega(\mathbf{k})\}}}\sqrt{\frac{f^*(\mathbf{k})}{\omega(\mathbf{k})}}, \quad c_B^c(\mathbf{k}) = -\sqrt{\frac{1}{2\{1-s\omega(\mathbf{k})\}}}\sqrt{\frac{f^*(\mathbf{k})}{\omega(\mathbf{k})}}. \end{aligned} \tag{3.30}$$

Note that substitution of the Eq. (3.30) to $\langle \Psi^c(\mathbf{r},\mathbf{k})|\Psi^v(\mathbf{r},\mathbf{k})\rangle$ yields zero. The corresponding wavevectors for electron–hole symmetry can be obtained by setting $s = 0$. From Eq. (3.30) it is furthermore clear, that by taking an inversion symmetry, that is changing atoms A→B, the valence band wavefunction goes to the complex conjugate and the conduction band wavefunction goes to minus complex conjugate. This is in agreement with general molecular orbitals where the valence (conduction) band wavefunction of a molecule is made up from symmetric (anti–symmetric) combination of atomic orbitals.

3.3.2 Expansion of π electrons into a Gaussian basisset

To calculate numerical values for the optical absorption matrix elements or the electron phonon coupling matrix elements, the $2p_z$ orbital is expanded into a Gaussian basis. The merit of this expansion is that we can do many integrals of matrix elements *analytically*. We thus expand the atomic orbital $\phi_{2p_z}(\mathbf{r}-\mathbf{r}_0)$ of an electron in a $2p_z$ orbital centered at $\mathbf{r}_0$ and the ion potential $v(\mathbf{r}-\mathbf{r}_0)$ of a free carbon atom into a Gaussian basis functions. In the expansion of the ion potential $v(\mathbf{r}-\mathbf{r}_0)$, screening from the two 1s core electrons is considered and then the fitted potential is spherical symmetric. The exact values can be fitted to an accurate calculation. The functional form we choose for the $2p_z$ orbital is given by

$$\phi_{2p_z}(\mathbf{r}-\mathbf{r}_0) = (z-z_0)\frac{1}{\sqrt{N}}\sum_{k=1}^{n} I_k \exp\left\{\frac{-(\mathbf{r}-\mathbf{r}_0)^2}{2\sigma_k^2}\right\}. \tag{3.31}$$

Here n, I_k and σ_k is the number of basis functions, the amplitude and width of the the basis function with index k. The fitting parameters are listed in Table 3.2(a). In Eq. (3.31) we have $\mathbf{r} = (x,y,z)$ and the atom is centered at $\mathbf{r}_0 = (x_0,y_0,z_0)$. The normalization constant for Eq. (3.31) is N and is given by

$$N = \sum_{l=1,k=1}^{n} \sqrt{8\pi^3} I_l I_k \left(\sqrt{\frac{1}{\frac{1}{\sigma_l^2}+\frac{1}{\sigma_k^2}}}\right)^5. \tag{3.32}$$

Using the values in Table 3.2(a) for $n = 4$, we get $N = 1.0$. The potential of the ion which is shielded by the 1s wavefunctions is given by $v(r)$. It is expanded similarly to the electronic wavefunctions into a set of p Gaussians. Since $v(r)$ goes to minus infinity for $r \to 0$, it is not possible to fit the potential directly. Instead we fit $rv(r)$ and divide later by r. The potential is

(a)

k	1	2	3	4
I_k	0.05	0.41	1.06	1.05
σ_k	2.16	0.91	0.13	0.39

(b)

k	1	2	3	4
v_k	–2.13	–1.00	–2.00	–0.74
τ_k	0.25	0.04	1.00	2.80

Table 3.2: The coefficients for the radial part of the electronic 2p wavefunction obtained by a fit to an ab–initio calculation. (a) The wavefunction is given by substituting I_k and σ_k into Eq. (3.31). The units for I_k is given in [at.u]$^{-5/2}$ and σ_k is given in [at.u]. (b) The potential is given by substituting I_k and τ_k into Eq. (3.33). The units of v_k are Hartree times [at.u] and τ_k is given in [at.u].

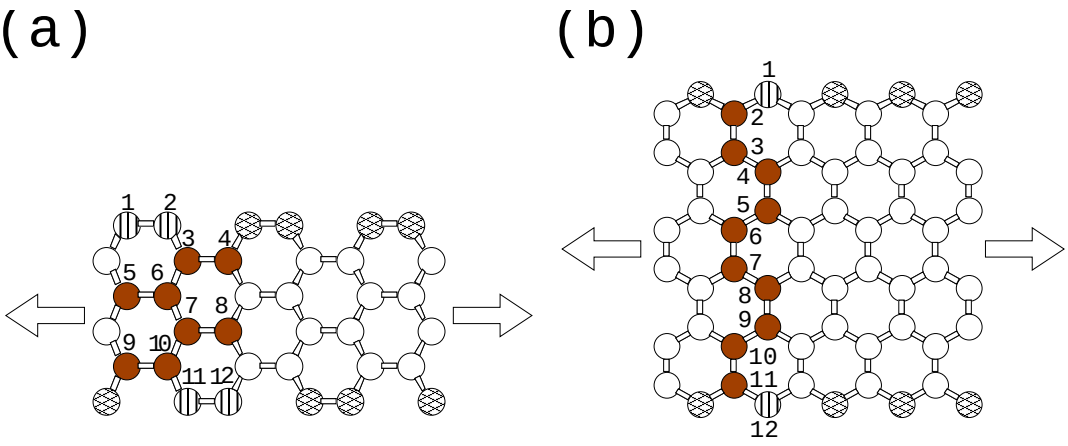

Figure 3.7: Geometry of $N = 6$ (a) armchair ribbons (b) zigzag ribbons. The atoms at the armchair edge and the zigzag edge are indicated by crosses. The unit cells are shown by shaded atoms and the atoms in the unit cell are labelled by their indices $1 \ldots 12$. Edge atoms in the unit cells are shown by vertical stripes. The atom indices are the same we use in Table 3.3 for the matrix elements.

given by

$$v(\mathbf{r} - \mathbf{r}_0) = -\frac{1}{r} \sum_{k=1}^{p} v_k \exp\left\{\frac{-(\mathbf{r} - \mathbf{r}_0)^2}{2\tau_k^2}\right\}. \tag{3.33}$$

The fitting parameters for the potential in Eq. (3.33) are listed in Table 3.2(b). Both the potential and the wavefunction fitting parameters were obtained from a fit to the output of an ab–inito calculation.

3.4 Edge states in nanographite ribbons

Using the electron energy dispersion of graphene, we will consider the one–dimensional materials nanographite ribbons and carbon nanotubes. Nanographite is a 1D graphite ribbon with a few atom layers width and macroscopic length (see Fig. 3.7) [32, 33]. The physical properties are determined mainly by the width and the shape of the edge along the ribbon's longitudinal direction, which is indicated by arrows in Fig. 3.7(a) and (b). There are two symmetric edges: armchair and zigzag edges. The geometry of a single–layer nanographite ribbon with $N = 6$ (N is the number of graphite unit cells in 1D unit cell) dimer lines is shown in Fig. 3.7(a) and (b) for armchair and zigzag ribbons, respectively. The unit cells with $2N = 12$ atoms are indicated by shaded atoms and the atoms in the unit cell are labelled by their atom indices. The atoms which do not have three neighbours (edge atoms) are indicated by crosses. If an edge atom is inside the unit cell, it is indicated by vertical stripes. In the case of armchair ribbons in Fig. 3.7(a) we have four edge atoms with indices 1, 2, 11 and 12. The zigzag ribbon in Fig. 3.7(b) has two edge atoms with indices 1 and 12. The two edge atoms of the zigzag edge are inequivalent to each other. A general edge is a combination of armchair and zigzag edges. We study the electronic structure of armchair and zigzag nanographite by the tight binding approximation. In Table 3.3(a) and (b) the value of the hopping matrix elements $H_{lm}(\mathbf{k})$ for wavevector $\mathbf{k}$ between nearest neighbour

Table 3.3: Matrix elements H_{lm} for (a) armchair and (b) zigzag nanographite ribbons. The hopping parameter between nearest neighbours is t. For the $N = 6$ ribbons in Fig. 3.7 the range for i, l and m is as follows: $i = 0 \ldots 6$, $l = 1 \ldots 12$ and $m = 1 \ldots 12$. If, for a given i, the l or m is outside the range, the matrix element equals to zero. In the lower panel, we show the geometries which correspond to Tables (a) and (b).

(a)

	$l = m-1$	$l = m+1$	$l = m-3$	$l = m+3$
$m = 2i$	$t\exp(-ika)$	$t\exp(ika/2)$	$t\exp(ika/2)$	0
$m = 2i+1$	$t\exp(-ika/2)$	$t\exp(ika)$	0	$t\exp(-ika/2)$

(b)

	$l = m-1$	$l = m+1$
$m = 2i$	$t\cos(ka/2)$	t
$m = 2i+1$	t	$t\cos(ka/2)$

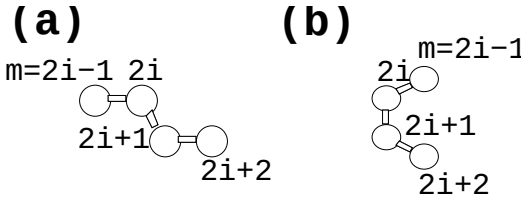

atoms l and m is tabulated for armchair and zigzag ribbons, respectively. In the lower panel of Table 3.3 we show a figure with the part of the nanoribbon unit cell, that corresponds to the possible values of i,l and m in Table 3.3. In this Figure, (a) is for armchair and (b) is for zigzag ribbons, respectively. The indices l and m are to be taken $l, m = 1 \ldots 2N$ and correspond to the atom numbers in Fig. 3.7. We calculate the energy bands by solving the $2N \times 2N$ Hamiltonian H_{lm} for $N = 5, 6, 7$ and show the calculated energy dispersion relation in Fig. 3.8 and Fig. 3.9 for armchair and zigzag ribbons, respectively. The program (2) in the appendix was used to calculate these results. Whereas the result for armchair is simply given by simple zonefolding (i.e. cutting along special $\mathbf{k}$) of graphene energy bands, zigzag ribbons show a so–called edge state at the Fermi level (set equal to zero in this calculation). This state cannot be obtained by zonefolding and it is localized entirely on the outermost layers at $ka = \pm\pi$. Because the edge state always appears on the zigzag edge, all zigzag ribbons have a singular DOS at the Fermi level. The existence of an edge state was also obtained by ab–initio calculations for single– and multi–layer ribbons [34]. The difference in the number of edge atoms for armchair and zigzag ribbons (four edge atoms versus two edge atoms per unit cell) is the reason why an edge state appears in the zigzag edge [32]. Armchair ribbons are metallic when $N = 3i - 1$, where i is an integer. See Fig. 3.8(a) for the case $N = 5$.

A zigzag nanographite ribbon has peculiar magnetic properties due to the appearance of the edge states [35], unlike graphene, which is not magnetic. This can be understood as follows: For electrons with $ka = \pm\pi$, the valence and conduction π bands touch each other as can be seen from Fig. 3.9(b). Considering the electron spin that can assume two values for each band, we have four electron states appearing at the Fermi energy. Thus in principle, a local

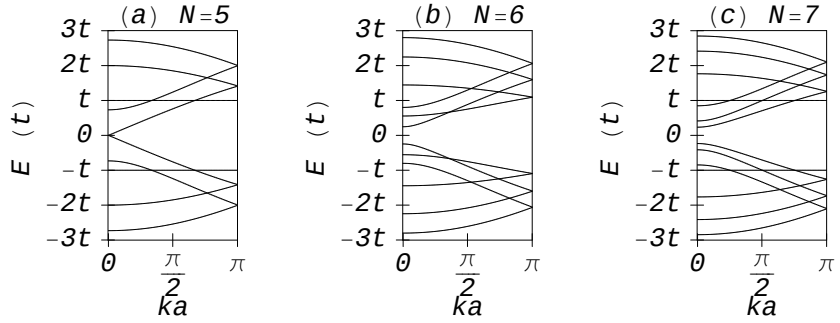

Figure 3.8: Energy band structure of armchair ribbons for (a) N=5, (b) N=6 and (c) N=7.

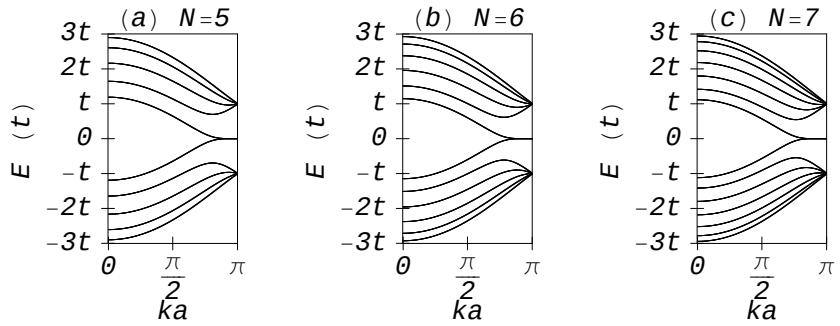

Figure 3.9: Energy band structure of zigzag ribbons for (a) N=5, (b) N=6 and (c) N=7.

magnetic moment is possible, if we have one electron in the valence band and one electron in the conduction band, both with the same spin. For electrons at the zigzag edge with $ka = \pm\pi$, this condition is given and calculations of the magnetization [35] suggest that a ribbon has a magnetic moment at its zigzag edges. Because the zigzag edge atoms are inequivalent to each other on opposite sides, the total magnetization of the zigzag ribbon is zero.

3.5 Carbon nanotubes

From nanographite, we have seen that reduction of direction to one dimension gives quantized electronic states along the ribbon width. Zone–folding of the 2D Brillouin zone (BZ) is a good approximation for SWNTs and means cutting the graphene π electron dispersions according to Eq. (2.15). Along the $\mathbf{k}$ given by Eq. (2.15) we can obtain $2N$ electron energy dispersion relations for π bands of a SWNT. The cutting lines and the graphene π electron energy contours for the $(6, 2)$ SWNT are shown in Fig. 3.10(a). In Fig. 3.10(b) we show the 1D electron dispersion relations for the $(6, 2)$ SWNT. In Fig. 3.10(c) we show the density of states (DOS) for the $(6, 2)$ SWNT.

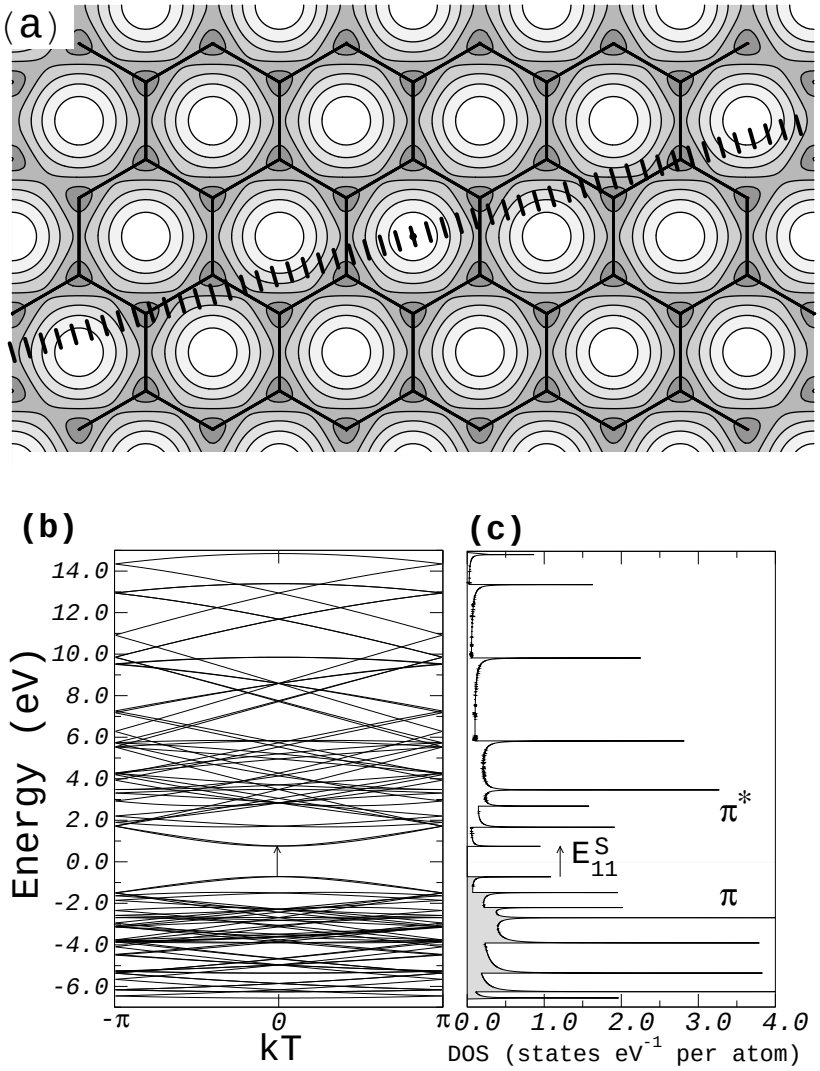

Figure 3.10: (a) Cutting lines of the $(6,2)$ SWNT and the energy contours of graphite. (b) The electron dispersion relations of the $(6,2)$ SWNT obtained by the zonefolding method. (c) The density of states (DOS) for the $(6,2)$ SWNT. The grey shaded part gives the occupied electron states. Integration over the grey shaded DOS is equal to 2. A transfer and overlap integral value of $t = 3.10$ eV and $s = 0.13$, respectively have been used. The $\pi \rightarrow \pi^*$ for the lowest VHS transition is indicated by an arrow.

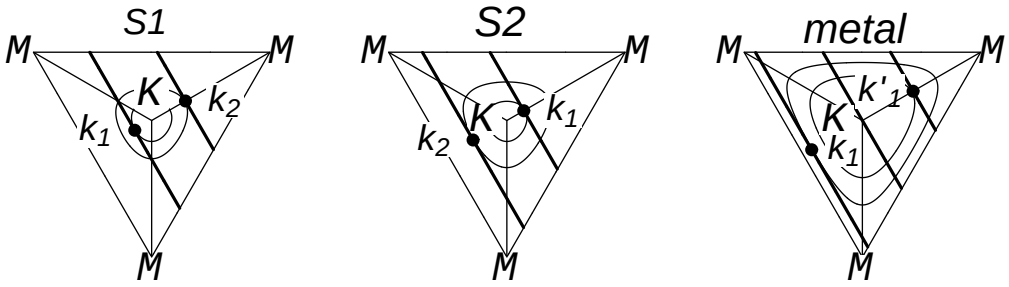

Figure 3.11: Difference of the position of the touching points of the cutting lines with the equi–energy circle, $\mathbf{k}_1$ and $\mathbf{k}_2$ in type I and II semiconducting and metal SWNTs. In semiconducting type I (II) SWNTs the E_{22}^S transition occurs outside (inside) the first BZ. In metal SWNTs, E_{11}^M is split due to the trigonal warping effect.

In the DOS profile we can see sharp peaks that are called van Hove singularities (VHS). Their origin is the one–dimensionality of SWNTs and this will be discussed in detail later. In Fig. 3.10(c) the lowest energy VHS is indicated by an arrow.

From Fig. 3.10(a) it is clear that if a cutting line for a given SWNT passes through the K point (see Fig. 2.3), that SWNT is metallic. The condition for metallicity in terms of (n, m) is derived now. We note that for any allowed $\mathbf{k}$ state, we get

$$\mathbf{C}_h \cdot \mathbf{k} = 2\pi\ell, \quad (\ell \text{ integer}). \tag{3.34}$$

This is the condition that the ratio of electron wavelength $\lambda = 2\pi/k$ around the circumference to the length of the circumference must be an integer. Since for metallic SWNTs there are allowed states crossing the K points, we substitute the coordinates of K point, $\mathbf{K}$, into Eq. (3.34). We write $\mathbf{K}$ in Fig. 2.2 in the basis of $\mathbf{b}_1$ and $\mathbf{b}_2$ as

$$\mathbf{K} = \frac{2\mathbf{b}_1 + \mathbf{b}_2}{3}. \tag{3.35}$$

Substitution of Eq. (3.35) into Eq. (3.34) and using the definitions of the reciprocal lattice vectors in Sec. (2.2) gives the important result $2n + m = 3\ell$ [3]. This can be written as

$$n - m = 3\ell. \tag{3.36}$$

Thus, if $n - m$ is a multiple of 3, the SWNT is metallic. If not, the SWNT is semiconducting. We now calculate the normal distances from the $\mu = 0$ cutting line to K point. The vector connecting two neighbouring cutting lines is $\mathbf{K}_1$. The normal distance is given by

$$\frac{\mathbf{K} \cdot \mathbf{K}_1}{\mathbf{K}_1 \cdot \mathbf{K}_1} = \frac{2n + m}{3}. \tag{3.37}$$

Eq. (3.37) gives the normal distance (in units of $|\mathbf{K}_1|$) to the K point. The normal distance from the $\mu = 0$ cutting line to K point is a multiple of $1/3$ of $\mathbf{K}_1$.

$$2n + m = 3\ell + 1 \quad \text{(S1)} \quad \text{or} \quad 2n + m = 3\ell + 2 \quad \text{(S2)}. \tag{3.38}$$

It implies further that the normal distances from K point to the two nearest cutting lines are multiples of $\mathbf{K}_1/3$. If the normal distances from K point to the cutting lines are $1/3$ or $2/3$ of $\mathbf{K}_1$, the SWNT is a semiconductor and else the SWNT is a metal. These three possibilities are shown in Fig. 3.11. The cutting lines shown in Fig. 3.11 are for zigzag SWNTs but the statements made hereafter are general. Firstly, we define the touching point of the cutting lines with the electron equi–energy contour in Fig. 3.11 as van Hove singularity (VHS). As we show in detail in the following section, the electronic density of states has a peak at the VHS point. The lowest VHS is labelled by $\mathbf{k}_1$ and the next higher VHS by $\mathbf{k}_2$. The difference between S1 and S2 SWNTs is, on which side of K the VHS occur. E.g. for S1 SWNTs, $\mathbf{k}_1$ occurs inside the first BZ and $\mathbf{k}_2$ occurs along the Γ–M line. For S2 SWNTs this order is reversed.

Metallic SWNTs have a cutting line through K point. The two cutting lines nearest to K point occur at the same distance measured from K point. Their energy is however slightly different. From Fig. 3.11 it can be seen that the two points contributing to the lowest VHS in metallic SWNTs are at $\mathbf{k}_1$ and $\mathbf{k}_1'$ and lie on a different equi–energy contour. This leads to the so–called trigonal warping effect in metallic SWNTs [36]. The trigonal warping effect induces a small splitting in the VHS peaks (≈ 0.1 eV for a $(18,0)$ SWNT with $d_t = 1.4$ nm). The splitting of the VHS is largest for zigzag SWNTs and equal to zero for armchair SWNTs. This can also be understood from Fig. (3.11): if the cutting lines are parallel to the vertical K–M line, then the energies at $\mathbf{k}_1$ and at $\mathbf{k}_1'$ are equal to each other and no splitting occurs. Metallic SWNTs can be classified according to the one–dimensional Fermi wavenumber k_F, at which the the cutting line and $\mathbf{K}$ cross. We now calculate the crossing point by projecting the $\mathbf{K}_2$ direction, similarly to what we did in Eq. (3.37) for the $\mathbf{K}_1$ direction. We expand $\mathbf{K}$ as in Eq. (3.35) and also $\mathbf{K}_2$ into a basis of $\mathbf{b}_1$ and $\mathbf{b}_2$. By noting $\mathbf{b}_1 \cdot \mathbf{b}_1 = b^2$ and $\mathbf{b}_1 \cdot \mathbf{b}_2 = -b^2/2$ we can obtain

$$\frac{\mathbf{K} \cdot \mathbf{K}_2}{\mathbf{K}_2 \cdot \mathbf{K}_2} = \frac{m}{d_R}. \tag{3.39}$$

For d_R we can substitute Eq. (2.5) and obtain $d_R = d$ or $d_R = 3d$, according to wether $n - m$ is a multiple of $3d$ or not. When we substitute $d_R = d$, we get an integer number, since d is defined to be a divisor of n and m. Thus, $\mathbf{K}$ occurs at an integer number of shifts by $\mathbf{K}_2$. Thus we can shift back this point and obtain the Fermi wavevector $k_\mathrm{F} = 0$. That is, the center of the metallic band is crossing $\mathbf{K}$ for $d_R = d$. We will call such SWNTs to be metallic type 1 or M1 type. If $d_R = 3d$, we can get $k_\mathrm{F} = 1/3$ (in units of K_2). Thus the Fermi wavevector occurs at $1/3$ of the length of a cutting line. Such SWNTs are metallic type 2 (M2). In summary, the conditions for metallic 1 and metallic 2 SWNTs are

$$d_R = d \quad \text{(M1)} \quad \text{or} \quad d_R = 3d \quad \text{(M2)}. \tag{3.40}$$

It is clear, that for armchair SWNTs, we have $d_R = 3d$ and thus all armchair SWNTs are M2 SWNTs, which have a Fermi wavevector $k_\mathrm{F} = \pm|\mathbf{K}_2|/3 = \pm 2\pi/(3a)$. Metallic zigzag SWNTs have $d_R = d$ and therefore $k_\mathrm{F} = 0$.

The chiral indices of all possible SWNTs form a hexagonal lattice as is shown in Fig. 3.12. We plot the semiconducting S1 and S2 SWNTs by a grey shaded circle and box and the metallic M1 and M2 SWNTs by a filled circle and box, respectively. The parallel lines in Fig. 3.12 denote the SWNTs for $2n + m = 14 \ldots 19$, which is called "family". The optical properties of the same family appear in the photoluminescence spectra.

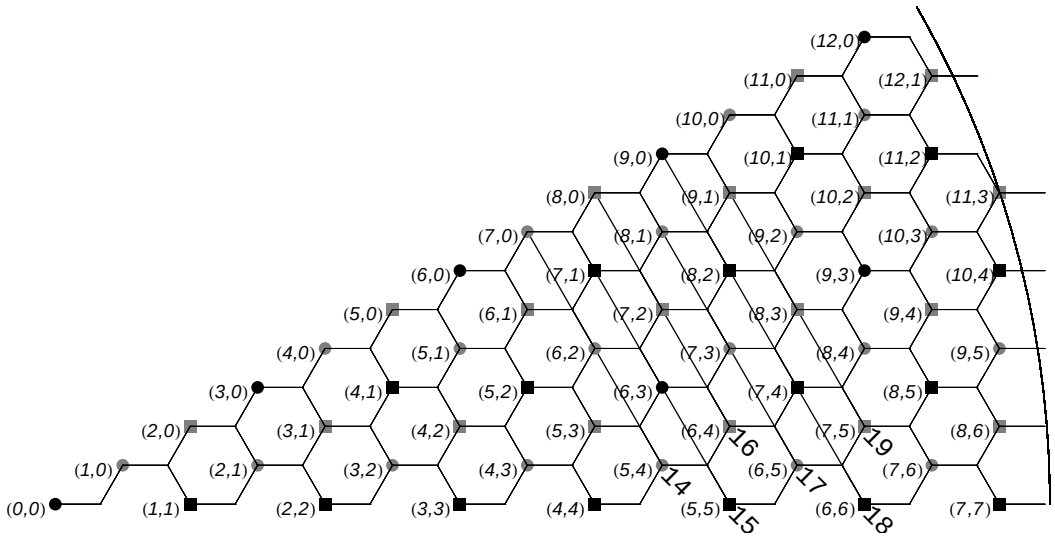

Figure 3.12: Chiral vectors for semiconducting (metallic) type I and II SWNTs. The (n,m) indices are written on the left side of the corresponding chiral vectors. Semiconducting (metallic) type I and type II SWNTs are labelled by a grey shaded (filled) circles and a grey shaded (filled) boxes, respectively. The SWNTs that belong to the same $2n + m = const$ family are connected by lines. The families for $2n+m = 14 \ldots 19$ are shown. The diameter region of 1 nm is indicated by an arc.

3.5.1 Density of electronic states and van Hove singularities

In SWNTs the one–dimensionality of electronic bands in the zone–folding scheme gives rise to flat regions in the band structure if the direction of zone–folding is parallel to the equi–energy contour in graphene. The cutting lines for a $(5, 5)$ SWNT are shown in Fig. 3.13 and the flat regions in the 1D electronic bands can be seen. The density of states per energy per C atom in a SWNT is calculated as

$$n(E) = \frac{2 \sum\limits_{\mu=-\frac{N}{2}}^{\frac{N}{2}-1} \sum\limits_{i=-\frac{U}{2}}^{\frac{U}{2}-1} \delta \left\{ E - E_\mu(k_i) \right\}}{\int_{-\infty}^{\infty} \sum\limits_{\mu=-\frac{N}{2}}^{\frac{N}{2}-1} \sum\limits_{i=-\frac{U}{2}}^{\frac{U}{2}-1} \delta \left\{ E' - E_\mu(k_i) \right\} dE'}. \tag{3.41}$$

In Eq. (3.41) the integration is to be taken over all valence and conduction π electronic bands. The factor 2 in Eq. (3.41) comes from spin degeneracy.

The DOS in Fig. 3.10(c) has been calculated with Eq. (3.41). The value of U in Eq. (3.41) is equal to the number of SWNT unit cells along the SWNT axis, if we neglect finite–size effects.

A quantity similar to the DOS from Eq. (3.41) is the JDOS (joint density of states). The

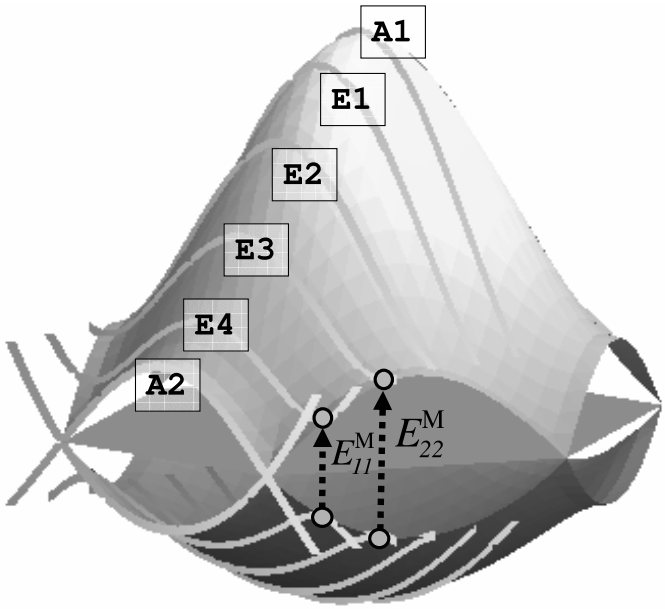

Figure 3.13: Cutting lines for a $(5,5)$ SWNT on the surface of graphite bands. Non–degenerate A symmetry and doubly degenerate E symmetry bands are labelled. The optical transitions at VHS E_{11}^{M} and E_{22}^{M} are indicated.

JDOS is related to experiments that measure absorption of light and is defined by

$$n_J(E) = \frac{\sum_{\mu,\mu'=-\frac{N}{2}}^{\frac{N}{2}-1} \sum_{i=-\frac{U}{2}}^{\frac{U}{2}-1} \delta\left[E - \{E_{\mu'}^{c}(k_i) - E_{\mu}^{v}(k_i)\}\right]}{\int_{-\infty}^{\infty} \sum_{\mu,\mu'=-\frac{N}{2}}^{\frac{N}{2}-1} \sum_{i=-\frac{U}{2}}^{\frac{U}{2}-1} \delta\left[E' - \{E_{\mu'}^{c}(k_i) - E_{\mu}^{v}(k_i)\}\right] dE'}. \tag{3.42}$$

From Eq. (3.42) it is clear that the JDOS has a maximum when valence and conduction bands run parallel. The cutting line indices for initial and final states are μ and μ', respectively. It is noted that previous calculations [37] have yielded $\mu' = \mu$ for light polarization parallel to the SWNT axis and $\mu' = \mu \pm 1$ for light polarization perpendicular to the SWNT axis. Thus, for parallel light polarization, optical transitions occur between the VHS in the valence and conduction bands.

The optical properties are largely determined by absorption of light with a photon energy equal to the energy difference between two VHS in the conduction and valence band as is illustrated in Fig. 3.13. Because of the enhancement in the optical absorption due to the high number of electronic states, it is possible to observe optical spectra from an isolated SWNT. Furthermore, the strong resonance enhancement can be used to pick up the resonant signal from only a few SWNTs in a sample with many different (n,m). By changing the laser energy, different SWNTs can be selectively probed. From Fig. 3.13 it is clear why the metallic VHS

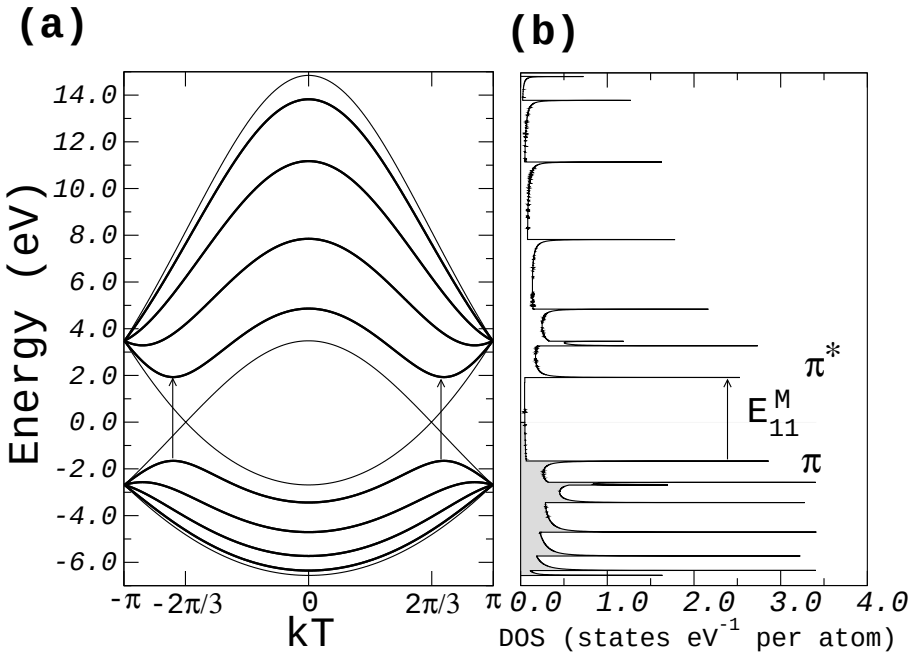

Figure 3.14: Electron energy dispersion relations (left) and DOS (right) for a $(5,5)$ SWNT . See Fig. 3.13 for cutting lines.

appear at a higher energy than semiconducting VHS for SWNTs with the same diameter. Since we have a metallic band (labelled by $A2$), which does not have a VHS (apart from M point at a high energy), the next cutting line is shifted further away from K point and thus has a higher energy. In Fig. 3.13 we label the non–degenerate bands by A and the doubly degenerate bands by E. The double degenerate bands are only shown on one side for simplicity. The 1D electron energy dispersion relations that correspond to Fig. 3.13 are shown in Fig. 3.14. Due to the crossing of K point by a cuttingline, the $(5,5)$ SWNT is a metal as can also be seen from the DOS at Fermi level.

For electronic states close to K, the equi–energy–contour is given by a circle as we derived in Eq. (3.23). When we substitute the k_i which are touching points to the circle of constant energy, we can obtain the VHS energy in the lowest order approximation. For semiconducting SWNTs, we substitute $\sqrt{k_x^2 + k_y^2} = 2i/(3d_t)$ and for metallic SWNTs, we substitute $\sqrt{k_x^2 + k_y^2} = 2i/(d_t)$ into Eq. (3.23). If we multiply the energy by 2 then we get the transition energy $\pi \to \pi^*$ at the VHS with index i as

$$E_{ii}^S = \frac{2ati}{\sqrt{3}d_t} \quad \text{and} \quad E_{ii}^M = \frac{2\sqrt{3}ati}{d_t}, \quad (i = 1, 2, 3). \tag{3.43}$$

Here E_{ii}^{S} and E_{ii}^{M} denote VHSs of semiconducting and metallic SWNTs, respectively. It is clear from Eq. (3.43) that the energy gap at the VHS with index i is inverse proportional to the SWNT diameter d_t and that the first metallic VHS occurs at three times the energy of a semiconducting SWNT.

3.5.2 Effective masses in semiconducting S1 and S2 SWNTs

We now consider the effective masses in the region of E_{11}^{S} and E_{22}^{S}. The effective electron mass m^* is defined as

$$\frac{1}{m^*} = \frac{1}{\hbar^2}\frac{\partial^2 E(k)}{\partial k^2}. \tag{3.44}$$

Thus for a flat band m^* will be larger. In fact, $(6n, 0)$ zigzag SWNTs have a completely flat band, connecting the M points. In such a band, the effective mass would be infinite. The flattness of a band is also related to the JDOS, since we get higher JDOS for flatter bands. Again, in the completely flat zigzag band, all electronic states along the cutting line appear at the same energy.

If we apply this concept to the cutting lines shown in Fig. 3.11, we can estimate the tendencies for m^* (or JDOS) for S1 and S2 SWNTs. From the equi–energy contours, we can see that m^* is increasing little if we go along K–M but increasing relatively more along the K–Γ direction. Thus we expect different effective masses at the same distances from K . The m^* along K–M is smaller in this case. For S1 in Fig. 3.11(a), the E_{11}^{S} occurs at $\mathbf{k}_1$ at 1/3 of a cutting line distance away from K in Γ direction. The E_{22}^{S} occurs at $\mathbf{k}_2$ at 2/3 of a cutting line distance away from K in the K–M direction. Thus, m^* at $\mathbf{k}_2$ and at $\mathbf{k}_1$ are not so different from each other because the distance in the direction of large increase (K–Γ) is smaller than the distance in the direction of little increase (K–M). For S2 in Fig. 3.11(b), the situation is quite different. Here, the distances to $\mathbf{k}_2$ along K–Γ is two times the distance to $\mathbf{k}_1$. Thus the differences of m^* at $\mathbf{k}_2$ and $\mathbf{k}_1$ are more different than in the case of S1 SWNTs with the same diameter.

Chapter 4

Raman spectroscopy of graphite and single wall carbon nanotubes

In this chapter the current status of research for optical properties of a SWNT is reviewed. We show the calculation of phonon dispersion relations and first–order Raman effect in graphite and SWNTs is reviewed. The double resonance Raman theory is explained and the formulas to calculate first–order Raman intensities are given.

4.1 Phonon dispersion relations in graphite and SWNTs

Phonon energy dispersion relations are a fundamental physical property of a solid, especially for determining the mechanical, thermal and other condensed–matter phenomena. The phonon energy dispersion relations of three-dimensional (3D) graphite (or two–dimensional (2D) turbostratic graphite) have been determined experimentally by inelastic neutron scattering [38, 39] and electron energy loss spectroscopy (EELS) [40, 41, 42]. These methods do generally not probe the whole BZ but are particularly accurate for zone–center phonons. For phonons in between the K point and M point, there are no experimental data. As a result of the lack of data, the discrepancy between different experimental methods is large between K and M point. Close to Γ point, all methods stated above agree on the shape of the dispersion. Furthermore, the zone–center phonons can be probed by Raman spectroscopy which is known to give accurate results with an error bar around only 1 cm^{-1}. Recently inelastic x–ray scattering has provided the phonon dispersion relations of graphite with experimental data–points in the region between K and M [43]. Theoretically, a force constant model [38] and ab–initio calculations [44, 43] have been used. In a tight binding force constant model (or a molecular dynamics method) a set of 8 or 12 force constants are fitted to reproduce the experimental data points. In ab–initio calculations, force constants are calculated by calculating the force on an atom when displacing the atom from its equilibrium position.

We will use a force constant model that can calculate phonon dispersion relations by fitting the force constants of four nearest neighbour atoms to experiments or to a more sophisticated ab–initio approach. The twelve force constants we use are sufficient to reproduce all experimental and theoretical data. We will first explain the force constant model [4] and then tabulate the

force constants that reproduce recent results. The force constant model has been used together with bond–polarization theory [45] to calculate non–resonant Raman spectra of SWNTs [46].

4.1.1 Force constant model

The phonon dispersion relations are calculated using a force constant model, in which the i–th atom is connected to its j–th neighbour atom through a force constant tensor $K^{(ij)}$. The components of the force constant tensors are made from the force constants. Since the force between two atoms decreases with increasing inter–atomic distance, interactions can be neglected for a longer distance than the cut–off radius. The cut–off distance was taken equal to the fourth nearest neighbour distance because the fitted phonon dispersion can reproduce well the observed neutron scattering data [38]. Since any A or B atom has 18 neighouring atoms up to the fourth nearest neighbour, we need 12 force constant tensors for the A (B) atom with symmetry considerations. Each shell has three force constants for in–plane radial (along bond direction), in–plane transversal (perpendicular to bond direction) and out–of–plane movements. Within a given shell, we put one atom on the x axis with coordinate of the radius of the shell. Then we can rotate the force constant tensor to any atom position on that shell by a rotation matrix U_m around the z axis perpendicular to the graphene plane. For the first shell U_m for the interaction of the type A atom with a B_m atom ($m = 1, 2, 3$) is given by [4]

$$U_m = \begin{pmatrix} \cos\theta_m & \sin\theta_m & 0 \\ -\sin\theta_m & \cos\theta_m & 0 \\ 0 & 0 & 1 \end{pmatrix}. \tag{4.1}$$

The force constant tensors in the first shell can be calculated using

$$K^{(A,Bm)} = U_m^{-1} K^{(A,B1)} U_m, \qquad (m = 2, 3). \tag{4.2}$$

For $m = 1$, U_m is the unity matrix and the force constant tensor has only diagonal elements and is given by

$$K^{(A,B1)} = \begin{pmatrix} \phi_r^{(1)} & 0 & 0 \\ 0 & \phi_{ti}^{(1)} & 0 \\ 0 & 0 & \phi_{to}^{(1)} \end{pmatrix}. \tag{4.3}$$

The force constant between an atom in the center and an atom on the positive x axis in the nth shell shall be $\phi_r^{(n)}$ for in–plane radial, $\phi_{ti}^{(n)}$ for in–plane tangential and $\phi_{to}^{(n)}$ for out–of–plane plane vibrations. Force constants up to fourth neighbor atoms are needed to reproduce the twisting vibrations of a C–C bond in which the fourth nearest neighbor C1 and C2 atoms in C1–C–C–C2 are vibrating. The vibrational frequencies are obtained by solving

$$\mathcal{D}(\mathbf{q})\mathbf{S}^{\nu}(\mathbf{q}) = 0. \tag{4.4}$$

Here $\mathbf{q}$ is the phonon wavevector and $\mathbf{S}^{\nu}(\mathbf{q})$ is the phonon eigenfunction of the ν–th phonon branch. The dynamical matrix $\mathcal{D}$ defined by

$$\mathcal{D} = \begin{pmatrix} D^{AA} & D^{AB} \\ D^{BA} & D^{BB} \end{pmatrix}, \tag{4.5}$$

Fitted force constants	Jishi et al. neutron [38]	initial set random	Dubay et al. ab–initio[44]	Maultzsch et al. x-ray [43]
		in–plane		
$\phi_r^{(1)} =$	36.50	44.80	44.58	39.28
$\phi_{ti}^{(1)} =$	24.50	11.25	11.68	11.36
$\phi_r^{(2)} =$	8.80	7.63	7.31	6.34
$\phi_{ti}^{(2)} =$	–3.23	–4.24	–3.74	–3.18
$\phi_r^{(3)} =$	3.00	–6.45	–5.70	–6.14
$\phi_{ti}^{(3)} =$	–5.25	6.47	6.67	9.27
$\phi_r^{(4)} =$	–1.92	1.94	1.82	2.53
$\phi_{ti}^{(4)} =$	2.29	0.90	0.52	–0.40
		out–of–plane		
$\phi_{to}^{(1)} =$	9.82	9.97	10.00	10.18
$\phi_{to}^{(2)} =$	–0.40	–0.73	–0.83	–0.36
$\phi_{to}^{(3)} =$	0.15	1.21	0.51	–0.46
$\phi_{to}^{(4)} =$	–0.58	–0.90	–0.54	–0.44

Table 4.1: Force constant parameters of graphite in units of 10^4dyn/cm. Here the subscripts r, ti, and to refer to radial, transverse in–plane and transverse out–of–plane, respectively.

with

$$\mathcal{D}^{(ij)}(\mathbf{q}) = \left(\sum_{j''} K^{(ij'')} - M_i \omega^2(\mathbf{q}) I \right) \delta_{ij} - \sum_{j'} K^{(ij')} e^{i\mathbf{q}\cdot\Delta\mathbf{R}_{ij'}}, \quad (i,j = A,B) \tag{4.6}$$

where the sum over j'' is taken for all neighbor sites from the i–th atom with $K^{(ij'')} \neq 0$, and the sum over j' is taken for the equivalent sites to the j–th atom. The first two terms of Eq. (4.6) have non-vanishing values only when $i = j$, and the last term appears only when the j–th atom is coupled to the i–h atom through $K^{(ij)} \neq 0$.

In a periodic system, the dynamical matrix elements are given by the product of the force constant tensor $K^{(ij)}$ and the phase difference factor $e^{i\mathbf{k}\cdot\Delta\mathbf{R}_{ij}}$, with $\mathbf{R}_{ij}$ being the distance vector between atoms i and j. This situation is similar to the case of the tight binding calculation for the electronic structure where the matrix element is given by the product of the atomic matrix element and the phase difference factor. Using the force constants that were obtained by a fit to neutron scattering data, we solve the 6×6 dynamical matrix in Eq. (4.4) for the phonon frequency and plot the phonon dispersion relation of graphene in Fig. 4.1(a) along with the experimental points denoted by circles. In Table 4.1, we list the force constants for the earliest result of a fit to inelastic neutron scattering data by Jishi et al.[38]. In Fig. 4.1(b), the ab–initio calculation of Dubay et al. [44] is shown by open circles. The lines in Fig. 4.1(b) denote the fitted dispersion relation. The force constant parameters for Fig. 4.1(b) are given in Table 4.1. In Fig. 4.1(c), we show a recently measured phonon dispersion relation, published by Maultzsch et al. [43]. In Fig. 4.1(c), inelastic x–ray scattering has been used to obtain a few data points along the K–M direction. These points can not be easily connected by a dispersion branch because

they are scattered in a wide frequency region. In the same paper [43] an ab–initio calculation was done and it was in good agreement with their inelastic x–ray scattering measurements.

In order to reproduce the experimental and theoretical data from different groups shown in Fig. 4.1, we find the set of force constants, that provides the best fit. This will enable us, to reproduce phonon dispersion relations of different groups by our force constant model. The force constants in Table 4.1 are obtained by a numerical fitting procedure that is explained in detail in Sec. 7.2.1. The numerical fitting procedure finds the minimum of the sum of squares of the difference between calculated and experimental data. Depending on the data, that we fit, there are several local minima. Thus, the choice of an initial force constant set as starting values for the fitting procedure becomes important for obtaining a good fit. In our fit of the force constant sets from Table 4.1, we define a starting set of force constants for each set of data, which we want to fit. To fit the data in Fig. 4.1(b), the initial set in Table 4.1 was used. To fit the data in Fig. 4.1(c), the output of the fit from Fig. 4.1(b) was used. The output of the fit from Fig. 4.1(b) is listed in Table 4.1 under "Dubay et al." and output of the fit from Fig. 4.1(c) is listed under "Maultzsch et al.". for future use.

From Fig. 4.1, it can be seen that most experimental data points are available from Γ to M and the rest of the BZ is not covered. We have six phonon mode branches that are in increasing frequency out of plane transverse accoustic (oTA), in–plane transverse accoustic (iTA), in–plane longitudinal accoustic (LA), out–of–plane transverse optic (oTO), in–plane transverse optic (iTO), in–plane longitudinal optic (LO).

4.1.2 Phonons in carbon nanotubes

Since SWNTs behave like solids along the axial direction but behave like molecules around the circumference direction, we expect four accoustic modes: three are translational modes and one mode is a rotation around the tube axis, which comes from the molecular nature of SWNTs. The rotational mode does not exist in graphite because it is a 3D solid. Thus we only have three accoustic modes in graphite. The number of phonon modes is given by zone–folding of graphite. Thus we expect $6N$ phonon modes in a SWNT, in which N is given by Eq. (2.6). The optical modes of a SWNT are generally well described by zone–folding of phonon dispersion of 2D graphite. There is, however, a small difference in phonon frequencies between iTO and LO in SWNTs whereas these modes are degenerate for graphite. The difference comes from the curvature which shifts the iTO phonons to a lower frequency in SWNTs when compared to graphite. As for accoustic modes in a SWNT, we have two accoustic modes with A1 symmetry [(in–plane longitudinal (LA), twisting mode (TW)]. The LA mode corresponds to a translational motion along the direction of the SWNT axis and the TW mode corresponds to a rotational motion around the SWNT axis. The two accoustic modes with E1 symmetry are a translational motion in the directions perpendicular to the SWNT axis. In Fig. 4.2 we show the Eigenvectors of the six $A1$ symmetry phonons of a $(10, 10)$ SWNT at $q = 0$. Two modes have zero frequency at $q = 0$. These are the in–plane longitudinal accoustic mode (LA) mode and the twisting mode (TW). For the LA mode, we have a movement of all atoms along the SWNT axis. Since this is a translation, the phonon energy must be zero, because it shifts the center of mass. In the case of TW, the SWNT is rotating along its axis and center of mass is not moving.

The lowest A1 mode with finite phonon energy is the radial breathing mode (RBM), where all atoms are moving in–phase in radial direction. The RBM mode at about 165 cm^{-1} is known to

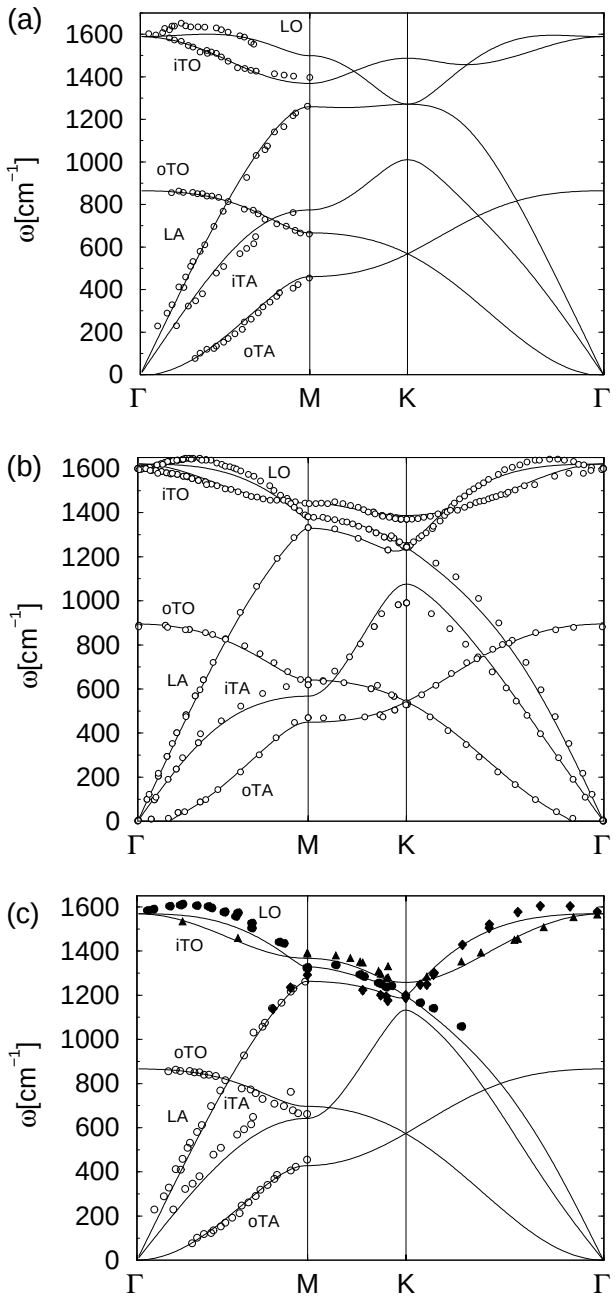

Figure 4.1: (a) Phonon dispersion as fitted to elastic neutron scattering data by Jishi et al. [38]. The circles denote experimental points. It can be seen, that there are no experimental data available for the region close to K. (b) Ab–initio calculations by Dubay et al. [44]. (c) Inelastic x–ray scattering data by Maultzsch et al. [43]. The open circles in the lower frequency range denote neutron scattering data, that were used to improve convergence of the fit.

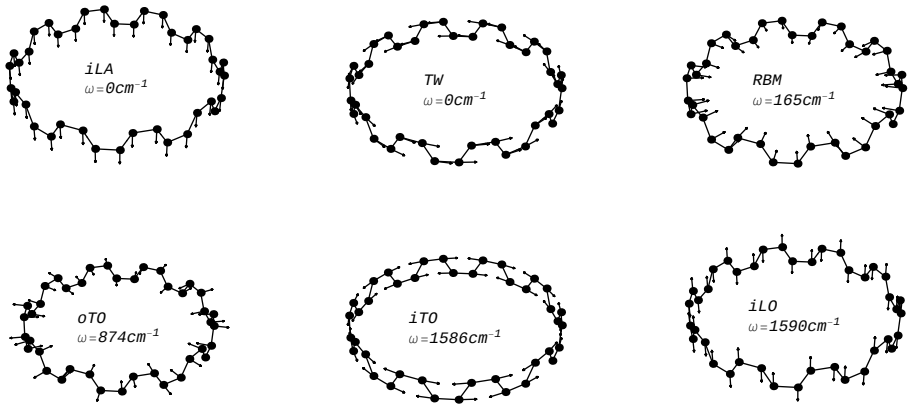

Figure 4.2: A1 symmetry phonon eigenvectors in a (10,10) SWNT ordered from lower to higher frequency. Force constants from Ref. [4] have been used to calculate the frequencies. The direction of phonon eigenvectors is independent of the force constants.

be Raman active. and appears at a frequency that is inversely proportional to d_t. Experimental Raman spectra are frequently used to estimate the d_t from the position of the RBM mode. The frequency of the RBM is generally described by a law of the form

$$\omega_{\mathrm{RBM}} = \frac{C_1}{d_t} + C_2 \quad \text{with} \quad C_1 = 248 \text{ cm}^{-1}\text{nm} \quad \text{and} \quad C_2 \approx 0 \ldots 20 \text{ cm}^{-1}. \tag{4.7}$$

C_1 and C_2 are obtained by fitting the experimental data. C_2 is a constant describing the upshift of ω_{RBM} due to bundling effects and should be equal to zero for isolated SWNTs. C_2 depends on both the bundle diameter and the diameters of SWNTs inside the bundle and has in general a different value for each sample.

At about 850 cm^{-1} out–of–plane optical mode (oTO) occurs. Although the oTO mode is Raman allowed by group theory, the first order Raman spectrum is weak in the experiment. However, we see this mode in the second–order Raman spectra.

The in–plane tangential optic (iTO) and in–plane longitudinal optic (LO) modes are not degenerate unlike in the case of graphite. Both, the iTO and the LO phonons are Raman active. The splitting of iTO and LO is a result of SWNT curvature. The frequency of the LO phonon, ω_G^+ is independent of d_t and the iTO phonon frequency, ω_G^- is inversely proportional to d_t^2 [47]. The proportionality constants for semiconducting and metallic SWNTs were determined by a fit to 62 chiralities. The fitting law and fitting parameter C are given by

$$\omega_G^- = \omega_G^+ - \frac{C}{d_t^2} \quad , \quad C = 47.7 \text{ cm}^{-1}(\text{semicond.}) \quad C = 79.5 \text{ cm}^{-1}(\text{metal}). \tag{4.8}$$

4.2 First–order resonance Raman spectroscopy

In the resonance Raman effect, an electron is photoexcited from the valence to the conduction band. The photo–excited electron creates (Stokes) or absorbs (anti–Stokes) a phonon,

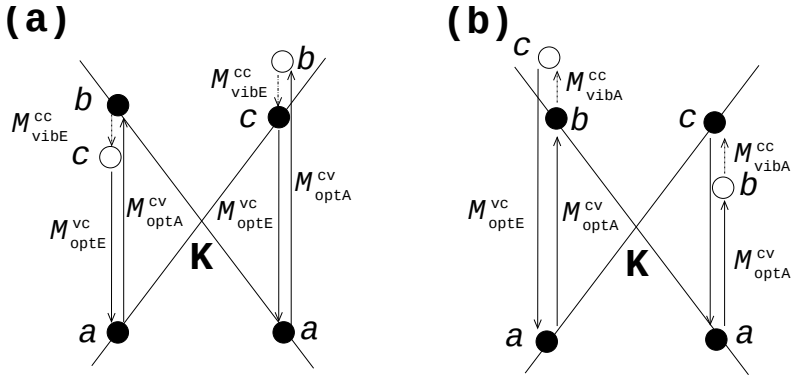

Figure 4.3: The first order Raman Stokes (a) and anti–Stokes (b) resonant Raman effect. Real electronic states are denoted by filled circles and virtual states are denoted by open circles. The transition from a to b occurs by absorption of a photon. Then the electron phonon interaction creates or absorbs a phonon. The electron goes from b to c, thereby changing its energy. Finally, the electron at c recombines with the hole at a by emitting a photon. The matrix elements for electron photon and electron phonon interaction are $M_{\rm opt}$ and $M_{\rm vib}$, respectively. See text for details.

respectively going to a lower or higher electronic energy state. In Fig. 4.3 we show these two possibilities for the RRS in Stokes and anti–Stokes geometry. If one of the two intermediate states are real electronic states, we have resonance Raman scattering (RRS). This condition is given if either the incident or scattered light is connecting real electronic states. In Fig. 4.3(a) we show for Stokes Raman processes the two resonance conditions, which are known as "incident resonance" and "scattered resonance". These two resonance conditions describe, if the incident or the scattered photon matches the energy between valence and conduction band. In other words, the processes are different according to which of the two intermediate states b and c is an eigenstate of the electron. The same distinction is made for Fig. 4.3(b) in which we describe the anti–Stokes process and its resonance with the incident and scattered photon. The behaviour can also be understood quantitatively by considering the formula, that we use to evaluate the Raman intensity:

$$I(E_{\rm laser}) = \int \left| \frac{M^{\rm cv}_{\rm optA}(\mathbf{k}) M^{\rm cc}_{{\rm vib}\rho}(\mathbf{k}) M^{\rm vc}_{\rm optE}(\mathbf{k})}{(E_{\rm laser} - E(\mathbf{k}) - i\Gamma_r)(E_{\rm laser} \pm E_{\rm vib} - E(\mathbf{k}) - i\Gamma_r)} \right|^2 d\mathbf{k}. \tag{4.9}$$

Here the first and second factors in the denominator, respectively, describe the resonance energy difference with the incident and scattered light, where the + (–) applies to the anti-Stokes (Stokes) process for a phonon of energy $E_{\rm vib}$, while Γ_r gives the inverse of the lifetime for the scattering process. The matrix element for the optical processes are given by $M^{\rm cv}_{\rm optA}(\mathbf{k})$ for absorption while $M^{\rm vc}_{\rm optE}(\mathbf{k})$ gives the matrix element for emission of a photon. $M^{\rm cc}_{{\rm vib}\rho}(\mathbf{k})$ denotes a phonon emission which is accompied by the transition of the photoexcited electron on the same k state in the conduction band. For phonon absorption (anti–Stokes), that is $\rho = A$ and for phonon emission (Stokes) processes, that is $\rho = E$. The $\rho = A$ and $\rho = E$ go together with the "+" and "–" signs in the denominator of Eq. (4.9), respectively. In 2D graphite, there are two possibilities for getting a high Raman intensity, which come from the resonance with incident

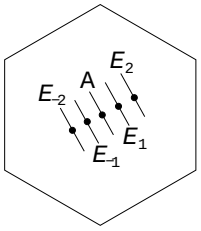

Scattering geometry	Phonon symmetry
ZZ	A
XZ,ZX	E_1
XX	A,E_2

Figure 4.4: The phonon symmetries which contribute to the first–order Raman effect in SWNTs are shown by the five cutting lines. The scattering geometries for X polarized light perpendicular to the SWNT axis and Z polarized light parallel to the SWNT axis are tabulated.

or scattered light that leads to a vanishing denominator.

The first–order Raman spectrum in graphene exists at about $1580\,\mathrm{cm}^{-1}$. This corresponds to a Raman active phonons of the iTO and LO modes, which are degenerate at Γ point. Furthermore, in graphite there is a Raman–active mode at around 49 cm^{-1} which corresponds to the in–phase movement of all the atoms in one graphene layers while neighbouring graphene layers are moving out–of–phase. However, this mode is not observed in Raman experiments because of a strong elastic Rayleigh scatting tail.

The second–order D–band feature lies at around $1355\,\mathrm{cm}^{-1}$ (for E_{laser}=2.41 eV) and its overtone, the G'–band at about twice the frequency of the D–band. While the D–band intensity depends on the presence of defects, the G'–band exists independent of defects. These features will be discussed with the double resonance Raman theory in Sec. 4.3.

4.2.1 Raman spectroscopy in carbon nanotubes

In SWNTs, there are $6N - 4$ phonon modes that have non–zero phonon frequency at $q = 0$. For a C_N symmetry group, A, E_1 and E_2 modes are symmetry allowed and the cutting lines with these symmetries are shown in Fig. 4.4. In Chapter 5, we will discuss the reason for this selection in terms of the electron photon matrix elements. The Raman active cutting lines in Fig. 4.4. Because only three cutting lines are non–degenerate, they give rise to $6 \times 3 - 3 = 15$ phonon frequencies that have non–zero phonon frequency at $q = 0$. Out of these, only two strong bands are observed experimentally. These are the radial breathing mode (RBM) occurs at around 180 cm^{-1} and the graphite derived G–mode at around 1580 cm^{-1}.

A typical experimental spectrum was shown in the introduction in Fig. 1.4 [11]. This spectrum was taken with a laser wavelength of 1024 nm and the SWNTs were oriented randomly. The four strongest peaks are indicated by labels. The first–order Raman features labelled by "RBM" and by "G" are the strongest peaks. The RBM consists of only one phonon branch but in the G–band 6 different phonon frequencies are contributing. The RBM mode is special to SWNTs in the sense that there is no corresponding mode in graphite. The RBM frequency ω_{RBM} is frequently used to determine the diameter d_t of a SWNT because the simple relationship between d_t and ω_{RBM} given in Eq. (4.7). Due to the strong diameter dependent frequency and the strong resonance enhancement that occurs, if the laser energy is equal to an E_{ii} transition, it is possible to assign an experimentally observed RBM peak to an (E_{ii}, d_t) data pair and thus obtain the structural information or a group of a few (n, m) indices, that are likely to identify the resonant SWNT for a given E_{laser}. The most striking features for the G–band of a

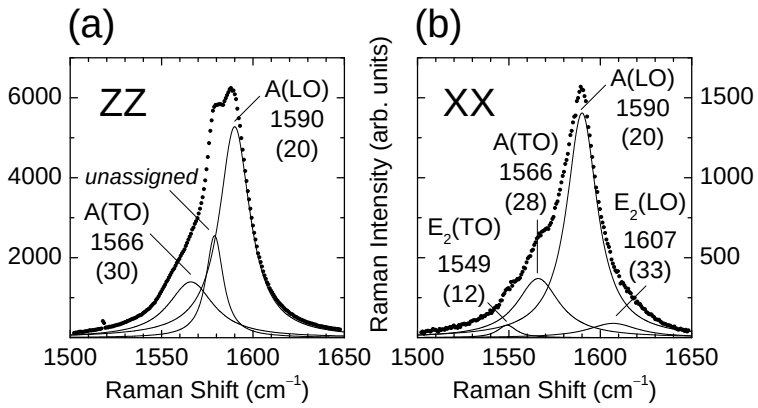

Figure 4.5: Experimental G–band spectra of SWNTS and their phonon symmetries [48].

SWNT are the splitting into a lower frequency TO and a higher frequency LO peak and changed lineshape of TO modes if metallic SWNTs are in resonance which can be observed in Raman experiments. The TO modes in metallic SWNTs are downshifted in frequency when compared to semiconducting SWNTs and their lineshape can be fitted to so–called Breit–Wigner–Fano lines. The latter was explained by a phonon–plasmon coupling that is enhanced for bundles and supressed for isolated SWNTs. The TO and LO components of the G–band consist of several peaks that can be associated with A_1, E_1 and E_2 phonon symmetries.

We now discuss the selection rules for various scattering geometries for incident and scattered light polarized parallel or perpendicular to the SWNT axis, which is along z direction. We can use the selection rules for electron photon and electron phonon scattering (which will be derived in Chapters 5 and 6, respectively) to analyze a first–order Raman process, in which the electron is excited at the valence band of the cutting line with index μ and energy $E_\mu^{(v)}$. Light, that is polarized along the z or x axis will be referred to as Z or X, respectively. We can get the following rules [49].

$$\begin{array}{lllllllll}
\text{(I)} & E_\mu^{(v)} & \xrightarrow{\mathrm{Z}} & E_\mu^{(c)} & \xrightarrow{\mathrm{A}} & E_\mu^{(c)} & \xrightarrow{\mathrm{Z}} & E_\mu^{(v)}, \\
\text{(II)} & E_\mu^{(v)} & \xrightarrow{\mathrm{X}} & E_{\mu\pm1}^{(c)} & \xrightarrow{\mathrm{A}} & E_{\mu\pm1}^{(c)} & \xrightarrow{\mathrm{X}} & E_\mu^{(v)}, \\
\text{(III)} & E_\mu^{(v)} & \xrightarrow{\mathrm{Z}} & E_\mu^{(c)} & \xrightarrow{\mathrm{E_1}} & E_{\mu\pm1}^{(c)} & \xrightarrow{\mathrm{X}} & E_\mu^{(v)}, \\
\text{(IV)} & E_\mu^{(v)} & \xrightarrow{\mathrm{X}} & E_{\mu\pm1}^{(c)} & \xrightarrow{\mathrm{E_1}} & E_\mu^{(c)} & \xrightarrow{\mathrm{Z}} & E_\mu^{(v)}, \\
\text{(V)} & E_\mu^{(v)} & \xrightarrow{\mathrm{X}} & E_{\mu\pm1}^{(c)} & \xrightarrow{\mathrm{E_2}} & E_{\mu\mp1}^{(c)} & \xrightarrow{\mathrm{X}} & E_\mu^{(v)}.
\end{array} \tag{4.10}$$

Here A, E_1, and E_2 denote phonon modes of different Γ-point symmetries of the cutting lines $\mu = 0$, $\mu = \pm1$, and $\mu = \pm2$, respectively, as shown in Fig. 4.4. Thus, by first–order Raman, we can probe the five cutting lines $E_{-2}, \ldots, E_2$ as shown in Fig. 4.4. By selecting a specific scattering geometry, we can selectively probe phonons from $\mu = 0$ for ZZ , $\mu = 1$ for XZ,ZX and $\mu = 2$ or $\mu = 0$ for XX geometry. An experimental G–band spectra for ZZ and XX geometry is shown in Fig. 4.5, in which the E_2 mode can be assigned to XX geometry. It shall be noted that the processes in Eq. (4.10) only occurs, if they are in resonance with the laser energy. Optical transitions along X are generally supressed due to the depolarization effect as discussed in Chapter 5. In 1D SWNTs, we have seen in Sec. 3.5.1 that the electronic density of

states shows van Hove singularities (VHS), in the density of states and thus we can expect that the Raman intensity is greatly enhanced if E_{laser} matches a VHS. Generally the resonance effect in the denominator is much stronger than the matrix elements and thus the matrix elements were assumed to be constant in the integration of Eq. (4.9) in previous analysis. However, in order to compare the absorption intensity of different chiralities at their E_{ii}, matrix elements are important.

4.3 Double resonant Raman scattering

4.3.1 Classification of Raman processes

Raman spectroscopy does not provide the phonon dispersion relations because the wave vector of the incoming photon is too small to create phonons at a large distance from the Γ point in the first–order Raman scattering process. In the first–order Raman spectra, only phonons with $\mathbf{q} = 0$ appear and thus no information about zone–boundary phonons is available. The reason for the $\mathbf{q} = 0$ selection rule in first–order Raman is that the initial and intermediate electron state are at almost the same $\mathbf{k}$ because the light has an energy dispersion $E = \hbar ck$ with almost zero wavevector. In the case of second–order Raman scattering, this condition can be removed because two phonons (or a phonon and a defect) are involved in the process as far as the sum of two phonon wavevectors gives total zero wavevector. Moreover, a scattering of an electron from K to K' points (hexagonal corners of 2D BZ) or vice versa is possible for $q \neq 0$ phonons. Hereafter, we call this process inter–valley scattering process, while the scattering within K (or K') is called intra–valley scattering. In second–order Raman scattering processes, there are low–intensity features in the Raman spectra which do not originate from phonons of the Γ point. These peaks can be classified into two–phonon peaks and disorder–induced one–phonon peaks. It is easy to distinguish most second–order Raman peaks from first–order features, since the Raman mode frequencies of the second-order Raman processes are generally dispersive, that is, the Raman shifts depend on the laser excitation energy E_{laser}. An example of a disorder–induced phonon mode is the D–band around $1350\,\text{cm}^{-1}$ for laser excitation energy $E_{\text{laser}} = 2.41\,\text{eV}$ [50, 28, 27, 51, 52, 53, 54]. This mode shifts with laser excitation energy by about $53\,\text{cm}^{-1}/\text{eV}$. The overtone mode of the D–band is known as the G'–band [27] (or the D*–band using another notation [54]) at about $2700\,\text{cm}^{-1}$ with a dispersion of about $106\,\text{cm}^{-1}/\text{eV}$. The G'–band spectrum is observed even in highly-order graphite, since the corresponding process involves the creation of two phonons with equal but oppositely directed momenta. Thomsen and Reich explained the dispersion of the D–band phonon frequency with E_{laser} by a double–resonance process [53]. This idea was then applied to all six branches for the phonon dispersion relations of graphite, for which many disorder–induced peaks can be assigned as non zone–center phonon modes when combined with theory [55]. The assignment is almost perfect near the Γ point. However the assignment is not so good near the K point phonons, which is ascribed to the lack of experimental data from inelastic neutron measurements for regions of the Brillouin zone near the K point. The first– and second–order intra–valley Raman processes are shown in Fig. 4.6. In Fig. 4.6(a), a first–order process, that consists of three interactions is shown: (1) the electron photon interaction to bring the electron from the valence to the conduction band, (2) the electron phonon interaction between two conduction band states, and (3) electron photon interaction that recombines the electron with the hole. In Fig. 4.6(b), a second–order,

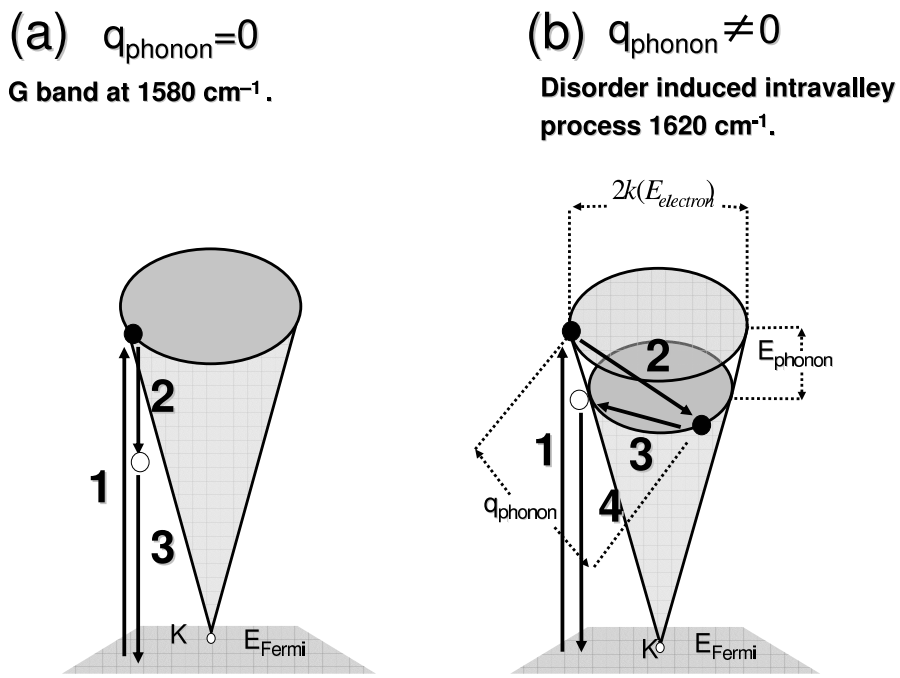

Figure 4.6: Intra–valley Raman processes, in which a photo–excited electron state scatters within one of the two K points. (a) The first–order Raman effect with $q = 0$ that leads to the G–band and (b) a second–order Raman process with $q \neq 0$ is responsible for a weak feature around 1620 cm^{-1}. See text for description of numbered, constituent scattering processes.

inter–valley, one–phonon process is shown. This process consists of four interactions: (1) the electron photon interaction to bring the electron from the valence to the conduction band, (2) the electron phonon interaction to scatter the photo–excited electron to an intermediate state, (3) the electron defect interaction that scatters the electron back to the initial electron wavevector $\mathbf{k}$, and (4) electron photon interaction, that recombines the electron with the hole.

In Fig. 4.7 an inter–valley process is shown. The processes (1) to (4) in Fig. 4.7 are the same processes as in Fig. 4.6(b) except for the length of $\mathbf{q}$.

It is noted, that the interaction (3) in Fig. 4.6(b) and in Fig. 4.7 is not necessarily a defect scattering but an electron phonon interaction is also possible. This corresponds to a second–order two–phonon process which does not depend on the presence of defects. The G'–band at about 2700 cm^{-1} is assigned to a second–order, two–phonon, inter–valley process. It involves two inter–valley phonons with opposite momenta. In the following section, we give a detailed description of the double–resonance Raman processes.

4.3.2 Double–resonance conditions

In the double–resonance Raman processes, the origin of the D–band and of the many weak dispersive phonon modes in the Raman spectra of graphite is explained by (1) a second–order

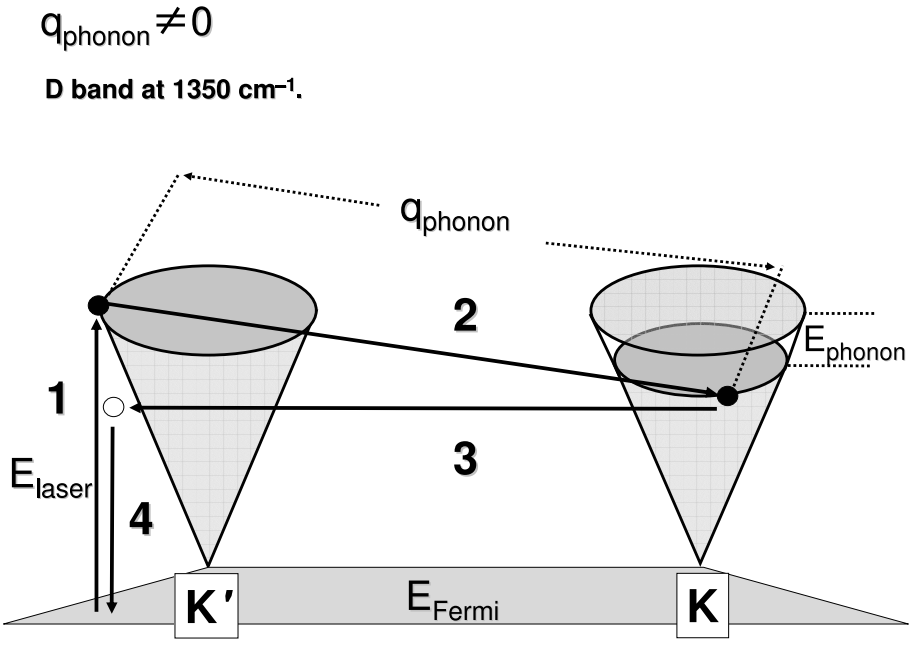

Figure 4.7: inter–valley process that leads to the D–band at 1350 cm^{-1}. The electron phonon (2) and electron defect (3) interactions connect K' with K and K with K' point, respectively.

scattering process, and (2) a resonant enhancement of the Raman intensity in two consecutive scattering processes. In the second-order scattering process, an electron with initial momentum k is: (a) at first excited to the energy $E^i(k)$ by the incident photon, (b) scattered to a state $k+q$, $[E(k+q)]$, and (c) then back-scattered to the state k, $[E^f(k)]$, and finally (d) recombined with a hole to yield the scattered photon. If $E(k+q)$ and either the $E^i(k)$ or $E^f(k)$ states correspond to real electronic states, the Raman intensity is enhanced twice by two resonant factors in the denominators occurring in the intensity formula, and this is known as the double resonance Raman process [56].

When we look at double-resonance Raman processes in the 2D BZ of graphite, we see that electrons around the K point are relevant to Raman processes. As far as we restrict the exciting laser energies, $E_{\rm laser}$, to be $E_{\rm laser} < 3$ eV, the equi–energy contours of π electrons can be treated as circles around the K point as a first approximation (see Fig. 4.8). Further, we assume that the electron energy dispersion is symmetric $\pm E(k)$ around the Fermi energy $E = 0$, where $E(k)$ and $-E(k)$ are anti–bonding π^* and bonding π bands, respectively. Here we adopt a simple tight binding result for $E(k)$ [4] with a nearest neighbor tight binding parameter $\gamma_0 = 2.89$ eV. For smaller laser energies, we can use the linearized energy dispersion relation for electrons, $E(k) = \sqrt{3}\gamma_0 ka/2$ in which a is the lattice vector $a = \sqrt{3}a_{\rm C-C}$ with $a_{\rm C-C}$=1.42Å. In this case the photon absorption occurs when $E_{\rm laser} = 2E(k)$. Hereafter, the k vectors which exist on the energy contour $E = E(k)$ are denoted by $k = k(E)$. When we consider double-resonance Raman processes involving an inelastic scattering event by emitting a phonon with an energy

$E_{\rm phonon}$ and an elastic scattering event due to a defect occurring for each forward and back scattering event, we have four different resonant processes. A factor of two (of the four) comes from two possibilities: whether inelastic or elastic scattering occurs first, and another factor of two comes from whether the incident $E^i(k)$ or the scattered $E^f(k)$ states are resonant. These four processes generally lead to different lengths from one another for the wavevector q of the scattering phonon. Moreover, there are two possibilities for selecting the q vectors, since there are two inequivalent energy-contours around the K and K' points in 2D BZ. A relatively small q vector is selected for scattering within the same energy contour (from K to K or from K' to K'), while a larger q vector is selected for scattering from K to K' (or from K' to K), which we call intra–valley see Fig. (4.6) and inter–valley scattering (see Fig. (4.7), respectively . In total, there are eight different double resonance Stokes scattering processes for the second–order, one–phonon emission, double–resonance D–band Stokes processes.

In Fig. 4.8 we show an example of the four q vectors for intra–valley scattering, where solid and dotted arrows denote inelastic and elastic scattering processes, respectively. Solid and open small circles denote, respectively, resonant and non–resonant conditions. That is, in the case of the solid circles, the corresponding energy of the state is that for the real electronic state $E(k)$, while the state for open circles has a virtual energy state different from $E(k)$. The electron-hole pair is created and recombined for the same k points at the labels of (a), (b), (c) or (d). From this point the electron is scattered to an intermediate $k+q$ state which is always resonant (one solid circle). In the case of processes (a) and (b), the incident laser with $E_{\rm laser}$ is in resonance with $E^i(k)$ and solid circles of (a) and (b) correspond to the initial states. Thus the initial k vectors are on the second largest circle denoted by $\rm k_3$ of energy contour of $E = E_{\rm laser}/2$. In the case of (a), the scattering to the $k+q$ state is inelastic (solid arrow), and the corresponding energy lies on the smallest circle ($\rm k_1$) where $E = E_{\rm laser}/2 - E_{\rm phonon}$. The back scattering to k now becomes elastic and $E^f(k) = E_{\rm laser}/2 - E_{\rm phonon}$ is smaller than $E^i(k)$ which is denoted by an open circle. In the case of (b), the scattering to the intermediate states is elastic and thus the intermediate states are on the same circle ($\rm k_3$) as the initial states. The back scattering to the initial states for (b) is inelastic and $E^f(k)$ is non-resonant and has an energy $E_{\rm laser}/2 - E_{\rm phonon}$. For processes (c) and (d), the final state with $E^f(k)$ are resonant with the scattered energy $E_{\rm laser} - E_{\rm phonon}$ and thus the final k vectors are selected on $k(E_{\rm laser}/2 - E_{\rm phonon}/2)$ which are the second smallest circles ($\rm k_2$) in Fig. 4.8. The corresponding initial k vectors for (c) and (d) lie on the circles $k(E_{\rm laser}/2 - E_{\rm phonon}/2)$. In the case of (c), since the back scattering is elastic, the intermediate states should have the same energy as $E^f(k)$, while in the case of (d), the back scattering is inelastic and thus the intermediate state has a higher energy than the final state by the phonon energy, namely $E_{\rm laser}/2 + E_{\rm phonon}/2$. Thus we can classify the four processes by either an incident or scattered resonance Raman event, and by the fact that either the elastic or inelastic event occurs first: (a) incident resonance, inelastic first, (b) incident resonance, elastic first, (c) scattered resonance, inelastic first, and (d) scattered resonance, elastic first. As a result, four electron energy contours separated by $E_{\rm phonon}/2$ are relevant for the double resonance processes, as shown in Fig. 4.8. Four energy surfaces correspond to the energies from the smallest energy (or circle) in Fig. 4.8, $E_{\rm laser}/2 - E_{\rm phonon}$, $E_{\rm laser}/2 - E_{\rm phonon}/2$, $E_{\rm laser}/2$ and $E_{\rm laser}/2 + E_{\rm phonon}/2$, for which the k vectors are denoted by from k_1 to k_4, respectively. It is noted here that $E_{\rm phonon}$ ($\leq$ 0.2 eV for G–band phonon) is generally much smaller than $E_{\rm laser}$ ($2 \sim 3$ eV) so that the distance between two of the circles circles $\delta k = k(E_{\rm phonon}/2)$ is smaller than the diameter of the circles and much smaller than the hexagonal edge of the 2D BZ. Figure 4.8

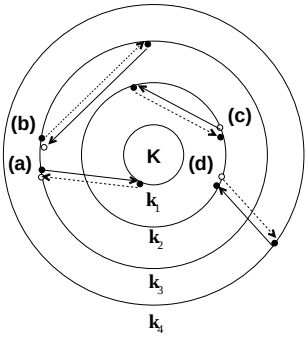

Figure 4.8: Four different, intra–valley, double resonance scattering processes occur around the K point in the 2D Brillouin zone of graphite. At each point of (a) (b) (c) and (d), an electron-hole pair is created. The electron is then scattered, and subsequently back scattered to the original position. Solid and dotted lines are, respectively, inelastic and elastic scattering processes. In (a) and (c), inelastic scattering occurs first, while in (b) and (d), elastic scattering occurs first. Solid and open circles denote resonant and non-resonant states, respectively. Processes (a) and (b), and (c) and (d) correspond, respectively, to incident and scattered resonance conditions. Four energy surfaces correspond to the energies from the smallest energy (or circle), $E_{\rm laser}/2 - E_{\rm phonon}$, $E_{\rm laser}/2 - E_{\rm phonon}/2$, $E_{\rm laser}/2$ and $E_{\rm laser}/2 + E_{\rm phonon}/2$, for which the k vectors are denoted by from k_1 to k_4, respectively. The separation between two circles is artificially enlarged compared to laser energy for clear understanding. [57]

is drawn schematically to convey a clear understanding of the physical processes. The phonon q vectors for the intra-valley scattering are related to phonon wave vectors around the Γ points. In the case of inter–valley scattering, the intermediate $k+q$ states exist at inequivalent K points with the same energy as in Fig. 4.8 (K' is not shown). The corresponding q vector has a value from K to K' (or from Γ to K). The q vectors for the inter–valley scattering are related to phonons around the K point [55].

For any k vector, possible q vectors exist on the circle of the $k+q$ states for each case, and the length of the q vectors can be changed from the closest to the most distant points on the circles. Since the q vectors are homogeneously distributed on the 2D BZ and especially on the circles, the density of the distance of q vectors from the K point, has a singularity for $|q|$ at the minimum and the maximum values which are shown in Fig. 4.9. The maximum $|q|$ vector corresponds to $2|k|$ if we neglect the small difference between the diameters of the circles, as mentioned above. In the case of the minimum $|q|$ values, we can assume $|q| = 0$, which is exact for the cases of (b) and (c). Since the phonon dispersion, except for the acoustic phonon mode, is flat around $|q| = 0$, the minimum $|q| \sim 0$ also gives a similar phonon frequency to that of $|q| = 0$. It is clear that the lengths of the q vectors are equal for the two processes of each figures. This gives two split Raman peaks in the dispersive phonon modes such as D–band for $|q| \neq 0$ and one peak for $|q| = 0$ when the distance is measured from the Γ and K points for intra– and inter–valley scattering, respectively.

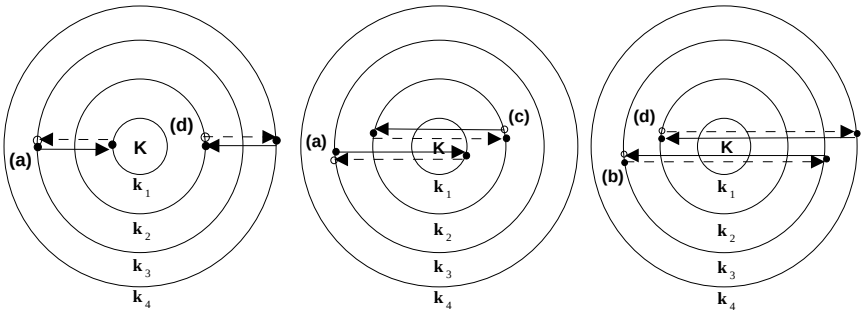

Figure 4.9: Here the three extreme cases, which lead to a high density of q-vectors for intra-valley scattering are shown. The left figure corresponds to $q \sim 0$ for (a) and (d) in Fig.4.8 and the center and the right figures correspond, respectively, to the $q \cong 2k$ and $q = 2k$ cases for (a) and (c) and for (b) and (d) [57].

Table 4.2: Experimental frequencies and widths [58] in cm^{-1} of the D–bands for different E_{laser} (in eV).

E_{laser}	ω_{D_1}	ω_{D_2}	ω_{D_3}	γ_D
1.91	1324	1333	1342	64
2.18	1336	1345	1354	66
2.41	1352	1361	1370	69
2.54	1357	1366	1375	72

4.3.3 Stokes and anti–Stokes spectra

In Fig. 4.10, we show a summary of the four possible Stokes processes (a-d) and the corresponding four anti–Stokes processes (e-h).

The length of the phonon wavevecor q is shown for each process. We can see that for the four Stokes processes, we can get only two different lengths (a and c) and (b and d) for q. Thus we expect two D–band peaks in the experimental spectra. For the corresponding anti–Stokes spectra the situation is similar and we also get two different lengths for q. From Fig. 4.10 we can now estimate the difference in phonon energy for the Stokes and anti–Stokes processes. It is known experimentally that the slope of the D–band is about $53\,\mathrm{cm}^{-1}/\mathrm{eV}$. We can thus write that $\partial\omega_D/\partial\Delta q = A \times 53\,\mathrm{cm}^{-1}/\mathrm{eV}$. The distance between the phonon singularities associated with the two peaks in both the S and the AS spectra is $\delta q = E_{\mathrm{phonon}}/A$, where $E_{\mathrm{phonon}} = 0.13\,\mathrm{eV}$. Therefore the shift between the two peaks which compose the D–band is expected to be $\delta\omega_D = E_{\mathrm{phonon}} \times 54\,\mathrm{cm}^{-1}/\mathrm{eV} = 9.2\,\mathrm{cm}^{-1}$. It can be seen in Fig. 4.11, that the two Stokes (or the two anti–Stokes) peaks can be fitted to two Lorentzians to the experimental Raman D–band though their spectral widths are much larger than their frequency separation $\delta\omega_D$.
Here we mention that at least two important facts contribute to the width of the peaks that constitute the D–band. First, due to the finite lifetime of the electronic excited states, phonons with wavevectors near $q = 2k$ can also contribute to the double resonance Raman process, thus

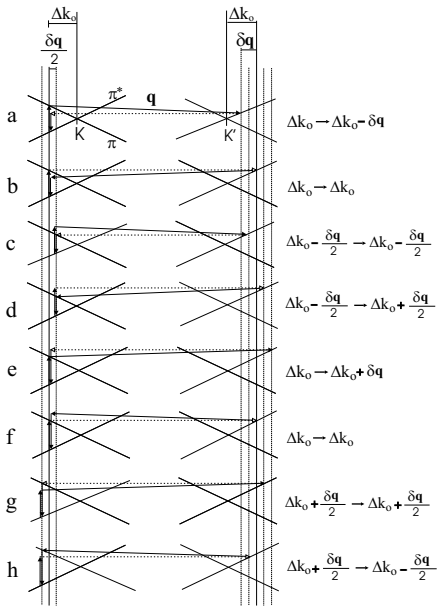

Figure 4.10: Fig. a-d (e-h) show Stokes (anti–Stokes) double resonance Raman processes. In processes (a) and (b) and (e) and (f), the incident photon is in resonance with a π-π^* transition, and in processes (c) and (d) and (g) and (h) the scattered photon is in resonance with a π-π^* transition [58].

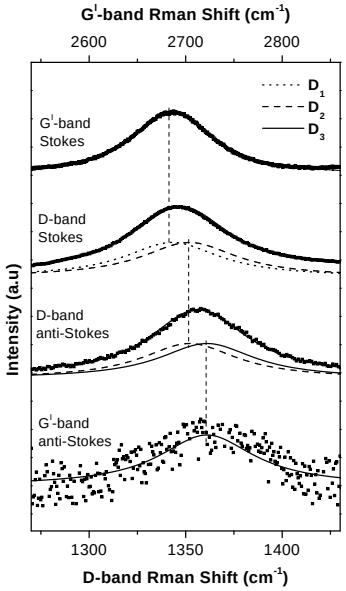

Figure 4.11: Stokes and anti–Stokes Raman spectra of the D–band in polyparaphenylene based graphite treated at 1500 ° (PPP1500) at $E_{\text{laser}} = 2.54\,\text{eV}$. D–band is fit by two Lorentzians, the Stokes band by the peaks D_1 and D_2, and the anti–Stokes band by the peaks D_2 and D_3 [58].

increasing the width of the D–band peaks. Another important contribution to the linewidth is the trigonal warping effect, since the energy contour of the electron dispersion is modified from a circle to a triangle with increasing Δk_0 [36]. Therefore, the distribution of wavevectors δk_0 associated with a given energy separation between the π and π^* bands increases with increasing Δk_0. Fig. 4.11 shows the fit of the Stokes and anti–Stokes D–bands for $E_{\rm laser} = 2.54\,{\rm eV}$ [58]. The D–band in the Stokes spectrum is fit by two Lorentzians centered at ω_{D_1} and ω_{D_2}, and in the anti–Stokes spectrum the D–band is fit by two Lorentzians at ω_{D_2} and ω_{D_3} which can be understood by the length of q shown in Fig. (4.10). In the Stokes spectra, the D_1 peak is associated with processes (a) and (c) in Fig. 4.10, whereas D_2 is associated with processes (b) and (d). For the anti–Stokes mechanisms illustrated in Fig. 4.10(e-h), the highest frequency peak D_3 is associated with processes (e) and (g), whereas processes (f) and (h) give rise to the intermediate peak D_2. Therefore, we conclude that the two peaks in the S and AS D–band are associated with the scattering from a point around K to a point around K$'$, by a phonon or by a defect.

Table 4.2 shows the fitting parameters of the Stokes and anti–Stokes Raman D–band, for incident laser energies $E_{\rm laser} = 1.91$, 2.18, 2.41 and 2.54 eV, respectively. The frequency ω_{D_2} is always the same in the Stokes and anti–Stokes spectra. Notice in Table 4.2 that the widths of the Lorentzians slightly increase with increasing $E_{\rm laser}$. This is a clear manifestation of the trigonal warping effect, which is more important for higher laser energies.

In the Stokes spectra in Fig. (4.11), though the D–band is composed by two peaks with frequencies ω_{D_1} and ω_{D_2}, and the overtone G'–band is composed by a single peak centered at $2\times\omega_{D_1}$. Since G'–band corresponds to a two–phonon process, the processes of b, d f and h in Fig. (4.10) do not exist and the processes a, c, e and g can be changed to two–phonon processes by changing the elastic scattering processes to the inelastic scattering processes. For the anti–Stokes spectra, the D–band is also composed by two peaks centered at ω_{D_2} and ω_{D_3}, and the G'–band is centered at twice the frequency of the highest frequency component D_3. The phonons related to the intermediate peak D_2 are thus only observed in the D–band.

Chapter 5

Optical absorption in graphite and carbon nanotubes

In this chapter, we show how to calculate the electron photon interaction matrix element using first–order time–dependent perturbation theory and tight binding wavefunctions for the $2p_z$ electrons.

5.1 Dipole approximation

The Hamiltonian for a charged particle with mass m and charge e in an electromagnetic field with vector potential $\mathbf{A}(t)$ and a periodic crystal potential $V(\mathbf{r})$ is given by

$$H = \frac{1}{2m}\left\{-i\hbar\nabla - e\mathbf{A}(t)\right\}^2 + V(\mathbf{r}). \tag{5.1}$$

where c is the velocity of light and m the electron mass. Here the electron π wavefunctions $\Psi^\imath(\mathbf{k})$ and $\Psi^\jmath(\mathbf{k})$ are eigenstates of an unperturbed tight binding Hamiltonian $H_0 = -\frac{\hbar^2}{2m}\Delta + V(\mathbf{r})$ for the bands $\imath$ and $\jmath$, respectively. When we neglect quadratic terms in $\mathbf{A}(t)$ and use the Coulomb gauge $\nabla \cdot \mathbf{A}(t) = 0$, the perturbation Hamiltonian $H_{\mathrm{opt}\rho}$ acting on the electron and causing its transition from valence to conduction band is given by

$$H_{\mathrm{opt}\rho} = \frac{ie\hbar}{m}\mathbf{A}_\rho(t)\cdot\nabla \quad \text{with} \quad \rho = \mathrm{A \text{ or } E}. \tag{5.2}$$

The ρ =A, E gives absorption or stimulated emission of light, respectively and determines the sign of $\pm i\omega t$ in the phase factors for electric and magnetic components of the wave. The Maxwell equation, which we need is in SI units given as

$$\nabla \times \mathbf{B} = \epsilon_0\mu_0\frac{\partial \mathbf{E}}{\partial t}. \tag{5.3}$$

The electric and magnetic fields of the light are $\mathbf{E}_\rho(t) = \mathbf{E}_0\exp[i(\mathbf{k}\cdot\mathbf{r} \pm \omega t)]$ and $\mathbf{B}_\rho(t) = \mathbf{B}_0\exp[i(\mathbf{k}\cdot\mathbf{r} \pm \omega t)]$, respectively. Thus $\mathbf{B} = \nabla\times\mathbf{A} = i\mathbf{k}\times\mathbf{A}$ and $\nabla\times\mathbf{B} = i\mathbf{k}\times\mathbf{B}$. Noting that [1] we write

$$\nabla\times\mathbf{B} = k^2\mathbf{A} = \frac{1}{c^2}\frac{\partial\mathbf{E}}{\partial t}. \tag{5.4}$$

[1] $(\mathbf{A}\times\mathbf{B})\times\mathbf{C} = (\mathbf{A}\cdot\mathbf{C})\mathbf{B} - (\mathbf{B}\cdot\mathbf{C})\mathbf{A}$

Since $\mathbf{E}$ is a plane wave, we just get $\partial\mathbf{E}/\partial t = -i\omega\mathbf{E}$. We also need $k = \omega/c$ and then $\mathbf{A}$ in vacuum becomes

$$\mathbf{A}_\rho = \frac{-i\mathbf{E}_\rho}{\omega}. \tag{5.5}$$

The energy density of the electromagnetic wave is given by I_ρ, the length of the Poynting vector,

$$I_\rho = \frac{E_\rho B_\rho}{\mu_0} = \frac{E_\rho^2}{\mu_0 c}. \tag{5.6}$$

The unit of I_ρ is [Joule/(m^{2}sec)]. The vector potential can be written in terms of light intensity I_ρ, and polarization of the electric field component $\mathbf{P}$ as

$$\mathbf{A}_\rho(t) = \frac{-i}{\omega}\sqrt{\frac{I_\rho}{c\epsilon_0}}\exp(\pm i\omega t)\mathbf{P}. \tag{5.7}$$

The "$\pm$" sign corresponds to emission("+") or absorption ("$-$") of a photon with frequency ω. Here ϵ_0 is the dielectric constant of vacuum with units [Farad/m]. The matrix element for optical transitions from an initial state $\imath$ at $\mathbf{k} = \mathbf{k}_\imath$ to a final state f at $\mathbf{k} = \mathbf{k}_f$ is defined by

$$\mathbf{M}^{f\imath}_{\mathrm{opt}\rho}(\mathbf{k}_f, \mathbf{k}_\imath) = \left\langle \Psi^f(\mathbf{k}_f)|H_{\mathrm{opt}\rho}|\Psi^\imath(\mathbf{k}_\imath)\right\rangle. \tag{5.8}$$

The matrix element in Eq. (5.8) is calculated by

$$\mathbf{M}^{f\imath}_{\mathrm{opt}\rho}(\mathbf{k}_f, \mathbf{k}_\imath) = \frac{e\hbar}{m\omega_\rho}\sqrt{\frac{I_\rho}{\epsilon_0 c}}e^{i(\omega_f - \omega_\imath \pm \omega_\rho)t}\mathbf{D}^{f\imath}(\mathbf{k}_f, \mathbf{k}_\imath)\cdot\mathbf{P} \tag{5.9}$$

where

$$\mathbf{D}^{f\imath}(\mathbf{k}_f, \mathbf{k}_\imath) \;=\; \left\langle \Psi^f(\mathbf{k}_f)|\nabla|\Psi^\imath(\mathbf{k}_\imath)\right\rangle \tag{5.10}$$

is the dipole vector between initial states $\imath$ and final states f. Fermi's golden rule gives transition probabilities between the initial state $\imath$ and the final state f for interaction time τ with the perturbation. For Ψ^f and $\Psi^\imath$, we put the tight binding wavefunctions of the π electrons in graphite. Using $H_{\mathrm{opt}\rho}$ from Eq. (5.2) and Eq. (5.7), we can write the optical absorption (A) and emission (E) probability per one second as as a function of $\mathbf{k}$.

$$W^{\rho=A,E}(\mathbf{k}_f, \mathbf{k}_\imath) \;=\; \frac{4e^2\hbar^4 I_\rho}{\tau\epsilon_0 m^2 c^3 E^2_{\mathrm{laser}}}|\mathbf{P}\cdot\mathbf{D}^{f\imath}(\mathbf{k}_f, \mathbf{k}_\imath)|^2\frac{\sin^2[(E^f(\mathbf{k}_f) - E^\imath(\mathbf{k}_\imath) \pm E_{\mathrm{laser}})\frac{\tau}{2\hbar}]}{(E^f(\mathbf{k}_f) - E^\imath(\mathbf{k}_\imath) \pm E_{\mathrm{laser}})^2} \tag{5.11}$$

Here, for absorption, $\rho = A$ goes with the "$-$" sign and emission $\rho = E$ goes with the "+" sign of "$\pm$". To derive Eq. (5.11), we considered the light propagation in vacuum. If we consider the real sample, which consists of a low density of SWNTs, we have to replace $\epsilon_0 \to \epsilon_0\epsilon$, where ϵ is the effective dielectric constant of the sample. The initial and final states can be valence or conduction bands $\imath, f = v$ or c. The meaning of I_ρ in Eq. (5.11) in the case of absorption of light and in the case of stimulated light emission is the intensity of the incoming light. The energy conservation $E^f(\mathbf{k}_f) - E^\imath(\mathbf{k}_\imath) \pm E_{\mathrm{laser}} = 0$ is fulfilled for long interaction times τ because $\frac{\sin^2(\alpha t)}{\pi\alpha^2 t} \to \delta(\alpha)$ for $\tau \to \infty$.

In summary, in this section we have shown that the optical absorption intensity is proportional to the absolute square of the inner product of light polarization with dipole vector.

$$W(\mathbf{k}_f, \mathbf{k}_i) \propto \left| \mathbf{P} \cdot \mathbf{D}^{fi}(\mathbf{k}_f, \mathbf{k}_i) \right|^2 \tag{5.12}$$

In the following we derive an expression for the dipole vector for transitions connecting π and π^* bands. In Sec. 5.2 we will derive an expression for the dipole vector for graphene and in Sec. 5.4 a derivation for the dipole vector for SWNTs is given.

5.2 Dipole vector

The wavefunction $\Psi = c_A \Phi_A + c_B \Phi_B$ is expressed by the sum of Bloch functions for $2p_z$ orbitals of carbon atoms at A and B sites, Φ_A and Φ_B {see Eq. (3.1)}. Further we decompose Φ_A and Φ_B into atomic orbitals with Bloch phase factors {see Eq. (3.2)}. The optical transition within a $2p_z$ orbital at the same atom is not possible because of the odd symmetry of $\mathbf{D}$ in x, y and z. Furthermore, the z component of $\mathbf{D}^{fi}$ is zero for all atomic matrix elements (also if the transition is between nearest neighbour atoms) which is also because of the odd symmetry of the z component of $\mathbf{D}^{fi}$. $\mathbf{D}^{fi}$ is given by

$$\begin{aligned} & \mathbf{D}^{fi}(\mathbf{k}_f, \mathbf{k}_i) \\ = \; & c_B^{f*}(\mathbf{k}_f) c_A^{i}(\mathbf{k}_i) \left\langle \Phi_B(\mathbf{k}_f, \mathbf{r}) | \nabla | \Phi_A(\mathbf{k}_i, \mathbf{r}) \right\rangle + c_A^{f*}(\mathbf{k}_f) c_B^{i}(\mathbf{k}_i) \left\langle \Phi_A(\mathbf{k}_f, \mathbf{r}) | \nabla | \Phi_B(\mathbf{k}_i, \mathbf{r}) \right\rangle . \end{aligned} \tag{5.13}$$

The magnitude of the inner product $\mathbf{D}^{fi} \cdot \mathbf{P}$ largely determines the polarization dependence of W, which is calculated on the electron equi–energy contour for $E^f - E^i \pm E_{\text{laser}} = 0$. Here the "$-$" sign is for absorption and the "$+$" sign is for emission of a photon. W becomes zero if $\mathbf{P}$ is perpendicular to the real and the imaginary part of $\mathbf{D}^{fi}$.

We now substitute the Bloch functions from Sec. 3.1 to the tight binding atomic wavefunctions. The coordinates of all atoms in the crystal can be split into $\mathbf{R}_A^j$ and $\mathbf{R}_B^j$ over the A and B sublattice respectively. To go to the nearest neighbour atom from the A (or B) atom with index i to the nearest neighbour atom of type B (or A) with index j we use the set of vectors $\mathbf{r}_A^\ell$ and $\mathbf{r}_B^\ell$, respectively. The vector $\mathbf{r}_A^\ell$ ($\mathbf{r}_B^\ell$) connects nearest neighbour atoms starting from an A (B) atom and is defined in Eq. (3.12).

$$\mathbf{R}_A^j = \mathbf{R}_B^i + \mathbf{r}_B^\ell, \quad \mathbf{R}_B^j = \mathbf{R}_A^i + \mathbf{r}_A^\ell, \quad (\ell = 1, 2, 3). \tag{5.14}$$

We substitute the Eq. (3.2) in Eq. (5.13) and get

$$\begin{aligned} & \mathbf{D}^{cv}(\mathbf{k}_f, \mathbf{k}_i) \\ = \; & \frac{1}{U} \sum_{i=0}^{U-1} \sum_{\ell=1}^{3} c_B^{c*}(\mathbf{k}_f) c_A^{v}(\mathbf{k}_i) \exp\left[i(\mathbf{k}_i - \mathbf{k}_f) \cdot \mathbf{R}_A^i \right] \exp(-i\mathbf{k}_f \cdot \mathbf{r}_A^\ell) \left\langle \phi(\mathbf{r} - \mathbf{r}_A^\ell) | \nabla | \phi(\mathbf{r}) \right\rangle \\ & + \frac{1}{U} \sum_{i=0}^{U-1} \sum_{\ell=1}^{3} c_A^{c*}(\mathbf{k}_f) c_B^{v}(\mathbf{k}_i) \exp\left[i(\mathbf{k}_i - \mathbf{k}_f) \cdot \mathbf{R}_B^i \right] \exp(-i\mathbf{k}_f \cdot \mathbf{r}_B^\ell) \left\langle \phi(\mathbf{r} - \mathbf{r}_B^\ell) | \nabla | \phi(\mathbf{r}) \right\rangle . \end{aligned} \tag{5.15}$$

The summation over the atoms $\mathbf{R}_A^i$ and $\mathbf{R}_B^i$ in Eq. (5.15) gives the selection rule for $\mathbf{k}$ as $\mathbf{k}_i$=$\mathbf{k}_f$, which means that the transitions occur vertical. Thus the dipole vector in Eq. (5.13) for graphite

is simply given by

$$\mathbf{D}^{fi}(\mathbf{k}) \;=\; \left\langle \Psi^f(\mathbf{k})|\nabla|\Psi^i(\mathbf{k})\right\rangle \;. \tag{5.16}$$

At this point, it will be useful to define the atomic dipole vector for the A and B sublattice as $\mathbf{v}_{gA}$ and $\mathbf{v}_{gB}$ respectively.

$$\begin{aligned}
\mathbf{v}_{gA}(\mathbf{k}) &= -\sum_{\ell}^{3}\exp(-i\mathbf{r}_A^\ell\cdot\mathbf{k})\int\phi^*(\mathbf{r}-\mathbf{r}_A^\ell)\nabla\phi(\mathbf{r})d\mathbf{r} = -\frac{\sqrt{3}m_{\rm opt}}{a}\sum_{\ell}^{3}\exp(-i\mathbf{r}_A^\ell\cdot\mathbf{k})\mathbf{r}_A^\ell \\
\mathbf{v}_{gB}(\mathbf{k}) &= -\sum_{\ell}^{3}\exp(-i\mathbf{r}_B^\ell\cdot\mathbf{k})\int\phi^*(\mathbf{r}-\mathbf{r}_B^\ell)\nabla\phi(\mathbf{r})d\mathbf{r} = -\frac{\sqrt{3}m_{\rm opt}}{a}\sum_{\ell}^{3}\exp(-i\mathbf{r}_B^\ell\cdot\mathbf{k})\mathbf{r}_B^\ell
\end{aligned} \tag{5.17}$$

Here $a/\sqrt{3}$ is the length of $\mathbf{r}_B^\ell$ and $\mathbf{r}_A^\ell$ as defined in Eq. (3.12). The direction of the vectors $\mathbf{v}_{gA}$ and $\mathbf{v}_{gB}$ can be understood by the fact that (1) these vector point along the bond between the two centers and (2) that the gradient gives a vector that points away from the origin because the wavefunction has a positive value, which is decreasing, when moving away from the origin. Thus the vectors point from the origin (center of one wavefunction) to the atom centered at $\mathbf{r}_A^\ell$ or $\mathbf{r}_B^\ell$. Thus each contribution is proportional to $-\mathbf{r}_A^\ell$ or $-\mathbf{r}_B^\ell$. In Eq. (5.17), $m_{\rm opt}$ is an atomic matrix element for nearest neighbour carbon pairs. Since the product of the atomic wavefunction and its derivative quickly decreases with increasing the distance between the atoms, we consider only nearest neighbour coupling. $m_{\rm opt}$ describes the optical properties of π electrons in graphite and is given by

$$m_{\rm opt} = \left\langle \phi(\mathbf{r}-\mathbf{r}_B^1)\left|\frac{\partial}{\partial x}\right|\phi(\mathbf{r})\right\rangle . \tag{5.18}$$

Note that in Sec. 5.9 we give an analytical result for $m_{\rm opt}$ in terms of Gaussian fitting parameters to the $2p_z$ electron wavefunctions. When we substitute the previously fitted LDA wavefunctions, with fitting parameters from Table 3.2(a) we obtain $m_{\rm opt} = 0.21$ [a.u.]$^{-1}$. Here 1 a.u. is 0.529Å. The value of $m_{\rm opt}$ is positive because we use the coordinates of B atom at $\mathbf{r}_B^1$. Further we note that $c_A^{c*}c_B^v = -(c_B^{c*}c_A^v)^*$, which can be shown analytically by substituting the expressions for the wavefunction coefficients from Eq. (3.28). Also, from Eq. (5.17), we can see that $\mathbf{v}_{gA}^*(\mathbf{k}) = -\mathbf{v}_{gB}(\mathbf{k})$. We can write the dipole vector from Eq. (5.15) as $\mathbf{D}^{cv}(\mathbf{k}) = c_B^{c*}c_A^v\mathbf{v}_{gA} + c_A^{c*}c_B^v\mathbf{v}_{gB}$.

$$\mathbf{D}^{cv}(\mathbf{k}) = -\frac{2\sqrt{3}m_{\rm opt}}{a}{\rm Re}\left[c_B^{c*}(\mathbf{k})c_A^v(\mathbf{k})\sum_l\exp(-i\mathbf{r}_A^l\cdot\mathbf{k})\mathbf{r}_A^l\right] \tag{5.19}$$

in which Re[...] denotes the real part of [...]. Eq. (5.19) says that $\mathbf{D}^{cv}(\mathbf{k})$ is a real vector and its direction depends on $\mathbf{k}$. Since we only have a real part in $\mathbf{D}^{cv}(\mathbf{k})$, we can always find a $\mathbf{P}$ that is perpendicular to $\mathbf{D}^{cv}(\mathbf{k})$ and that excludes special $\mathbf{k}$ so that do not contribute to the optical absorption $W(\mathbf{k})$. If $\mathbf{D}^{cv}(\mathbf{k})$ would have non–parallel real and imaginary parts, such an effect would not be possible.

In Fig. 5.1(a) we plot the normalized direction of $\mathbf{D}^{cv}(\mathbf{k})$ from Eq. (5.19) as arrows and in Fig. 5.1(b) we plot the value of the oscillator strength $O(\mathbf{k})$ in the units of $m_{\rm opt}$ on a contour plot. $O(\mathbf{k})$ is defined by

$$O(\mathbf{k}) = \sqrt{\mathbf{D}^{cv*}(\mathbf{k})\cdot\mathbf{D}^{cv}(\mathbf{k})}. \tag{5.20}$$

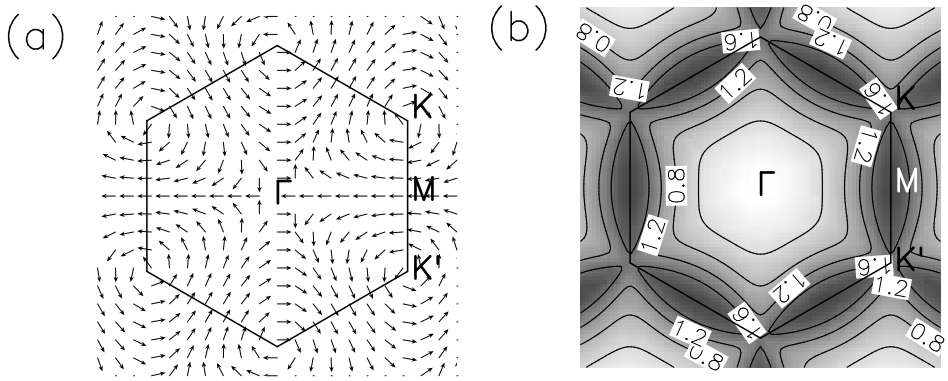

Figure 5.1: (a) The normalized dipole vector is plotted as a function of $\mathbf{k}$ over the 2D BZ. (b) The oscillator strength in units of $m_{\rm opt}$ as a function of $\mathbf{k}$ is plotted over the 2D BZ. The separation of two adjacent contour lines is 0.4 $m_{\rm opt}$.

From Fig. 5.1(a) it can be seen that close to K and K' points, $\mathbf{D}^{cv}(\mathbf{k})$ has a direction approximately parallel to the equi–energy contour. The rotational direction of $\mathbf{D}^{cv}(\mathbf{k})$ is clockwise (K point) or counterclockwise (K' point). The position of the node in $W(\mathbf{k})$ is approximately given by the direction of light polarization, when we see the direction from the K (K') points, i.e. the node is rotating in the same direction around the K and K' points. From Fig. 5.1(b) it is clear that the oscillator strength has a maximum at M points and a minimum at the Γ point. For a given laser excitation energy $E_{\rm laser}$, the δ function in Eq. (5.11) selects optical transitions along an equi–energy line around K and K' points. In Fig. 5.2 the optical absorption around K point is shown and it can be seen that two nodes lie along the equi–energy contour. Detail analysis will be given in the next section. In Fig. 5.3 we plot the optical aborption $W(\mathbf{k})$ as defined in Eq. (5.11) for $E_{\rm laser} = 3.0$eV for three different values of the light polarization. In (a) $\mathbf{P} = (0, 1)$, (b) $\mathbf{P} = (-1/2, \sqrt{3}/2)$ and (c) $\mathbf{P} = (1, 0)$. The bright (dark) shading indicates $\mathbf{k}$ with low (high) optical absorption. The rotation of the node with polarization can be seen. Based on the results given here, an ab–initio calculation of the dipole vector in graphene has been performed by a different group [60] and their results fully confirm our calculation.

5.3 Expansion around K point

In Sec. 5.2 we have seen that in graphene, the transitions occur vertically and the dipole vector is equal to the zero vector for the case that initial and final $\mathbf{k}$ are not equal to each other. The optical absorption intensity in graphene is thus only a function of $\mathbf{k}$ and given as

$$W(\mathbf{k}) \propto |\mathbf{P} \cdot \mathbf{D}^{cv}(\mathbf{k})|^2 . \tag{5.21}$$

The fact that the optical absorption around K points shows a node as a function of $\mathbf{k}$ can be understood by expanding $\mathbf{D}^{cv}(\mathbf{k})$ around K (K') point. We take the Eq. (5.19) and expand the $c_B^{c*}(\mathbf{k})c_A^v(\mathbf{k})$ and the $-\sum_l \exp(-i\mathbf{r}_A^\ell \cdot \mathbf{k})\mathbf{r}_A^\ell$ around K points. The wavefunction coefficients for are given by Eq. (3.29) and Eq. (3.28). We are free to choose the phase factors Φ_v and Φ_c appearing in Eq. (3.29) and we set $\Phi_v = \Phi_c = 0$. Furthermore, we set the wavefunction overlap

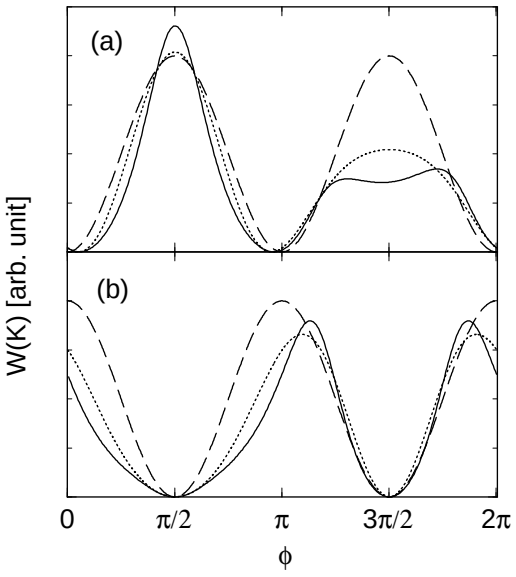

Figure 5.2: The absorption probability $W(\mathbf{k})$ as a function of angle ϕ around the K point. Solid, dashed and dotted lines, respectively, denote the numerical results obtained from use of the eigenvectors, and the linear and quadratic approximation in Eq. (5.26). The plots are made for $E_{\rm laser} = 2.5$eV and the polarization vectors are (a) $\mathbf{P} = (1, 0)$ and (b) $\mathbf{P} = (0, 1)$ [59].

$s = 0$. The expansion of $f(\mathbf{K}+\mathbf{k})$ and $f(\mathbf{K}'+\mathbf{k})$ from Eq. (3.22) is substituted into the definition for the wavefunction coefficient from Eq. (3.29). Then the wavefunction coefficients in Eq. (3.29) and Eq. (3.28) around $\mathbf{K} = (0, -4\pi/(3a))$ become

$$c_A^c(\mathbf{K}+\mathbf{k}) = \frac{1}{\sqrt{2}}, \quad c_B^c(\mathbf{K}+\mathbf{k}) = \frac{-k_y + ik_x}{\sqrt{2}k}, \quad c_A^v(\mathbf{K}+\mathbf{k}) = \frac{1}{\sqrt{2}}, \quad c_B^v(\mathbf{K}+\mathbf{k}) = \frac{k_y - ik_x}{\sqrt{2}k}. \tag{5.22}$$

Around $\mathbf{K}' = (0, 4\pi/(3a))$ we get

$$c_A^c(\mathbf{K}'+\mathbf{k}) = \frac{1}{\sqrt{2}}, \quad c_B^c(\mathbf{K}'+\mathbf{k}) = \frac{k_y + ik_x}{\sqrt{2}k}, \quad c_A^v(\mathbf{K}'+\mathbf{k}) = \frac{1}{\sqrt{2}}, \quad c_B^v(\mathbf{K}'+\mathbf{k}) = \frac{-k_y - ik_x}{\sqrt{2}k}. \tag{5.23}$$

In Eq. (5.22) and in Eq. (5.23) we use $k = \sqrt{k_x^2 + k_y^2}$, the distance from the K or K' point. Note, that the products of wavefunction coefficients $c_A^v c_B^{c*}$ and $c_B^v c_A^{c*}$ are linear function in k_x and k_y. Similarly, we expand $e^{i\mathbf{k}\cdot\mathbf{r}_A^\ell}\mathbf{r}_A^\ell$ appearing in Eq. (5.19) around the K points. We only keep terms of linear order of the dipole vector. The product of wavefunction coefficients for A and B atom is already linear in k with no constant term. Therefore it is sufficient, if we only consider the constant terms around $\mathbf{K} = (0, -4\pi/(3a))$ in $e^{i\mathbf{k}\cdot\mathbf{r}_A^\ell}\mathbf{r}_A^\ell$ as

$$-\frac{1}{a}\sum_{\ell=1}^{3} e^{i(\mathbf{K}+\mathbf{k})\cdot\mathbf{r}_A^\ell}\mathbf{r}_A^\ell = -\frac{\sqrt{3}}{2}\begin{pmatrix}1\\ i\end{pmatrix} + \ldots, \quad \text{and} \quad -\frac{1}{a}\sum_{\ell=1}^{3} e^{i(\mathbf{K}'+\mathbf{k})\cdot\mathbf{r}_A^\ell}\mathbf{r}_A^\ell = -\frac{\sqrt{3}}{2}\begin{pmatrix}1\\ -i\end{pmatrix} + \ldots. \tag{5.24}$$

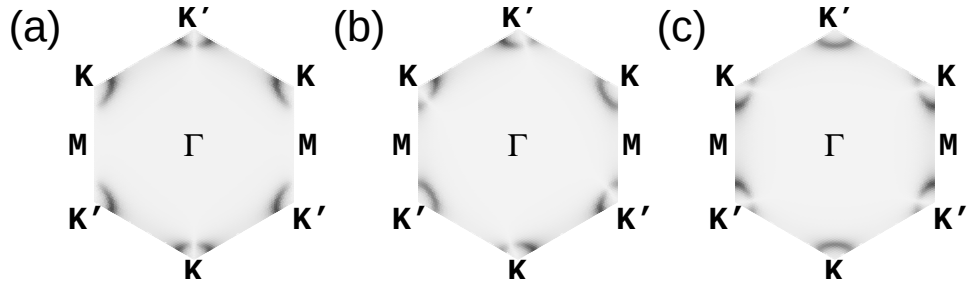

Figure 5.3: Optical absorption intensity (dark area for strong optical absorption) as a function of electron wavevector $\mathbf{k}$ over the 2D BZ of graphite. The light polarization vectors $\mathbf{P}$ are selected as (a) $\mathbf{P} = (0, 1)$, (b) $\mathbf{P} = (-1/2, \sqrt{3}/2)$ and (c) $\mathbf{P} = (1, 0)$. The laser energy is $E_{\text{laser}} = 3$ eV. The optical absorption is zero if the electron wavevector measured from nearest K point is parallel to $\mathbf{P}$. The node is rotating with rotating $\mathbf{P}$ [59, 61].

When we substitute the constant term in Eq. (5.24) and the wavefunction coefficients in Eq. (5.22), we get an approximation to lowest (=linear) order for the dipole vector around $\mathbf{K}$

$$\mathbf{D}^{cv}(\mathbf{K}+\mathbf{k}) = \frac{3m_{\text{opt}}}{2k}(k_y, -k_x, 0) \quad \text{and} \quad \mathbf{D}^{cv}(\mathbf{K}'+\mathbf{k}) = \frac{3m_{\text{opt}}}{2k}(-k_y, k_x, 0) \tag{5.25}$$

Eq. (5.25) says that the direction of the dipole vector is tangential along a circle around $\mathbf{K}$ and $\mathbf{K}'$. The vortex of rotation is opposite for $\mathbf{K}$ and $\mathbf{K}'$. For simplicity we omitted the z component of $\mathbf{D}^{cv}$ which is equal to zero. For getting the optical absorption, we take the inner product $\mathbf{D}^{cv}(\mathbf{k}) \cdot \mathbf{P}$ up to the linear terms in k_x and k_y for a given polarization vector $\mathbf{P} = (p_x, p_y, p_z)$.

$$\mathbf{P} \cdot < \Psi^c(\mathbf{k}) | \vec{\nabla} | \Psi^v(\mathbf{k}) > = \pm \frac{3m_{\text{opt}}}{2k}(p_y k_x - p_x k_y)\,. \tag{5.26}$$

This result shows that the line $p_y k_x - p_x k_y = 0$ in the 2D BZ becomes a node in the optical absorption for a given $\mathbf{P} = (p_x, p_y)$. For a given laser energy, the equi–energy line for optical absorption gives a circle around the K point. Thus we expect no optical absorption around the two crossing points of the line $p_y k_x - p_x k_y = 0$ with the circle. This result holds for both the K and the K' points to first order, i.e. the location of the node rotates in the same direction by rotating the polarization direction. However, higher order terms modify this behavior, since the corrections for K and K' are different from each other.

The existence of a node in the absorption coefficient as a function of $\mathbf{k}$ is a special effect that has never been observed in other materials. It occurs in graphite because the wavefunction coefficients and the energy dispersion around K point are linear functions in k. In Sec.3.3, we have shown, that the electronic structure around K point of graphene is special because of the existence of two inequivalent atoms in the unit cell of graphene. In most materials, a quadratic term in k_x, k_y is the leading term in the energy dispersion relation, so that the optical absorption then does not have a node.

Nevertheless, it is difficult to observe the existence of such a node in the optical absorption of graphite experimentally. The constraints on the electron wavevector in nanographite ribbons have been used to observe the node in optical experiments [62, 63]. We will next discuss the effect of the node for graphite and for carbon nanotubes in more detail in the following sections. As

far as the linear k approximation for the energy and the wavefunction is valid, the expression in Eq. (5.26) works well for specifying the node position. However, when the laser energy increases, the equi–energy contour is no longer a circle, but it is changed into a triangle due to the trigonal warping effect[36]. In this case, the higher–order corrections for Eq. (5.26) become important for describing the node positions and the absolute value of $W(\mathbf{k})$.

In Fig. 5.2, we plot $W(\mathbf{k})$ as a function of the polar angle ϕ of the node around the K point, that is $k_x = k\cos\phi$ and $k_y = k\sin\phi$, with $E_{\rm laser}$=2.5 eV, for (a) $\mathbf{P} = (1,0)$ and (b) $\mathbf{P} = (0,1)$. Solid, dashed and dotted lines in Fig. 5.2 correspond to numerical results and the analytic expression within the linear and quadratic k approximations for Eq. (5.26), respectively. In the case of Fig. 5.2(a), $\phi = 0, \pi$ (or $k_y = 0$) correspond to the node positions of $W(\mathbf{k})$, while in the case of Fig. 5.2(b), $\phi = \pi/2, 3\pi/2$ (or $k_x = 0$) correspond to the node positions. In the case of (b), since $\phi = 0$ and π are equivalent $\mathbf{k}$ positions, the value of $W(\mathbf{k})$ is identical, while this is not the case for (a). It is clear from Fig. 5.2 that the linear approximation of Eq. (5.26) is sufficient for describing the node position for $E_{\rm laser} < 3$ eV; however, we need to use at least the quadratic term of $\mathbf{k}$ for describing the asymmetric peaks of $W(\mathbf{k})$. This asymmetry will be important for describing the chirality dependence of $W(\mathbf{k})$ for SWNTs, as discussed in the next section.

5.4 Dipole vector in carbon nanotubes

In the previous section, we showed that the dipole vector in graphite is special which is relevant to the node of optical absorption. In this section, we derive the dipole vector for single wall carbon nanotubes. The main difference is that the atomic dipole vector $\mathbf{d}_A^j$ ($\mathbf{d}_B^j$) for the A (B) atom with index j is not parallel to the atomic dipole vector at a different j. This is due to the curvature on the cylindrical surface of the SWNT. The SWNT dipole vector $\mathbf{D}^{fi}(\mathbf{k}_f, \mathbf{k}_i)$ can be written as a sum over $\mathbf{d}_A^j$ and $\mathbf{d}_B^j$ multiplied by the corresponding phase factors of Bloch functions. The sum is taken over N different sites for A (B) atoms in the 1D unit cell of a SWNT.

$$\begin{aligned}&\mathbf{D}^{fi}(\mathbf{k}_f, \mathbf{k}_i)\\ &= \frac{\sqrt{3}m_{\rm opt}}{Na}\left[c_A^{f*}(\mathbf{k}_f)c_B^{i}(\mathbf{k}_i)\sum_{j=0}^{N-1} e^{i(\mathbf{k}_i-\mathbf{k}_f)\cdot\mathbf{R}_B^j}\mathbf{d}_B^j(\mathbf{k}_i) + c_B^{f*}(\mathbf{k}_f)c_A^{i}(\mathbf{k}_i)\sum_{j=0}^{N-1} e^{i(\mathbf{k}_i-\mathbf{k}_f)\cdot\mathbf{R}_A^j}\mathbf{d}_A^j(\mathbf{k}_i)\right].\end{aligned} \tag{5.27}$$

Here the $\mathbf{R}_B^j$ and $\mathbf{R}_A^j$ are, respectively, the coordinates of the B and A carbon atoms in the 2D unrolled SWNT unit cell. We put the SWNT in a coordinate system with tube axis axis along z and R_A^j for $j = 0$ at the x axis ith zero y component. The vectors $\mathbf{k}_i$ and $\mathbf{k}_f$ are the initial and final wavevectors of the electron, respectively. It is noted here that the second term of Eq. (5.27) is not the complex conjugate of the first term.

The $\mathbf{d}_A^j$ ($\mathbf{d}_B^j$) are related to one another by rotations around the z axis for different j. Additionally, we need one rotation around y axis to account for the chiral angle of a SWNT.

The $\mathbf{d}_A^j(\mathbf{k}_i)$ and $\mathbf{d}_B^j(\mathbf{k}_i)$ are given by

$$\begin{aligned} \mathbf{d}_A^j(\mathbf{k}_i) &= -U_y(-\pi/6+\theta)U_z(\alpha_j)\sum_{\ell}^{3} e^{i\mathbf{k}_i\cdot\mathbf{r}_A^\ell}\mathbf{r}_A^\ell, \\ \mathbf{d}_B^j(\mathbf{k}_i) &= -U_y(-\pi/6+\theta)U_z(\beta_j)\sum_{\ell}^{3} e^{i\mathbf{k}_i\cdot\mathbf{r}_B^\ell}\mathbf{r}_B^\ell. \end{aligned} \tag{5.28}$$

where θ is the chiral angle of the nanotube. The angle α_j is measured from the x axis. The $U_z(\alpha_j)$ and $U_z(\beta_j)$ are rotational operators for A and B atom, respectively around z axis and U_y is a rotation around y axis. The contribution of each atom to $\mathbf{d}_A^j$ is multiplied by a phase factor $e^{i(\mathbf{k}_i-\mathbf{k}_f)\cdot\mathbf{R}_j^A}$ and similarly for the B atom. This cancels most of the dipole vectors except for the dipole-allowed transitions.

5.5 Selection rules and optical absorption intensity in SWNTs

In the case of a vertical transition, ($\mathbf{k}_i = \mathbf{k}_f$), only the z components of the dipole vector can be added, and the x and y components are cancelled with one another for N dipole vectors. Thus, when the polarization vector $\mathbf{P}$ is parallel to the nanotube axis, only those transitions (so–called "vertical transitions") are possible which do not change either the electronic k state along the nanotube axis z or the electron wavefunction symmetry in the circumferential direction (i.e., within the same cutting line). On the other hand, when $\mathbf{P}$ is perpendicular to the nanotube axis (cross polarization), $|\mathbf{k}_i - \mathbf{k}_f| = 2/d_t = |\mathbf{K}_1|$, where $\mathbf{K}_1$ is a reciprocal lattice vector of a SWNT[4, 36], a phase change of π is introduced into the expression for the optical matrix vectors for the opposite carbon sites, which in turn gives non–zero values for the x and y dipole vectors. Thus the transition from $E_\mu^v(k)$ to $E_{\mu\pm1}^c(k)$ is possible for the cross polarization, which is consistent with previous results using effective mass theory [37]. Here, $E_\mu^v(k)$ and $E_\mu^c(k)$ denote the valence and conduction band energy of the μ–th cutting line.

It is interesting to calculate $\mathbf{D}$ in Eq. (5.27) as a function of $\mathbf{k}$. In Fig. 5.4 we plot the z component of $\mathbf{D}^{cv}$ for a $(5,5)$ armchair SWNT with $d_t = 0.70$ for $\mu = -4\ldots5$ along a continuous 1D k wavevector. As stated in the previous paragraph, only the z component of $\mathbf{D}^{cv}$ is non–zero in the case of parallel polarization. In the upper panel of Fig. 5.4 we show the matrix element for transitions with parallel polarized light for different cutting lines and in the lower panel, we show the corresponding transitions. It can be seen that for the A symmetry bands, optical absorption completely disappears. It is also clear from Fig. 5.4 that the optical absorption at the VHS has a maximum along k but is zero at $k = 0$. It is interesting to note the zero photoconductivity for the metallic $(5,5)$ SWNT since the matrix element along the metallic band with $\mu = 5$ is equal to zero for all k states. The Fig. 5.5 shows a similar plot to Fig. 5.4 for a $(9,0)$ zigzag SWNT. The diameter of the $(9,0)$ SWNT ($d_t = 0.70$ nm) is almost the same to the $(5,5)$ SWNT ($d_t = 0.68$ nm). In the case of zigzag SWNTs, however, the optical absorption for the metallic band $\mu = -6, 6$ is not zero along the whole band except for $k = 0$. Thus we could separate an armchair SWNT by means of a photoconductivity measurement.

In Fig. 5.6(a) the initial and final states for transitions with perpendicularly polarized light are shown for a (10,2) type I semiconducting SWNT. Only transitions related to van Hove singularities (VHS) in the joint density of states (JDOS) are shown. For parallel polarization, the

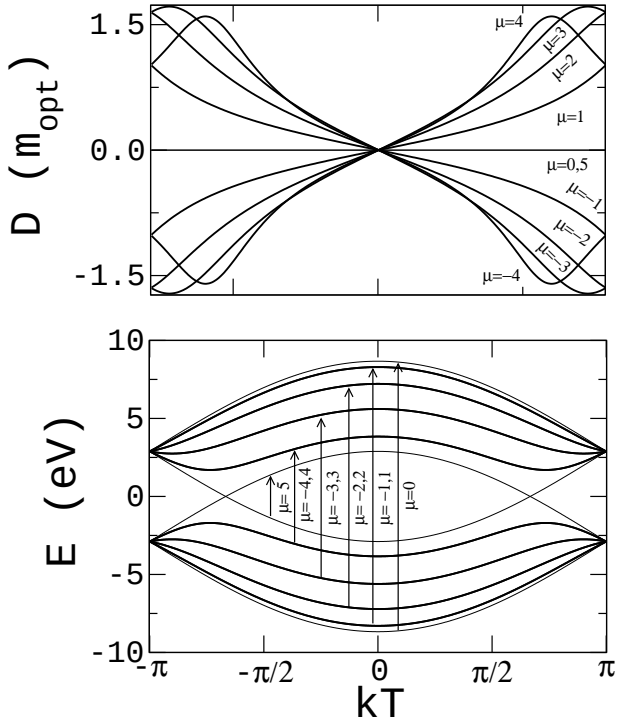

Figure 5.4: Length of the dipolevector for parallel light polarization in a $(5,5)$ SWNT with $d_t = 0.68$ nm as a function of 1D k vector. The upper (lower) panel shows the matrix elements (transitions) that are allowed for parallel polarization. Doubly degenerate electronic states (E) are indicated by thick lines and not degenerate states (A) are indicated by thinner lines [64].

VHS are denoted by $\mathbf{k}_i$ (with i=1,2,3) in which the van Hove singularity k point is expressed by a touching of the cutting lines to the equi–energy contour. The energy gaps between valence and conduction bands at each $\mathbf{k}_i$ point are usually labelled E_{ii}^{M} and E_{ii}^{S} , where the i orders the transition energy magnitude in increasing order, and M and S denote metallic and semiconducting SWNTs, respectively. These E_{ii} energies are usually observed with parallel polarized light and plotted vs. d_t in a Kataura plot [66]. In the case of perpendicular polarization, the k, that contributes to the JDOS, is the point where the valence and conduction bands have the same slope. Generally, these points occur for a 1D k value in between the 1D k_i VHS wavenumbers for adjacent cutting lines (see Fig. 5.6). Hereafter we use k_{ij} to denote the 1D wavenumber at which the VHS transitions between cutting lines of the E_{ii} and E_{jj} singularities occur (see Fig. 5.6). There are in general two VHS–enhanced transitions starting from a given initial μ index as is shown by labels (p1) and (p2) in Fig. 5.6(a). In Fig.5.6(a), only transitions originating from the μ–th line are considered and illustrated by arrows pointing towards the $\mu \pm 1$ cutting lines:

$$\begin{array}{ll} \text{(p1)} & E_{12}^{S} = E_{\mu-\ell}^{c}(k_{12}) - E_{\mu}^{v}(k_{12}), \\ \text{(p2)} & E_{13}^{S} = E_{\mu+\ell}^{c}(k_{13}) - E_{\mu}^{v}(k_{13}). \end{array} \tag{5.29}$$

The parameter ℓ depends on which of the two inequivalent corners of the 2D BZ, K or K', the transition occurs, and whether the SWNT is semiconducting type I or II. In Eq. (5.29) we

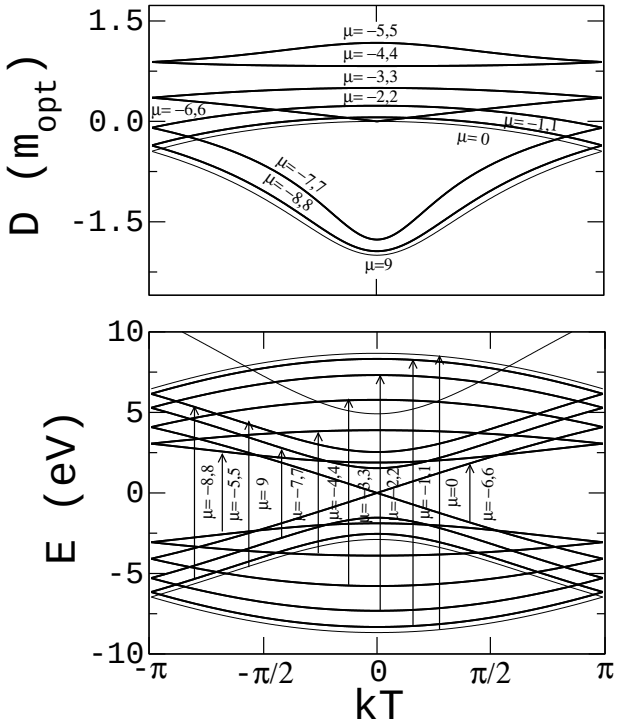

Figure 5.5: The same plot of Fig. (5.4) for a $(9,0)$ SWNT. The matrix elements for the metallic bands ($\mu = -6, 6$) are not zero here [64].

have selected the two transitions that start from the cutting line with the $E_{11}^{\rm S}$ singularity. In Eq. (5.29) we have $\ell = -1$ for a semiconducting type I tube for k_{ij} on μ cutting line near the K point. When we select μ around K' we get $\ell = 1$. For a semiconducting type II SWNT, the situation is just the opposite and we get $\ell = 1$ ($\ell = -1$) for μ near the K (K) point.

In Eq. (5.29) we use the label $E_{ij}^{\rm S}$ for a semiconducting SWNT, for which the electron goes from E_{μ}^{v} to $E_{\mu+\ell}^{c}$ with $\ell = \pm 1$. Here the labels "i" and "j" in E_{ij}^{S} are defined by the fact the cutting line with index μ has the E_{ii} singularity and the cutting line with index $\mu + \ell$ has the E_{jj} singularity. The two transitions in Eq. (5.29) are shown in Fig.5.6(a). When we consider relatively small transition energies, we can neglect both the trigonal warping effect and the electron–hole asymmetry (see Sec. 3.3). Then we can use the following simplification:

$$E_{12}^{S} = \frac{E_{22}^{S} + E_{11}^{S}}{2}, \quad E_{13}^{S} = \frac{E_{33}^{S} + E_{11}^{S}}{2}. \tag{5.30}$$

Thus the resonance energy $E_{12}^{\rm S}$ for perpendicular polarization appears in the energy gap of E_{11}^{S} and E_{22}^{S}, as is shown in Fig. 5.6(b). Similar results can be obtained for other transitions. The splitting of the E_{11}^{S} transition is however somewhat special, since both E_{12}^{S} and E_{13}^{S} are larger than E_{11}^{S}. So far we assumed that the overlap parameter s vanishes ($s = 0$) in calculating the electron energy dispersion in the tight binding calculation [4]. A non-zero s value is essential for obtaining a larger (smaller) energy band width in the conduction (valence) bands. However,

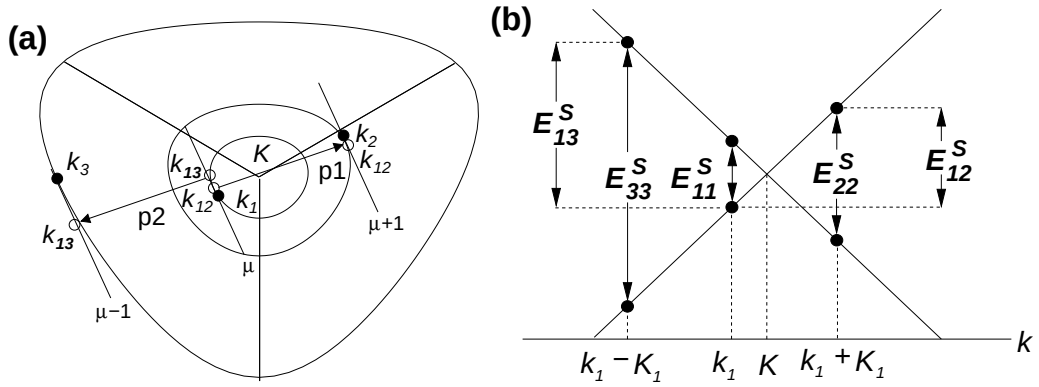

Figure 5.6: (a) The three parallel lines labelled by $\mu - 1$, μ and $\mu + 1$ are cutting lines for a (10,2) tube near the K point. For parallel light polarization, transitions occur at VHS k points k_1, k_2 and k_3, denoted by a filled circle, and for perpendicular polarization, the k_{12} and k_{13}, are indicated by open circles. For perpendicular polarization, the two transitions at VHS in the JDOS, labeled by p1 and p2 are shown {Eq. (5.29)}. (b) Energy dispersion along 2D $\mathbf{k}$ parallel to $\mathbf{K}_1$. The energies at the VHSs $\mathbf{k}_i$ are denoted by E_{ii}. If we neglect the trigonal warping effect and electron-hole asymmetry, the resonant energies for perpendicular polarization are given by E_{12}^S and E_{13}^S [65] .

as far as we consider parallel polarization, an enlargement of the conduction band width and a shrinking of the valence band width for the same μ value cancel each other to linear order in s, and the effect of s will only appear to order s^2. Thus for the value of $s = 0.129$, this effect can be neglected around the K point of the 2D BZ {see Eq. (3.20)}.
However, it is no longer true for perpendicular polarization. The energy difference between E_{ij} and E_{ji} depends on the amount of the electron–hole asymmetry, which is contained in the tight binding overlap parameter s. In Fig. 5.7(a) we show an example of the band structures of a (10,10) metallic SWNT with $s = 0$ (left) and $s = 0.129$ (right). Solid circles indicate VHS $\mathbf{k}$ points. In Fig. 5.7(b) we plot the joint density of states (JDOS) for these band structures. We find a splitting between the E_{12} and E_{21} transition energies when $s \neq 0$ (solid line). For $s = 0$, the E_{12} and E_{21} transitions occur at the same energies (dashed line). The splitting in $E_{12} - E_{21}$ for $s = 0.129$ is about 0.2 eV and thus should be observable in optical experiments. Alternatively, the dependence $E_{12} - E_{21}$ on s could be used to determine the exact value of s for different SWNT diameters. Further experimental work is needed to measure s.

5.6 The Kataura plot for parallel and perpendicular polarization

The selection rules for parallel and perpendicular polarization allow us to calculate singularities in the joint density of electronic states (JDOS) for light polarization parallel and perpendicular to the SWNT axis. Plotting the $E_{\rm ii}$ and $E_{\rm ij}$ vs. SWNT diameter d_t gives the so–called Kataura plot [66], that is used to analyze optical and Raman spectra. This plot is originally given for parallel polarization and the E_{ii} are plotted vs. SWNT diameters d_t. Experimentally the E_{ii}

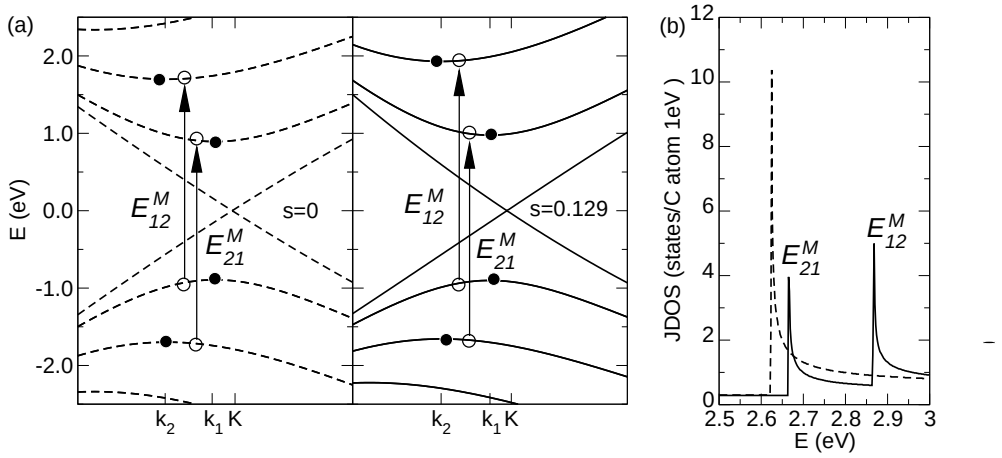

Figure 5.7: The electron-hole asymmetry leads to different energies for the electronic transitions for perpendicularly polarized light. In (a) we show $E(k)$ for a (10,10) tube around the K point. The dashed lines (left) are for tight binding parameters $t = -2.89\,\text{eV}$ and $s = 0$ and for the solid lines (right) $t = -3.033\,\text{eV}$ and $s = 0.129$ was used. (b) JDOS for transitions with perpendicularly polarized light for a (10,10) SWNT. The dashed and solid lines in (b) are the calculated absorption spectra for (a) left and right, respectively [65].

energies can be obtained by Raman experiments, using a tunable laser [27] or by comparing Stokes and anti–Stokes intensities [67] or by photoluminescence (PL) experiments [68], where the ratio between two E_{22} and E_{11} can be determined.

Alternatively, we can also take peaks in the RBM Raman spectra of bundles and assign them to resonance of a particular SWNT diameter with E_{laser}. In this way we analyzed the experimental data that we use. The experimental points have been measured using six different E_{laser} : $1.17, 1.59, 1.92, 2.41, 2.54$ and 2.71eV [69]. In order to compare them to the calculated Kataura plot for parallel and perpendicular polarization, shown in Fig. 5.8(a) and in Fig. 5.8(b), respectively, we plot the same set of experimental points "X" in Fig. 5.8(a) and in Fig. 5.8(b). Each "X" corresponds to a peak in the RBM Raman spectra obtained from randomly aligned bundles [69]. If we assume only resonance for parallel polarization, we would expect each "X" to lie in a region of E_{ii} points. However, when we plot all features that appear in the experimental spectra of SWNT bundles, several small intensity peaks cannot be explained by this method, since they appear in the gap region of E_{ii} transitions in Fig. 5.8(a). Comparision with calculated values of VHS energies of perpendicular polarization suggests that an "X" that lies in between two E_{ii} transition regions in Fig. 5.8(a), lies in an E_{ij} transition region in Fig. 5.8(b). This most clearly holds for the experimental data around 1.6 eV, which are in the gap region between E_{22}^{S} and E_{11}^{M}. Most of these points can be seen to be far (i.e. ~ 0.2 eV) from the E_{22}^{S} and E_{11}^{M} transitions but do lie in the E_{13}^{S} region. We thus assign these experimental data points to the E_{13}^{S} transition with perpendicular polarization. Smaller RBM data around 1.2 eV may consist of E_{22}^{S} (parallel polarization) or E_{12}^{S} and E_{10}^{M} (perpendicular polarization) transitions. When we go to energies above 2.2 eV, the situation is no longer clear, and the orientation of the resonant

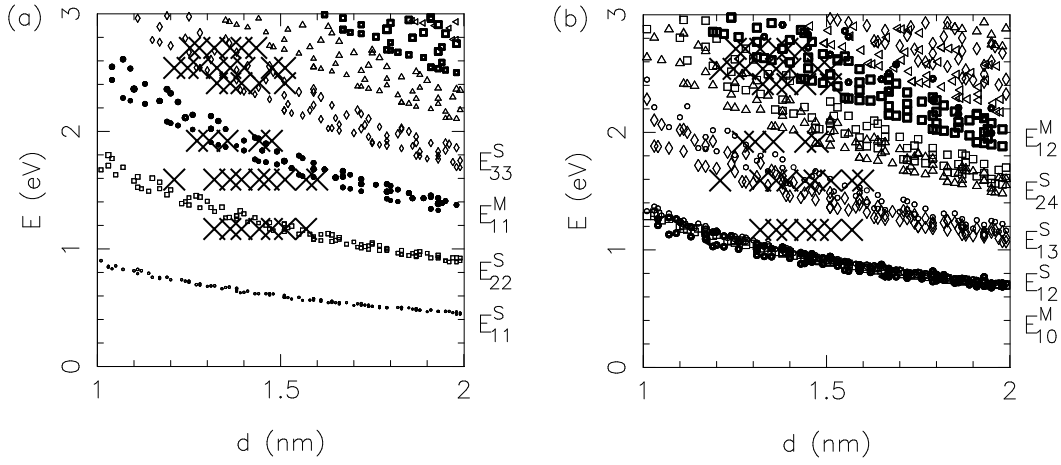

Figure 5.8: Energies of van Hove singularities vs. tube diameter (Kataura plot) for (a) parallel polarization and (b) perpendicular polarization. In (a) the transitions are indicated as follows: ◯ E^{S}_{11} , □ E^{S}_{22}, • E^{M}_{11}, ◇ E^{S}_{33}, △ E^{S}_{44}, ■ E^{M}_{22}, ◁ E^{S}_{55}. In (b) we use the same symbols to denote the initial state and plot transitions that have a VHS in the JDOS for neighbouring cutting lines. The "X" show experimental data for SWNT bundles [69]. The plots are made for the values of $t = -3.033$ eV and $s = 0.129$ [65].

SWNTs with respect to the light polarization should be known in order to make an assignment for transitions with parallel or perpendicular polarization.

5.7 Optical absorption at van Hove singularities

In Fig. 5.9 we plot for a (10,0) semiconducting nanotube the optical absorption spectra (thick solid line) and joint density of states (JDOS, thin solid line) for parallel polarization. The thick and thin dotted lines show, respectively, the optical absorption spectra and the JDOS for perpendicular polarization. As was discussed, the resonant energy positions depend on the polarization direction of light. When we compare the optical absorption spectra and JDOS, the optical spectra become more sharp than JDOS as a function of energy when we explicitly consider the matrix element, though the spectral shape near the singular points for the two cases are similar. It should be mentioned that we do not consider the depolarization effect discussed by Ajiki and Ando [70] in which the optical absorption disappears almost perfectly for the perpendicular polarization. The self–consistent screening effect might be supressed in the case of SWNT bundles, since we do observe the perpendicular polarization spectra experimentally in SWNT bundles[48, 71, 72, 73].

In Fig. 5.10 we plot the optical absorption matrix element at k points along the K-M and K-Γ lines as a function of the distance of the k vectors from the K point in the 2D BZ. The value of the matrix element in Fig. 5.10 is given by Eq. (5.27) for parallel polarization (z component of the optical matrix vector). The matrix element is increasing in the direction from K to M but decreasing from K to Γ. At the Γ point, we do not have an optical absorption of the π band. Thus, depending on the position k_{i} of the VHS in the 2D BZ of graphite, we can expect a

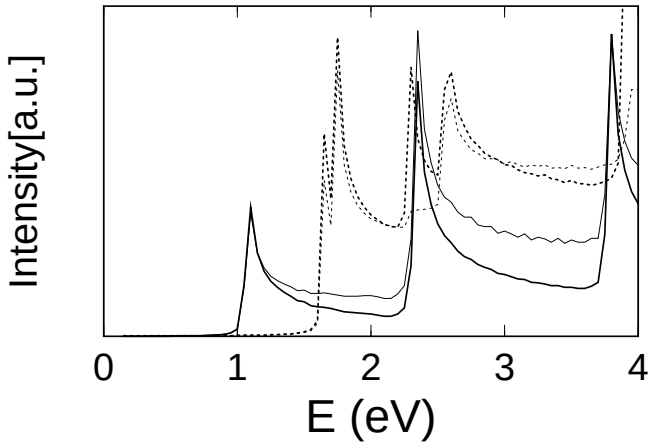

Figure 5.9: Energy dependence of the optical absorption of a (10,0) tube with parallel (solid line) and perpendicular (dotted line) polarization. The thick (thin) line is calculated with (without) the matrix element included, and the results show that the van Hove peaks are enhanced by explicit consideration of the matrix element in calculating the optical absorption [59].

corresponding chirality dependence of the optical absorption intensity. In Fig. 5.11, we plot the optical matrix element of Eq. (5.27) at the van Hove singular point k_i as a function of chiral angle for parallel polarization. The figure is plotted for a given laser energy of 2.41eV (as is commonly used in Raman experiments) and the (n, m) values are selected within the resonant window of $|E_{ii} - E_{\rm laser}| < 0.05$eV. The solid lines in Fig. 5.11 correspond to a smooth evaluation of the matrix element along the equi–energy contour of 2.41eV. Each point in Fig. 5.11 corresponds to a different (n, m) nanotube, and the solid and open symbols correspond to metallic and semiconducting nanotubes, respectively. From Fig. 5.11, most points on the two lines in the figure, show a chirality dependence of the absorption matrix elements. The relative asymmetric appearance of the two curves in Fig. 5.11 comes from the fact that the k_i positions exist on inequivalent cutting lines of the 1D BZ relative to the 2D BZ as is shown in the inset, and this inequivalence arises from the trigonal warping effect [36]. In the inset of Fig. 5.11, we show the k_i positions as the bold parts of the equi–energy contours for the laser energies from 1.0 eV to 2.5 eV in steps of 0.5 eV. When the chiral angle θ of a SWNT changes from $\theta = 0$ (zigzag) to $\theta = \pi/6$ (armchair), the k_i position will change in the 2D BZ from Z1 (or Z2) to A1 (or A2) of the bold parts of the contours. Around the K (or K') point, the value of the absorption matrix element has a three-fold rotational symmetry, and depending on the position of the cutting line relative to the K point, the two cases of the bold parts (the long or short ones) can be considered. Thus the matrix element has relatively large values for chiral angle close to $\pi/6$. The chirality dependence of the matrix element comes from the trigonal warping effect of the optical matrix element, as is shown in Fig. 5.10. In the case of semiconducting nanotubes, the k_i point is along either the A1–Z1 or the A2–Z2 curve, depending on their (n, m) values, while in the case of metallic nanotubes, two k_i points appear on the A1–Z1 and the A2–Z2 curves. It is noted that the corresponding two E_{ii} values at two k_i position are different from each other. Because of the trigonal warping effect, in the case of armchair nanotubes, the two E_{ii} values are

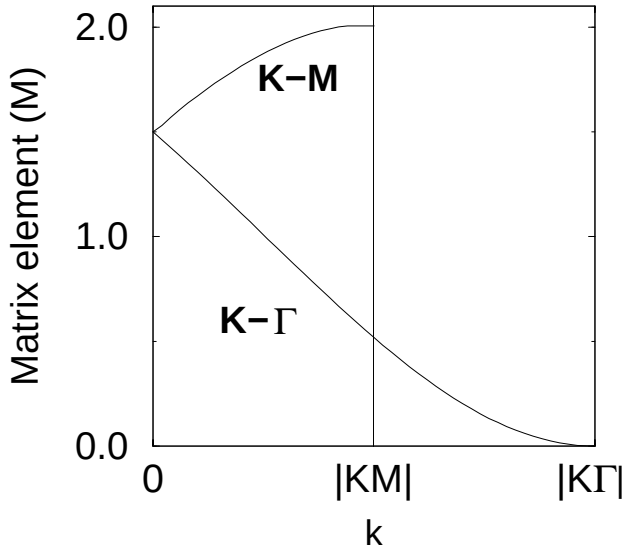

Figure 5.10: The optical absorption matrix element for parallel polarization along the high symmetry lines from K to M and from K to Γ as a function of distance of the $\mathbf{k}$ vector from K [59].

equal to each other [36].

From Fig. 5.11, it can also be seen that the splitting between the two lines is a maximum for zigzag tubes ($\theta = 0$). In the case of armchair tubes ($\theta = \pi/6$), the splitting becomes zero because the k_i points aer equivalent to each other. For a given nanotube chirality, except for the armchair case, the width of the splitting increases with increasing laser energy.

5.8 Possible experimental setup for observing the theoretical predictions

Although all the present results are based on the standard theory of optical absorption, the results presented here are of particular interest in connection with the recent progress in single nanotube Raman spectroscopy. Here, we discuss possible experimental setups for observing the node phenomena in graphite and the chirality dependence of the optical matrix elements in SWNTs.

The nodes in the absorption matrix element cannot be observed easily by optical absorption spectra of graphite, since the optical absorption does in general not select the k vector of the electron. However, we can propose some possible circumstances under which the effect of the nodes in graphite and in SWNTs can be observed. One possibility is to carry out the optical absorption experiment on a nanographite ribbon. The nanographite ribbon is defined as a strip of a graphene layer with a fixed width and its geometry and electronic structure was given in Sec. 3.4. Because of the finite size in the direction of the width of the ribbon, the wave vector in the direction perpendicular to the ribbon direction becomes discrete. The situation is similar to that for a SWNT, but the difference is that the dipole vectors, $< \phi(\mathbf{r} - \mathbf{R}_j)|\nabla|\phi(\mathbf{r} - \mathbf{R}'_j) >$,

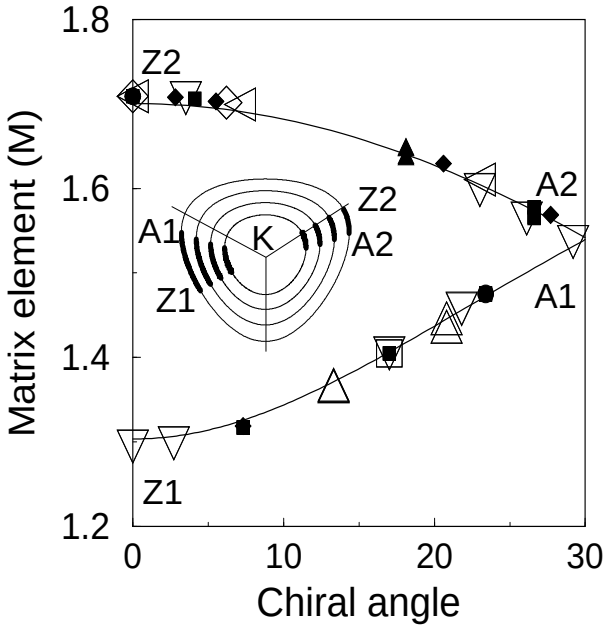

Figure 5.11: Chirality dependence of the optical matrix element at the van Hove singular point k_i for 2.41 eV in units of $m_{\rm opt}$ in Eq. (5.27). The symbols correspond to SWNTs which have a van Hove singularity in a window of 0.05 eV around the laser energy. Full symbols correspond to metallic tubes and open symbols to semiconducting tubes. The transitions are indicated as follows: $\bigcirc$ E_{11} , $\Box$ E_{22}, $\Diamond$ E_{33}, $\triangle$ E_{44}, $\triangleleft$ E_{55}, and $\triangledown$ E_{66}. The inset shows the equi–energy contours from 1.0 eV to 2.5 eV in steps of 0.5 eV. The possible van Hove singular k_i points are given by the bold part of the equi–energy contours. A1 and A2 show k_i positions and the corresponding matrix element of armchair nanotubes, while Z1 and Z2 show those of zigzag nanotubes [59].

are parallel to one another on a plane of the ribbon, while that is not the case for the cylindrical surface of SWNTs. The nanographite ribbon lies entirely in plane, the two dimensional electron wavevector is conserved. Unlike in SWNTs, transitions $\mu \to \mu \pm 1$ are not possible in nanographite ribbons. Thus we should be able to detect the node by a rotation of the polarization vector in the graphene plane relative to the direction of the nano-graphite ribbon. The second possibility for observing the node is a study of the polarization dependence of the D–band spectra of 2D graphite. In the double resonance Raman theory, the observation of the D–band spectra depends on the condition $q \sim 2k$ where q and k are the phonon and electron wavevectors, respectively [55]. As is discussed in Sec. 4.3, all q vectors which satisfy $q \sim 2k$ around the K point contribute to yield a broad D–band feature. If there is a node in the absorption spectra, some q vectors will not contribute to the D–band spectra, and this effect results in a narrow spectral width of the D–band frequency as a function of the polarization because of the trigonal warping effect of the phonon energy dispersion around the K point. The third possibility is that we can observe the chirality dependence of the resonance Raman intensity, as discussed in Sec. 4.2.

The chirality dependence of the optical absorption should be observed both in semiconducting and metallic SWNTs, if we can observe their single nanotube spectra. In the case of semiconducting nanotubes, the k_i positions depend on the i value of E_{ii} and on (n, m) which satisfies $2n+m = 3\ell+1$ or $2n+m = 3\ell+2$ (ℓ integer) [36]. When $2n+m = 3\ell+1$ (semiconducting 1), the VHS point for $i = 1$ exists around the K–Γ symmetry line, while for $2n+m = 3\ell+2$ (semiconducting 2), the VHS point for $i = 1$ exists around the K–M symmetry line as shown in Fig. 3.11. The situation becomes opposite for $i = 2$. In fact, most experimental data we have are for the laser energy in resonance with the VHS E_{22}. For semiconducting 1 SWNTs, E_{22} occurs at K–Msymmetry line and for semiconducting 2 SWNTs, E_{22} occurs at K–Γ symmetry line as is shown in Fig. 3.11. Thus by comparing the relative intensities corresponding to $E_{11}^{\rm S}$ and to $E_{22}^{\rm S}$, we might be able to establish whether the SWNT is semiconducting type 1 or type 2. For the experimentally important $E_{22}^{\rm S}$ singularity, we predict that the $2n+m = 3\ell+1$ (semiconducting 1) have stronger optical absorption.

In metallic nanotubes, the $E_{ii}^{\rm M}$ VHS peaks are split into two peaks as can be seen from Fig. 3.11. The higher and the lower energy peaks are related to the k_i positions around the K–Γ and K–M lines, respectively. Thus the lower energy peaks have relatively larger optical intensity than the higer energy peaks whose difference in intensity is the largest for zigzag nanotubes and zero for armchair nanotubes. Actually in the case of armchair SWNTs, for which there is no splitting, we should not observe such an effect. These observations in SWNTs will be possible by using many different laser lines or a tunable laser, which will be useful for assigning (n, m) values using single nanotube Raman spectroscopy.

5.9 Derivation of electron light interaction

Before finishing this section, we derive an analytical expression for the $m_{\rm opt}$ defined in Eq. (5.18) which will be useful for calculating the optical absorption intensity. The numerical value is important when we want to get a quantitative value for the absorption or relaxation time for a photoexcited electron by recombination with a hole. This is related to the PL process because hot electron recombination reduces the PL or Raman spectra. We used the calculated value of $m_{\rm opt} = \langle\phi_1|\frac{\partial}{\partial x}|\phi_2\rangle$, where ϕ_1 and ϕ_2 are the two $2{\rm p}_z$ wavefuntions for atoms located on the xy plane that are separated by a_0 when evaluating the dipole vector in Eq. (5.19). In the definition of $m_{\rm opt}$ in Eq. (5.18), the two electrons are at the origin and at $\mathbf{r}_B^1$. Their coordinates are given by $(0, 0, 0)$ and $(-a_0, 0, 0)$, where $a_0 = 2.712$ is the C–C distance in units of [at.u].
For the analytical calculation of Eq. (5.18) we expand the wavefunctions in a sum over Gaussians. The origin is in between the two atoms so that α and β as shown in Fig. 5.12 are the x coordinates of the two atoms. We get $\beta = -(a_0 - \alpha)$ and thus a definition equivalently to Eq. (5.18) for $m_{\rm opt}$ is

$$m_{\rm opt} = \left\langle z f_1(\mathbf{r}) \left| \frac{\partial}{\partial x} \right| z f_2(\mathbf{r}) \right\rangle, \tag{5.31}$$

where f_1 and f_2 are radial parts and given by a sum over Gaussians. The coordinates of the atoms are chosen to be different for each overlap of Gaussians with indices k and l. Thus we have α_{kl} and $-(a_0-\alpha_{kl})$ for the x coordinates of the two atoms. The radial parts of the wavefunctions

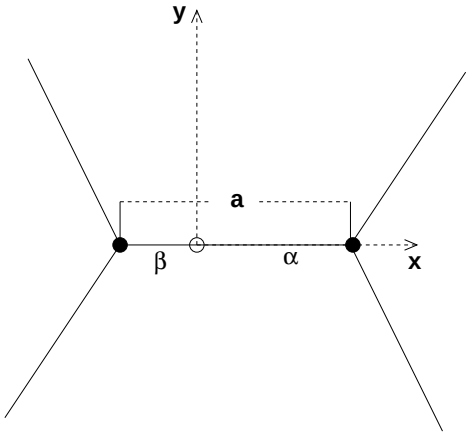

Figure 5.12: The coordinate system used for calculating $m_{\rm opt}$. The origin is located along a bond between nearest neighbours. The distances of the two atoms from the origin are α and β.

therefore are

$$\begin{aligned} f_1 &= \sum_k I_k \exp\left[\frac{-(x+(a_0-\alpha_{kl}))^2-y^2-z^2}{2\sigma_k^2}\right], \quad \text{and} \\ f_2 &= \sum_l I_l \exp\left[\frac{-(x-\alpha_{kl})^2-y^2-z^2}{2\sigma_l^2}\right]. \end{aligned} \tag{5.32}$$

The $\frac{\partial}{\partial x}$ is acting on the wavefunction ϕ_2 and gives

$$\frac{\partial}{\partial x} f_2 = \sum_l I_l \exp\left[\frac{-(x-\alpha_{kl})^2-y^2-z^2}{2\sigma_l^2}\right] \frac{\alpha_{kl}-x}{\sigma_l^2}. \tag{5.33}$$

We substitute f_1 of Eq. (5.32) and Eq. (5.33) into the definition of $m_{\rm opt}$ and get

$$\begin{aligned} m_{\rm opt} &= \sum_{k,l} I_k I_l \int z^2 \exp\left[\frac{-(x+(a_0-\alpha_{kl}))^2-y^2-z^2}{2\sigma_k^2}\right] \frac{\alpha_{kl}-x}{\sigma_l^2} \\ &\quad \times \exp\left[\frac{-(x-\alpha_{kl})^2-y^2-z^2}{2\sigma_l^2}\right] d\mathbf{r} \\ &= \sum_{k,l} I_k I_l \exp\left[\frac{-(a_0-\alpha_{kl})^2}{2\sigma_k^2}\right] \exp\left[-\frac{\alpha_{kl}^2}{2\sigma_l^2}\right] \int z^2 \frac{(\alpha_{kl}-x)}{\sigma_l^2} \exp\left[\frac{-r^2}{2}\left(\frac{1}{\sigma_l^2}+\frac{1}{\sigma_k^2}\right)\right] \\ &\quad \times \exp\left[x\left(\frac{\alpha_{kl}}{2\sigma_l^2}-\frac{a_0-\alpha_{kl}}{2\sigma_k^2}\right)\right] d\mathbf{r}. \end{aligned} \tag{5.34}$$

To simplify the integration, we choose a special value for α_{kl} (shifting the origin in Fig. 5.12) that one exponential function in the integral disappears. This condition is given by

$$\frac{\alpha_{kl}}{\sigma_l^2} - \frac{a_0-\alpha_{kl}}{\sigma_k^2} = 0, \quad \text{and thus} \quad \alpha_{kl} = \frac{\dfrac{a_0}{\sigma_k^2}}{\dfrac{1}{\sigma_l^2}+\dfrac{1}{\sigma_k^2}}. \tag{5.35}$$

When we substitute α_{kl} of Eq. (5.35), the integration over x disappears. We now change the integration from cartesian to spherical coordinates by substituting $x = r\sin\theta\cos\phi$, $x = r\sin\theta\sin\phi$ and $z = r\cos\theta$ and the Jacobian for $d\mathbf{r}$ and get

$$\begin{aligned} m_{\text{opt}} &= \sum_{k,l} I_k I_l \alpha_{kl} \exp\left[\frac{-(a_0-\alpha_{kl})^2}{2\sigma_k^2}\right] \exp\left[\frac{-\alpha_{kl}^2}{2\sigma_l^2}\right] \frac{1}{\sigma_l^2} \\ &\quad \times \int r^4 \cos^2\theta \exp\left[\frac{-r^2}{2}\left(\frac{1}{\sigma_k^2}+\frac{1}{\sigma_l^2}\right)\right] \sin\theta dr d\theta d\phi. \end{aligned} \tag{5.36}$$

Substitution of $x = \cos\theta$ and integration over x and ϕ gives

$$m_{\text{opt}} = \sum_{k,l} \frac{4\pi}{3} I_k I_l \alpha_{kl} \exp\left[\frac{-(a_0-\alpha_{kl})^2}{2\sigma_k^2}\right] \exp\left[\frac{-\alpha_{kl}^2}{2\sigma_l^2}\right] \frac{1}{\sigma_l^2} \int r^4 \exp\left[-\frac{r^2}{2}\left(\frac{1}{\sigma_k^2}+\frac{1}{\sigma_l^2}\right)\right] dr. \tag{5.37}$$

To evaluate this integral we use

$$\int_0^\infty r^4 \exp[\frac{-r^2}{2\alpha_{kl}}] = 3\alpha_{kl}^{5/2}\sqrt{\frac{\pi}{2}}. \tag{5.38}$$

The final formula for m_{opt} becomes

$$m_{\text{opt}} = \sum_{k,l} \frac{4\pi\alpha_{kl} I_k I_l}{\sigma_l^2}\sqrt{\frac{\pi}{2}} . \exp\left[\frac{-(a_0-\alpha_{kl})^2}{2\sigma_k^2}\right] \exp\left[\frac{-\alpha_{kl}^2}{2\sigma_l^2}\right] \left[\frac{1}{\frac{1}{\sigma_k^2}+\frac{1}{\sigma_l^2}}\right]. \tag{5.39}$$

For α_{kl} , we must evaluate and substitute Eq. (5.35)x for each term in the sum. We use the values of I_k and σ_k from Tab. 3.2(a) The result is $m_{\text{opt}} = 0.21$ in units of $[\text{at.u.}]^{-1}$.

Chapter 6

Electron phonon interaction

In this section we show how to calculate electron phonon coupling constants with tight binding approximations for graphite and single–wall carbon nanotubes. Calculated results of electron phonon matrix elements for photo–excited electrons are given as a function of electron wavevector $\mathbf{k}$ and phonon mode ν.

6.1 Electron phonon interaction in graphite

The value of the crystal potential at position $\mathbf{r}$ in the crystal is generally a time–dependent function because of the atomic vibrations of a phonon mode ν with frequency $\omega^{\nu}_{\rm vib}(\mathbf{q})$ and wavevector $\mathbf{q}$. In the following, we adopt the "rigid–ion approximation" or "adiabatic approximation", which means that the potential of the atom is perfectly following the movement of the atom. In such a model, the total potential is given by a sum over atomic screened ion potentials $v(\mathbf{r}-\mathbf{R}^{\upsilon}_{\sigma})$. Here $\mathbf{R}^{\upsilon}_{\sigma}$ is the coordinate of the atom σ=A,B in the υ–th unit cell of graphene that are displaced from equilibrium position due to the phonon. For time dependent $\mathbf{R}^{\upsilon}_{\sigma}$, the displacement is described by the phonon eigenfunction $\mathbf{S}^{\nu}_{\sigma}(\mathbf{q})$, where ν is the phonon branch and $\sigma = A, B$ are the atom indices. For small amplitudes of the vibration (in order of a few percent of the bond length), we can expand the potential around the equilibrium position in the normalized phonon eigenfunction $\mathbf{S}^{\nu}_{\sigma}(\mathbf{R}^{\upsilon}_{\sigma},\mathbf{q},t) = \mathbf{S}^{\nu}_{\sigma}(\mathbf{R}^{\upsilon}_{\sigma},\mathbf{q})\exp\{i\omega^{\nu}_{\rm vib}(\mathbf{q})t\}$. The correction to the potential at position $\mathbf{r}$ due to the vibration is then given by the deformation potential

$$V_D(\mathbf{r},t) = -\sum_{\upsilon=0}^{N_u-1}\sum_{\sigma=A,B}\sum_{\nu=1}^{6}\sum_{\mathbf{q}} A^{\nu}_{\rho}(\mathbf{q})\nabla v\left(\mathbf{r}-\mathbf{R}^{\upsilon}_{\sigma}\right)\cdot\mathbf{S}^{\nu}_{\sigma}(\mathbf{R}^{\upsilon}_{\sigma},\mathbf{q})\exp\left\{\pm i\omega^{\nu}_{\rm vib}(\mathbf{q})t\right\}. \qquad (6.1)$$

The "$\pm$" and ρ indices refer to whether a phonon is created ("$-$" and $\rho = E$) or absorbed ("+" and $\rho = A$). The amplitude of the vibration, $A^{\nu}_{\rho}(\mathbf{q})$ depends on the temperature T through the number of phonons in the mode with index ν given by $N^{\nu}_{{\rm vib}\rho}$ and the number of atoms N_a, that contribute to the phonon. The potential energy at the maximum displacement is given by $k(A^{\nu}_{\rho})^2/2 = \hbar\omega$ with the spring constant $k = m\omega^2$. where $m = 1.9927\times10^{-26}$ kg is the mass of a carbon atom. Thus the vibration amplitude is given by

$$A^{\nu}_{\rho}(\mathbf{q}) = \sqrt{\frac{2\hbar N^{\nu}_{{\rm vib}\rho}(\mathbf{q})}{m\omega^{\nu}(\mathbf{q})N_a}} \quad , \quad (\rho = A, E). \qquad (6.2)$$

The number of phonons N^{ν}_{vibA} and N^{ν}_{vibE} at phonon wavevector $\mathbf{q}$ for the phonon absorption and phonon emission processes, respectively, are given by Bose–Einstein distributions

$$N^{\nu}_{\mathrm{vibA}}(\mathbf{q}) = \frac{1}{\exp\left(\frac{\hbar\omega^{\nu}_{\mathrm{vib}}(\mathbf{q})}{k_{\mathrm{B}}T}\right) - 1} \quad \text{and} \quad N^{\nu}_{\mathrm{vibE}}(\mathbf{q}) = \frac{1}{\exp\left(\frac{\hbar\omega^{\nu}_{\mathrm{vib}}(\mathbf{q})}{k_{\mathrm{B}}T}\right) - 1} + 1. \tag{6.3}$$

Here $k_{\mathrm{B}} = 8.617 \times 10^{-5}$ eV/K is the Boltzmann constant and the additional term "+1" in N^{ν}_{vibE} corresponds to spontaneous emission of one phonon. In first–order, time–dependent perturbation theory the matrix element between initial electron state $\mathbf{k}_i$ and final electron state $\mathbf{k}_f$ with energies E_i and E_f, respectively is given by

$$M^{f_i,\nu}_{\mathrm{vib}\rho}(\mathbf{k}_f,\ \mathbf{k}_i) = -\sum_{\upsilon=0}^{N_\upsilon - 1} \sum_{\sigma=A,B} \langle \Psi^f(\mathbf{r},\mathbf{k}_f)|A^{\nu\rho}(\mathbf{q})\nabla v\,(\mathbf{r}-\mathbf{R}^{\upsilon}_{\sigma})\cdot\mathbf{S}^{\nu}_{\sigma}(\mathbf{R}^{\upsilon}_{\sigma},\mathbf{q})|\Psi^i(\mathbf{r},\mathbf{k}_i)\rangle \tag{6.4}$$

Here $\Psi^{i(f)}$ denotes an electron eigenfunction with the indices i, f being the initial and final band index, respectively. $\mathbf{k}_i$ and $\mathbf{k}_f$ are the initial and final wavevectors of the electrons, respectively. $\mathbf{S}^{\nu}_{\sigma}(\mathbf{q})$ is the phonon eigenfunctions at an atom position $\mathbf{R}^{\upsilon}_{\sigma}$ with wavevector $\mathbf{q}$, which is given by multiplying a phase factor to the solution of the 6×6 dynamical matrix $\mathbf{S}^{\nu}_{\sigma}(\mathbf{q})$.

$$\mathbf{S}^{\nu}_{\sigma}(\mathbf{R}^{\upsilon}_{\sigma},\mathbf{q}) = \mathbf{S}^{\nu}_{\sigma}(\mathbf{q})\exp(i\mathbf{q}\cdot\mathbf{R}^{\upsilon}_{\sigma}) \tag{6.5}$$

Similarly the electron eigenfunctions are expanded as

$$\Psi^i(\mathbf{r},\mathbf{k}) = \frac{1}{\sqrt{N_u}}\sum_{u=0}^{N_u}\sum_{s=A,B}\exp(i\mathbf{k}\cdot\mathbf{R}^{u}_{s})c^{i}_{s}(\mathbf{k})\varphi(\mathbf{r}-\mathbf{R}^{u}_{s}). \tag{6.6}$$

We can substitute

$$\mathbf{R}^{u}_{s} = \mathbf{R}^{\upsilon}_{\sigma} + \mathbf{r}^{\ell s}_{\sigma} \tag{6.7}$$

where ℓ is for the ℓ–th atom of type s. The relative vector $\mathbf{r}^{\ell s}_{\sigma}$ starts from a σ atom at $\mathbf{R}^{\upsilon}_{\sigma}$ and goes to a s atom at $\mathbf{R}^{u}_{s}$. When we substitute Eq.(6.6) and Eq.(6.7) into Eq.(6.4) we can obtain the momentum conservation null, $\mathbf{k}_i = \mathbf{k}_f \pm \mathbf{q}$. Here the "+" is for the emission and the "–" is for phonon absorption. Eq.(6.4) becomes

$$\begin{aligned} & M^{f_i,\nu}_{\mathrm{vib}\rho}(\mathbf{k}_i,\mathbf{k}_f) \\ = & \sum_{l,l',\sigma,s,s'} A^{\nu\rho}(\mathbf{q})c^{f*}_{s'}(\mathbf{k}_f)c^{i}_{s}(\mathbf{k}_i)\exp(-i\mathbf{r}^{\sigma}_{l's'}\cdot\mathbf{k}_f)\exp(i\mathbf{r}^{\sigma}_{ls}\cdot\mathbf{k}_i)\mathbf{S}^{\nu}_{\sigma}(\mathbf{q})\cdot\mathbf{m}_D(\mathbf{r}^{\sigma}_{l's'},\mathbf{r}^{\sigma}_{ls}), \end{aligned} \tag{6.8}$$

where $\mathbf{m}_D$ is the atomic deformation potential vector, that is the value of the three center integral

$$\mathbf{m}_D(\mathbf{r}^{\sigma}_{l's'},\mathbf{r}^{\sigma}_{ls}) = \int \varphi^*(\mathbf{r}-\mathbf{r}^{\sigma}_{l's'})\nabla v(\mathbf{r})\varphi(\mathbf{r}-\mathbf{r}^{\sigma}_{ls})d\mathbf{r}. \tag{6.9}$$

From Eq.(6.8) it is clear that if the phonon eigenfunction $\mathbf{S}^{\nu}_{\sigma}$ and $\mathbf{m}_D$ are perpendicular to each other, there is no electron−phonon coupling. In Sec. 6.2 we can show analytically that $\mathbf{m}_D$ does not have a z component and therefore only in–plane vibrations can make electron phonon interactions in graphite. We need to calculate $\mathbf{m}_D$ for many different combinations of the three centers. However, a numerical integration in 3D real space takes a huge computational time.

6.2 Calculation of atomic deformation potential vector in graphene

To get a numerical value, we use electronic wavefunctions $\varphi(\mathbf{r})$ of the form given in Eq. (3.31) and a potential $v(\mathbf{r})$ of the form in Eq. (3.33). Both $\varphi(\mathbf{r})$ and $v(\mathbf{r})$, which are obtained from a first–principle calculation for graphite are expanded into a Gaussian basis set to solve the three center integral in Eq. (6.9) analytically. The coefficients for the expansions of the π wavefunctions and the screened potential v are given in Sec. 3.3 in Table 3.2. We choose the graphene plane in the yz plane. The center of the potential can be put to the origin and the A and B atom to $\mathbf{r}_A$ and $\mathbf{r}_B$ respectively and have values

$$\mathbf{r}_V = (0,0,0), \quad \mathbf{r}_A = (0, y_A, z_A), \quad \mathbf{r}_B = (0, y_B, z_B).$$

The potential of the electrons in the field of an atom is

$$v(\mathbf{r}) = \frac{1}{r}\sum_k^N v_k \exp\left(\frac{-\mathbf{r}^2}{2\tau_k^2}\right). \tag{6.10}$$

Here v_k and τ_k are given by the fitting of the screened potential and listed in Table 3.2(b). When we apply the gradient to the potential in Eq. (6.10) we get:

$$\nabla v(\mathbf{r}) = \frac{dv}{dr}\nabla r = \frac{-1}{r^3}\sum_k^N v_k \exp\left(\frac{-\mathbf{r}^2}{2\tau_k^2}\right)\left(1+\frac{r^2}{\tau_k^2}\right)\begin{pmatrix} x \\ y \\ z \end{pmatrix} \tag{6.11}$$

For the wavefunctions in Eq. (6.9) we substitute the form we gave in Eq. (3.31) located at positions $\mathbf{r}_A$ and $\mathbf{r}_B$, respectively. Substituting the wavefunctions and Eq. (6.11) for the gradient of the potential into Eq. (6.9) yields

$$\begin{aligned}\mathbf{m}_D = \sum_{i,j,k} -I_i I_j V_k \int_{-\infty}^{\infty}\int_{-\infty}^{\infty}\int_{-\infty}^{\infty} \exp\left[\frac{-1}{2\sigma_i^2}\{x^2+(y-y_A)^2+(z-z_A)^2\}\right] \\ \times \exp\left[\frac{-1}{2\sigma_j^2}\{x^2+(y-y_B)^2+(z-z_B)^2\}\right]\left(1+\frac{r^2}{\tau_k^2}\right)\frac{1}{r^2}\exp\left(\frac{-\mathbf{r}^2}{2\tau_k^2}\right)x^2\begin{pmatrix} x/r \\ y/r \\ z/r \end{pmatrix} d\mathbf{r}.\end{aligned} \tag{6.12}$$

Here we defined $r^2 = x^2+y^2+z^2$. Sine $\mathbf{r}_A$ and $\mathbf{r}_B$ lie in the yz plane and the value of the integral does not change when rotating $\mathbf{r}_A$ and $\mathbf{r}_B$ around the x–axis. The integral can only be done analytically if one of the exponential terms such as $\exp\{y(..)\}$ or $\exp\{z(..)\}$ disappears. A transformation is made to a new coordinate system by rotating the two points $\mathbf{r}_A$ and $\mathbf{r}_B$ around the x axis by an angle α_{ij}. The indices ij are for the two electronic wavefunctions and the potential. The angle of rotation, we choose to do the integration is different for each Gaussian overlap combination from the three centers. The rotation is shown in Fig. 6.1.

The new coordinates for the atomic wavefunction at $\mathbf{r}_A$ are

$$\begin{aligned} y'_A &= y_A\cos\alpha_{ij} - z_A\sin\alpha_{ij}, \\ z'_A &= y_A\sin\alpha_{ij} + z_A\cos\alpha_{ij}. \end{aligned}$$

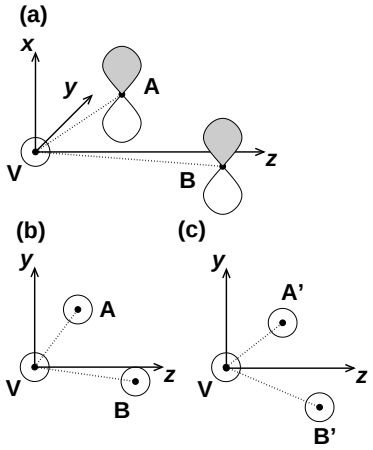

Figure 6.1: The electronic wavefunctions for atoms A and B and the potential V are located as shown in (a). In (b) the top view is shown. The integration can be done analytically, when rotating A and B atom to A' and B' because the y component of deformation potential vector vanishes. After integration, we must rotate back the obtained deformation potential vector.

We use the same form for the rotation of $\mathbf{r}_B$. When we substitute the new coordinates for $\mathbf{r}_A$ and $\mathbf{r}_B$ into Eq. (6.12), the new $\mathbf{m}'_D$ is rotated with respect to $\mathbf{m}_D$ by an angle α_{ij}.

$$\mathbf{m}'_D = \sum_{i,j,k} -I_i I_j V_k \int_{-\infty}^{\infty}\int_{-\infty}^{\infty}\int_{-\infty}^{\infty} \exp\left[\frac{-1}{2\sigma_i^2}\left\{x^2+(y-y'_A)^2+(z-z'_A)^2\right\}\right]$$
$$\times \exp\left[\frac{-1}{2\sigma_j^2}\left\{x^2+(y-y'_B)^2+(z-z'_B)^2\right\}\right]\left(1+\frac{r^2}{\tau_k^2}\right)\frac{1}{r^2}\exp\left(\frac{-\mathbf{r}^2}{2\tau_k^2}\right)x^2\begin{pmatrix} x/r \\ y/r \\ z/r\end{pmatrix} d\mathbf{r}. \tag{6.13}$$

Multiplying out the exponents gives

$$\mathbf{m}'_D = \sum_{i,j,k} -I_i I_j V_k \exp\left(\frac{-r'^2_A}{2\sigma_i^2}\right)\exp\left(\frac{-r'^2_B}{2\sigma_j^2}\right)\int_{-\infty}^{\infty}\int_{-\infty}^{\infty}\int_{-\infty}^{\infty} \tag{6.14}$$
$$\exp\left(\frac{-r^2}{2\sigma_{ijk}^2}\right)\exp\left\{y\left(\frac{y'_A}{\sigma_i^2}+\frac{y'_B}{\sigma_j^2}\right)\right\}\exp\left\{z\left(\frac{z'_A}{\sigma_i^2}+\frac{z'_B}{\sigma_j^2}\right)\right\}\left(1+\frac{r^2}{\tau_k^2}\right)\frac{1}{r^2}x^2\begin{pmatrix} x/r \\ y/r \\ z/r\end{pmatrix} d\mathbf{r}.$$

Here we used

$$\frac{1}{\sigma_{ijk}^2} = \frac{1}{\sigma_i^2}+\frac{1}{\sigma_j^2}+\frac{1}{\tau_k^2}.$$

We can now always choose a coordinate system in which the $\exp[y(..)]$ disappears. That is a value α_{ij} must be found so that

$$\frac{y'_A}{\sigma_i^2}+\frac{y'_B}{\sigma_j^2} = 0. \tag{6.15}$$

In terms of the old coordinate system and the rotation angle α_{ij} this can be written as

$$\frac{y_A \cos\alpha_{ij} - z_A \sin\alpha_{ij}}{\sigma_i^2} + \frac{y_B \cos\alpha_{ij} - z_B \sin\alpha_{ij}}{\sigma_j^2} = 0. \tag{6.16}$$

The solution to this equation is given by

$$\alpha_{ij} = \arctan \frac{y_A\sigma_j^2 + y_B\sigma_i^2}{z_A\sigma_j^2 + z_B\sigma_i^2}. \tag{6.17}$$

Thus in the system which is given by the solution to the above equation, the integral reduces to the easy form

$$\begin{aligned}\mathbf{m}_D = \sum_{i,j,k} -I_iI_jV_k \exp\left(\frac{-r_A'^2}{2\sigma_i^2}\right)\exp\left(\frac{-r_B'^2}{2\sigma_j^2}\right) \\ \times \int_{-\infty}^{\infty}\int_{-\infty}^{\infty}\int_{-\infty}^{\infty} \exp\left(\frac{-r^2}{2\sigma_{ijk}^2}\right)\exp\left\{z\left(\frac{z_A'}{\sigma_i^2}+\frac{z_B'}{\sigma_j^2}\right)\right\}\left(1+\frac{r^2}{\tau_k^2}\right)\frac{1}{r^2}x^2\begin{pmatrix} x/r \\ y/r \\ z/r\end{pmatrix} d\mathbf{r}.\end{aligned} \tag{6.18}$$

Hereafter, the following abbrevations are used:

$$\begin{aligned} A_{ijk} &= -I_iI_jV_k \exp\left(\frac{-r_A'^2}{2\sigma_i^2}\right)\exp\left(\frac{-r_B'^2}{2\sigma_j^2}\right), \\ A'_{ijk} &= -\frac{1}{\tau_k^2} I_iI_jV_k \exp\left(\frac{-r_A'^2}{2\sigma_i^2}\right)\exp\left(\frac{-r_B'^2}{2\sigma_j^2}\right) = \frac{A_{ijk}}{\tau_k^2}, \\ c_{ij} &= \frac{z_A'}{\sigma_i^2} + \frac{z_B'}{\sigma_j^2}. \end{aligned} \tag{6.19}$$

Another transformation to spherical coordinates is made to get rid of the singularity at $r = 0$. We set

$$\begin{aligned} r^2 = x^2 + y^2 + z^2, \quad d\mathbf{r} = r^2 \sin\theta dr d\theta d\varphi, \\ x = r\sin\theta\cos\varphi, \quad y = r\sin\theta\sin\varphi, \quad z = r\cos\theta. \end{aligned} \tag{6.20}$$

The atomic deformation potential vector becomes in spherical coordinates

$$\begin{aligned}\mathbf{m}'_D \;=\; & \sum_{i,j,k} A_{ijk}\int_{-\infty}^{\infty}\int_0^{\pi}\int_0^{2\pi} r^2 \exp\left(\frac{-r^2}{2\sigma_{ijk}^2}\right)\exp\left(c_{ij}r\cos\theta\right)\sin\theta(\sin\theta\cos\varphi)^2 \\ & \times \begin{pmatrix}\sin\theta\cos\varphi \\ \sin\theta\sin\varphi \\ \cos\theta\end{pmatrix} d\varphi d\theta dr + \sum_{i,j,k} A'_{ijk}\int_{-\infty}^{\infty}\int_0^{\pi}\int_0^{2\pi} r^4 \\ & \times \exp\left(\frac{-r^2}{2\sigma_{ijk}^2}\right)\exp\left(c_{ij}r\cos\theta\right)\sin\theta(\sin\theta\cos\varphi)^2 \begin{pmatrix}\sin\theta\cos\varphi \\ \sin\theta\sin\varphi \\ \cos\theta\end{pmatrix} d\varphi d\theta dr. \end{aligned} \tag{6.21}$$

The integration over components involving $\cos\varphi$ and $\sin\varphi$ gives zero and only the $\cos\theta$ gives a nonzero integral. m'_{Dx} , m'_{Dy} are therefore equal to zero.

$$m'_{Dz} = \sum_{i,j,k} A_{ijk} \int_{-\infty}^{\infty}\int_{0}^{\pi}\int_{0}^{2\pi} r^2(\sin\theta\cos\varphi)^2\cos\theta\exp\left(\frac{-r^2}{2\sigma_{ijk}^2}\right)\exp\left(c_{ij}r\cos\theta\right)\sin\theta d\varphi d\theta dr+$$
$$\sum_{i,j,k} A_{ijk} \int_{-\infty}^{\infty}\int_{0}^{\pi}\int_{0}^{2\pi} r^4(\sin\theta\cos\varphi)^2\cos\theta\exp\left(\frac{-r^2}{2\sigma_{ijk}^2}\right)\exp\left(c_{ij}r\cos\theta\right)\sin\theta d\varphi d\theta dr. \tag{6.22}$$

With a substitution of $t = \cos\theta$ and $\sin^2\theta = 1 - t^2$ the integrals become:

$$m'_{Dz} = \sum_{i,j,k} A_{ijk} \int_{-\infty}^{\infty}\int_{1}^{-1}\int_{0}^{2\pi} r^2(\cos\varphi)^2(t-t^3)\exp\left(\frac{-r^2}{2\sigma_{ijk}^2}\right)\exp\left(c_{ij}rt\right)d\varphi dt dr+$$
$$\sum_{i,j,k} A'_{ijk} \int_{-\infty}^{\infty}\int_{1}^{-1}\int_{0}^{2\pi} r^4(t-t^3)(\cos\varphi)^2\exp\left(\frac{-r^2}{2\sigma_{ijk}^2}\right)\exp\left(c_{ij}rt\right)d\varphi dt dr. \tag{6.23}$$

These integrals can be done analytically. First we integrate ϕ, which gives a factor π. For the integrations over r and t we define temporary variables t_1 and t_2 as

$$\begin{aligned} t_1 &= \int_{1}^{-1}\int_{0}^{\infty} r^2 t(1-t^2)\exp(-r^2b+rct)drdt \quad \text{and} \\ t_2 &= \int_{1}^{-1}\int_{0}^{\infty} r^4 t(1-t^2)\exp(-r^2b+rct)drdt. \end{aligned} \tag{6.24}$$

We substitute the following values for b and c :

$$b = b_{ij} = \frac{1}{2\sigma_{ijk}^2} \quad \text{and} \quad c = c_{ij}. \tag{6.25}$$

To evaluate t_1 we first remove the r^2 by writing

$$t_1 = \frac{d^2}{dc^2}\int_{1}^{-1}\int_{0}^{\infty}\frac{1}{t}(1-t^2)\exp(-r^2b+rct)drdt. \tag{6.26}$$

Then we make a full square by using

$$\exp(-r^2b+rct) = \exp\left\{-(r-\frac{ct}{2b})^2b\right\}\exp(\frac{c^2t^2}{4b}). \tag{6.27}$$

We also shift the integration boundaries and get

$$t_1 = \frac{d^2}{dc^2}\int_{1}^{-1}\int_{-ct/2b}^{\infty}\frac{1}{t}(1-t^2)\exp(-r^2b)\exp(\frac{c^2t^2}{4b})drdt. \tag{6.28}$$

We now do the integration over r that gives an error function Erf defined as

$$\mathrm{Erf}(z) = \frac{2}{\sqrt{\pi}} \int_0^z \exp(-t^2) dt. \tag{6.29}$$

We thus get

$$t_1 = \frac{d^2}{dc^2} \int_1^{-1} \frac{1}{t}(1-t^2)\sqrt{\pi} \left(\frac{1+\mathrm{erf}(ct/2\sqrt{b})}{2\sqrt{b}} \right) \exp(\frac{c^2t^2}{4b}) dt. \tag{6.30}$$

We first carry out the derivative for c and then the singularity at $t = 0$ disappears. Note that for $c = 0$ the integral disappears because of the odd function in t. Then we can integrate and get

$$t_1 = \frac{2\left(-6\sqrt{b}\,c + \left(6\,b - c^2\right)\, e^{\frac{c^2}{4b}} \sqrt{\pi}\,\mathrm{Erf}(\frac{c}{2\sqrt{b}})\right)}{\sqrt{b}\,c^4} \quad (c \neq 0) \quad \text{and} \quad t_1 = 0 \quad (c = 0). \tag{6.31}$$

We now evaluate t_2. One "t" and one "r" can be removed by writing

$$t_2 = \frac{d^4}{dc^4} \int_1^{-1} \int_0^{\infty} \frac{1}{t^3}(1-t^2) \exp(-r^2 b + rct) dr dt. \tag{6.32}$$

Now we make a full square for the exponential function in r. Then t_2 becomes

$$t_2 = \frac{d^4}{dc^4} \int_1^{-1} \frac{1}{t^3}(1-t^2)\sqrt{\pi} \left(\frac{1+\mathrm{erf}(ct/2\sqrt{b})}{2\sqrt{b}} \right) \exp\left(\frac{c^2t^2}{4b}\right) dr dt. \tag{6.33}$$

The final result for t_2 is

$$t_2 = \frac{2\sqrt{b}\,c\,\left(6\,b - c^2\right) - \left(12\,b^2 - 4\,b\,c^2 + c^4\right)\, e^{\frac{c^2}{4b}} \sqrt{\pi}\,\mathrm{Erf}(\frac{c}{2\sqrt{b}})}{2\,b^{\frac{5}{2}}\,c^4} \quad \text{and} \quad t_2 = 0 \quad (c = 0). \tag{6.34}$$

Then the final result for the dipole vector is

$$m'_{Dz} = \pi \sum_{ijk} A_{ijk} t_1(ijk) + A'_{ijk} t_2(ijk). \tag{6.35}$$

We now go back to the coordinate system, in which the A and B atoms are in the xy plane. We therfore exchange z and x axes and the y axis stays the same. In this system the atomic deformation potential vector $\mathbf{m}_D$ is given by

$$m_{Dx} = \sum_{ijk} \cos(\alpha_{ij}) m'_{Dz} \tag{6.36}$$

$$m_{Dy} = \sum_{ijk} \sin(\alpha_{ij}) m'_{Dz} \tag{6.37}$$

$$m_{Dz} = 0. \tag{6.38}$$

6.3 Calculated results

We calculate the x and y components of m_D by evaluating the Eq. (6.36) and Eq. (6.37). This is done as follows. For each triple of Gaussians, denoted by indices i, j, and k, we calculate A_{ijk}, A'_{ijk} and c_{ij} as defined in Eq. (6.19) and b_{ij} in Eq. (6.25). Hereafter, we calculate t_1 and t_2 as defined in Eq. (6.31) and Eq. (6.34) for each triple of indices i, j and k. This result is then substituted into Eq. (6.35). Hereafter, we substitute Eq. (6.35) and Eq. (6.17) into Eq. (6.36) and Eq. (6.37) to get the value of $\mathbf{m}_D$. The coefficients I_k and σ_k for the expansion of the wavefunction into Gaussians are given in Table 3.2(a). Similarly, the coefficients V_k and τ_k for the expansion of the potential into Gaussians are given in Table 3.2(b).

We also have to substitute the coordinates of the centers of the two wavefunctions, which are denoted by $\mathbf{r}_A$ and $\mathbf{r}_B$, respectively. Since we have two electron wavefunctions, we fix $\mathbf{r}_A$ and calculate $\mathbf{m}_D$ for different positions of $\mathbf{r}_B$. In Fig. 6.2(a) we plot the direction and magnitude of $\mathbf{m}_D$ with a fixed $\mathbf{r}_A$ in the first neighbour shell to the potential. We denote the lattice site of the potential by a triangle and the lattice site of $\mathbf{r}_A$ by a square. The value of $\mathbf{m}_D$ is calculated for changing $\mathbf{r}_B$. The value of $\mathbf{m}_D$ is largest, if both wavefunctions are located on the same atom site, that is $\mathbf{r}_A = \mathbf{r}_B$. In Fig. 6.2(a), the largest value occurs at about 3.3 eV/at.u. Such a value is typical for solids. We have to keep in mind, that the deformation potential is much smaller than the values in Fig. 6.2, since we multiply each vector $\mathbf{m}_D$ by the phonon displacement given in Eq. (6.2), which has a typical length of a few percent of the bondlength, that is in the order of 0.01 at.u. In Fig. 6.2(b) we show a similar plot for the second neighour shell and it can be seen that the maximum interaction occurs at 0.7 eV/at.u. In Fig. 6.2(c) and Fig. 6.2(d), we fix $\mathbf{r}_A$ in the third and fourth neighbour shell. It is clear that the fourth neighbour shell's contribution is already negligibly small when compared to the largest value in In Fig. 6.2(a). In fact, the maximum value of $\mathbf{m}_D$ in the fourth neighbour shell of the potential is 0.1 eV/at.u. and that value is about 3 percent of the maximum value of the first shell. Thus in our calculations, we omit interactions from the fifth and more distant neighbours.

We now evaluate the electron phonon coupling matrix element in Eq. (6.4). Since the wavevector of the phonon, $\mathbf{q}$ is determined by the initial and final electron wavevector, $\mathbf{k}_i$ and $\mathbf{k}_f$, respectively, we plot the electron phonon coupling for a fixed $\mathbf{k}_i$ around K. All possible $\mathbf{k}_f$ and $\mathbf{q}$ are determined by electron–momentum conservation. In Fig. 6.3 we fix $\mathbf{k}_i$ at an angle of 90° measured from positive k_x axis. The electron phonon coupling with electron states around K' is shown for different phonon branches. The atomic deformation potential vector defined in Eq. (6.9) has a special symmetry property that allows us to understand why accoustic modes at $\mathbf{q} = 0$ have zero electron phonon coupling in graphite. This fact can be understood when considering

$$\mathbf{m}_D(\mathbf{r}_{l's'}, \mathbf{r}_{ls}) = -\mathbf{m}_D(-\mathbf{r}_{l's'}, -\mathbf{r}_{ls}). \tag{6.39}$$

Eq. (6.39) says that the sign of $\mathbf{m}_D$ changes, when we invert the relative coordinates for two electron centers at vectors $\mathbf{r}_{ls}$ and $\mathbf{r}_{l's'}$. When we invert the relative coordinates $\mathbf{r}_{ls}$ and $\mathbf{r}_{l's'}$, we also change the potential from A to B or vice versa. Because of inversion symmetry of the graphene lattice, we can always find atoms located at $-\mathbf{r}_{l's'}$ and $-\mathbf{r}_{l's'}$ when we change the potential.

The results are shown in Fig. 6.4 for intra–valley scattering around K point. It is clear that an electron does not scatter to the same state because the line for initial angle equal to the final angle is zero.

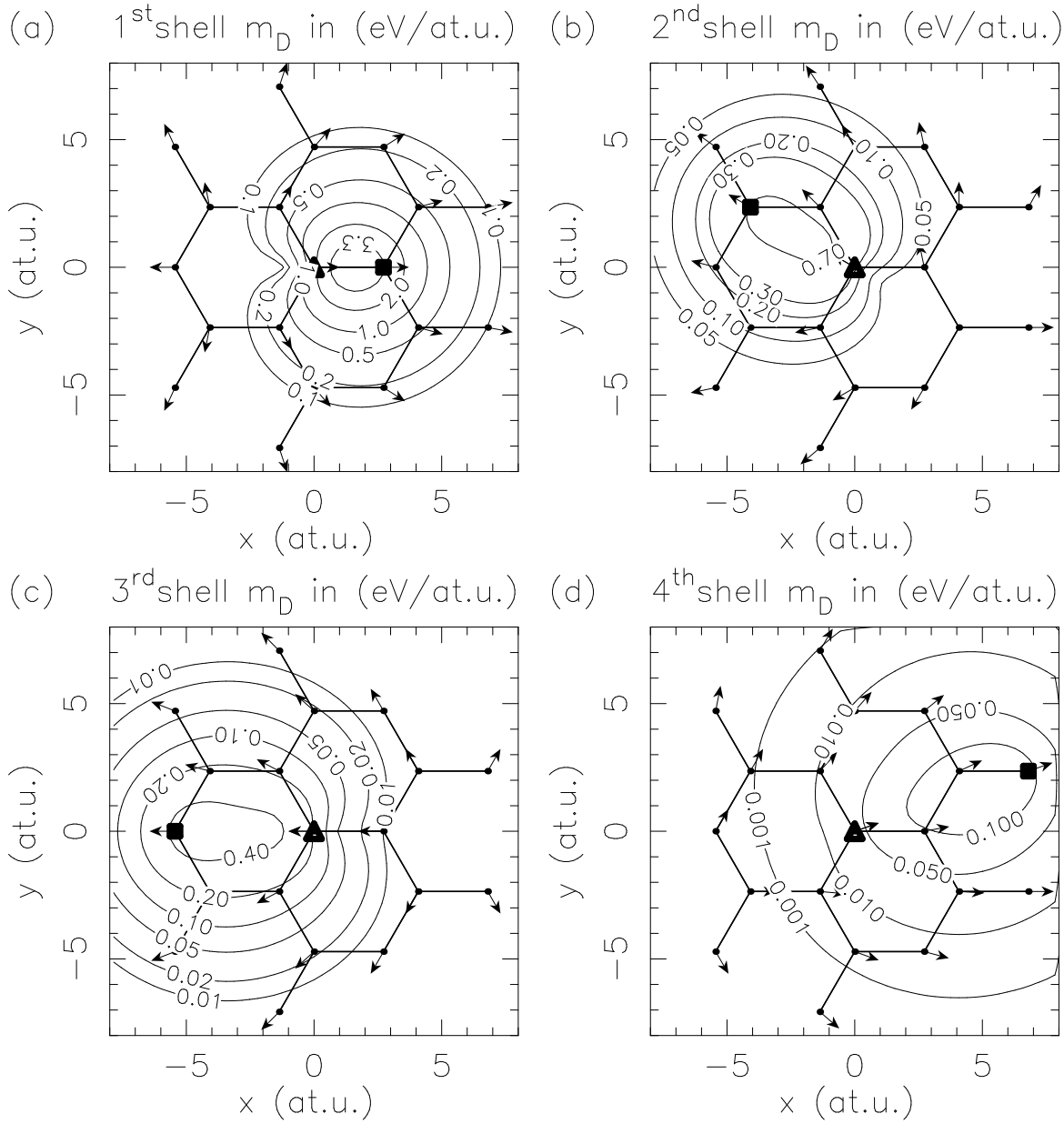

Figure 6.2: The magnitude and direction of the deformation potential are indicated by contour lines (value in eV per atomic unit) and unit vectors. The plot is made keeping two centers of the three center integral in Eq. (6.9) fixed. The potential and one electron wavefunction are indicated by a triangle and a box, respectively. One electron wavefunction is fixed in the (a) first, (b) second, (c) third or (d) fourth neighbour shell. One electron wavefunction is at variable positions and denoted by a filled circle.

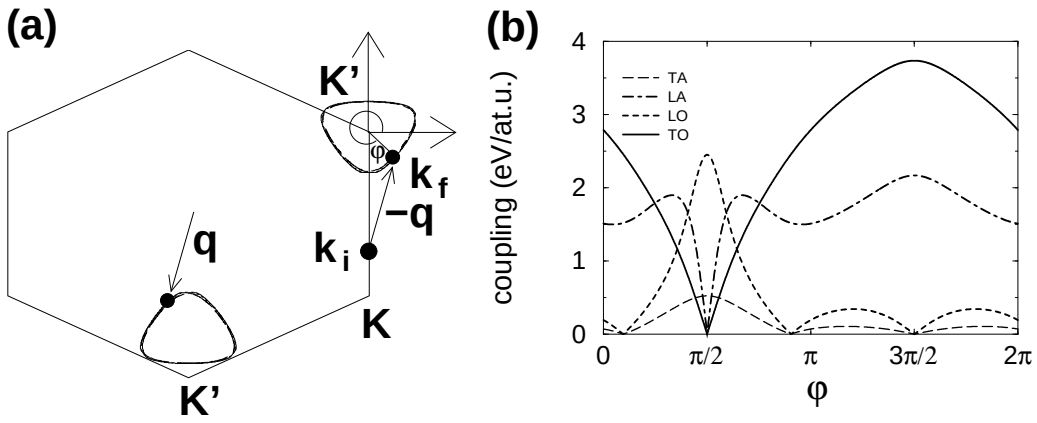

Figure 6.3: In (a) the initial electron state is indicated by k_i and the angle φ for a final state k_f is shown. The phonon contour is shown around K' point. In (b) we show the electron phonon coupling between a fixed electron state around the K point and states at an angle φ around the K' point, plotted for four in–plane modes.

Such a conclusion is discussed in solid state physics [74]. Because of the linear dependence of the accoustic modes on the phonon wavevector, the electron phonon scattering for small energies is usually written as a linear function of the phonon energy times the electron phonon coupling constant.

In Fig. 6.4 the case of intra–valley optic phonons is discussed. It can be seen that only the iLO mode strongly couples electron states at opposite angles around K. We can thus associate the iLO mode to the overbending, which means that the highest phonon frequency in graphite occurs slightly away from Γ. This is also a common feature that LO occurs at higher frequency that TO mode.

In Fig. 6.5 it can be seen that the coupling for the iTO band is by far the largest. Especially we note that the double resonant Raman intensity is proportional to the square of the matrix element. The iTO band has zero coupling for electrons at the same angle as can be seen by the 45° line with zero value. At the opposite angles between K and K' point, the coupling is highest and this is why we can assign only this mode to the experimentally observed strong G' and D bands. The LO mode has a strong coupling for the same angle and will be responsible for Raman features with little dispersion.

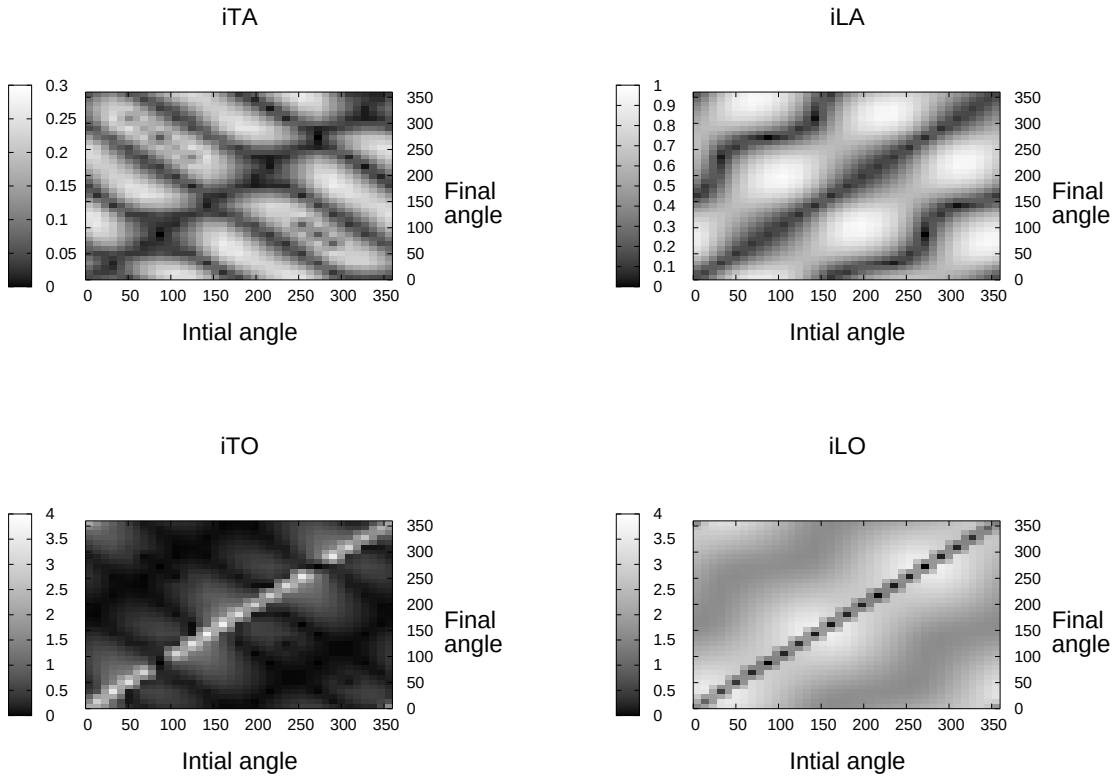

Figure 6.4: Intra–valley in–plane mode electron phonon coupling for iTA, LA, iTO and LO modes. For accoustic modes, the electron phonon interaction is equal to zero, if initial and final state are identical. All are given in values in eV/at.u.

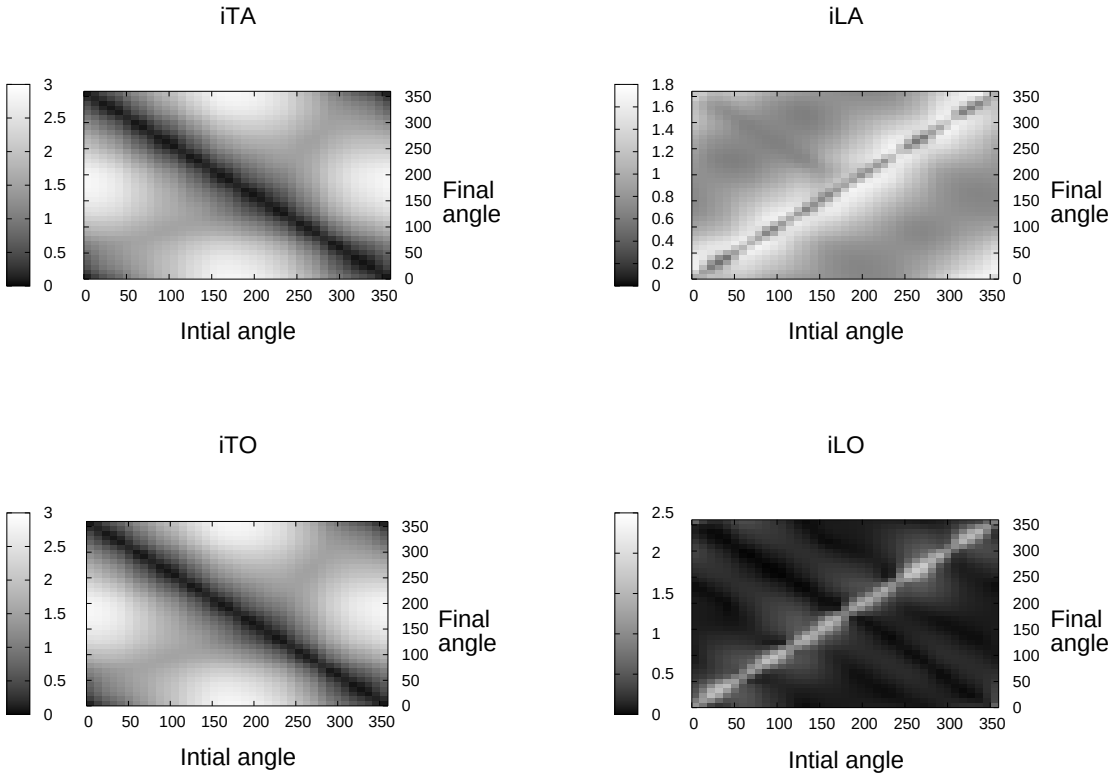

Figure 6.5: Inter valley accoustic and optic modes electron phonon coupling. All are given in values in eV/at.u.

Chapter 7

Raman intensity calculation in graphite and carbon nanotubes

Raman spectra are calculated using the electron photon and electron phonon matrix elements from previous chapters. Comparision of the calculated results with observed Raman spectra allows a phonon mode assignment. Using double resonance Raman spectroscopy, we fit the phonon dispersion to the observed Raman spectra. Here we propose that Raman spectroscopy is an alternative experimental technique for observing the phonon dispersion at the zone boundary. Analytical expressions for the phonon frequencies at high symmetry points are presented. These formulas can decouple the fitting procedure and are useful for understanding the sum rules of phonon frequencies. Localized phonon modes for a nanographite ribbon are calculated.

7.1 Resonant Raman intensity calculation

Here we give two examples for calculating results of resonance Raman spectra. Those are the G'–band for graphite and the G–band for SWNTs, which are two–phonon and one–phonon Raman processes, respectively. Other Raman active modes can be calculated similarly by the computer–programs.

The two–phonon, double resonance Stokes Raman mode appears in the spectrum at a position $\omega = \omega_1 + \omega_2$, where ω_1 and ω_2 are the phonon frequencies of the double resonance process described in detail in Sec. 4.3. In the double resonance processes, two phonons with opposite phonon wavevectors $\mathbf{q}$ and $-\mathbf{q}$ contribute to Raman spectra (see Fig. 7.1). The two phonons generally belong to different phonon branches ν and ν'. The intensity of the two–phonon Stokes process with phonons $\omega_1^{\nu}(-\mathbf{q})$ and $\omega_2^{\nu'}(\mathbf{q})$ from branches ν and ν' is calculated by

$$I(\omega_1+\omega_2) = \sum_i \left| \sum_{a,b,c,\nu,\nu'} \frac{M_{\mathrm{optA}}^{vc} M_{\mathrm{vibE}}^{cc,\nu} M_{\mathrm{vibE}}^{cc,\nu'} M_{\mathrm{optE}}^{cv}}{(E_{\mathrm{laser}} - E_{\mathrm{ai}} - i\gamma)(E_{\mathrm{laser}} - E_{\mathrm{bi}} - \hbar\omega_1^{\nu} - i\gamma)(E_{\mathrm{laser}} - E_{\mathrm{ci}} - \hbar\omega_1^{\nu} - \hbar\omega_2^{\nu'} - i\gamma)} \right|^2 . \tag{7.1}$$

The labels i, a, b and c for the initial and the three intermediate states, respectively are shown

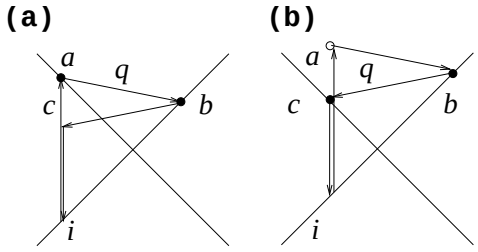

Figure 7.1: Two–phonon double resonance Stokes Raman processes. (a) and (b) give the two double resonant two–phonon processes with incident and scattered resonance, respectively. An electron is photo–excited from an initial state i to the conduction band state a. It then scatters by a phonon from a to b and scatters back to c by another phonon with opposite wavevector. It recombines at c by emitting a photon.

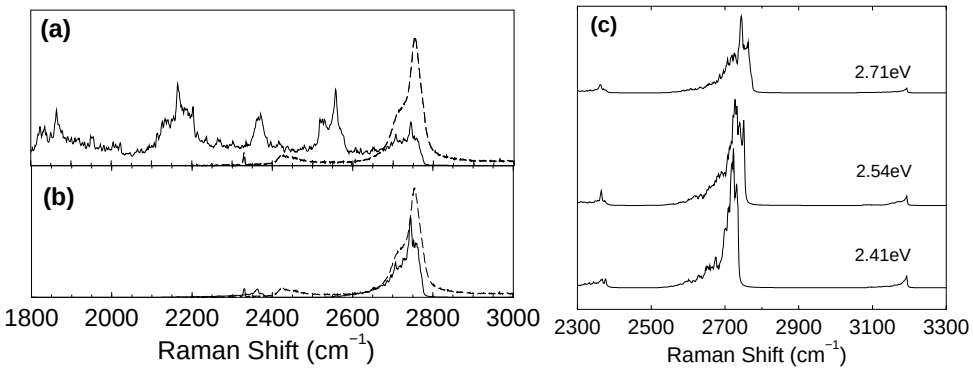

Figure 7.2: Calculated Raman spectra (solid line) compared to experimental spectra (dashed line) for $E_{\rm las} = 2.71$ eV. In (a) we set all matrix elements equal to unity. In (b) the electron phonon matrix elements are included. In (c) we show three features that appear in our calculation as a function of laser energy.

in Fig. 7.1. $E_{\rm ai}$, $E_{\rm bi}$ and $E_{\rm ci}$ are energies between the initial state and the three intermediate states and $E_{\rm laser}$ is the laser energy. Note that $E_{ai} = E_{ci}$, since we take the energy of the real state. The optical matrix elements for absorption and emission in Eq. (7.2) are $M^{vc}_{\rm optA}$ and $M^{cv}_{\rm optE}$, respectively. The absorption and emission matrix elements are given in in Eq. (5.9). The electron phonon matrix elements in Eq. (7.2) are given by $M^{cc,\nu}_{\rm vibE}$ and $M^{cc,\nu'}_{\rm vibE}$ for a photo–excited electron in the conduction energy band. The electron phonon interaction connects two conduction bands states. The formula to calculate the electron phonon matrix elements is given in Eq. (6.8). In Fig. 7.2 we show the calculated Raman intensity for the double resonance Raman process shown in Fig.7.1.

We briefly explain the computational procedure to calculate the Raman spectra shown in Fig. 7.2. To save a computational time, we only include the in–plane phonon branches, since from Chapter 6 we know that the out–of–plane phonon branches always give a coupling equal to zero. Thus we can decouple the dynamical matrix in Eq. (4.6) into an in–plane and an out–of–plane sub–matrix. The calculated results (solid line) reproduce well the experimental results (dashed

line). If all electron phonon matrix elements are taken to be constant, the integration of Eq. (7.2) becomes the JDOS. It is clear that the JDOS alone is not sufficient for understanding the Raman active frequencies. In Fig. 7.2(c) we show the calculated Raman spectra for three different laser energies, 2.41 eV, 2.54 eV and 2.71 eV. We obtain two peaks, of which the energetically higher peak at around $2700\,\mathrm{cm}^{-1}$ is dispersive and the lower peak is nearly at a constant frequency at about $2450\,\mathrm{cm}^{-1}$. This behaviour is observed by experiment and confirms the matrix element. The appearance of the two peaks at $2700\,\mathrm{cm}^{-1}$ and $2450\,\mathrm{cm}^{-1}$ comes from the two resonance conditions at $q = 2k$ and $q = 0$, respectively [55].

In order to do an integration over the 2D BZ, we first made a mesh for the electron and phonon states in the 2D BZ around K and K' points. The mesh for the phonon states is twice the size because in the double resonance process, the phonon wavevector q is given by $q = 2k$, where k is an electron wavevector. The wavevectors k and q are measured from K points as is described in Sec. 4.3. After specifying E_{laser}, we find k vectors on the mesh, that are resonant with the laser energy in a resonance window of $2 \times \omega_{\mathrm{max}}$, where $\omega_{\mathrm{max}} = 0.2$ eV is the maximum phonon energy. Hereafter we calculate resonant intermediate states on the inequivalent K point, by taking a loop over all phonon branches. Then we have another loop for the second phonon scattering back to the initial electron wavevector. This loop is also taken over all phonon branches. If we identify a resonant process according to Fig. 7.1, we evaluate Eq. (7.2). This process is repeated until the loop over initial and final electron states and the loops over the phonon modes are finished. The Fig. (7.2) was calculated with a mesh size of 150×150 for electrons and 300×300 for phonons for a small region around the K points.

In Fig. 7.3 we show the calculated result for the Raman intensity of SWNTs for the G–band as a function of chiral angle. LO and TO phonon modes are denoted by Boxes and circles. LO and TO phonon modes split th G–band into the higher (ω_G^+) and the lower (ω_G^-) frequency Raman peaks, respectively. Each symbol corresponds to a (n, m) SWNT. For a given chiral angle, the smaller diameter gives to the larger intensity per length of a SWNTs. From Fig. 7.3, we can see that LO peaks are relatively larger for small θ (zigzag nanotube) and that TO peaks are relatively smaller for large chiral angle (armchair nanotube). This results is consistent with the experimental results of isolated SWNT Raman spectra in which there is the chirality dependence of the relative G+ and G– band intensity as a function of (n, m) [72, 75].

7.2 Fitting of graphite phonon dispersions

With double resonance theory from Sec. 4.3, it is possible to assign a measured double resonant Raman peak to a given certain phonon branch. First we can generally decide if it is a Γ or K point phonon from the phonon frequency. Furthermore, double resonant Raman spectra, that are measured by a set of a few laser lines show a dispersive behaviour $\partial\omega/\partial E_{\mathrm{laser}}$ and the magnitude of the dispersion helps us to assign the phonon dispersion correctly.

7.2.1 Fitting procedure

Based on the double resonance theory, we can now correlate the laser energy to the double resonant phonon by the simple formula $q \sim 2k$. Together with observed Raman data ω_{obs}, this gives us data pairs $(q, \omega_{\mathrm{obs}})$, that can be used to fit the phonon dispersion relations of graphite. We use a simple steepest descent algorithm that minimizes a function of least square values

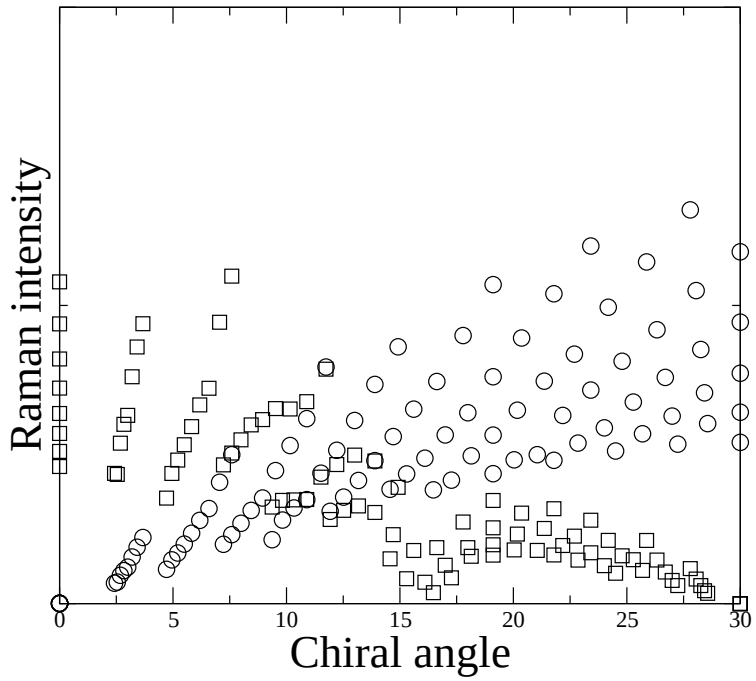

Figure 7.3: LO and TO Raman Intensity as a function of chiral angle. Boxes circles denote LO and TO phonons, respectively. Each symbol corresponds to the E_{22} resonance at for a (n, m) SWNT.

between experiment and calculated values

$$S(\mathbf{\Phi}) = \sum_{i}^{N} W(\nu_i, \mathbf{q}_i) \left[\omega_{\rm obs}(\nu_i, \mathbf{q}_i) - \omega_{\rm calc}(\mathbf{\Phi}, \nu_i, \mathbf{q}_i)\right]^2 . \tag{7.2}$$

If the function contains only a few minima, the most efficient algorithm is a conjugate gradient method which is known to converge much faster than steepest descent. However, the function shape that we try to minimize is not so suitable for a conjugate gradient method and thus we use a steepest descent method. The fitting procedure consists of minimizing the sum of squares S of the difference between observed and calculated phonon frequencies, $\omega_{\rm obs}(\nu_i, \mathbf{q}_i)$, respectively. The fitting parameters are the graphite force constants Φ_ℓ, with $\ell = 1 \ldots N_\Phi$. Here ν_i and $\mathbf{q}_i$ are the phonon branch and phonon wavevector, respectively. $N_{\rm data}$ and $W(\nu_i, \mathbf{q}_i)$, denote the number of data points and the weight of the $i-$ th data point, respectively. The condition that we have found force constants that give a minimum value of S is given by the set of N_Φ equations

$$\frac{\partial S}{\partial \Phi_\ell} = 0 \quad \text{with} \quad \ell = 1, \ldots, N_\Phi. \tag{7.3}$$

The equations are written as

$$\frac{\partial S}{\partial \Phi_\ell} = \sum_{i} 2W(\nu_i, \mathbf{q}_i) \left[\omega_{\rm obs}(\nu_i, \mathbf{q}_i) - \omega_{\rm calc}(\mathbf{\Phi}, \nu_i, \mathbf{q}_i)\right] \frac{\partial \omega_{\rm calc}(\mathbf{\Phi}, \nu_i, \mathbf{q}_i)}{\partial \Phi_\ell} = 0. \tag{7.4}$$

Since the calculated phonon frequencies are the root of the eigenvalues of the dynamical matrix, we do not have an analytical expression at general $\mathbf{q}$ points. However, we can expand the phonon frequencies for force constants $\mathbf{\Phi}$ into a Taylor series around $\mathbf{\Phi}_0$ as

$$\omega_{\mathrm{calc}}(\mathbf{\Phi}, \nu_i, \mathbf{q}_i) = \omega_{\mathrm{calc}}(\mathbf{\Phi}_0, \nu_i, \mathbf{q}_i) + \sum_{k=1}^{N_\Phi} \frac{\partial \omega_{\mathrm{calc}}(\mathbf{\Phi}, \nu_i, \mathbf{q}_i)}{\partial \Phi_k} \cdot (\Phi_k - \Phi_{k0}) + O\left\{(\Phi_k - \Phi_{k0})^2\right\}. \quad (7.5)$$

We then substitute the expansion of phonon frequencies of Eq. (7.5) into Eq. (7.4). The following equation only holds to linear order in a small region around $\mathbf{\Phi}_0$.

$$\begin{aligned} & \frac{\partial S}{\partial \Phi_\ell} \\ = & \sum_i 2W(\nu_i, \mathbf{q}_i) \left[\omega_{\mathrm{obs}}(\nu_i, \mathbf{q}_i) - \omega_{\mathrm{calc}}(\mathbf{\Phi}_0, \nu_i, \mathbf{q}_i) - \sum_k \frac{\partial \omega_{\mathrm{calc}}(\mathbf{\Phi}, \nu_i, \mathbf{q}_i)}{\partial \Phi_k} (\Phi_k - \Phi_{k0}) \right] \times \\ & \frac{\partial \omega_{\mathrm{calc}}(\mathbf{\Phi}, \nu_i, \mathbf{q}_i)}{\partial \Phi_\ell} \\ = & 0. \end{aligned}$$

For evaluation it is convenient to write this equation in a more compact form as

$$A \cdot \Delta\mathbf{\Phi} = \mathbf{c}. \quad (7.6)$$

Here the matrix A and the vector $\mathbf{c}$ are defined as

$$\begin{aligned} & A_{\ell k} = \sum_i 2W(\nu_i, \mathbf{q}_i) \sum_{k=1}^{N_\Phi} \frac{\partial \omega_{\mathrm{calc}}(\mathbf{\Phi}, \nu_i, \mathbf{q}_i)}{\partial \Phi_\ell} \frac{\partial \omega_{\mathrm{calc}}(\mathbf{\Phi}, \nu_i, \mathbf{q}_i)}{\partial \Phi_k} \\ & \text{and} \\ & c_\ell = \sum_i 2W(\nu_i, \mathbf{q}_i) \left[\omega_{\mathrm{obs}}(\nu_i, \mathbf{q}_i) - \omega_{\mathrm{calc}}(\mathbf{\Phi}_0, \nu_i, \mathbf{q}_i) \right] \frac{\partial \omega_{\mathrm{calc}}(\mathbf{\Phi}, \nu_i, \mathbf{q}_i)}{\partial \Phi_\ell} = 0. \end{aligned} \quad (7.7)$$

The problem is thus reduced to finding the root of a linear equation. As a solution we obtain $\Delta\mathbf{\Phi} = \mathbf{\Phi} - \mathbf{\Phi}_0$. All partial derivatives in Eq. (7.7) are for $\mathbf{\Phi} = \mathbf{\Phi}_0$. After solving Eq. (7.6) for $\Delta\mathbf{\Phi}$, we put $\mathbf{\Phi}_0 \to \mathbf{\Phi}_0 + s\Delta\mathbf{\Phi}$, where s is a small value in the order of $s = 0.1$ for a reasonable, not–too–fast convergence. Then we solve again, taking the derivatives at the new $\mathbf{\Phi}_0$. This steps are repeated until the values of S stops decreasing. Then we have found a local minimum and the process is stopped.

7.2.2 Numerical fitting of the phonon dispersion relations

To get the input data for our force constant fitting program, we went through a number of published results in the field and and extracted dispersive Raman features. Using the the double resonance theory from Sec. 4.3, we can assign them to an electron wavevector. In this manner, we can obtain many data points shown in Table 7.1. In Fig. 7.4, the fitted phonon dispersion relations are shown by solid lines. The dashed lines are the phonon dispersion relations that are fitted to inelastic neutron scattering data. Solid dots, solid square, cross, and triangle are Raman data of highly ordered pyrolytic graphite (HOPG)[78, 79], single–wall carbon nanotube

Table 7.1: Observed double resonance Raman peaks.[76]

Mode assignment	Theoretical value $\omega, [\partial\omega/\partial E_{\rm laser}]$ in $\rm cm^{-1}$	Experimental value $\omega, [\partial\omega/\partial E_{\rm laser}]$ in $\rm cm^{-1}$
oTA(Γ,q=2k)	45 [26]	–
iTA(Γ,q=2k)	300 [121]	288[129]
LA (Γ,q=2k)	430 [173]	453[216]
oTA (K,q=2k)	500 [-28]	–
oTO (Γ,q=2k)	640 [26]	–
oTO (Γ,q=2k)	850 [–5]	865[13]
oTO (Γ,q=0)	855 [0]	860[0]
iTA (K,q=2k)	900 [-58]	820[-57],865[-53],1084[-74],1094[-77]
iTA (K,q=0)	1000 [0]	970[129],1060[0],1081[22]
LA (K,q=2k)	1250 [–5]	–
LA/LO (K,q=0)	1260 [0]	–
LO (K,q=2k)	1350 [48]	1352[43],1345[50],1354[46]
iTO (K,q=2k)	1450 [-11]	1480[-83]
iTO (K,q=0)	1490 [0]	1500[–]
iTO (Γ,q=2k)	1555 [-20]	–
iTO/LO (Γ,q=0)	1580 [0]	1582[0]
LO (Γ,q=2k)	1600 [4]	1622[0],1623[0],1623[9]

(SWNT)[54], HOPG and SWNT[80] and graphite whisker(GW) [81], respectively. In order to improve the convergence of the iterative fitting, we have also used inelastic neutron scattering data (open circles in Fig. 7.4) in the low frequency region near the M point that were used in the previous fitting [4]. The data points at the Γ point are taken from first-order Raman scattering, and those at the K point are taken from dispersionless weak features which are assigned to $q = 0$ singular phonon modes. When we compare the phonon dispersion of the solid and dotted lines, only the higher frequency region around the K point is different. In the lower frequency region, the dispersive Raman data are in good agreement with the previous phonon dispersion relations. There are dispersive Raman data around $1050\,\rm cm^{-1}$ which shift the longitudinal acoustic (LA) mode to a lower frequency region. In the phonon dispersion relations obtained by inelastic neutron data, this LA mode is highly anisotropic around the K point. Since the double resonance theory gives the phonon frequencies in terms of the distance from the K (or the Γ) point, we cannot determine the anisotropy of the phonon branches around the K point. However no experimental inelastic neutron data are available near the K point, and the lowering of the LA curve from the Γ to the K point seems to be in good agreement with experiment.

The second highest phonon dispersion branch around the K point gives the D-band frequency. The fitted phonon dispersion in Fig. 7.4 gives a smaller slope for the phonon dispersion relation than that given by the previous one. It should be mentioned that we excluded some experimental points for higher $E_{\rm laser}$ values on the K–M line. Along the K–M line the anisotropy of the phonon dispersion is large compared with the K–Γ line. Since our double resonance model calculation only gives the distance of the q vector, which is the $|q|$ value from the K point, the calculation might not be adequate for the fitting procedure for larger laser energies if there is a large anisotropy ($\sim 30\rm cm^{-1}$) in the phonon dispersion relations for large $|q|$. Such an anisotropy is known as the trigonal warping effect and the circles are modified to show an approximate triangular shape. In this case, since the edge section which gives a singular $|q|$ is given around

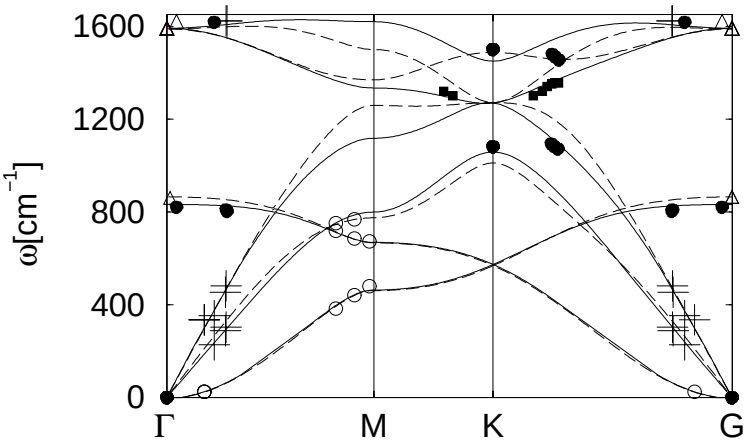

Figure 7.4: The fitted phonon dispersion relations (solid lines) for 2D graphite. The dashed lines are the previous phonon dispersion relation fitted to inelastic neutron scattering measurements [4, 77, 38]. Solid dots, solid square, cross, and triangle are Raman data of highly ordered pyrolytic graphite (HOPG) [78, 79], single wall carbon nanotube (SWNT) [54], HOPG and SWNT [80] and graphite whisker(GW) [81], respectively. Open circles are inelastic neutron scattering data for graphite [4].

the K–Γ line, the treatment that we give for the experimental points on the K–Γ line is justified. When D-band phonon data become available for smaller laser energies, it will be nice to have more reliable data around the K point (or the Γ point), which can then be used in a future study.

For use in future studies, we list in Table 7.2 an updated summary of the twelve fitted force constants in which $\Phi_r^{(n)}$, $\Phi_{ti}^{(n)}$, and $\Phi_{to}^{(n)}$ denote, respectively, the force constants of the radial, in-plane, and out-of-plane modes for the n-th nearest neighbors ($n = 1, \ldots, 4$). When we compare Table 7.2 with the previous force constants in parentheses [4], the radial force constants for the second and third nearest neighbors of Table 7.2 become relatively weak, and the tangential force constants become relatively hard, reflecting some modification to the values of the optical phonon modes.

Table 7.2: Calculated force constant parameters for 2D graphite in units of 10^4dyn/cm [38]. Here the subscripts r, ti, and to refer to radial, transverse in-plane and transverse out-of-plane, respectively. The previous force constants are listed in parentheses [4].

Radial			Tangential		
$\phi_r^{(1)} =$	40.37(36.50)	$\phi_{ti}^{(1)} =$	25.18(24.50)	$\phi_{to}^{(1)} =$	9.40(9.82)
$\phi_r^{(2)} =$	2.76(8.80)	$\phi_{ti}^{(2)} =$	2.22(−3.23)	$\phi_{to}^{(2)} =$	−0.08(−0.40)
$\phi_r^{(3)} =$	0.05(3.00)	$\phi_{ti}^{(3)} =$	−8.99(−5.25)	$\phi_{to}^{(3)} =$	−0.06(0.15)
$\phi_r^{(4)} =$	1.31(−1.92)	$\phi_{ti}^{(4)} =$	0.22(2.29)	$\phi_{to}^{(4)} =$	−0.63(−0.58)

7.3 Analytic expressions for the phonon modes

If we can get some relationship between the force constants and phonon frequencies at some high symmetry points, they can be used for fitting the force constants to experimental data. Force constant sum rules are conditions which give a zero phonon frequency for the translational and rotational motion at $q = 0$. In the Appendix we show how to obtain the analytical form of the dynamical matrix at Γ, M and K points. The zero phonon frequency condition follows directly from the special shape of the matrix at $q = 0$. This condition is included by generating the force constant tensors through rotation of one initial force constant tensor. Another relationship is related to the eigenstates at high symmetry points where the phonon frequencies are given by a simple formula for the force constants, which decouples the problem into a smaller number of fitting parameters. Although we do not directly use these equations in the numerical fitting program, they will be useful for understanding the various phonon dispersion relation for sp^2 carbons.

Here we show some analytical results of the phonon eigenmodes for 2D graphite which are analytically determined as functions of the twelve force constants. Since there are two carbon atoms A and B in the unit cell, we expect an eigenfunction with six components, i.e. $(A_x, A_y, A_z, B_x, B_y, B_z)$ where A_x is related to the displacement in the x axis. An analytical calculation of the diagonalization of the 6×6 dynamical matrix is solved by *Mathematica* (see Appendix) at the three high symmetry points of 2D graphite BZ (Γ, K and M). For the six eigenvalues, three are acoustic phonon modes with zero frequency which are independent of the force constants. The other three eigenvalues are are singly and doubly degenerate phonon modes, which is consistent with group theoretical arguments [82]. Their frequency depends on the force constants but the double degeneracy of optical modes is independent of the force constants we use and a result of symmetry. Thus we get twelve formulae, which consist of eight in–plane and four out–of–plane modes. Since in-plane and out-of-plane phonon modes are orthogonal to each other in the graphene plane, the corresponding eigenvalues are given, respectively, in terms of in-plane and out-of-plane force constants. In Table 7.3, we list the corresponding phonon frequencies and normal modes which are obtained by the set of force constants fitted to the neutron data.

For the Γ point, the in-plane tangential phonon frequencies (LO and TO) ω_{i1} and ω_{i2} are degenerate at $1589\,\mathrm{cm}^{-1}$, which is known as E_{2g}. This degeneracy comes from the facts that graphite is not an ionic crystal and that there is a three-fold symmetry around each carbon atom [4]. For all phonon modes at the Γ point, all A (or B) atoms in the unit cells of 2D graphite move in the same phase, and therefore no second-nearest neighbor force constants, $\Phi^{(2)}$, appear in the expressions Eq. (7.8). Here, when we consider an A(B) atom for the central atom, the first, the third, and the fourth nearest neighbors are B(A) atoms, while the second nearest neighbors are A(B) atoms.

Although we have twelve relations between non-zero phonon frequencies at the high symmetry points and twelve unknown force constants, we can not solve directly for all of the twelve force constants. The number of independent equations of the twelve equations is nine, which is understood in terms of the rank of the matrix for the twelve simultaneous equations. This means that three dependent equations between phonon frequencies at the different symmetry

points exist. After some analytic calculation, we get the following three relations:

$$\omega_{i2}(K)^2 + \omega_{i3}(K)^2 - 2\omega_{i1}(K)^2 = 0, \qquad 2\omega_{i1}(\Gamma)^2 - 9\sum_{j=1}^{4}\omega_{ij}(M)^2 + 32\omega_{i1}(K)^2 = 0,$$

$$\text{and} \quad \omega_{o1}(\Gamma)^2 - 9\sum_{j=1}^{2}\omega_{oj}(M)^2 + 16\omega_{o1}(K)^2 = 0.$$

These equations are independent of the set of force constants and thus they are useful for estimating the data which yield the phonon dispersion relations over the whole BZ of 2D graphite.

In Fig. 7.5, we show examples of the eigenstates for the in-plane optic phonon modes for the (a) $\omega_{i2}(K)$ and (b) $\omega_{i2}(M)$ whose phonon frequencies are 1272 and 1369cm^{-1}, respectively. Starting from a lattice point of B atom denoted by solid circles in Fig. 7.5, the vibration of other atoms are given by multiplying the factor $\exp(iqR)$ to the complex eigenfunctions of the unit cell of 2D graphite as shown in Table 7.3 when we shift the vibration by a lattice vector R. For the q vectors at the K and M points, the vibration has a periodicity, respectively, of the $\sqrt{3}\times\sqrt{3}$ and 2×2 super-cells of 2D graphite, which are shown by dotted lines in Fig. 7.5. In Table 7.3 we show the eigenfunctions of four in-plane modes and two out-plane modes with calculated eigenvalues at $\Gamma = (0,0)$, $K = (2\pi/\sqrt{3}a, 2\pi/3)$ and $M = (2\pi/\sqrt{3}a, 0)$. The eigenvectors have six components: x, y, z for the A and B atoms of 2D graphite: $\{(A_x, A_y, A_z), (B_x, B_y, B_z)\}$. For the K point modes, the in-plane tangential optic phonon modes, (ω_{i2}, ω_{i3}), and the tangential out-of-plane modes (ω_{o1}, ω_{o2}) are degenerate as is shown in Eq. (7.9). At the K point, either the A or B atoms move in the eigenfunction, while the other atoms do not move. All eigenvectors at the symmetry point show the required symmetry between the A and B atoms, in which the normal modes for each atom are normalized to unity. All vectors have a length of unity, and the real part of the eigenfunction corresponds to the vectors shown in Fig. 7.5. A similar situation appears, also, in the case of the electronic wavefunctions, where either the A or B components of the Bloch functions in the eigenfunctions have the finite value and the other components become zero at the K point. In the 2D BZ, we have two inequivalent K and K' points, and three inequivalent M, M$'$ and M$''$ points. The corresponding eigenfunctions are given by the rotational operations of 2D graphite in k-space.

Table 7.3: Eigenvectors R_A, R_B and frequencies in cm^{-1} are listed for in-plane (ω_i) and out-of-plane (ω_o) phonon modes at the $\Gamma = (0,0)$, $K = (2\pi/\sqrt{3}a, 2\pi/3a)$ and $M = (2\pi/\sqrt{3}a, 0)$, points.

	Γ		K		M	
Mode	freq.	$\{R_A, R_B\}$	freq.	$\{R_A, R_B\}$	freq.	$\{R_A, R_B\}$
ω_{i1}	1589	{(1,0,0),(-1,0,0)}	1487	{(α,iα,0),(-i,-1,0)}	1500	{(γ,0,0),(-1,0,0)}
ω_{i2}	1589	{(0,1,0),(0,-1,0)}	1272	{(0,0,0),(-i,1,0)}	1369	{(0,γ,0),(0,1,0)}
ω_{i3}	0	{(1,0,0),(1,0,0)}	1272	{(i,1,0),(0,0,0)}	1259	{(γ,0,0),(1,0,0)}
ω_{i4}	0	{(0,1,0),(0,1,0)}	1011	{(α,iα,0),(i,1,0)}	775	{(0,γ,0),(0,-1,0)}
ω_{o1}	865	{(0,0,1),(0,0,-1)}	568	{(0,0,1),(0,0,0)}	667	{(0,0,γ),(0,0,1)}
ω_{o2}	0	{(0,0,1),(0,0,1)}	568	{(0,0,0),(0,0,1)}	461	{(0,0,γ),(0,0,-1)}

$\alpha = e^{-\pi i/6}$, $\gamma = e^{2\pi i/3}$

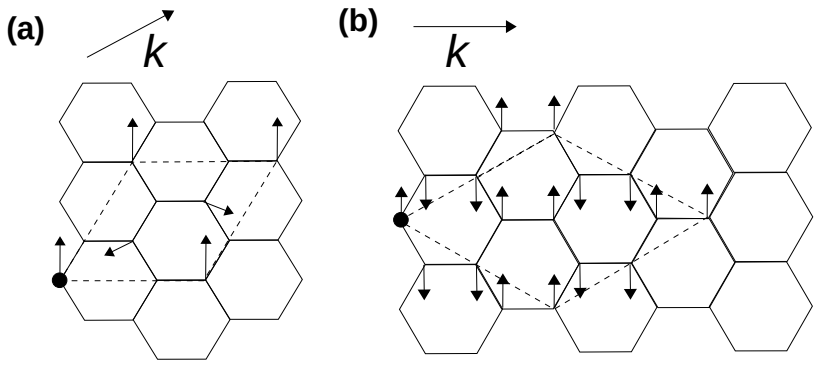

Figure 7.5: (a) Eigenvectors $\{(0,0,0),(-i,1,0)\}$ of $\omega_{i2}(K)$=1272 cm^{-1}, and (b) eigenvectors {(0,γ,0),(0,1,0)} of $\omega_{i2}(M)$ = 1369 cm^{-1}. The dashed diamond of each figure is the super–cell for the K and M points. The arrows outside of the hexagonal lattice show the directions of the k vectors.

Finally we show the analytic expressions of eigenvalues of 2D graphite obtained by the *Mathematica* program listed in appendix A. Analytic expressions for the phonon frequencies for the 2D graphite phonon modes are given here for the three high symmetry points in graphite. $\mathcal{C}$=1.18928 $(\mathrm{cm}^{-1}/\mathrm{dyn})^{1/2}$ is the conversion constant from a force constant in dyn/cm to a phonon frequency in cm^{-1}. The phonon frequencies at the Γ point are

$$\omega_{i1}(\Gamma) = \mathcal{C}\sqrt{3\Phi_r^{(1)} + \Phi_{ti}^{(1)} + \Phi_r^{(3)} + \Phi_{ti}^{(3)} + 2\Phi_r^{(4)} + 2\Phi_{ti}^{(4)}}, \quad \omega_{o1}(\Gamma) = \mathcal{C}\sqrt{6\Phi_{to}^{(1)} + 6\Phi_{to}^{(3)} + 12\Phi_{to}^{(4)}}. \tag{7.8}$$

The phonon frequencies at the K point are

$$\begin{aligned} &\omega_{i1}(K) = \sqrt{0.5(\omega_i(\Gamma)^2 + 9\mathcal{C}^2(\Phi_r^{(2)} + \Phi_{ti}^{(2)}))}, \quad \omega_{i2}(K) = \sqrt{\omega_{i1}(K)^2 - \Delta}, \quad \text{and} \\ &\omega_{i3}(K) = \sqrt{\omega_{i1}(K)^2 + \Delta}, \qquad\qquad \omega_{o1}(K) = \sqrt{9\mathcal{C}^2\Phi_{to}^{(2)} + 0.5\omega_o^2(\Gamma)}, \end{aligned} \tag{7.9}$$

with:

$$\Delta = \mathcal{C}^2\left\{1.5(\Phi_r^{(1)} - \Phi_{ti}^{(1)} + \Phi_r^{(3)} - \Phi_{ti}^{(3)}) - 2.79(\Phi_r^{(4)} - \Phi_{ti}^{(4)})\right\}.$$

The phonon frequencies at the M point are

$$\begin{aligned} \omega_{i1}(M) &= \mathcal{C}\left(2\Phi_r^{(1)} + 6\Phi_r^{(2)} + 2\Phi_{ti}^{(2)} + 3\Phi_r^{(3)} + 3\Phi_{ti}^{(3)} + 2.29\Phi_r^{(4)} + 1.71\Phi_{ti}^{(4)}\right)^{1/2}, \\ \omega_{i2}(M) &= \mathcal{C}\left(\Phi_r^{(1)} + 3\Phi_{ti}^{(1)} + 6\Phi_r^{(2)} + 2\Phi_{ti}^{(2)} + 3.71\Phi_r^{(4)} + 4.29\Phi_{ti}^{(4)}\right)^{1/2}, \\ \omega_{i3}(M) &= \mathcal{C}\left(3\Phi_r^{(1)} + \Phi_{ti}^{(1)} + 2\Phi_r^{(2)} + 6\Phi_{ti}^{(2)} + 4.29\Phi_r^{(4)} + 3.71\Phi_{ti}^{(4)}\right)^{(1/2)}, \\ \omega_{i4}(M) &= \mathcal{C}\left(2\Phi_{ti}^{(1)} + 2\Phi_r^{(2)} + 6\Phi_{ti}^{(2)} + 3\Phi_r^{(3)} + 3\Phi_{ti}^{(3)} + 1.71\Phi_r^{(4)} + 2.29\Phi_{ti}^{(4)}\right)^{(1/2)}, \\ \omega_{o1}(M) &= \mathcal{C}\sqrt{4\Phi_{to}^{(1)} + 8\Phi_{to}^{(2)} + 8\Phi_{to}^{(4)}}, \\ \text{and} \quad \omega_{o2}(M) &= \mathcal{C}\sqrt{2\Phi_{to}^{(1)} + 8\Phi_{to}^{(2)} + 6\Phi_{to}^{(3)} + 4\Phi_{to}^{(4)}}. \end{aligned} \tag{7.10}$$

It is interesting to see the result in Eq. (7.9), that the degenerate eigenvalues are expressed by eigenvalues at the Γ points and the second nearest neighbor force constant. The reason why a second nearest neighbor force constant appears here is that the direction of movement of the two second nearest neighbors is not parallel. At the M point, both the A and B atoms move in the eigenfunctions differently, and thus all force constants appear mixed and all eigenstates are not degenerate as is shown in Eq. (7.10).

7.4 Localized phonon modes at the graphite edge

Before finishing this chapter, let us briefly mention the localized phonon mode of a nanographite ribbon, since a new experiment is recently reported and it is closely related to the present thesis. As we have seen in Sec. 3.4, the zigzag edge structure of nanographite ribbons gives rise to a special electronic band, that is entirely localized on the edge. The recent progress in Raman spectroscopy with a high spatial resolution [83], enables us to probe the local Raman spectra experimentally, which in turn are related to the local phonon density of states (LPDOS). Near field Raman spectroscopy is done with a sharp metal tip that enhances the field locally close to its position. By moving the metal tip, we can investigate the Raman signal as a function of position with spacial resolution of a few nanometers. Only atoms that are close to the metal tip are contributing to the measured signal. This technique is applied when we want to characterize defects in the crystal structure such as edges, junctions between different chiralities or point defects. Here we consider the simplest such defect, the edge of a nanographite ribbon. We calculate the LPDOS close to the edge of a ribbon. The ribbon we used for this purpose was selected to have sufficient width in order to obtain the result for a graphite plane, if we were to measure the LPDOS in the middle of the ribbon. We consider the nanographite ribbon shown in Fig. 7.6. It is in the xy plane and has its longitudinal direction along x axis. We define the LPDOS for a nanographite ribbon at position d and phonon frequency ω by

$$\mathrm{LPDOS}(d,\omega) = \sum_{i,q,\nu} S_i^*(q) S_i(q) \delta(R_{iy} - d) \delta\{\omega - \omega_\nu(q)\}. \tag{7.11}$$

Here we take a sum over all eigenfunctions $S_i(q)$ at wavenumber q and atom number i that are have an y coordinate equal to d and an frequency equal to ω. These conditions are expressed by the δ function and are relaxed slightlty in the numerical calculation, where we take a width $\Delta d = 0.3$ nm and a frequency width $\Delta\omega = 10\mathrm{cm}^{-1}$. The LPDOS calculated according to Eq. (7.11) for the ribbon in Fig 7.6(a) is shown in Fig. 7.6(b). It is clear from Fig. 7.6(b) that the LPDOS strongly depends on the distance from the edge. If we are close to the edge we see localized phonon modes with a frequency of about 890 cm^{-1} and 1360 cm^{-1}. It is well known from experiment that these phonon modes exist at defects and one such defect is an edge. In this way, by solving the ekectron and phonon states, we can predict Raman spectra for any geometry made of hexagonal graphite lattice structure.

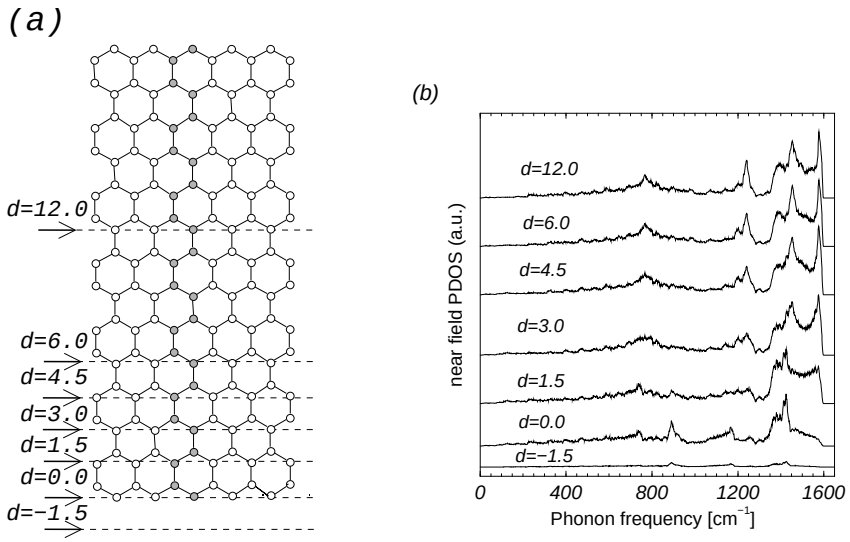

Figure 7.6: (a) The ribbon for which we calculate local in–plane phonon density of states (LPDOS) for near field Raman spectra. The distances in units of a_0 at which we consider the LPDOS are shown by arrows. The unit cell is marked by shaded atoms. (b) The calculated local phonon density of states (LPDOS). A Gaussian broadening for the near field Raman tip is assumed. The FWHM was chosen to be a_0.

Chapter 8

Summary

In summary, we have calculated the optical response and Raman spectra for graphite and single–wall carbon nanotubes (SWNTs) and developed computer programs for determining the phonon dispersion relations of graphite by double resonance Raman spectroscopy. Such a calculation involves calculating the electron and the phonon dispersion relations and also a calculation of the electron–photon and the electron–phonon interaction matrix elements for resonant electron wavevectors $\mathbf{k}$ in the Brillouin zone (BZ) of graphite and SWNTs. For the dispersion relations of electrons and phonons, a simple tight–binding method has been adopted. The tight–binding method relies on parameters that are usually fitted to experiments or are calculated by an ab–initio calculation. In the present thesis, we used tight–binding parameters for electrons fitted to optical measurements and force constants for phonons fitted to neutron scattering and double resonance Raman data.

In order to evaluate resonant Raman intensities, we calculated both, the electron–photon and the electron–phonon matrix elements. In the case of graphite, we found that there is a node in the optical absorption in $\mathbf{k}$ space and the position of the node changes with changing the polarization direction of light. This effect was recently observed in nanographite ribbon, where the electronic states are quantized due to the reduced dimensions along the ribbon width. If the electron–photon selection rule gives zero coupling for an allowed electronic state in nanographite, a dramatic change in the Raman spectra has been observed. A direct experimental observation of a node for graphite has not yet been achieved and might be possible by angle resolved photoemission spectroscopy. For SWNTs, from the selection rules, which we obtain from the matrix elements, we can give an explanation concerning the appearance of Raman data in the gap region of the Kataura plot for parallel polarization. Observation of perpendicular polarized light also allows us to determine the asymmetry in the valence and conduction band energies with respect to the Fermi energy. From such an observation, the wavefunction overlap parameter can be deduced.

The matrix elements for parallel and perpendicular polarization also give the strengths of the optical transitions. Particularly, the maximum value of the matrix element occurs at the van Hove singularities in the joint density of electronic states. We also predict that there is no photoconductivity in the metallic bands of armchair SWNTs.

Electron–phonon matrix element is calculated by calculating atomic deformation potential vectors. The calculated results shows for the first time, a strong $\mathbf{k}$ dependent matrix elements, which is relevant to chirality dependent Raman intensity of SWNTs. Furthermore, we calcu-

lated double resonant Raman spectra of G'–band (two–phonon Raman process) and G–band (one–phonon Raman process) as a function of laser energy and as a function of chiral angle, respectively. In this calculation, we show a non–dispersive feature at 2450 cm^{-1} which originates from a $q = 0$ double resonance condition. This feature is reproduced for the first time by calculation. As for G–band, chirality dependent relative intensity for G^+ and G^- bands is shown to be consistent with experimental observation of Raman spectra for isolated SWNTs. A new method that determines the phonon dispersion relations of graphite by double resonance Raman spectroscopy is proposed in this thesis. These technique is sensitive to phonons close to the BZ boundary and a small crystal size (≈ 1 μm) is sufficient for observing Raman spectra. Since the double resonance Raman spectroscopy gives us a large peak from phonons close to the BZ boundary, the newly developed method gives us accurate phonon dispersions near zone boundary.

Appendix A

Programs

In this Appendix, we show Mathematica programs. In Sec. A.1 we show the program to calculate the phonon dispersion of graphite analytically at the high symmetry points and numerically at a general k point. In Sec. A.2 the program to calculate π electron energy dispersion relations of a nanographite ribbon is shown. In Sec. A.3 a program to calculate σ and π electron energy dispersion relations of graphite is given. These programs are useful for future work.

A.1 Analytical solution for phonons

The output of the program[1] is the analytical expression at Γ point and the numerical solution and is shown in Fig. A.1. Other analytical solutions are obtained by changing the k point variable in the program. The Eqs. (7.8),(7.10) and (7.9) were calculated with this program. The program first defines a the force constant tensors `KAA` and `KAB` etc. for generating dynamical matrix according to Eq. (4.6) which is stored in `DD`. Then the eigenvalues and eigenvectors are calculated analytically at the symmetry points and numerically at general k points. The input which is relevant for the numerical calculation are the force constants stored in variables `phir1,...,phito4` and can be changed by the user. In Fig. A.1 we show the output of this program.

```
(* See R.Saito Phys.Prop.Carbon Nanotubes page 163 *)
Clear[phir1, phiti1, phir2, phiti2, phir3, phiti3, phir4, phiti4, phito1,
  phito2, phito3, phito4]
mul = 118.928;
"2nd shell AA pairs (six pairs)";
Raa22 = {{-1.5, Sqrt[3]/2}};
Raa23 = {{0, Sqrt[3]}};
Raa2 = {{1.5, Sqrt[3]/2}};
Raa3 = {{1.5, -(Sqrt[3]/2)}};
Raa24 = {{0, -Sqrt[3]}};
Raa21 = -{{1.5, Sqrt[3]/2}};
"2nd shell BB pairs (six pairs)";
Rbb2 = {{-1.5, Sqrt[3]/2}};
Rbb21 = {{0, Sqrt[3]}};
Rbb22 = {{1.5, Sqrt[3]/2}};
Rbb23 = {{1.5, -(Sqrt[3]/2)}};
Rbb24 = {{0, -Sqrt[3]}};
Rbb3 = -{{1.5, Sqrt[3]/2}};
```

[1] `mathematica/thesis/phon_gamm.nb`

```
"nearest pairs AB (3 pairs)";
Rab2 = {{-0.5, Sqrt[3]/2}};
Rab1 = {{1, 0}};
Rab3 = -{{0.5, Sqrt[3]/2}};
"nearest pairs BA (3 pairs)";
Rba1 = {{-1, 0}};
Rba2 = {{0.5, Sqrt[3]/2}};
Rba3 = {{0.5, -(Sqrt[3]/2)}};
"3rd shell AB 3 pairs";
Rab31 = {{-2, 0}};
Rab32 = {{1, Sqrt[3]}};
Rab33 = {{1, -Sqrt[3]}};
"3rd shell BA 3 pairs";
Rba31 = {{2, 0}};
Rba32 = {{-1, Sqrt[3]}};
Rba33 = {{-1, -Sqrt[3]}};
"4th shell AB 6 pairs";
Rab41 = {{5/2, Sqrt[3]/2}};
Rab42 = {{5/2, -(Sqrt[3]/2)}};
Rab43 = {{-(1/2), -((3*Sqrt[3])/2)}};
Rab44 = {{-2, -Sqrt[3]}};
Rab45 = {{-2, Sqrt[3]}};
Rab46 = {{-(1/2), (Sqrt[3]*3)/2}};
"4th shell BA 6 pairs";
Rba41 = {{2, -Sqrt[3]}};
Rba42 = {{1/2, (1/2)*(-Sqrt[3])*3}};
Rba43 = {{-(5/2), -(Sqrt[3]/2)}};
Rba44 = {{-(5/2), Sqrt[3]/2}};
Rba45 = {{1/2, (3*Sqrt[3])/2}};
Rba46 = {{2, Sqrt[3]}};
"*************************************************************************\
**";
U[a_] = {{Cos[(2*Pi*a)/360], Sin[(2*Pi*a)/360], 0},
    {-Sin[(2*Pi*a)/360], Cos[(2*Pi*a)/360], 0}, {0, 0, 1}};
"*************************************************************************\
**********";
"the three force tensors for AB interaction in the 1st shell";
KAB1[phir1_, phiti1_, phito1_] = {{phir1, 0, 0}, {0, phiti1, 0},
    {0, 0, phito1}};
KAB2[phir1_, phiti1_, phito1_] = Inverse[U[120]] .
    KAB1[phir1, phiti1, phito1] . U[120];
KAB3[phir1_, phiti1_, phito1_] = Inverse[U[120]] .
    KAB2[phir1, phiti1, phito1] . U[120];
"*************************************************************************\
**********";
"the three force tensors for BA interaction in the 1st shell";
KBA2[phir1_, phiti1_, phito1_] = Inverse[U[60]] .
    KAB1[phir1, phiti1, phito1] . U[60];
KBA1[phir1_, phiti1_, phito1_] = Inverse[U[120]] .
    KBA2[phir1, phiti1, phito1] . U[120];
KBA3[phir1_, phiti1_, phito1_] = Inverse[U[120]] .
    KBA1[phir1, phiti1, phito1] . U[120];
"*************************************************************************\
**********";
"the six force tensors for AA interaction in the 2nd shell";
KAA2S[phir2_, phiti2_, phito2_] = {{phir2, 0, 0}, {0, phiti2, 0},
    {0, 0, phito2}};
KAA2[phir2_, phiti2_, phito2_] = Inverse[U[30]] .
    KAA2S[phir2, phiti2, phito2] . U[30];
KAA23[phir2_, phiti2_, phito2_] = Inverse[U[60]] .
    KAA2[phir2, phiti2, phito2] . U[60];
KAA22[phir2_, phiti2_, phito2_] = Inverse[U[60]] .
    KAA23[phir2, phiti2, phito2] . U[60];
```

```
KAA21[phir2_, phiti2_, phito2_] = Inverse[U[60]] .
    KAA22[phir2, phiti2, phito2] . U[60];
KAA24[phir2_, phiti2_, phito2_] = Inverse[U[60]] .
    KAA21[phir2, phiti2, phito2] . U[60];
KAA3[phir2_, phiti2_, phito2_] = Inverse[U[60]] .
    KAA24[phir2, phiti2, phito2] . U[60];
"*************************************************************************\
***********";
"the six force tensors for BB interaction in the 2nd shell";
KBB22S[phir2_, phiti2_, phito2_] = {{phir2, 0, 0}, {0, phiti2, 0},
    {0, 0, phito2}};
KBB22[phir2_, phiti2_, phito2_] = Inverse[U[30]] .
    KBB22S[phir2, phiti2, phito2] . U[30];
KBB21[phir2_, phiti2_, phito2_] = Inverse[U[60]] .
    KBB22[phir2, phiti2, phito2] . U[60];
KBB2[phir2_, phiti2_, phito2_] = Inverse[U[60]] .
    KBB21[phir2, phiti2, phito2] . U[60];
KBB3[phir2_, phiti2_, phito2_] = Inverse[U[60]] .
    KBB2[phir2, phiti2, phito2] . U[60];
KBB24[phir2_, phiti2_, phito2_] = Inverse[U[60]] .
    KBB3[phir2, phiti2, phito2] . U[60];
KBB23[phir2_, phiti2_, phito2_] = Inverse[U[60]] .
    KBB24[phir2, phiti2, phito2] . U[60];
"*************************************************************************\
***********";
"the 3 force tensors for AB interaction 3rd shell";
KAB32S[phir3_, phiti3_, phito3_] = {{phir3, 0, 0}, {0, phiti3, 0},
    {0, 0, phito3}};
KAB32[phir3_, phiti3_, phito3_] = Inverse[U[60]] .
    KAB32S[phir3, phiti3, phito3] . U[60];
KAB31[phir3_, phiti3_, phito3_] = Inverse[U[120]] .
    KAB32[phir3, phiti3, phito3] . U[120];
KAB33[phir3_, phiti3_, phito3_] = Inverse[U[120]] .
    KAB31[phir3, phiti3, phito3] . U[120];
"*************************************************************************\
*************";
"the 3 force tensors for BA interaction 3rd shell";
KBA31[phir3_, phiti3_, phito3_] = {{phir3, 0, 0}, {0, phiti3, 0},
    {0, 0, phito3}};
KBA32[phir3_, phiti3_, phito3_] = Inverse[U[120]] .
    KBA31[phir3, phiti3, phito3] . U[120];
KBA33[phir3_, phiti3_, phito3_] = Inverse[U[120]] .
    KBA32[phir3, phiti3, phito3] . U[120];
"*************************************************************************\
*************";
"AB interaction in the 4th shell";
KAB41S[phir4_, phiti4_, phito4_] = {{phir4, 0, 0}, {0, phiti4, 0},
    {0, 0, phito4}};
winkel = (ArcTan[Sqrt[3]/5]*360)/(2*Pi);
KAB41[phir4_, phiti4_, phito4_] = Inverse[U[winkel]] .
    KAB41S[phir4, phiti4, phito4] . U[winkel];
KAB42[phir4_, phiti4_, phito4_] = Inverse[U[(-winkel)*2]] .
    KAB41[phir4, phiti4, phito4] . U[(-winkel)*2];
KAB43[phir4_, phiti4_, phito4_] = Inverse[U[-120 + winkel*2]] .
    KAB42[phir4, phiti4, phito4] . U[-120 + winkel*2];
KAB44[phir4_, phiti4_, phito4_] = Inverse[U[(-winkel)*2]] .
    KAB43[phir4, phiti4, phito4] . U[(-winkel)*2];
KAB45[phir4_, phiti4_, phito4_] = Inverse[U[-120 + winkel*2]] .
    KAB44[phir4, phiti4, phito4] . U[-120 + winkel*2];
KAB46[phir4_, phiti4_, phito4_] = Inverse[U[(-winkel)*2]] .
    KAB45[phir4, phiti4, phito4] . U[(-winkel)*2];
"*************************************************************************\
```

```
*************";
"BA interaction in the 4th shell";
KBA43S[phir4_, phiti4_, phito4_] = {{phir4, 0, 0}, {0, phiti4, 0},
    {0, 0, phito4}};
KBA43[phir4_, phiti4_, phito4_] = Inverse[U[-180 + winkel]] .
    KBA43S[phir4, phiti4, phito4] . U[-180 + winkel];
KBA44[phir4_, phiti4_, phito4_] = Inverse[U[(-winkel)*2]] .
    KBA43[phir4, phiti4, phito4] . U[(-winkel)*2];
KBA45[phir4_, phiti4_, phito4_] = Inverse[U[-120 + winkel*2]] .
    KBA44[phir4, phiti4, phito4] . U[-120 + winkel*2];
KBA46[phir4_, phiti4_, phito4_] = Inverse[U[(-winkel)*2]] .
    KBA45[phir4, phiti4, phito4] . U[(-winkel)*2];
KBA41[phir4_, phiti4_, phito4_] = Inverse[U[-120 + winkel*2]] .
    KBA46[phir4, phiti4, phito4] . U[-120 + winkel*2];
KBA42[phir4_, phiti4_, phito4_] = Inverse[U[(-winkel)*2]] .
    KBA41[phir4, phiti4, phito4] . U[(-winkel)*2];
"now building the (2 X 2) matrices DAA, DBB, DAB and DBA. from these \
construct D.";
DAA[kx_, ky_, phir1_, phiti1_, phir2_, phiti2_, phir3_, phiti3_, phir4_,
    phiti4_, phito1_, phito2_, phito3_, phito4_] =
   (KAA22[phir2, phiti2, phito2]*(E^(I*Raa22 . {{kx}, {ky}}))[[1]][[1]] +
      KAA23[phir2, phiti2, phito2]*(E^(I*Raa23 . {{kx}, {ky}}))[[1]][[1]] +
      KAA2[phir2, phiti2, phito2]*(E^(I*Raa2 . {{kx}, {ky}}))[[1]][[1]] +
      KAA3[phir2, phiti2, phito2]*(E^(I*Raa3 . {{kx}, {ky}}))[[1]][[1]] +
      KAA24[phir2, phiti2, phito2]*(E^(I*Raa24 . {{kx}, {ky}}))[[1]][[1]] +
      KAA21[phir2, phiti2, phito2]*(E^(I*Raa21 . {{kx}, {ky}}))[[1]][[1]])*
     -1 + KAB2[phir1, phiti1, phito1] + KAB1[phir1, phiti1, phito1] +
    KAB3[phir1, phiti1, phito1] + KAA22[phir2, phiti2, phito2] +
    KAA23[phir2, phiti2, phito2] + KAA2[phir2, phiti2, phito2] +
    KAA3[phir2, phiti2, phito2] + KAA24[phir2, phiti2, phito2] +
    KAA21[phir2, phiti2, phito2] + KAB31[phir3, phiti3, phito3] +
    KAB32[phir3, phiti3, phito3] + KAB33[phir3, phiti3, phito3] +
    KAB41[phir4, phiti4, phito4] + KAB42[phir4, phiti4, phito4] +
    KAB43[phir4, phiti4, phito4] + KAB44[phir4, phiti4, phito4] +
    KAB45[phir4, phiti4, phito4] + KAB46[phir4, phiti4, phito4];
DAB[kx_, ky_, phir1_, phiti1_, phir2_, phiti2_, phir3_, phiti3_, phir4_,
    phiti4_, phito1_, phito2_, phito3_, phito4_] =
   (KAB1[phir1, phiti1, phito1]*(E^(I*Rab1 . {{kx}, {ky}}))[[1]][[1]] +
     KAB2[phir1, phiti1, phito1]*(E^(I*Rab2 . {{kx}, {ky}}))[[1]][[1]] +
     KAB3[phir1, phiti1, phito1]*(E^(I*Rab3 . {{kx}, {ky}}))[[1]][[1]] +
     KAB31[phir3, phiti3, phito3]*(E^(I*Rab31 . {{kx}, {ky}}))[[1]][[1]] +
     KAB32[phir3, phiti3, phito3]*(E^(I*Rab32 . {{kx}, {ky}}))[[1]][[1]] +
     KAB33[phir3, phiti3, phito3]*(E^(I*Rab33 . {{kx}, {ky}}))[[1]][[1]] +
     KAB41[phir4, phiti4, phito4]*(E^(I*Rab41 . {{kx}, {ky}}))[[1]][[1]] +
     KAB42[phir4, phiti4, phito4]*(E^(I*Rab42 . {{kx}, {ky}}))[[1]][[1]] +
     KAB43[phir4, phiti4, phito4]*(E^(I*Rab43 . {{kx}, {ky}}))[[1]][[1]] +
     KAB44[phir4, phiti4, phito4]*(E^(I*Rab44 . {{kx}, {ky}}))[[1]][[1]] +
     KAB45[phir4, phiti4, phito4]*(E^(I*Rab45 . {{kx}, {ky}}))[[1]][[1]] +
     KAB46[phir4, phiti4, phito4]*(E^(I*Rab46 . {{kx}, {ky}}))[[1]][[1]])*-1;
DBA[kx_, ky_, phir1_, phiti1_, phir2_, phiti2_, phir3_, phiti3_, phir4_,
    phiti4_, phito1_, phito2_, phito3_, phito4_] =
   (KBA1[phir1, phiti1, phito1]*(E^(I*Rba1 . {{kx}, {ky}}))[[1]][[1]] +
     KBA2[phir1, phiti1, phito1]*(E^(I*Rba2 . {{kx}, {ky}}))[[1]][[1]] +
     KBA3[phir1, phiti1, phito1]*(E^(I*Rba3 . {{kx}, {ky}}))[[1]][[1]] +
     KBA31[phir3, phiti3, phito3]*(E^(I*Rba31 . {{kx}, {ky}}))[[1]][[1]] +
     KBA32[phir3, phiti3, phito3]*(E^(I*Rba32 . {{kx}, {ky}}))[[1]][[1]] +
     KBA33[phir3, phiti3, phito3]*(E^(I*Rba33 . {{kx}, {ky}}))[[1]][[1]] +
     KBA41[phir4, phiti4, phito4]*(E^(I*Rba41 . {{kx}, {ky}}))[[1]][[1]] +
     KBA42[phir4, phiti4, phito4]*(E^(I*Rba42 . {{kx}, {ky}}))[[1]][[1]] +
     KBA43[phir4, phiti4, phito4]*(E^(I*Rba43 . {{kx}, {ky}}))[[1]][[1]] +
```

```
     KBA44[phir4, phiti4, phito4]*(E^(I*Rba44 . {{kx}, {ky}}))[[1]][[1]] +
     KBA45[phir4, phiti4, phito4]*(E^(I*Rba45 . {{kx}, {ky}}))[[1]][[1]] +
     KBA46[phir4, phiti4, phito4]*(E^(I*Rba46 . {{kx}, {ky}}))[[1]][[1]])*-1;
DBB[kx_, ky_, phir1_, phiti1_, phir2_, phiti2_, phir3_, phiti3_, phir4_,
    phiti4_, phito1_, phito2_, phito3_, phito4_] =
   (KBB2[phir2, phiti2, phito2]*(E^(I*Rbb2 . {{kx}, {ky}}))[[1]][[1]] +
      KBB21[phir2, phiti2, phito2]*(E^(I*Rbb21 . {{kx}, {ky}}))[[1]][[1]] +
      KBB22[phir2, phiti2, phito2]*(E^(I*Rbb22 . {{kx}, {ky}}))[[1]][[1]] +
      KBB23[phir2, phiti2, phito2]*(E^(I*Rbb23 . {{kx}, {ky}}))[[1]][[1]] +
      KBB24[phir2, phiti2, phito2]*(E^(I*Rbb24 . {{kx}, {ky}}))[[1]][[1]] +
      KBB3[phir2, phiti2, phito2]*(E^(I*Rbb3 . {{kx}, {ky}}))[[1]][[1]])*-1 +
    KBA1[phir1, phiti1, phito1] + KBA2[phir1, phiti1, phito1] +
    KBA3[phir1, phiti1, phito1] + KBB2[phir2, phiti2, phito2] +
    KBB21[phir2, phiti2, phito2] + KBB22[phir2, phiti2, phito2] +
    KBB23[phir2, phiti2, phito2] + KBB24[phir2, phiti2, phito2] +
    KBB3[phir2, phiti2, phito2] + KBA31[phir3, phiti3, phito3] +
    KBA32[phir3, phiti3, phito3] + KBA33[phir3, phiti3, phito3] +
    KBA41[phir4, phiti4, phito4] + KBA42[phir4, phiti4, phito4] +
    KBA43[phir4, phiti4, phito4] + KBA44[phir4, phiti4, phito4] +
    KBA45[phir4, phiti4, phito4] + KBA46[phir4, phiti4, phito4];
<< "LinearAlgebra`MatrixManipulation`"
DD[kx_, ky_, phir1_, phiti1_, phir2_, phiti2_, phir3_, phiti3_, phir4_,
    phiti4_, phito1_, phito2_, phito3_, phito4_] =
   BlockMatrix[{{DAA[kx, ky, phir1, phiti1, phir2, phiti2, phir3, phiti3,
       phir4, phiti4, phito1, phito2, phito3, phito4],
      DAB[kx, ky, phir1, phiti1, phir2, phiti2, phir3, phiti3, phir4, phiti4,
       phito1, phito2, phito3, phito4]}, {DBA[kx, ky, phir1, phiti1, phir2,
       phiti2, phir3, phiti3, phir4, phiti4, phito1, phito2, phito3, phito4],
      DBB[kx, ky, phir1, phiti1, phir2, phiti2, phir3, phiti3, phir4, phiti4,
       phito1, phito2, phito3, phito4]}};
"*************************************************************************";
"*************************************************************************";
"***************   FORCE CONSTANTS OF 2D GRAPHITE   **********************";
"*************************************************************************";
"*************************************************************************";
"*************************************************************************";
"Coordinates of the high symmetry points in units a_0 (1.42 Angstrom)";
K = {(2*Pi)/3, (2*Pi)/(Sqrt[3]*3)}; GA = {0, 0}; M = {(2*Pi)/3, 0};
fGA = neuGA[p1_, p2_, p3_, p4_, p5_, p6_, p7_, p8_, p9_, p10_, p11_, p12_] =
    Chop[Simplify[DD[GA[[1]], GA[[2]], p1, p2, p3, p4, p5, p6, p7, p8, p9,
       p10, p11, p12]]];
"*************************************************************************\
********";
"GAMMA - POINT";
"*************************************************************************\
********";
"Here we can see the three accoustic modes which give zero Eigenfrequency at \
the Gamma Point";
"The corresponding Eigenvectors show that ";
Print["The dynamical Matrix looks like this:"]
MatrixForm[fGA]
Eigenvalues[fGA]
Eigenvectors[fGA]
F = 1; phir1 = 36.5*F;
phiti1 = 24.5*F; phito1 = 9.82*F; phir2 = 8.8*F; phiti2 = -3.23*F;
  phito2 = -0.4*F;
phir3 = 3*F; phiti3 = -5.25*F; phito3 = 0.15*F;
phir4 = -1.92*F; phiti4 = 2.29*F; phito4 = -0.58*F;
<< "LinearAlgebra`MatrixManipulation`"
DD1[kx_, ky_] = DD[kx, ky, phir1, phiti1, phir2, phiti2, phir3, phiti3,
    phir4, phiti4, phito1, phito2, phito3, phito4];
"******************* solving DD along GAMMA->K->M ********************";
"*************************************************************************";
"the coordinates of gamma point, K point and M point in units of a_0 (1.42 \
```

```
Angstrom)";
K = {2*(Pi/3), 2*(Pi/(Sqrt[3]*3))}; GA = {0, 0}; M = {2*(Pi/3), 0};
"vectors of Gamma->M, M->K and K->Gamma. each divided by an appropriate \
constant fact.";
fact = 20; stepsGAM = Ceiling[Sqrt[(M - GA) . (M - GA)]*fact];
  stepsMK = Ceiling[Sqrt[(K - M) . (K - M)]*fact];
stepsKGA = Ceiling[Sqrt[(GA - K) . (GA - K)]*fact];
dGAM = (M - GA)/stepsGAM; dMK = (K - M)/stepsMK; dKGA = (GA - K)/stepsKGA;
"THE 6 Dispersion Relations from Gamma to M";
valGAM = Table[{GA + dGAM*i}, {i, 1, stepsGAM}];
finGAM1 =
   Table[{i, Sqrt[Abs[Eigenvalues[DD1[valGAM[[i]][[1]][[1]],
           valGAM[[i]][[1]][[2]]]][[1]]]]*mul}, {i, 1, stepsGAM}];
finGAM2 =
   Table[{i, Sqrt[Abs[Eigenvalues[DD1[valGAM[[i]][[1]][[1]],
           valGAM[[i]][[1]][[2]]]][[2]]]]*mul}, {i, 1, stepsGAM}];
finGAM3 =
   Table[{i, Sqrt[Abs[Eigenvalues[DD1[valGAM[[i]][[1]][[1]],
           valGAM[[i]][[1]][[2]]]][[3]]]]*mul}, {i, 1, stepsGAM}];
finGAM4 =
   Table[{i, Sqrt[Abs[Eigenvalues[DD1[valGAM[[i]][[1]][[1]],
           valGAM[[i]][[1]][[2]]]][[4]]]]*mul}, {i, 1, stepsGAM}];
finGAM5 =
   Table[{i, Sqrt[Abs[Eigenvalues[DD1[valGAM[[i]][[1]][[1]],
           valGAM[[i]][[1]][[2]]]][[5]]]]*mul}, {i, 1, stepsGAM}];
finGAM6 =
   Table[{i, Sqrt[Abs[Eigenvalues[DD1[valGAM[[i]][[1]][[1]],
           valGAM[[i]][[1]][[2]]]][[6]]]]*mul}, {i, 1, stepsGAM}];
"THE 6 Dispersion Relations from M to K";
valMK = Table[{M + dMK*i}, {i, 1, stepsMK}];
finMK1 = Table[{i + stepsGAM,
     Sqrt[Abs[Eigenvalues[DD1[valMK[[i]][[1]][[1]], valMK[[i]][[1]][[2]]]][[
         1]]]]*mul}, {i, 1, stepsMK}];
finMK2 = Table[{i + stepsGAM,
     Sqrt[Abs[Eigenvalues[DD1[valMK[[i]][[1]][[1]], valMK[[i]][[1]][[2]]]][[
         2]]]]*mul}, {i, 1, stepsMK}];
finMK3 = Table[{i + stepsGAM,
     Sqrt[Abs[Eigenvalues[DD1[valMK[[i]][[1]][[1]], valMK[[i]][[1]][[2]]]][[
         3]]]]*mul}, {i, 1, stepsMK}];
finMK4 = Table[{i + stepsGAM,
     Sqrt[Abs[Eigenvalues[DD1[valMK[[i]][[1]][[1]], valMK[[i]][[1]][[2]]]][[
         4]]]]*mul}, {i, 1, stepsMK}];
finMK5 = Table[{i + stepsGAM,
     Sqrt[Abs[Eigenvalues[DD1[valMK[[i]][[1]][[1]], valMK[[i]][[1]][[2]]]][[
         5]]]]*mul}, {i, 1, stepsMK}];
finMK6 = Table[{i + stepsGAM,
     Sqrt[Abs[Eigenvalues[DD1[valMK[[i]][[1]][[1]], valMK[[i]][[1]][[2]]]][[
         6]]]]*mul}, {i, 1, stepsMK}];
"THE 6 Dispersion Relations from K back to GAMMA";
valKGA = Table[{K + dKGA*i}, {i, 1, stepsKGA}];
finKGA1 = Table[{i + stepsGAM + stepsMK,
     Sqrt[Abs[Eigenvalues[DD1[valKGA[[i]][[1]][[1]], valKGA[[i]][[1]][[2]]]][[
         1]]]]*mul}, {i, 1, stepsKGA}];
finKGA2 = Table[{i + stepsGAM + stepsMK,
     Sqrt[Abs[Eigenvalues[DD1[valKGA[[i]][[1]][[1]], valKGA[[i]][[1]][[2]]]][[
         2]]]]*mul}, {i, 1, stepsKGA}];
finKGA3 = Table[{i + stepsGAM + stepsMK,
     Sqrt[Abs[Eigenvalues[DD1[valKGA[[i]][[1]][[1]], valKGA[[i]][[1]][[2]]]][[
         3]]]]*mul}, {i, 1, stepsKGA}];
finKGA4 = Table[{i + stepsGAM + stepsMK,
     Sqrt[Abs[Eigenvalues[DD1[valKGA[[i]][[1]][[1]], valKGA[[i]][[1]][[2]]]][[
         4]]]]*mul}, {i, 1, stepsKGA}];
```

```
finKGA5 = Table[{i + stepsGAM + stepsMK,
     Sqrt[Abs[Eigenvalues[DD1[valKGA[[i]][[1]][[1]], valKGA[[i]][[1]][[2]]]][[
         5]]]]*mul}, {i, 1, stepsKGA}];
finKGA6 = Table[{i + stepsGAM + stepsMK,
     Sqrt[Abs[Eigenvalues[DD1[valKGA[[i]][[1]][[1]], valKGA[[i]][[1]][[2]]]][[
         6]]]]*mul}, {i, 1, stepsKGA}];
"****** test of coordinates *************";
"this translational vector is used to go from A atom to B atom in the same \
unitcell";
transl = {{1, 0}}[[1]];
"the six AA and BB pairs in the 2nd shell";
AA = {PointSize[0.02], RGBColor[1, 0, 0], {Point[Raa22[[1]]],
     Point[Raa23[[1]]], Point[Raa2[[1]]], Point[Raa3[[1]]],
     Point[Raa24[[1]]], Point[Raa21[[1]]]}};
BB = {PointSize[0.02], RGBColor[0, 0, 1], {Point[Rbb21[[1]] + transl],
     Point[Rbb22[[1]] + transl], Point[Rbb23[[1]] + transl],
     Point[Rbb24[[1]] + transl], Point[Rbb3[[1]] + transl],
     Point[Rbb2[[1]] + transl]}};
"nearest neighbours, 3pairs";
AB = {PointSize[0.02], RGBColor[1, 0.5, 0], {Point[Rab2[[1]]],
     Point[Rab1[[1]]], Point[Rab3[[1]]]}};
BA = {PointSize[0.02], RGBColor[1, 1, 0], {Point[Rba1[[1]] + transl],
     Point[Rba2[[1]] + transl], Point[Rba3[[1]] + transl]}};
"third shell , three atoms AB and BA";
AB3 = {PointSize[0.02], RGBColor[0, 0, 0], {Point[Rab31[[1]]],
     Point[Rab32[[1]]], Point[Rab33[[1]]]}};
BA3 = {PointSize[0.02], RGBColor[0, 0, 0], {Point[Rba31[[1]] + transl],
     Point[Rba32[[1]] + transl], Point[Rba33[[1]] + transl]}};
"4th shell AB and BA pairs (six)";
BA4 = {PointSize[0.02], RGBColor[0, 1, 0], {Point[Rba41[[1]] + transl],
     Point[Rba42[[1]] + transl], Point[Rba43[[1]] + transl],
     Point[Rba44[[1]] + transl], Point[Rba45[[1]] + transl],
     Point[Rba46[[1]] + transl]}};
AB4 = {PointSize[0.02], RGBColor[0, 1, 0], {Point[Rab41[[1]]],
     Point[Rab42[[1]]], Point[Rab43[[1]]], Point[Rab44[[1]]],
     Point[Rab45[[1]]], Point[Rab46[[1]]]}};
"circles in A Atom graph";
crcAB = Circle[{0, 0}, 1];
crcAA = Circle[{0, 0}, Sqrt[3]];
crcAB3 = Circle[{0, 0}, 2];
crcAB4 = Circle[{0, 0}, Sqrt[4 + Sqrt[3]^2]];
Aat = {PointSize[0.03], RGBColor[0, 0, 0], Point[{0, 0}]};
"circles in B Atom graph";
crcBA = Circle[{0, 0} + transl, 1];
crcBB = Circle[{0, 0} + transl, Sqrt[3]];
crcBA3 = Circle[{0, 0} + transl, 2];
crcBA4 = Circle[{0, 0} + transl, Sqrt[4 + Sqrt[3]^2]];
Bat = {PointSize[0.03], RGBColor[0, 0, 0], Point[{0, 0} + transl]};
totallist = Flatten[Join[finGAM1, finGAM2, finGAM3, finGAM4, finGAM5,
     finGAM6, finMK1, finMK2, finMK3, finMK4, finMK5, finMK6, finKGA1,
     finKGA2, finKGA3, finKGA4, finKGA5, finKGA6], 0];
Clear[K]; ListPlot[totallist, Frame -> True,
   FrameTicks -> {{{0.01, "\[CapitalGamma]"}, {stepsGAM, "M"}, {stepsGAM + stepsMK, "K"},
      {stepsGAM + stepsMK + stepsKGA, "\[CapitalGamma]"}}, {{0.01, "0"}, 200, 400, 600,
      800, 1000, 1200, 1400, 1600}, {}, {}}, AxesLabel -> {{False}, {True}},
   GridLines -> {{stepsGAM, stepsGAM + stepsMK, stepsGAM + stepsMK +
       stepsKGA}, None}, Frame -> True, AspectRatio -> 1,
   PlotRange -> {{0, stepsGAM + stepsMK + stepsKGA}, {0, 1650}},
   TextStyle -> {FontSlant -> "Italic", FontSize -> 20},
   FrameLabel -> {"k", "Energy (\!\(cm\^\(-1\)\))"}, RotateLabel -> True]
```

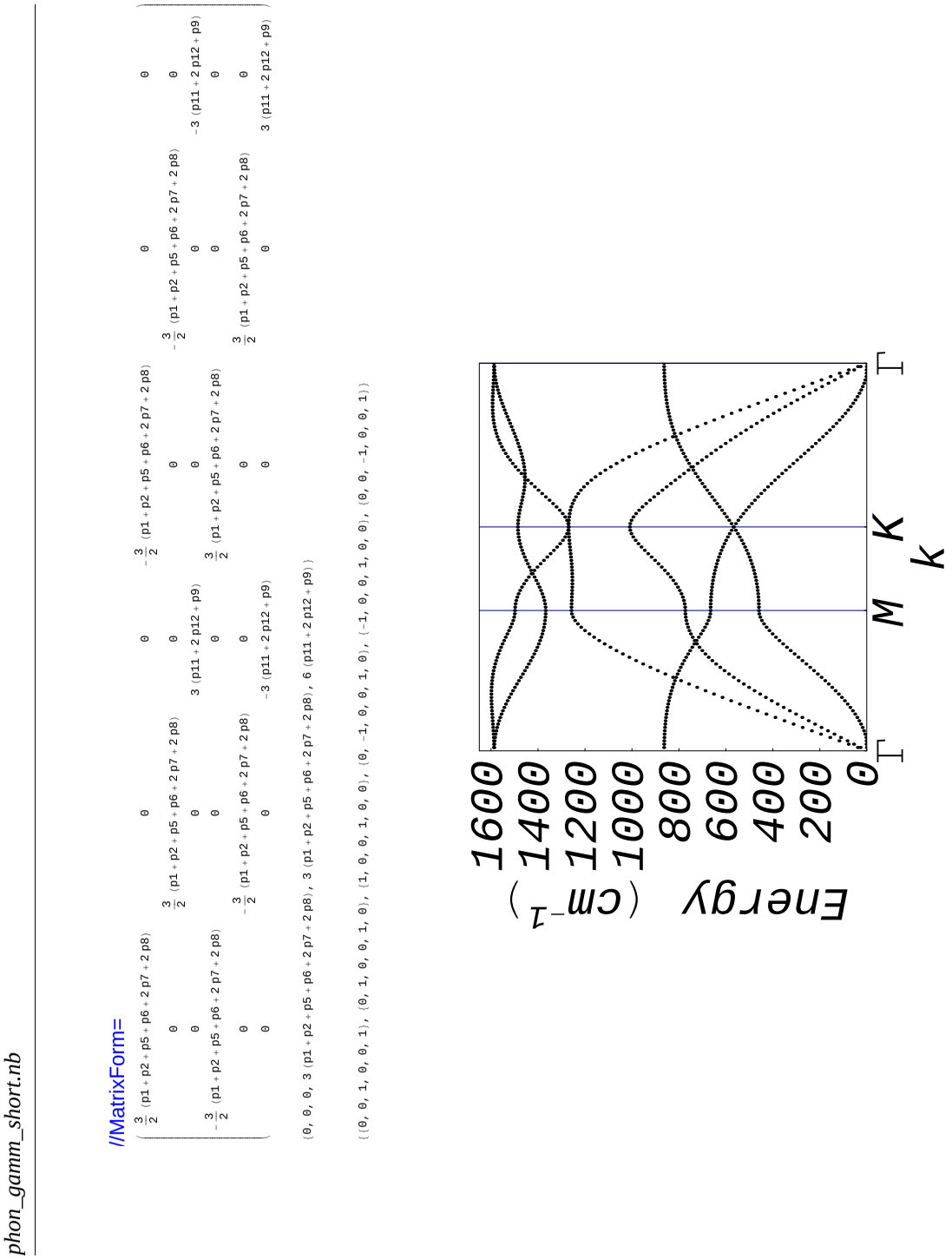

Figure A.1: Output of the Mathematica program for phonon calculation is the dynamical matrix at Γ, the analytical phonon eigenvalues and eigenfunctions and the numerically solved dispersion relations. Note that `p1,...,p8` are in plane and `p9,...,p12` are out of plane constants.

A.2 Nanographite ribbon π electron energy dispersion relations

The electron energy dispersion of a nanographite ribbon is calculated by tight–binding method. The output of the program [2] is shown in Fig. (A.2).

```
(* Calculate the electronic energy dispersion of armchair and zigag \
nanoribbons *)(* A. Grueneis July 2004  alex@flex.phys.tohoku.ac.jp *)
(*
  METHOD : thight binding. nearest neighbour integrals are considered *)
(*
  atoms are indexed by an integer number l =
    1 to  the nearest neighbour atoms are found *)
(*
  from this number by a simple algorithm.
      See chapter 4 thesis and reference Lin. et. al. *)
(*
  t is the energy overlap parameter.
      symmetric valence and conduction bands are assumed. *)
(*
  NN is the number of dimers. 2N is the number of atoms in the ribbon. *)
(*
  step is the delta k value. *)
t = 2.9;
NN = 6;
step = 0.01;
(* ZigZag Hamiltonian Z(k) *)

Z[k_] = Table[cond1a = l == m - 1 && EvenQ[m];
      cond1b = l == m + 1 && EvenQ[m]; cond2a = l == m - 1 && Not[EvenQ[m]];
      cond2b = l == m + 1 && Not[EvenQ[m]];
      Which[cond1a, -2*t*Cos[k/2], cond1b, -t, cond2a, -t,
        cond2b, -2*t*Cos[k/2], Not[cond1a || cond1b || cond2a || cond2b],
        0], {l, 1, 2*NN}, {m, 1, 2*NN}];
resZ = Table[{k, Eigenvalues[Z[k]]}, {k, 0, Pi, step}];
res1Z = Table[{resZ[[i]][[1]], resZ[[i]][[2]][[j]]}, {i, 1, Length[resZ]}, {j,
         1, 2*NN}];
(* Armchair Hamiltonian A(k) *)

A[k_] = Table[cond1a = (l == m - 1) && EvenQ[m];
      cond1b = l == m + 1 && EvenQ[m]; cond1c = (l == m - 3) && EvenQ[m];
      cond2a = (l == m - 1) && OddQ[m]; cond2b = l == m + 1 && OddQ[m];
      cond2c = (l == m + 3) && OddQ[m];
      Which[cond1a, -t*Exp[-I*k], cond1b, -t*Exp[I*k/2],
        cond1c, -t*Exp[I*k/2], cond2a, -t*Exp[-I*k/2], cond2b, -t*Exp[I*k],
        cond2c, -t*Exp[-I*k/2],
        Not[cond1a || cond1b || cond1c || cond2a || cond2b || cond2c], 0], {l,
         1, 2*NN}, {m, 1, 2*NN}];
resA = Table[{k, Chop[Eigenvalues[A[k]]]}, {k, 0, Pi/3, step}];
res1A = Table[{resA[[i]][[1]]*3, resA[[i]][[2]][[j]]}, {i, 1,
        Length[resA]}, {j, 1, 2*NN}];
(* Make a plot *)

picA = ListPlot[Flatten[res1A, 1], PlotJoined -> False,
      TextStyle -> {FontSlant -> "Italic", FontSize -> 20},
      AxesOrigin -> {0, 0}, Frame -> True,
      FrameLabel -> {ka, "E(eV)", "(b) N=6", ""}, RotateLabel -> True,
      PlotRange -> {-3*t - 0.01, 3*t + 0.01},
      FrameTicks -> {{0, Pi/2,
            Pi}, {{-t, "-t"}, {-2*t, "-2t"}, {-3*t, "-3t"}, {0, "0"}, {t,
              "t"}, {2*t, "2t"}, {3*t, "3t"}}, {}, {}},
      AspectRatio -> GoldenRatio, Axes -> False];
(* Export to eps file *)
Export["zigzag10.eps", picA];
```

[2] mathematica/thesis/nanographite.nb

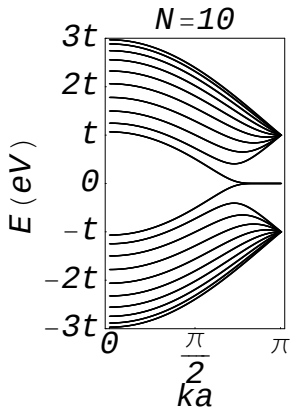

Figure A.2: Output of the Mathematica program (2) for nanographite electronic structure.

A.3 Graphite σ and π electron energy dispersion relations.

The 2D and 3D output of this program is shown in Fig. A.3 and in Fig. A.4, respectively. [3]

```
(* Notebook to calculate electronic sigma and pi bands of graphite in LCAO \
approximation*)
(* A. Grueneis 2004 April *)
Off[General::"spell"]
  << LinearAlgebra`MatrixManipulation`
resultlist = Table[Chop[Solve[Det[H[klist[[i]][[1]], klist[[i]][[2]]] -
         S[klist[[i]][[1]], klist[[i]][[2]]]*energy1] == 0, energy1],
     1/10^8], {i, 1, Length[klist]}];
distlist = Table[Sum[Sqrt[(klist[[i]][[1]] - klist[[i - 1]][[1]])^2 +
       (klist[[i]][[2]] - klist[[i - 1]][[2]])^2], {i, 2, j}],
    {j, 2, Length[klist]}];
distlist2 = Flatten[Insert[distlist, 0, 1]];
res = Table[{distlist2[[i]], energy1 /. resultlist[[i]][[j]]},
    {i, 1, Length[resultlist], 1}, {j, 1, 8}];
resultlist2 = Flatten[Table[Flatten[res[[i]], 0],
     {i, 1, Length[resultlist]}], 1];
Export["band2D.dat", Table[{res[[i]][[1]][[1]], res[[i]][[1]][[2]],
     res[[i]][[2]][[2]], res[[i]][[3]][[2]], res[[i]][[4]][[2]],
     res[[i]][[5]][[2]], res[[i]][[6]][[2]], res[[i]][[7]][[2]],
     res[[i]][[8]][[2]]}, {i, 1, Length[res]}]];
plot1 = ListPlot[resultlist2, Axes -> {False, True},
    PlotRange -> {{0, KGAM + MK}, {-20 - 0.01, 35}}, Frame -> True,
    FrameTicks -> {{{0.01, " K "}, {GAK, "\[CapitalGamma]"}, {KGAM, "M"},
       {KGAM + MK, "K"}}, {-10, -20, -30, 0, 10, 20, 30}, {}, {}},
    GridLines -> {{GAK, KGAM, KGAM + MK}, None}, AspectRatio -> 1,
    PlotRange -> {{0, KGAMK}, {emin, emax}},
    TextStyle -> {FontSlant -> "Italic", FontSize -> 20},
    FrameLabel -> {"electron wavevector", "Energy (eV)", "(a)", ""},
    RotateLabel -> True, Prolog -> hex];
coords1p = {{4, -10}}; label1p = Table[Text["\!\(pp\[Pi]\_g\)", coords1p[[i]],
     TextStyle -> {FontSlant -> "Italic", FontSize -> 11},
     Background -> RGBColor[1, 1, 1]], {i, 1, Length[coords1p]}];
coords2p = {{4, 18}}; label2p = Table[Text["\!\(\(pp\[Pi]\_u\^*\)\)",
```

[3] mathematica/thesis/graphite_sigma.nb

```
     coords2p[[i]], TextStyle -> {FontSlant -> "Italic", FontSize -> 11},
     Background -> RGBColor[1, 1, 1]], {i, 1, Length[coords2p]}];
coords1s = {{4, -15}}; coords1s2 = {{4.8, 0}};
label1s = Table[Text["\!\(ss\[Sigma]\_g\)", coords1s[[i]],
     TextStyle -> {FontSlant -> "Italic", FontSize -> 11},
     Background -> RGBColor[1, 1, 1]], {i, 1, Length[coords1s]}];
label1s2 =
   Table[Text["\!\(pp\[Sigma]\_g\)+\!\(\(pp\[Pi]\_u\^*\)\),\!\(\(pp\[Sigma]\_u\^*\)\)+\!\
\(pp\[Pi]\_g\)", coords1s2[[i]], TextStyle -> {FontSlant -> "Italic",
       FontSize -> 11}, Background -> RGBColor[1, 1, 1]],
    {i, 1, Length[coords1s]}];
coords2s = {{4.2, 26.3}}; coords2s2 = {{4, 10}}; coords2s3 = {{4, 6}};
label2s = Table[Text["\!\(\(ss\[Sigma]\_u\^*\)\)", coords2s[[i]],
     TextStyle -> {FontSlant -> "Italic", FontSize -> 11},
     Background -> RGBColor[1, 1, 1]], {i, 1, Length[coords2s]}];
labels = Join[Table[label1p[[i]], {i, 1, Length[label1p]}],
    Table[label2p[[i]], {i, 1, Length[label2p]}],
    Table[label1s[[i]], {i, 1, Length[label1s]}],
    Table[label1s2[[i]], {i, 1, Length[label1s2]}],
    Table[label2s[[i]], {i, 1, Length[label2s]}]];
Show[plot1, Graphics[labels]]
Export["/misc/flex/students/alex/mathematica/thesis/graphene_el_band.eps", %]
```

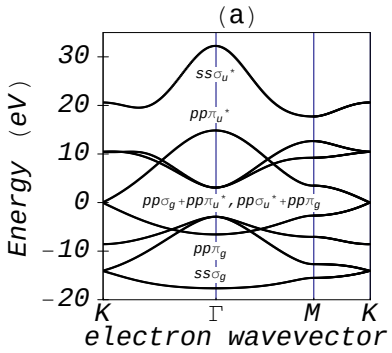

Figure A.3: Output of the Mathematica program (3) for σ and π electron dispersion relations.

```
K1 = {2*(Pi/Sqrt[3]), 2*(Pi/3)}; M1 = {K1[[1]], 0}; GAMMA = {0, 0};
K2 = {0, 4*(Pi/3)}; K3 = {-K1[[1]], K1[[2]]}; K4 = -K1;
  K5 = -K2; K6 = -K3;
data = {K1, K2, K3, K4, K5, K6, K1};
bz = ListPlot[data, PlotJoined -> True];
bztri[xa_, ya_, xb_, yb_, xc_, yc_, steps_] := Module[{vec1, vec2, vec3, b1, b2, points},
    vec1 = {xa, ya}; vec2 = {xb, yb}; vec3 = {xc, yc};
b1 = (vec2 - vec1)/steps; b2 = (vec3 - vec2)/steps;
     points = Flatten[Table[Table[vec1 + b1*(i - 1) +
b2*(j - 1), {j, 1, i}], {i, 1, steps + 1}], 1]; Return[points]];
anz = 10;
p1 = N[bztri[GAMMA[[1]], GAMMA[[2]], K1[[1]], K1[[2]], K2[[1]], K2[[2]], anz]];
p2 = N[bztri[GAMMA[[1]], GAMMA[[2]], K2[[1]], K2[[2]], K3[[1]], K3[[2]], anz]];
p3 = N[bztri[GAMMA[[1]], GAMMA[[2]], K3[[1]], K3[[2]], K4[[1]], K4[[2]], anz]];
p4 = N[bztri[GAMMA[[1]], GAMMA[[2]], K4[[1]], K4[[2]], K5[[1]], K5[[2]], anz]];
p5 = N[bztri[GAMMA[[1]], GAMMA[[2]], K5[[1]], K5[[2]], K6[[1]], K6[[2]], anz]];
p6 = N[bztri[GAMMA[[1]], GAMMA[[2]], K6[[1]], K6[[2]], K1[[1]], K1[[2]], anz]];
<< "Graphics`MultipleListPlot`"
MultipleListPlot[p1, p2, p3, p4, p5, p6]
```

```
kpoint3D = Join[p1, p2, p3, p4, p5, p6];
resultlist3D = Table[Chop[Solve[Det[H[kpoint3D[[i]][[1]],
kpoint3D[[i]][[2]]] - S[kpoint3D[[i]][[1]], kpoint3D[[i]][[2]]]*
          energy1] == 0, energy1], 0.01], {i, 1, Length[kpoint3D]}];
res3D = Table[energy1 /. resultlist3D[[i]][[j]], {i, 1, Length[resultlist3D], 1}, {j, 1, 8}];
resultlist3 = Table[Flatten[res3D[[i]]], {i, 1, Length[resultlist3D]}];

band1 = Table[{kpoint3D[[i]][[1]], kpoint3D[[i]][[2]], resultlist3[[i]][[1]]},
{i, 1, Length[kpoint3D]}];
band2 = Table[{kpoint3D[[i]][[1]], kpoint3D[[i]][[2]], resultlist3[[i]][[2]]},
{i, 1, Length[kpoint3D]}];
band3 = Table[{kpoint3D[[i]][[1]], kpoint3D[[i]][[2]], resultlist3[[i]][[3]]},
{i, 1, Length[kpoint3D]}];
band4 = Table[{kpoint3D[[i]][[1]], kpoint3D[[i]][[2]], resultlist3[[i]][[4]]},
{i, 1, Length[kpoint3D]}];
band5 = Table[{kpoint3D[[i]][[1]], kpoint3D[[i]][[2]], resultlist3[[i]][[5]]},
{i, 1, Length[kpoint3D]}];
band6 = Table[{kpoint3D[[i]][[1]], kpoint3D[[i]][[2]], resultlist3[[i]][[6]]},
{i, 1, Length[kpoint3D]}];
band7 = Table[{kpoint3D[[i]][[1]], kpoint3D[[i]][[2]], resultlist3[[i]][[7]]},
{i, 1, Length[kpoint3D]}];
band8 = Table[{kpoint3D[[i]][[1]], kpoint3D[[i]][[2]], resultlist3[[i]][[8]]},
{i, 1, Length[kpoint3D]}];
<< "DiscreteMath`ComputationalGeometry`"
b1p = TriangularSurfacePlot[band1, ViewPoint -> {1.484, -2.073, 2.225},
AmbientLight -> RGBColor[1, 0, 0], Axes -> True];
b2p = TriangularSurfacePlot[band2, ViewPoint -> {1.484, -2.073, 2.225},
AmbientLight -> RGBColor[1, 1, 0], Axes -> True];
b3p = TriangularSurfacePlot[band3, ViewPoint -> {1.484, -2.073, 2.225},
AmbientLight -> RGBColor[0, 0, 1], Axes -> True];
b4p = TriangularSurfacePlot[band4, ViewPoint -> {1.484, -2.073, 2.225},
AmbientLight -> RGBColor[1, 1, 0], Axes -> True];
b5p = TriangularSurfacePlot[band5, ViewPoint -> {1.484, -2.073, 2.225},
AmbientLight -> RGBColor[1, 0, 0], Axes -> True];
b6p = TriangularSurfacePlot[band6, ViewPoint -> {1.484, -2.073, 2.225},
AmbientLight -> RGBColor[0, 0, 1], Axes -> True];
b7p = TriangularSurfacePlot[band7, ViewPoint -> {1.484, -2.073, 2.225},
AmbientLight -> RGBColor[0, 0, 1], Axes -> True];
b8p = TriangularSurfacePlot[band8, ViewPoint -> {1.484, -2.073, 2.225},
AmbientLight -> RGBColor[0, 0, 1], Axes -> True];

kpoint3D = Join[p1, p2, p3, p4, p5, p6];
resultlist3D = Table[Chop[Solve[Det[H[kpoint3D[[i]][[1]], kpoint3D[[i]][[2]]] -
S[kpoint3D[[i]][[1]], kpoint3D[[i]][[2]]]*
          energy1] == 0, energy1], 0.01], {i, 1, Length[kpoint3D]}];
res3D = Table[energy1 /. resultlist3D[[i]][[j]], {i, 1, Length[resultlist3D], 1}, {j, 1, 8}];
resultlist3 = Table[Flatten[res3D[[i]]], {i, 1, Length[resultlist3D]}];

In[38]:=
band1 = Table[{kpoint3D[[i]][[1]], kpoint3D[[i]][[2]], resultlist3[[i]][[1]]},
{i, 1, Length[kpoint3D]}];
band2 = Table[{kpoint3D[[i]][[1]], kpoint3D[[i]][[2]], resultlist3[[i]][[2]]},
{i, 1, Length[kpoint3D]}];
band3 = Table[{kpoint3D[[i]][[1]], kpoint3D[[i]][[2]], resultlist3[[i]][[3]]},
{i, 1, Length[kpoint3D]}];
band4 = Table[{kpoint3D[[i]][[1]], kpoint3D[[i]][[2]], resultlist3[[i]][[4]]},
{i, 1, Length[kpoint3D]}];
band5 = Table[{kpoint3D[[i]][[1]], kpoint3D[[i]][[2]], resultlist3[[i]][[5]]},
{i, 1, Length[kpoint3D]}];
band6 = Table[{kpoint3D[[i]][[1]], kpoint3D[[i]][[2]], resultlist3[[i]][[6]]},
{i, 1, Length[kpoint3D]}];
```

```
band7 = Table[{kpoint3D[[i]][[1]], kpoint3D[[i]][[2]], resultlist3[[i]][[7]]},
{i, 1, Length[kpoint3D]}];
band8 = Table[{kpoint3D[[i]][[1]], kpoint3D[[i]][[2]], resultlist3[[i]][[8]]},
{i, 1, Length[kpoint3D]}];
<< "DiscreteMath`ComputationalGeometry`"
b1p = TriangularSurfacePlot[band1, ViewPoint -> {1.484, -2.073, 2.225},
AmbientLight -> RGBColor[1, 0, 0], Axes -> True];
b2p = TriangularSurfacePlot[band2, ViewPoint -> {1.484, -2.073, 2.225},
AmbientLight -> RGBColor[1, 1, 0], Axes -> True];
b3p = TriangularSurfacePlot[band3, ViewPoint -> {1.484, -2.073, 2.225},
AmbientLight -> RGBColor[0, 0, 1], Axes -> True];
b4p = TriangularSurfacePlot[band4, ViewPoint -> {1.484, -2.073, 2.225},
AmbientLight -> RGBColor[1, 1, 0], Axes -> True];
b5p = TriangularSurfacePlot[band5, ViewPoint -> {1.484, -2.073, 2.225},
AmbientLight -> RGBColor[1, 0, 0], Axes -> True];
b6p = TriangularSurfacePlot[band6, ViewPoint -> {1.484, -2.073, 2.225},
AmbientLight -> RGBColor[0, 0, 1], Axes -> True];
b7p = TriangularSurfacePlot[band7, ViewPoint -> {1.484, -2.073, 2.225},
AmbientLight -> RGBColor[0, 0, 1], Axes -> True];
b8p = TriangularSurfacePlot[band8, ViewPoint -> {1.484, -2.073, 2.225},
AmbientLight -> RGBColor[0, 0, 1], Axes -> True];
Export["bands2.dat", band1];
Export["bands2.dat", band2];
Export["bands3.dat", band3];
Export["bands4.dat", band4];
Export["bands5.dat", band5];
Export["bands6.dat", band6];
<< "Graphics`Graphics3D`"
<< "Graphics`Shapes`"
bz3D = Graphics3D[Polygon[{{K1[[1]], K1[[2]], 0}, {K2[[1]], K2[[2]], 0},
{K3[[1]], K3[[2]], 0}, {K4[[1]], K4[[2]], 0},
      {K5[[1]], K5[[2]], 0}, {K6[[1]], K6[[2]], 0}}]];
Show[bz3D];
labeltext=Graphics3D[Text["Energy (eV)",{-3,0,0},{-5.5,0},{0,-1}] ] ;
totalplot = Show[ b1p, b2p, b3p, b4p, b5p, b6p, b7p, b8p, labeltext,
Graphics3D[{Text["", {0, 0, 0}, {0, 0}]}], AspectRatio -> 1,
   ViewPoint -> {1,1.3, 0}, Axes -> {True, True, True}, Boxed -> True,
TextStyle -> {FontSlant -> "Italic", FontSize -> 17},
   AxesLabel -> {"", "", ""}, Ticks -> {{}, {},
{-20, -15, -10, -5, 0, 5, 10, 15, 20, 25, 30, 35}},
   LightSources -> {{{1., 0., 1.}*3, RGBColor[1, 0, 0]}, {{1., 1., 1.}*3,
RGBColor[0, 1, 0]}, {{0., 1., 1.}*3, RGBColor[0, 0, 1]}},
   Shading -> True, PlotLabel -> "(b)", PlotRange -> {-20.1, 35.1}]
Export["/misc/flex/students/alex/mathematica/thesis/totalplot2.eps", totalplot]
```

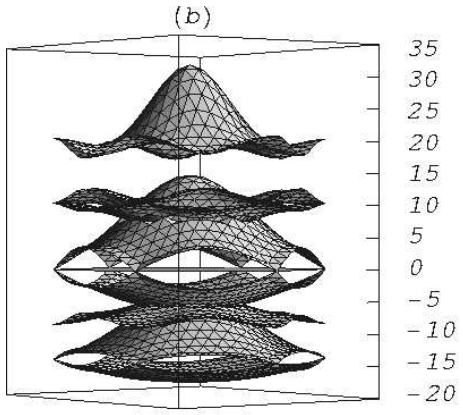

Figure A.4: Output of the Mathematica program (3) for σ and π electron dispersion relations.

Bibliography

[1] S. Iijima, Nature (London) **354**, 56–58 (1991).

[2] S. Iijima and T. Ichihashi, Nature (London) **363**, 603 (1993).

[3] R. Saito, M. Fujita, G. Dresselhaus, and M. S. Dresselhaus, Appl. Phys. Lett. **60**, 2204–2206 (1992).

[4] R. Saito, G. Dresselhaus, and M. S. Dresselhaus, *Physical Properties of Carbon Nanotubes* (Imperial College Press, London, 1998).

[5] Y. Cheng and O. Zhou, C. R. Physique **4**, 1021 (2003).

[6] J. Zhang, J. Tang, G. Yang, Q. Qiu, Lu-Chang Qin, and O. Zhou, Advanced Materials **16**, 1219 (2004).

[7] S. J. Tans, R. M. Verschueren, and C. Dekker, Nature **393**, 49–52 (1998).

[8] H. W. C. Postma, T. Teepen, Z. Yao, M. Grifoni, and C. Dekker, Science **293**, 76–79 (2001).

[9] S. J. Tans, M. H. Devoret, H. Dai, A. Thess, R. E. Smalley, L. J. Geerligs, and C. Dekker, Nature (London) **386**, 474–477 (1997).

[10] M. Milnera, J. Kürti, M. Hulman, and H. Kuzmany, Phys. Rev. Lett. **84**, 1324–1327 (2000).

[11] H. Kuzmany, W. Plank, M. Hulman, Ch. Kramberger, A. Grüneis, Th. Pichler, H. Peterlik, H. Kataura, and Y. Achiba, Euro. Phys. J. B **22**, 307–320 (2001).

[12] G. S. Duesberg, I. Loa, M. Burghard, K. Syassen, and S. Roth, Phys. Rev. Lett. **85**, 5436–5439 (2000).

[13] A. Jorio, R. Saito, J. H. Hafner, C. M. Lieber, M. Hunter, T. McClure, G. Dresselhaus, and M. S. Dresselhaus, Phys. Rev. Lett. **86**, 1118–1121 (2001).

[14] S. M. Bachilo, M. S. Strano, C. Kittrell, R. H. Hauge, R. E. Smalley, and R. B. Weisman, Science **298**, 2361–2366 (2002).

[15] S. Maruyama, Y. Miyauchi, Y. Murakami, and S. Chiashi, New Journal of Physics **5**, 149 (2004).

[16] S. Grace Chou et al., Phys. Rev. Lett. **unpublished** (2004).

[17] H. Kataura, Y. Kumazawa, Y. Maniwa, I. Umezu, S. Suzuki, Y. Ohtsuka, and Y. Achiba, Synthetic Metals **103**, 2555–2558 (1999).

[18] C. Journet, W. K. Maser, P. Bernier, A. Loiseau, M. Lamy de la Chapelle, S. Lefrant, P. Deniard, R. Lee, and J. E. Fischer, Nature (London) **388**, 756–758 (1997).

[19] A. Thess, R. Lee, P. Nikolaev, H. Dai, P. Petit, J. Robert, C. Xu, Y. H. Lee, S. G. Kim, A. G. Rinzler, D. T. Colbert, G. E. Scuseria, D. Tománek, J. E. Fischer, and R. E. Smalley, Science **273**, 483–487 (1996).

[20] C. Bowerm, O. Zhou, W. Zhu, D.J. Werder, and S. Jin, Applied Physics Letters **77**, 17 (2000).

[21] M. J. Bronikowski, P. A. Willis, D. T. Colbert, K. A. Smith, and R. E. Smalley, Journal of Vacuum Science and Technology **19**, 1800 (2001).

[22] T. Tomonari and M.A. Pimenta, unpublished. This work was carried out during the visit of M.A. Pimenta to University of Electro–Communications, Tokyo. (2002).

[23] M. J. O'Connell, S. M. Bachilo, X. B. Huffman, V. C. Moore, M. S. Strano, E. H. Haroz, K. L. Rialon, P. J. Boul, W. H. Noon, C. Kittrell, J. Ma, R. H. Hauge, R. B. Weisman, and R. E. Smalley, Science **297**, 593–596 (2002).

[24] X. Liu, T. Pichler, M. Knupfer, M.S.Golden, J. Fink, H. Kataura, and Y. Achiba, Phys. Rev. B **66**, 45411 (2002).

[25] M. Yudasaka, M. Zhang, and S. Iijima, Chemical Physics Letters **374**, 132 (2003).

[26] Y. Miyauchi, S. Chiashi, Y. Murakami, Y. Hayashida, and S. Maruy, Chem. Phys. Lett. **387**, 198 (2004).

[27] M. S. Dresselhaus, G. Dresselhaus, A. Jorio, A. G. Souza Filho, and R. Saito, Carbon **40**, 2043–2061 (2002).

[28] M. S. Dresselhaus and P. C. Eklund, Advances in Physics **49**, 705–814 (2000).

[29] P.J. Herrero, S. Sapmaz, L.P.Kouwenhoven, and H.S.J. van der Zant, Nature **429**, 389 (1958).

[30] A. Rubio, J. L. Corkill, and M. L. Cohen, Phys. Rev. B **49**, 5081 (1994).

[31] P. R. Wallace, Phys. Rev. **71**, 622 (1947).

[32] K. Nakada, M. Fujita, G. Dresselhaus, and M. S. Dresselhaus, Phys. Rev. B **54**, 17954–17961 (1996).

[33] Ming-Fa Lin and Shyu F. Journal Phys. Soc. Japan. **69**, 3529 (2000).

[34] Y. Miyamoto, K. Nakada, and M. Fujita, Phys. Rev. B **59**, 9858 (1998).

[35] M. Fujita, K. Wakabayashi, K. Nakadw, and K. Kusakabe, J. Phys. Soc. Japan **65**, 1920–1923 (1996).

[36] R. Saito, G. Dresselhaus, and M. S. Dresselhaus, Phys. Rev. B **61**, 2981–2990 (2000).

[37] H. Ajiki and T. Ando, Physica B Condensed Matter **201**, 349 (1994).

[38] R. A. Jishi, L. Venkataraman, M. S. Dresselhaus, and G. Dresselhaus, Chem. Phys. Lett. **209**, 77–82 (1993).

[39] N. Wakabayashi, R. M. Nicklow, and H. G. Smith, Phys. Rev. B **5**, 4951 (1972).

[40] T. Aizawa, R. Souda, S. Otani, Y. Ishizawa, and C. Oshima, Phys. Rev. B **42**, 11469 (1990).

[41] R. E. Palmer, J. L. Wilkes, and R. F. Willis, Journal of Electron Spectroscopy **44**, 355 (1987).

[42] S. Siebentritt, R. Pues, K.-H. Rieder, and A. M. Shikin, Phys. Rev. B **55**, 7927–7934 (1997).

[43] J. Maultzsch, S. Reich, C. Thomsen, and H. Requardt, Phys. Rev. Lett. **92**, 75501 (2004).

[44] O. Dubay and G. Kresse, Phys. Rev. B **67**, 35401 (2002).

[45] S. Guha, J. Menéndez, J. B. Page, and G. B. Adams, Phys. Rev. B **53**, 13106 (1996).

[46] R. Saito, T. Takeya, T. Kimura, G. Dresselhaus, and M. S. Dresselhaus, Phys. Rev. B **57**, 4145–4153 (1998).

[47] A. Jorio, A. G. Souza Filho, G. Dresselhaus, M. S. Dresselhaus, A. K. Swan, M. S. Ünlü, B. Goldberg, M. A. Pimenta, J. H. Hafner, C. M. Lieber, and R. Saito, Phys. Rev. B **65**, 155412 (2002).

[48] A. Jorio, G. Dresselhaus, M. S. Dresselhaus, M. Souza, M. S. S. Dantas, M. A. Pimenta, A. M. Rao, R. Saito, C. Liu, and H. M. Cheng, Phys. Rev. Lett. **85**, 2617–2620 (2000).

[49] Ge. G. Samsonidze, R. Saito, A. Jorio, A. G. Souza Filho, A. Grüneis, M. A. Pimenta, G. Dresselhaus, and M. S. Dresselhaus, Phys. Rev. Lett. **90**, 027403 (2003).

[50] F. Tuinstra and J. L. Koenig, J. Phys. Chem. **53**, 1126 (1970).

[51] M. A. Pimenta, E. B. Hanlon, A. Marucci, P. Corio, S. D. M. Brown, S. A. Empedocles, M. G. Bawendi, G. Dresselhaus, and M. S. Dresselhaus, Brazilian J. Phys. **30**, 423–427 (2000).

[52] M. J. Matthews, M. A. Pimenta, G. Dresselhaus, M. S. Dresselhaus, and M. Endo, Phys. Rev. B **59**, R6585–R6588 (1999).

[53] C. Thomsen and S. Reich, Phys. Rev. Lett. **85**, 5214 (2000).

[54] J. Kürti, V. Zólyomi, A. Grüneis, and H. Kuzmany, Phys. Rev. B **65**, 165433–(1–9) (2002).

[55] R. Saito, A. Jorio, A. G. Souza Filho, G. Dresselhaus, M. S. Dresselhaus, and M. A. Pimenta, Phys. Rev. Lett. **88**, 027401 (2002).

[56] R. M. Martin and L. M. Falicov, in *Light Scattering in Solids I: edited by M. Cardona*, pages 70–145, (Springer-Verlag, Berlin, 1983), Vol. 8. Chapter 3, Topics in Applied Physics.

[57] A. Grüneis, R. Saito, T. Kimura, L. G. Cançado, M. A. Pimenta, A. Jorio, A. G. Souza Filho, G. Dresselhaus, and M. S. Dresselhaus, Phys. Rev. B **65**, 155405–1–7 (2002).

[58] L. G. Cançado, M. A. Pimenta, R. Saito, A. Jorio, L. O. Ladeira, A. Grüneis, A. G. Souza Filho, G. Dresselhaus, and M. S. Dresselhaus, Phys. Rev. B **66**, 035415 (2002).

[59] A. Grüneis, R. Saito, Ge. G. Samsonidze, T. Kimura, M. A. Pimenta, A. Jorio, A. G. Souza Filho, G. Dresselhaus, and M. S. Dresselhaus, Phys. Rev. B **67**, 165402–1–165402–7 (2003).

[60] Y. Zhao, X. Wang, C.C. Ma, and G. Chen, Chem. Phys. Lett. **387**, 149 (2004).

[61] R. Saito, A. Grüneis, Ge. G. Samsonidze, G. Dresselhaus, M. S. Dresselhaus, A. Jorio, L. G. Cançado, M. A. Pimenta, and A. G. Souza, Appl. Phys. A **78**, 1099–1105 (2004).

[62] Cançado, M. A. Pimenta, A. Jorio, R. A. Neves, G. Medeiros-Ribeiro, T. Enoki, Y. Kobayashi, K. Takai, K. Fukui, M. S. Dresselhaus, and R. Saito, Phys. Rev. Lett. (2004). submitted 12/15/03.

[63] Cançado, M. A. Pimenta, A. Jorio, R. A. Neves, G. Medeiros-Ribeiro, T. Enoki, Y. Kobayashi, K. Takai, K. Fukui, M. S. Dresselhaus, and R. Saito, Phys. Rev. Lett. (2004).

[64] J. Jiang, R. Saito, A. Grüneis, G. Dresselhaus, and M. S. Dresselhaus, Phys. Rev. B (2004).

[65] A. Grüneis, R. Saito, J. Jiang, Ge. G. Samsonidze, M. A. Pimenta, A. Jorio, A. G. Souza Filho, G. Dresselhaus, and M. S. Dresselhaus, Chem. Phys. Lett. **387**, 301–306 (2004).

[66] H. Kataura, Y. Kumazawa, Y. Maniwa, I. Uemezu, S. Suzuki, Y. Ohtsuka, and Y. Achiba, Synt. Met. **103**, 2555 (1999).

[67] A. G. Souza Filho, S. G. Chou, Ge. G. Samsonidze, G. Dresselhaus, M. S. Dresselhaus, Lei An, J. Liu, Anna K. Swan, M. S. Ünlü, B. B. Goldberg, A. Jorio, A. Grüneis, and R. Saito, Phys. Rev. B **69**, 115428 (2004).

[68] R. B. Weisman and S. M. Bachilo, Nano Lett. (Communication) **3**, 1235 (2003).

[69] M. A. Pimenta, A. Marucci, S. D. M. Brown, M. J. Matthews, A. M. Rao, P. C. Eklund, R. E. Smalley, G. Dresselhaus, and M. S. Dresselhaus, J. Mater. Research **13**, 2396–2404 (1998).

[70] H. Ajiki and T. Ando, J. Phys. Soc. Jpn. **62**, 2470–2480 (1993). Erratum: ibid page 4267.

[71] A. Jorio, A. G. Souza Filho, V. W. Brar, A. K. Swan, M. S. Ünlü, B. B. Goldberg, A. Righi, J. H. Hafner, C. M. Lieber, R. Saito, G. Dresselhaus, and M. S. Dresselhaus, Phys. Rev. B Rapid **65**, R121402 (2002).

[72] Z. Yu and L. E. Brus, J. Phys. Chem. B **105**, 1123 (2001).

[73] A. M. Rao, A. Jorio, M. A. Pimenta, M. S. S. Dantas, R. Saito, G. Dresselhaus, and M. S. Dresselhaus, Phys. Rev. Lett. **84**, 1820–1823 (2000). see also: Comment in PRL 85, 3545 (2000).

[74] M. Ziman J. (1958).

[75] R. Saito, A. Jorio, J. H. Hafner, C. M. Lieber, M. Hunter, T. McClure, G. Dresselhaus, and M. S. Dresselhaus, Phys. Rev. B **64**, 085312–085319 (2001).

[76] R. Saito, A. Jorio, A. G. Souza Filho, A. Grüneis, M. A. Pimenta, G. Dresselhaus, and M. S. Dresselhaus, Physica B **323**, 100–106 (2002). (Carbon Nanotubes: Tenth anniversary Symposium Proceedings, Tsukuba, October 2001).

[77] R. Al-Jishi and G. Dresselhaus, Phys. Rev. B **26**, 4514 (1982).

[78] Y. Kawashima and G. Katagiri, Phys. Rev. B **52**, 10053–10059 (1995).

[79] Y. Kawashima and G. Katagiri, Phys. Rev. B **59**, 62–64 (1999).

[80] P. H. Tan, C. Y. Hu, J. Dong, W. C. Shen, and B. F. Zhang, Phys. Rev. B **64**, 214301 (2001).

[81] P.-H. Tan, Y. Tang, Y.-M. Deng, F. Li, Y. L. Wei, and H. M. Cheng, Appl. Phys. Lett. **75**, 1524–1526 (1999).

[82] C.M. Mapelli, C. Castiglioni, G. Zerbi, and K. Müllen, Phys. Rev. B **60**, 12710–12725 (1999).

[83] A. Hartschuh, E. J. Sanchez, X. S. Xie, and L. Novotny, Phys. Rev. Lett. **90**, 95503 (2003).

Publication list

PUBLICATION LIST (4.2001 - present):
First Author Publications:

1. **Determination of two-dimensional phonon dispersion relation of graphite by Raman spectroscopy**. A. Grüneis, R. Saito, T. Kimura, L. G. Cancado, M. A. Pimenta, A. Jorio, A. G. Souza Filho, G. Dresselhaus, and M. S. Dresselhaus, *Phys. Rev.* **B 65** 155405 (2002).

2. **Inhomeogeneous optical absorption around K point in graphite and carbon nanotubes**. A. Grüneis, R. Saito, Ge.G. Samsonidze, T. Kimura, L. G. Cancado, M. A. Pimenta, A. Jorio, A. G. Souza Filho, G. Dresselhaus, and M. S. Dresselhaus, *Phys. Rev.* **B 67** 165402 (2003).

3. **Resonant Raman spectra of carbon nanotubes observed by perpendicularly polarized light**. A. Grüneis, R. Saito, J.Jiang, Ge.G. Samsonidze, L. G. Cancado, M. A. Pimenta, A. Jorio, A. G. Souza Filho, G. Dresselhaus, and M. S. Dresselhaus, *Chem. Phys. Lett.* **387** 301-306 (2004).

Co-Author Publications:

1. **Determination of SWCNT diameters from the Raman response of the radial breathing mode**. Kuzmany H, Plank W, Hulman M, Kramberger C, Grüneis A, Pichler T, Peterlik H, Kataura H, Achiba Y, *Eur. J. Phys.* **B 22** 307 (2001).

2. **Dispersive Raman spectra observed in graphite and single wall carbon nanoubes**. R. Saito, A. Jorio, A. G. Souza Filho, A. Grueneis, M. A. Pimenta, G. Dresselhaus, and M. S. Dresselhaus *Physica B* **323** 100-106 (2002).

3. **Double resonance Raman spectra in disordered graphite and single wall carbon nanotubes**. R. Saito, A. Grüneis, L. G. Cancado, M. A. Pimenta, A. Jorio, A. G. Souza Filho, G. Dresselhaus and M. S. Dresselhaus *Liq. Crys. Mol. Crys.* **387** (287-296) (2002).

4. **Stokes and anti-Stokes double resonance Raman scattering in two-dimensional graphite**. L. G. Cancado, M. A. Pimenta, R. Saito, A. Jorio, L. O. Ladeira, A. Grüneis, A. G. Souza-Filho, G. Dresselhaus, and M. S. Dresselhaus, *Phys. Rev.* **B 66** 035415 (2002).

5. **First and second-order resonance Raman process in graphite and single wall carbon nanotubes**. Saito R, Jorio A, Souza AG, Dresselhaus G, Dresselhaus MS, Grüneis A, Cancado LG, Pimenta MA, *Japanese Journal of Applied Physics* **41** 4878 (2002).

6. **Double resonant Raman phenomena enhanced by van Hove singularities in single-wall carbon nanotubes**. J. Kürti, V. Zolyomi, A. Grüneis, and H. Kuzmany , *Phys. Rev.* **B 65** 165433 (2002).

7. **Phonon trigonal warping effect in graphite and carbon nanotubes**. Samsonidze GG, Saito R, Jorio A, Souza AG, Grüneis A, Pimenta MA, Dresselhaus G, Dresselhaus MS, *Phys. Rev. Lett.* **90** 027403 (2003).

8. **Origin of the fine structure of the Raman D band in single-wall carbon nanotubes**. Zolyomi V, Kürti J, Grüneis A, Kuzmany H , *Phys. Rev. Lett.* **90** 157401 (2003).

9. **The Concept of Cutting Lines in Carbon Nanotube Science**. Ge. G. Samsonidze, R. Saito, A. Jorio, M. A. Pimenta, A. G. Souza Filho, A. Grüneis, G. Dresselhaus. and M. S. Dresselhaus , *Journal of Nanoscience and Nanotechnology* **3** 431-458 (2003).

10. **Interband optical transitions in left and right handed single wall carbon nanotubes**. Ge.G. Samsonidze, A. Grüneis, R. Saito, A. Jorio, M. A. Pimenta, A. G. Souza Filho, G. Dresselhaus, M. S. Dresselhaus, *Phys. Rev.* **B 64**, 205402 (2003).

11. **Optical absorption in single wall carbon nanotubes**. Jie Jiang, R. Saito, A. Grüneis, G. Dresselhaus, M. S. Dresselhaus, *accepted Carbon*, (2004).

12. **Stokes and anti-Stokes Raman spectra of small diameter isolated carbon nanotubes**. A. G. Souza Filho , S. G. Chou,a Ge. G. Samsonidze, G. Dresselhaus, M. S. Dresselhaus Lei An, J. Liu , Anna K. Swan, M. S. Unlu, B. B. Goldberg, A. Jorio, A. Grüneis, R. Saito, Phys. Rev. **B 69**, 115428 (2004).

13. **Optical absorption of graphite and single wall carbon nanotubes**. R. Saito, A.Grüneis, Ge. G. Samsonidze, G. Dresselhaus, M. S. Dresselhaus, L. G. Cancado, M. A. Pimenta, A. G. Souza Filho, *Applied Physics A* **78** Number 8 1099 (2003).

14. **Double resonance Raman spectroscopy of single wall carbon nanotubes**. R. Saito, A. Grüneis, Ge. G. Samsonidze, V. W. Brar, G. Dresselhaus, M. S. Dresselhaus, A. Jorio, L. G. Cancado, C. Fantini, M. A. Pimenta, A. G. Souza Filho, *New Journal of Physics* **5** 157 (2003).

15. **Electron–phonon interaction and relaxation time in graphite**. J.Jiang, R. Saito, A. Grüneis, G. Dresselhaus, M. S. Dresselhaus *accepted Chem. Phys. Lett.* (2004).

TALKS:

1. **Determination of Graphite Force constants by Raman Spectroscopy**. A.Grüneis, R.Saito, T.Kimura, C.C.Cancado,M.A.Pimenta, A.Jorio, A.G.Souza Filho, G.Dresselhaus, M.S.Dresselhaus, *Japanese Physical Society Meeting, Ritsumeikan University, Kyoto*, March 24-27 , 2002.

2. **Inhomogeneous optical absorption around K edge in Nanographite and Carbon Nanotubes**. A. Grüneis, R.Saito, T.Kimura, M.A.Pimenta, A.Jorio, A.G.Souza Filho, G.Dresselhaus, M.S.Dresselhaus, *Japanese Physical Society Meeting , Chubu University, Nagoya*, Sept. 6-9 , 2002.

3. **Characterization of nanographite and carbon nanotubes by polarization dependent optical spectroscopy**. A. Grüneis, R. Saito, Ge.G. Samsonidze, M.A. Pimenta, A. Jorio, A.G. Souza Filho, G. Dresselhaus, M.S. Dresselhaus, *MRS Fall Meeting, Boston, USA*, Dec.2-6 , 2002.

4. **Anisotropic Raman scattering in the k space of graphite and carbon nanotubes**. A. Grüneis, R. Saito, Ge.G. Samsonidze, M.A. Pimenta, A. Jorio, A.G. Souza Filho, M.S. Dresselhaus, G. Dresselhaus, *APS Meeting Austin, USA*, March 2-6 , 2003

5. **Electron-phonon interaction in graphite and Carbon Nanotubes**. A.Grüneis, R.Saito, T. Kimura, A. Jorio, A. G. Souza Filho, G. Dresselhaus, M. S. Dresselhaus , M. A. Pimenta, *Japanese Physical Society Meeting Tohoku University, Sendai*, March 28-31 , 2003.

6. **Tight binding method and Raman spectra in small diameter carbon nanotubes**. A. Grüneis, R.Saito, Ge.G.Samsonidze, A. Jorio, M.A.Pimenta, A.G.Souza Filho, G.Dresselhaus, M.S.Dresselhaus, *Japanese Physical Society Meeting Tsushima Campus, Okayama University* Sept. 20-23 , 2003.

7. **Resonant Raman Intensity calculations in graphite and carbon nanotubes**. A. Grüneis, R.Saito, J.Jiang, G.Dresselhaus, M. S. Dresselhaus *Fullerene Symposium, Okazaki* Jan. 6-9 , 2004.

Proceedings:

1. **Optical properties of Nanographite and Carbon Nanotubes** Grüneis, A., Saito, R., Samsonidze, Ge. G., Pimenta, M. A., Jorio, A., Souza Filho, A. G., Dresselhaus, G., Dresselhaus, M. S., *Quantum Confined Semiconductor Nanostructures* , MRS Symposium Proceedings, Eds. Buriak, J. M. , Wayner, D. D. M., Priolo, F., White, B., Klimov, V., Tsybeskov, L. , Materials Research Society Press, Vol. 737-C, F3.47, 2003

2. **Electron–phonon interaction and Raman intensities in graphite** Grüneis, A., Saito, R., J.jiang, Cancado, M.A.Pimenta, A. Jorio, C. Fantini, M.A.Pimenta, Samsonidze, Ge. G., Dresselhaus, G., Dresselhaus, M. S., Souza Filho, A. G. *International Winterschool on electronic properties of new materials* Eds. H. Kuzmany (2004)